



Saurashtra University

Re – Accredited Grade 'B' by NAAC
(CGPA 2.93)

Lakhani, Vinay K., 2011, “*Studies on pre- and post effect of rapid thermal quenching on magnetic and transport properties of copper-ferri-aluminates*”, thesis PhD, Saurashtra University

<http://etheses.saurashtrauniversity.edu/id/877>

Copyright and moral rights for this thesis are retained by the author

A copy can be downloaded for personal non-commercial research or study, without prior permission or charge.

This thesis cannot be reproduced or quoted extensively from without first obtaining permission in writing from the Author.

The content must not be changed in any way or sold commercially in any format or medium without the formal permission of the Author

When referring to this work, full bibliographic details including the author, title, awarding institution and date of the thesis must be given.

Saurashtra University Theses Service
<http://etheses.saurashtrauniversity.edu>
repository@sauuni.ernet.in

Studies on pre- and post effect of rapid thermal
quenching on magnetic and transport properties
of copper-ferri-aluminates

THESIS

Submitted to the
Saurashtra University, Rajkot, India
For
The Degree of
DOCTOR OF PHILOSOPHY
In PHYSICS

By

Vinay K. Lakhani

Under the supervision of

Dr. Kunal B. Modi

Associate Professor
Department of Physics
Saurashtra University
RAJKOT, INDIA

May - 2011

Statements under O.Ph.D.7 of Saurashtra University

The work presented in this thesis is my own work carried out under the supervision of Dr. K. B. Modi, leads to some important contributions in Physics supported by necessary references.

Date: 30th May 2011

Place: Rajkot

(V. K. Lakhani)


CERTIFICATE

This is to certify that the present work submitted for the Ph.D. degree in Physics of Saurashtra University, Rajkot, by Vinay K. Lakhani has been the result of about six years of work under my supervision and is a valuable contribution in the field of Condensed Matter Physics.

Date: 30th May 2011

Place: Rajkot

(K. B. Modi)
Associate Professor
Department of physics
Saurashtra University
Rajkot (INDIA)



ACKNOWLEDGEMENTS

First of all, I would like to acknowledge with sincere gratitude to my guide **Dr. Kunal B. Modi**, who provided a meaningful insight into the study and helped to understand the several concepts of physics. His inspiring guidance and consistent encouragement made this work in the present form.

I am highly indebted to Dr. G. J. Baldha for his continues encouragement and useful discussion during the course of work.

I am truly grateful to Professor H. H. Joshi, Head Department of Physics, Saurashtra University, Rajkot, for his kind support during this work. I am pleased to acknowledge the support received from Professors K. N. Iyer, B. J. Mehta, M. J. Joshi, H. P. Joshi, D. G. Kuberkar and Dr. J. A. Bhalodia.

I am thankful to Professor B. C. Zhao and Dr. L. Wang, Division of Physics and Applied Physics, Nanyang technology University, Singapore for the PPMS facility. Thank is also due to Dr. Uday N. Trivedi for his help in PPMS measurements. The X-ray, EDAX, SEM, facilities provided by SICART, V. V. Nagar are gratefully acknowledged. I wish to express special thanks to Dr. A. K. Yahya, School of Physics and Materials studies, University Technology Mara, Malayasia for his help in elastic properties data collection and Professor K. M. Jadhav, Department of Physics, Dr. B.A.M. University, Aurangabad, Maharashtra for providing experimental facility of low field a.c. susceptibility measurements.

I place on record thanks to my research colleagues and friends Mr. Nimish Vasoya, Mr. Tushar Pathak and Mr. Janmejy Buch for their self-less and untiring co-operation during my thesis work.

My sincere thanks are due for senior colleagues and friends Mr. Mitesh Pandya, for their help and moral support.

I am thankful to my research colleagues Mr. Kiran G. Saija, Mr. Kiritsinh B. Zankat, Mr. Raj Bhesania, Mr. Kunal Mehta, Mr. Ashish Tanna and Mrs. Daxa Mehta for their company and making my time cheerful during the laboratory work.

I am thankful to my research colleagues and friends Dr. Bharat Parekh, Dr. Niraj Pandya, Dr. Ritweej Rajiv Ranjan, Mr. Ketan Pareekh, Mr. Chetan Chauhan, Mr. Dipak Dave, Mr. Poorvesh Vyas, Mr. Rakesh Hajiyani, Mr. Kaushal Mehta, Mr. Savan Makadia, Mr. Jagdish Baraliya for providing friendly environment at the department.

I am grateful to come across several life-long friends Atul, Bhavesh, Bharat, Chetan, Himanshu, Jaysukh, Nilesh, Rajnikant, Tejas, Prashant, Sanjay, Mitul and Ravi for sharing my joy and sadness, and offering instant help whenever needed.

I express my thanks to Dr. H. J. Pandya for providing me technical advice regarding the experimental set - up. I am thanks to the workshop staff for their cooperation. I specially thank Mr. M. J. Meghapara for fabricating sample holder and other technical help during my work.

Many thanks to Purvi Madam and Shrey for a good hospitality during the course work.

I express my sincere gratitude to my family, for their moral support to complete this work successfully.

Finally, I would like to thank to all those who helped me knowingly or unknowingly during the completion of this work.

Vinay K. Lakhani



Academic Achievements (Award)

Prof. Dolarrai Mankand Award for Excellence in Research, by Saurashtra University, Rajkot, Gujarat for published Research paper in the year 2009-2010, confirmed on 23 May 2011.

Chandubhai Patel (Vakil) Foundation for the Shri N. M. Patel **Research Award for the Best Indigenous, Innovative research paper during the year 2006-07** Published in the subject of Materials Science and Nano Technology.

List of Publications

1. **Ultrasonic studies on aluminium substituted Bi(Pb)-2223 superconductors**
M. B. Solunke, P. U. Sharma, M. P. Pandya, **V. K. Lakhani**, K. B. Modi, P. V. Reddy and S. S. Shah
PRAMANA- Journal of Physics **65** (3) (2005) 481-490
2. **Study on the electrical and dielectric behaviour of Zn-substituted cobalt ferri aluminates**
N. H. Vasoya, **V. K. Lakhani**, P. U. Sharma, K. B. Modi, Ravi Kumar and H. H. Joshi
Journal of Physics: Condensed Matter **18** (2006) 8063-8092
3. **Study of elastic properties of fine particle copper-zinc ferrites through Infrared spectroscopy**
K. B. Modi, U. N. Trivedi, P. U. Shrama, **V. K. Lakhani**, M. C. Chhantbar and H. H. Joshi
Indian Journal of Pure & Applied Physics **44** (2006) 165-168
4. **Study of electric and dielectric properties of Mn⁴⁺- substituted cobalt ferrite**
V. K. Lakhani, P. U. Sharma, K. G. Saija K. B. Zankat and K. B. Modi
Indian Journal of Physics **80** (8) (2006) 789-796
5. **Effect of Ag⁺- addition on elastic behaviour of Bi-2212 superconductors**
M. B. Solunke, K. B. Modi, **V. K. Lakhani**, K. B. Zankat, P. U. Sharma, P. V. Reddy and S. S. Shah

6. **Effect of nickel substitution on structural, infrared and elastic properties of lithium ferrite.**
S. S. Bhatu, **V. K. Lakhani**, A. R. Tanna, N. H. Vasoya, J. U. Buch, P. U. Sharma, U. N. Trivedi, H. H. Joshi and K. B. Modi
Indian Journal of Pure & Applied Physics, **45** (2007) 596-608
7. **Elastic properties of gallium substituted Bi(Pb)-2212 superconducting system at 300K**
M. B. Solunke, P. U. Sharma, **V. K. Lakhani**, M. P. Pandya, K. B. Modi, P. V. Reddy, S. S. Shah
Ceramics International **33** (2007) 21-26
8. **Mossbauer Spectroscopic studies of Fe³⁺-substituted YIG**
P. U. Sharma, K. B. Modi, **V. K. Lakhani**, K. B. Zankat and H. H. Joshi
Ceramics International **33** (2007) 1543-1546
9. **High temperature thermoelectric power study on calcium substituted lanthanum manganites**
J. J. U. Buch, T. K. Pathak, **V. K. Lakhani**, N. H. Vasoya, and K. B. Modi
Journal of Physics D: Applied Physics **40** (2007) 5306-5312
10. **Structure and elastic properties of Ca-substituted LaMnO₃ at 300K**
J. J. U. Buch, G. Lalitha, T. K. Pathak, N. H. Vasoya, **V. K. Lakhani**, P. V. Reddy, Ravi Kumar and K. B. Modi
Journal of Physics D: Applied Physics **41**(2) (2008) 025406
11. **CCNR type high field instability in Ti⁴⁺-substituted Mn-Zn ferrites**
K G Saija, U S Joshi, **V K Lakhani** and K B Modi
Journal of Physics D: Applied Physics **42** (2009) 165402 (5pp)
12. **Structural and magnetic phase evolution study on needle-shaped nanoparticles of magnesium ferrite**
T.K. Pathak, N.H. Vasoya, **V.K. Lakhani** and K.B. Modi
Ceramics International **36** (2010) 275–281
13. **Synthesis of nanostructured material by mechanical milling and study on structural property modifications in Ni_{0.5}Zn_{0.5}Fe₂O₄**
N.H. Vasoya, L.H. Vanpariya, P.N. Sakariya, M.D. Timbadiya, T.K. Pathak, **V.K. Lakhani** and K.B. Modi
Ceramics International **36** (2010) 947–954

14. **X-ray Debye temperature of mechanically milled $\text{Ni}_{0.5}\text{Zn}_{0.5}\text{Fe}_2\text{O}_4$ spinel ferrite**
K. B. Modi, T. K. Pathak, N. H. Vasoya, **V. K. Lakhani**, G. J. Baldha and P. K. Jha
Indian Journal of Physics 85(3) (2011)411-420
15. **Al^{3+} - modified elastic properties of copper ferrite**
V. K. Lakhani and K. B. Modi
Solid State Sciences, 12 (2010) 2134-2143
16. **Structural parameters and x-ray Debye temperature determination study on copper-ferrite-aluminates**
V. K. Lakhani, T. K. Pathak, N. H. Vasoya and K. B. Modi
Solid State Sciences, 13 (2011) 539-547
17. **Effect of Al^{3+} - substitution on the transport properties of copper ferrite**
V. K. Lakhani and K. B. Modi
Journal of Physics D: Applied Physics 44 (2011)
18. **Negative magnetization, magnetic anisotropy and magnetic ordering studies on Al^{3+} -substituted copper ferrite**
V. K. Lakhani, Bangchuan Zhao, Lan Wang, U. N. Trivedi and K. B. Modi
Journal of Alloys and Compounds 509 (2011) 4861-4867
19. **Structural parameters and resistive switching phenomenon study of $\text{Cd}_{0.25}\text{Co}_{0.75}\text{Fe}_2\text{O}_4$ ferrite thin film**
U. V. Chhaya, **V. K. Lakhani**, K. B. Modi and U. S. Joshi
Indian journal of Pure & Applied Physics (2011)
20. **Infrared spectral analysis, optical, elastic and thermodynamical properties of Al^{3+} - substituted Cupro-spinel**
V. K. Lakhani and K. B. Modi
Vibrational Spectroscopy (2011)

Research Papers Presented at National Conferences

- 1. Comparative study of Magnetic Behaviour of $\text{Co}_{1+x}\text{R}_x\text{Fe}_{2-2x}\text{O}_4$ Spinel Ferrite System**
M. C. Chhantbar, K. P. Thummer, U. N. Trivedi, S. S. Bhatu,
V. K. Lakhani
48th DAE Solid State Physics Symposium **46**(2003) 839 Jiwaji University,
Gwalior.
- 2. Temperature Dependent Dielectric Behaviour of Mn^{4+} Substituted Cobalt Ferrite**
V. K. Lakhani, H. G. Vora, K. G. Saija, K. B. Modi and G. J. Baldha
49th DAE Solid State Physics Symposium (2004) 744 Guru Nanak Dev
University, Amritsar.
- 3. Elastic constants determination for bulk metallic glasses and alloys- A Simple theoretical approach**
K. B. Zankat, **V. K. Lakhani**, N. H. Vasoya, V. R. Rathod and K. G. Saija
51st DAE Solid State Physics Symposium (2006) Barkatullah University,
Bhopal.
- 4. Unusual magnetic properties of nanocrystalline $\text{Mg}_x\text{Mn}_{1-x}\text{Fe}_2\text{O}_4$ ($x = 0.2, 0.4$) synthesized by co-precipitation method**
T. K. Pathak, **V. K. Lakhani**, N. H. Vasoya, K. G. Saija, A. G. Makwana
and K. B. Modi
52nd DAE Solid State Physics Symposium (2007) University of Mysore,
Mysore.
- 5. Jahn-Teller distortion and structural property study on quenched Copper-ferri aluminates**
V. K. Lakhani, T. K. Pathak and K. B. Modi
53rd DAE Solid State Physics Symposium (2008) BARC Mumbai.

Conferences & Workshops Attended

International

1. **International symposium on “Nanostructured Materials: Structure, Properties and Applications (ISNM-2009)” Jalandhar (Punjab) October 2009**

Magnetic phase evolution and particle size estimation study on nanocrystalline Mg-Mn ferrites

T. K. Pathak, N. H. Vasoya, **V. K. Lakhani** and K. B. Modi

National

1. **Operation, Maintenance and Utilization of Electronic Instruments**
Organized by IAPT Kanpur & Department of Physics, Saurashtra University, Rajkot
During 7 to 13 October, 2002
2. **National Seminar on Progress in Luminescence and its applications**
Organized by Department of Physics, Bahauddin Science College, Junagadh & Luminescence Society of India. During 14th December, 2002
3. **National Workshop On Prospects of Astronomy Research in Universities**
Department of Physics, Saurashtra University Rajkot. During 25-27 February 2004.
4. **XVIII Gujarat Science Congress**
Department of Physics, Saurashtra University Rajkot on 13th March 2004.
5. **Ph.D. Teaching Programme**
Nuclear Science Centre, New Delhi. During 15th March – 2nd April 2004.
6. **National Workshop on Advanced Methods for Materials Characterization**
BARC, Anushaktinagar, Mumbai. During October, 11-15 2004.
7. **Seminar on Current Trends In Materials research**
Organized by UGC-SAP Programme at Department of Physics, Saurashtra University, Rajkot on February 28, 2005.

8. **One Day National Seminar on Recent Advances in Condensed Matter and Space Physics**
Organized by UGC-SAP Programme at Department of Physics, Saurashtra University, Rajkot on 21st March, 2006.
9. **National Workshop on “Nanotechnology: Opportunities & Challenges”**
Jointly Organized by Dept. of Physics & GUJCOST Gandhinagar at Department of Physics, Saurashtra University, Rajkot on 17th October, 2005.
10. **Workshop on Exploring & Using MATLAB**
Organized by Department of Computer Science & IQAC, Saurashtra University, Rajkot on 29th March, 2006.
11. **One Day National Seminar on Recent Trends in Materials Science**
Organized by UGC-SAP Programme at Department of Physics, Saurashtra University, Rajkot on 25th March, 2007.

CONTENTS

Chapter 1

Introduction

1.1	Introduction	1.2
	(A) Brief history of magnetism	1.2
	(B) Introduction to ferrites	1.3
1.2	Aim and outline of the present work	1.7
	References	

Chapter 2

Crystal structure and magnetism in spinel ferrite

2.1	Crystal structure and chemistry	2.2
2.2	Magnetic interactions in spinel ferrites	2.13
2.3	Magnetic ordering in a substituted ferrites	2.21
2.4	Neel's model, Random Canting of Spin model	2.22
	References	

Chapter 3

Synthesis and characterization techniques

3.1	Synthesis of spinel ferrites	3.2
3.2	Structural and micro-structural characterization	3.5
	(A) Energy dispersive analysis of X-rays	3.5
	(B) X-ray powder diffractometry	3.8
	(C) Scanning Electron Microscopy	3.17
3.3	Elastic properties	3.20
	Ultrasonic pulse echo overlap technique	3.20
3.4	Magnetic properties	3.36
	(A) Physical properties measurement system (PPMS)	3.36
	(B) Low field ac Susceptibility	3.42

3.5	Electrical properties	3.47
	(A) D.C. resistivity	3.47
	(B) Thermo electric power	3.54
	References	

Chapter 4

Slow cooled $\text{CuAl}_x\text{Fe}_{2-x}\text{O}_4$ system

4.1	Structural parameters and x-ray Debye temperature determination study on copper-ferrite-aluminates	
	(A) Introduction	4.2
	(B) Experimental details	4.3
	(C) Results and discussion	4.4
	(D) Conclusions	4.29
	References	
4.2	Effect of Al^{3+} - substitution on the transport properties of copper ferrite	
	(A) Introduction	4.35
	(B) Experimental details	4.38
	(C) Results and discussion	4.40
	(D) Conclusions	4.66
	References	
4.3	Al^{3+} - modified elastic properties of copper ferrite	
	(A) Introduction	4.71
	(B) Experimental details	4.74
	(C) Results and discussion	4.76
	(D) Conclusions	4.105
	References	
4.4	Negative magnetization, magnetic anisotropy and magnetic ordering studies on Al^{3+} -substituted copper ferrite	
	(A) Introduction	4.114
	(B) Experimental details	4.119
	(C) Results and discussion	4.120

(D) Conclusions	4.138
References	

Chapter 5

Quenched $\text{CuAl}_x\text{Fe}_{2-x}\text{O}_4$ system

5.1 Structural analysis, cation distribution and structural parameters determination	
(A) X-ray powder diffraction patterns analysis	5.2
5.2 Microstructural Characterization	5.12
5.3 Magnetic properties of quenched $\text{CuAl}_x\text{Fe}_{2-x}\text{O}_4$ system	
(A) M-H loop characteristics and dc magnetization studies	5.14
(B) Low field ac susceptibility measurements	5.22
5.4 Variation of dc resistivity (ρ_{dc}) as a function of Al^{3+} - content (x) and temperature (T)	5.25
5.4 Conclusions	5.29
References	

Chapter 1

Introduction

1.1 Introduction

(A) Brief history of magnetism

Magnetism has its roots in antiquity. The history of magnetic materials appears to go with the development of human civilization. It appears that magnet and its properties were known quite well even in Vedic period (several centuries B.C.) in India [1]. The staunch philosopher Sankara (788 – 820 A.D.) also had known the properties of magnet [2].

Magnetism has very long history. This is due to the existence of a natural mineral called 'magnetite' an iron oxide $\text{Fe}^{2+}\text{Fe}_2^{3+}\text{O}_4$ (Fe_3O_4). It is believed that the Chinese used magnets to make compasses at around 400 B.C. and magnetism was known as one of the four great inventions in ancient China. The word 'Magnet' is derived from the Greek word "Magnesia", a place where magnetite was widely distributed. In old English it was used for direction finding and was called 'Lodestone', meaning 'Waystone'.

Much later, William Gilbert (1540 - 1603), an Englishman, made the first truly scientific study of magnetism "De Magnete". Gilbert realized that earth is a huge magnet and the compass works on this principle. The great experimental genius of his century Michel Faraday (1791 - 1867) classified all materials into diamagnetic and paramagnetic types by really monumental scientific experiments. For about 200 years after his study, there were no fundamental discoveries in this field and applications were developed slowly. During the late 1700s the early 1800, compound magnets comprising magnetized steel strips were manufactured by rubbing steel with a lodestone of another magnet. These were able to lift 28 times their own weight of iron. In 1819 Hans Christian Oersted observed that an electric current in wire

affected magnetic compass needle. With further contribution by Maxwell, Hertz and many others, the new science of electromagnetism developed. Magnetism is more of an experimental one than the others in the area of physics: in the sense that our experimental knowledge far exceeds the theoretical understanding of the fundamental properties of mater. To mention one example, how a high quality magnetic recording tape of disk works is not much understood but these media are made by trial and error method [3]. Magnetism has now become a very vast subject and a broad view can be obtained from a diagrammatic presentation in the form of a tree with many branches as shown in Figure 1.1.

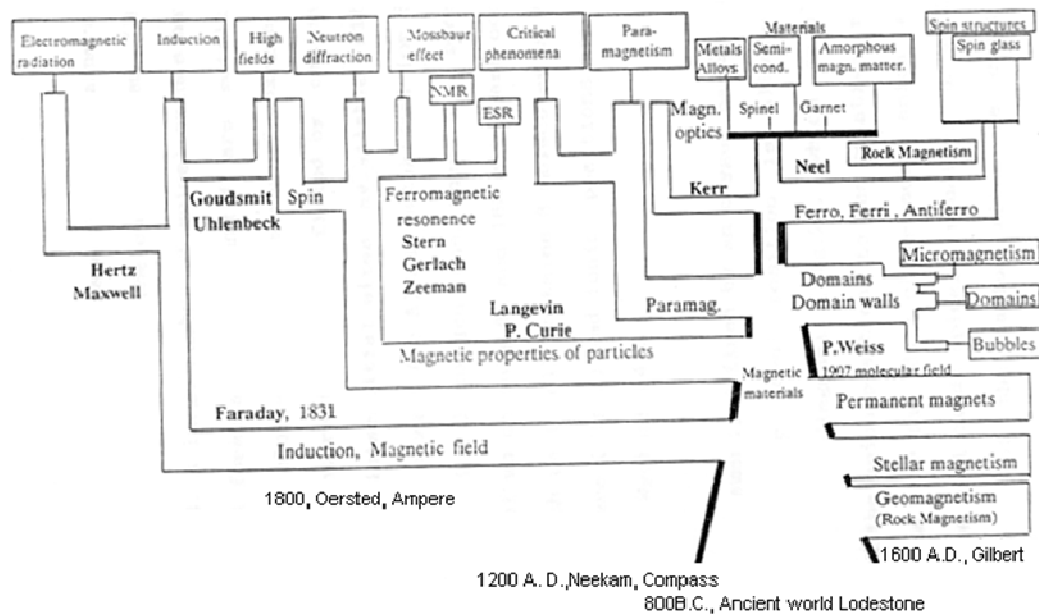


Figure 1.1 Fully grown magnetism tree with its many branches. Some important names and dates marked.

(B) Introduction to ferrites

Materials containing ferric oxide (Fe_2O_3) as one of the components are generally regarded as ferrites. Ferrites crystallize in four different crystal types, namely (i) Spinel ferrite (fcc structure) (ii) Garnet (bcc structure)

(iii) Ortho ferrite (orthorhombic structure) and (iv) Hexa ferrite or magneto plumbite (hexagonal structure).

There are basically two varieties of ferrites: soft ferrite and hard ferrite. This is not a tactile quality but rather a magnetic characteristic. 'Soft ferrite' does not retain significant magnetism whereas 'Hard ferrite' magnetization is considered permanent. With the advent of 'Spinel' ferrites [4], spin glasses and amorphous magnetic materials [5], a link between these emerging fields and 'rock' magnetism was established by Neel [6]. The terms antiferromagnetism and ferrimagnetism were introduced by Neel to explain the properties of MnO and Fe₃O₄ respectively. Explanation for antiferromagnetism behaviour was proposed by Neel on the basis of the negative inters atomic exchange coupling whereby the spins of neighbouring atoms align antiparallel to each other. Thus, an antiferromagnetic material consists of two identical sublattices each of which is ferromagnetically ordered but one is antiparallel to the other. For compounds exhibiting ferrimagnetism, the magnetic moments of the two sublattices are unequal; they do not cancel out but give rise to a net magnetic moment. Thus, ferrimagnetism can be considered as an uncompensated antiferromagnetism. The present day classification of materials is more elaborate and all different types of 'magnetism' and their interrelationships have been discussed by Hurd [7]. Naturally occurring magnetite is a weak 'hard' ferrite. 'Hard' ferrites possess a magnetism which is essentially permanent. In time, man-made; 'hard' ferrites with superior properties were developed but producing an analogous 'soft' magnetic material in the laboratory proved elusive.

During the 1930's research on 'soft' ferrites continued, primarily in Japan and the Netherlands. However, it was not until 1945 that J. L. Snoek of the Philips Research Laboratories in the Netherlands succeeds in producing a 'soft' ferrite for commercial applications. Originally manufactured in a few selected shapes and sizes, primarily for inductor and antenna applications, 'soft' ferrite has proliferated into countless sizes and shapes for a multitude of uses (Figure 1.2).

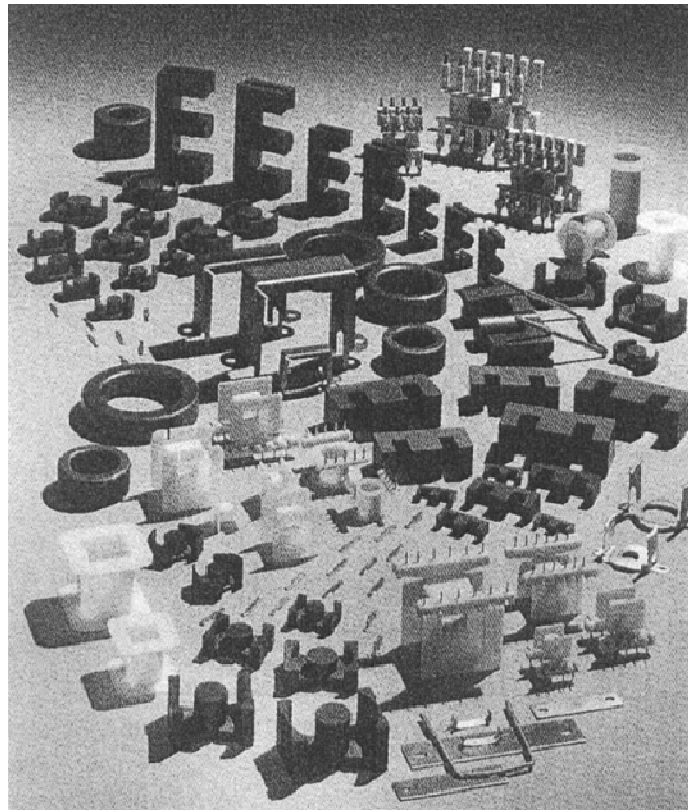


Figure 1.2 Typical ferrite cores for power applications with the mounting and winding accessories.

Ferrites are used predominately in three areas of electronic: low level applications, power applications and Electro-Magnetic Interference (EMI) suppression.

The field of ferrite is well cultivated but due to its potential applications in various fields, and interesting physics involved in it, even after seven-eight

decades of its first artificial synthesis, scientists, engineers, technologists and researchers are still interested in various types of ferrite materials synthesized by different preparative techniques, parameters and conditions in bulk, nanocrystalline and thin film forms and in the study of structural, magnetic, electrical, dielectric, elastic, optical etc properties as a function of composition, substitution, frequency, temperature etc.

Ferrite is rigid and brittle. Like other ceramics, ferrite can chip and break if handled roughly. Luckily it is not as fragile as porcelain and often such chips and cracks will be mere cosmetic. Ferrite varies from silver gray to black in colour.

Ferrites have a high magnetic permeability which allows them to store stronger magnetic field than iron. Ferrites are often produced as powder, which can be sintered into solid core. Ferrite shrinks when sintered. Depending on the specific ferrites, this shrinkage can range from 10 – 17% in each dimension. Then, the unfired component's volume may be as much as 60% larger than the sintered value. Maintaining correct dimensional tolerances as well as the prevention of cracking and warp age related to this shrinkage are fundamental concerns of the manufacturing process. Ferrite cores are used in electronic inductors and electro-magnets. Early computer memories stored data in the magnetic field of ferrite cores, which were assembled into arrays of core memory. Ferrite powder is used in the coatings of magnetic recording tapes. The breadth of application of ferrites in electric circuitry continues to grow. The wide range of possible geometrics, the continuing improvements in material characteristics and their relative cost-

effectiveness make ferrite components the choice for both conventional and innovative applications.

1.2 Aim and outline of the present work

The Cu-Fe-O system is of long standing interest in solid state physics, mineralogy, ceramic and metallurgy. By virtue of magnetic and semiconducting properties copper ferrite (CuFe_2O_4) and its solid solution with other ferrites are widely used in electronic industry [8]. CuFe_2O_4 is a unique spinel because due to a relatively small energy difference between Cu^{2+} ions in the tetrahedral and octahedral sites cation redistribution is possible and strongly dependent upon the annealing temperature, cooling rate, microstructure etc. CuFe_2O_4 is one of the most investigated ferrite by various experimental techniques. Copper ferrite in bulk polycrystalline [9, 10] and thin film [11 - 15] forms has shown very interesting multifunctional properties upon the application of external stimuli. On the other hand, nanoparticles of CuFe_2O_4 have been shown to be useful as a catalyst for CO_2 decomposition hydrogen production and as a gas sensor [16].

Copper ferrite (CuFe_2O_4) is known to exist in tetragonal and cubic structure. Since, Cu^{2+} is a Jahn-Teller ion, it gives the anomalous favorable properties and also exhibits phase transition from tetragonal to cubic, depending on the temperature. The Jahn-Teller transition is argued to be order-disorder in character, but its exact nature is still not fully understood. The temperature of the order-disorder transformation depends on the content of octahedral (B-site) cupric ions and on the non stoichiometry. When the spinel is synthesized using classical ceramic technologies (sufficiently high temperature treatment of the initial oxides of the metal cations) with strict

stoichiometry, it has a tetragonal structure of hausmannite type with crystal cell parameters $a = 8.20 \text{ \AA}$ and $c = 8.60 \text{ \AA}$: $c/a \sim 1.05$. The c/a ratio can be changed via decreasing the copper concentration, or alternatively by heat treatment, temperature and cooling rate. Part of the Cu^{2+} ions can be frozen in tetrahedral sites when the ferrites are quenched in air from above 673 K. The resulting ferrites show a smaller tetragonal distortion since great properties of the cupric ions are located on tetrahedral sites. Moreover, the quenching treatments at room temperature from temperature higher than 1023K leads to the formation of oxygen-deficient spinel ferrites, the non-stoichiometry arising from the reduction of some Cu^{2+} ions to Cu^{1+} ions. Some reports consider that Cu^{1+} ion is located in the interstitial sites i.e. sites normally not occupied in the spinel structure. Recently, it has been found that Cu-ferrite films can be stabilized in either tetragonal or cubic phase even at room temperature depending on depositions conditions and post-deposition heat treatment. The samples annealed in air at high temperatures ($> 800^\circ\text{C}$) and slowly cooled to room temperature were tetragonal, while those rapidly quenched in liquid nitrogen were cubic [10].

Till today, there arose a considerable interest in the synthesis and characterization of pure and substituted copper ferrite system.

The Al^{3+} - ion possesses noble gas outer electron shell structure; it is less compressible than ions with a full or half filled d-shell (Zn^{2+} , In^{3+} , Sn^{3+} etc) [17], thus it cannot easily be accommodated in A-sites but statistically distributed among the available A- and B- sites.

The substitution of Al^{3+} - ions has some beneficial effects on power handling capability [18]. The addition of Al^{3+} - ions have shown to modify the

structural properties [19], electrical properties [20, 21], including switching characteristics [7, 22], magnetic properties [22, 23 - 27], dielectric properties [28, 29] and elastic properties [30] of spinel ferrite materials in an interesting manner.

The studies on magnetic, electrical and dielectric properties of typical compositions by means of low temperature high field magnetization DC magnetization, low field ac susceptibility behaviours are not properly understood. On the other hand, thermoelectric power and dc resistivity studies as a function of composition and temperature still need further investigation.

Four ferrite samples with nominal composition CuFe_2O_4 ($x = 0.0$), $\text{CuAl}_{0.2}\text{Fe}_{1.8}\text{O}_4$ ($x = 0.2$), $\text{CuAl}_{0.4}\text{Fe}_{1.6}\text{O}_4$ ($x = 0.4$) and $\text{CuAl}_{0.6}\text{Fe}_{1.4}\text{O}_4$ ($x = 0.6$) have been prepared by the usual double sintering ceramic technique.

One set of the samples is quenched from final sintering temperature (~ 1273 K) to liquid nitrogen temperature (80 K).

The effect of rapid thermal quenching on structural, micro-structural, elastic, magnetic and electrical properties have been studied by means of various characterization techniques.

(i) Energy dispersive analysis of X-rays (300K)

The stoichiometry of synthesized compositions is verified by EDAX.

(ii) X-ray powder diffractometry (300K)

The mono-phase nature of the prepared ferrite materials has been confirmed by x-ray powder diffraction pattern analysis using computer software. The x-ray diffraction line intensity calculations are carried out for the precise determination of cation distribution that in turn used to calculate various structural parameters including Debye temperature.

(iii) Scanning electron microscopy (300K)

The microstructural study i.e. grain morphology: grain size, grain size distribution, shape, presence / absence of pores etc. is carried out by means of scanning electron microscopy.

(iv) Ultrasonic pulse echo overlap technique (300K, 9 MHz)

Ultrasonic pulse echo overlap technique has been employed to obtain longitudinal and shear wave velocities of ultrasonic wave that in turn used to calculate various elastic moduli. The elastic moduli are corrected to zero porosity using five different semi-empirical models. Lattice energy has been calculated.

(v) High field magnetization measurement ($H_{\max} = 2\text{Tesla}$, $T = 10\text{K}$ & 300K)

The high field magnetization study has been employed to obtain saturation magnetization, magneton number that in turn used to calculate canting angle and exchange integrals.

(vi) DC magnetization measurement ($H = 10\text{mTesla}$, $T = 4.2 - 350\text{K}$)

The DC magnetization study has been performed to study anisotropy effect and possibility of cluster spin glass type of magnetic ordering.

(vii) Low field ac susceptibility measurement ($H = 50\text{Oe}$, $T = 300 - 750\text{K}$)

The low field ac susceptibility measurements have been carried out to determine the Neel temperature and magnetic ordering study.

The Neel temperature for different compositions is theoretically calculated from molecular field theory.

(viii) Thermoelectric power measurement ($T = 300 - 473\text{K}$)

The type of charge carriers responsible for conduction mechanism, concentration of Cu^{1+} and Fe^{2+} ions, oxygen deficiency, mobility of charge carriers in the system are obtained by thermoelectric power study.

(ix) DC resistivity measurement ($T = 300 - 750\text{K}$)

The variation of DC resistivity with temperature is used to determine the Neel temperature, activation energies etc.

References

1. Vaimanika Sastra (Science of Aeronautics) and T. Subbaraya Sastry, 1918, Ed. G. R. Josyar, Coronation Press, Mysore, India, 1973.
2. Sivananda Lahiri and Adi Sankaracharya, Staza. No. 61.
3. E. P. Wohlforth, Physica B. 86 – 88 (1976) 852.
4. J. Smit and H. P. J. Wijn, "Ferrites" John Wiley & Sons, New York (1959).
5. K. Binder and A. P. Young, Rev. Mod. Phys. 58 (1986) 801.
6. L. Neel, Adv. Phys. 4(1955)191.
7. C. M. Hurd, Contemp. Phys. 23(1982)469.
8. G. F. Goya, H. R. Rechenberg and J. Z. Jian, J. Appl. Phys. 84 (2) (1998) 1101.
9. K. G. Saija, U. S. Joshi, V. K. Lakhani and K. B. Modi, J. Phys. D: Appl. Phys. 42 (2009) 165402 (5pp).
10. J. Darul, Z. Kristallogr. Suppl. 30(2009)335.
11. A. Yang, Z. Chen, S. M. Islam, C. Vittoria and V. G. Harris, J. Appl. Phys. 103(2008) 07E509.
12. A. Yang, Z. Chen, Xu. Zuo, D. Arena, J. Kirkland, C. Vittoria and V. G. Harris, J. Appl. Phys. 86(2005) 252510.
13. M. M. Ibrahim, M. S. Seehra and G. Srinivasan, J. Appl. Phys. 75 (1994) 6822.
14. M. Desai, S. Prasad, N. Venkataramani, I. Samajdar, A. K. Nigam and R. Krishan, J. Appl. Phys. 91(4) (2002) 2220.
15. M. Sultan and R. Singh, Mater. Lett. 63(21)(2009)1764.

16. D. Thapa, N. Kulkarni, S. N. Mishra, P. L. Paulose and P. Ayyub, J. Phys.D.: Appl.Phys. 43 (2010) 195004.
17. F. C. Romeijn, Philips. Res. Rep. 8 (1953)304
18. P. V. Reddy, J. Appl. Phys. 63 (1998) 3783.
19. V. K. Lakhani, T. K. Pathak, N. H. Vasoya and K. B. Modi, Solid State Sci. 13 (2010) 539.
20. K. B. Modi, H. H. Joshi and R. G. Kulkarni, J. Mater. Sci. 31 (1996) 1311.
21. U. V. Chhaya and R. G. Kulkarni, Mater. Lett. 39 (1999) 91.
22. K. G. Saija and K. B. Modi, Unpublished work.
23. M. Almokhtar, A. M. Abdalla, and M. A. Gaffar, J. Magn. Magn. Mater. 272-276(2004)2216.
24. R. G. Kulkarni, B. S. Trivedi, H. H. Joshi and G. J. Baldha, J. Magn. Mater. 159(1996)375.
25. I. Maghsoudi, M. J. Hadianfard and H. Shokrollahi, J. Alloys Compd. 481(1-2) (2009)539.
26. B. S. Trivedi and R. G. Kulkarni, Solid State Commun. 86(1993)327.
27. M. M. Eltabey, K. M. El-Shokrofy, and S. A. Gharbia, J. Alloys Compd. 509(5) (2011)2473.
28. S. S. Ata-Allah, and M. Kaiser, J. Alloys Compd. 74(2009)303.
29. S. M. Patange, S. E. Shirsath, K. S. Lohar, S. S. Jadhav, N. Kulkarni, and K. M. Jadhav, Physica B: Condens. Matt. 406(3)(2011)663.
30. V. K. Lakhani, and K. B. Modi, Solid State Sci. 12(2010)2134 and references there in.

Chapter 2

Crystal structure and magnetism in spinel ferrite

2.1 Crystal Structure and Chemistry

Spinel structure

The spinel crystal structure is the most well-known, diverse and useful example of uncompensated antiferromagnetism. The spinel structure is named after the mineral spinel (MgAl_2O_4) and can be represented as $\text{M}'\text{M}''_2\text{X}_4$, where X represents oxygen or one chalcogenic bivalent anion (S^{2-} , Se^{2-} , Te^{2-}) and M' and M'' are metallic ions. The valences have to fulfill the electroneutrality requirements. Due to large electronegativity of Oxygen, the ionic type of bonds prevails in almost all oxide spinels. The crystallographic structure is formed by a nearly closed packed face centred cubic (fcc) array of anions with two unequivalent sites for cations. These differ in oxygen coordination; four oxygen ions surround tetrahedral cationic sites and octahedral sites by six oxygen ions. These are also called A- and B- sites, respectively. In a cubic unit cell, 64 tetrahedral sites and 32 octahedral sites are present. of which only 8 and 16 sites are occupied by metal ions respectively. The geometry of the occupied interstitial sites is shown in Figure 2.1, where the primitive cell contains two formula units is shown [1].

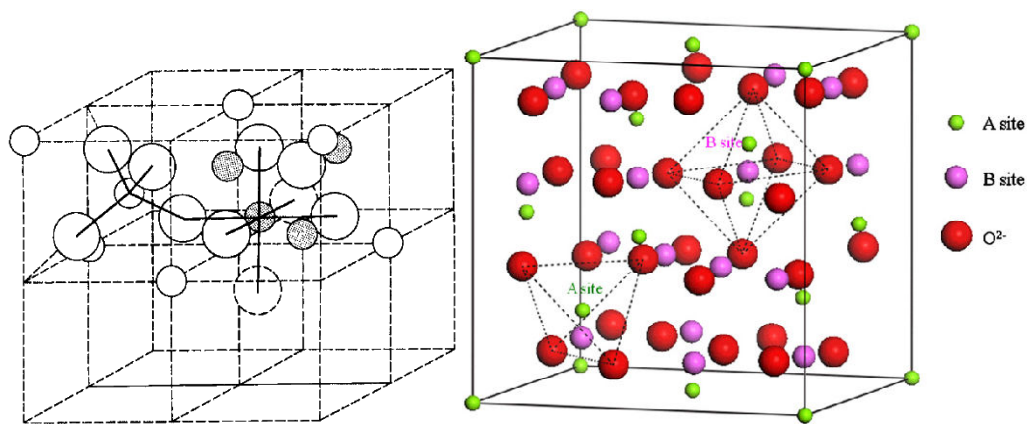


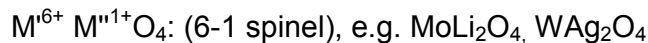
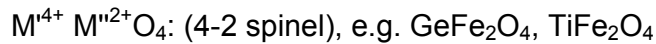
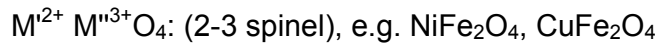
Figure 2.1 The geometry of the occupied interstitial sites in spinel structure

The symmetry of the structure is cubic and belongs to the space group O_h^7 (Fd3m). A small displacement defined by a single parameter 'u' of the anions, from their ideal position is allowed along the corresponding body diagonal which enables a better matching of anion positions to the relative radii of A- and B- sites cations. For the ideal closed packed anion lattice, $u = 3/8$, but in real situations it is more than $3/8$. The local symmetry of the cation sites is cubic in the case of tetrahedral (A) site and trigonal in the case of octahedral (B) site, the trigonal axis being one of the body diagonals. The trigonal symmetry is due to both the configurations of neighbouring cations and the distortion of the anion octahedron if $u \neq 3/8$. Each of the body diagonals belongs to just one of the B cations in the primitive cell. On the other hand the local symmetry of the A positions remain cubic even if $u \neq 3/8$. When considering the aspects for which the local symmetry is irrelevant, all the A positions may be treated as belonging to one sublattice (tetrahedral or A-site), and all the B positions may be unified to form another sublattice (octahedral or B-site).

Both translational and local symmetries corresponding to the O_h^7 space group strictly apply only if each sublattice contains only one kind of cations, i.e. if all M' ions in $M' M''_2 X_4$ are in tetrahedral and all M'' ions are in octahedral positions. The spinel is then called normal spinel. We also have so called inverse spinel structure in which half the cations M'' are in A positions and the rest, together with the M' ions, are randomly distributed among the B positions. There are many examples of intermediate cases between a normal and an inverse spinel where a fraction of M' and M'' ions are inverted, that is M' occupies B positions and M'' occupies A positions. They are termed as

partially inverse spinels. Therefore, in order to characterize the spinel structure fully, a further parameter is needed describing the degree of inversion. The formula may be explicitly written as, $(M'_{1-\delta} M''_{\delta}) [M'_{\delta} M''_{2-\delta}] X_4$, where, δ is known as inversion parameter, and is equal to zero in case of normal spinel and one in case of inverse spinel. As a part of convention, the cations at the tetrahedral (A) sites are written in parentheses “()” and those at the octahedral (B) sites in square brackets “[]”.

The electroneutrality leads to three basic types, according to the cation valency combinations. These are,



It is found that practically any cation with radius within the limits 0.4 to 1Å may be incorporated into the spinel structure and most of them can occur in both octahedral and tetrahedral positions. The smallest cations with valency ≥ 4 , however, are found in the tetrahedral coordination only, while the monovalent cations occurring mainly in 6-1 spinels are confined to the octahedral sites. Besides the geometrical factors, the distributions of cations among the A and B positions is influenced by many other factors.

Site Preferences of the Ions

The preference of the individual ions for the two types of lattice sites is determined by;

1. The ionic radii of the specific ions
2. The size of the interstices
3. Temperature

4. The orbital preference for specific coordination

The most important consideration would appear to be the relative size of the ion compared to the size of the lattice site. The divalent ions are generally larger than the trivalent (because the larger charge produces greater electrostatic attraction and so pulls the outer orbits inward). Table 2.1 lists several of the applicable ionic radii. The octahedral sites are also larger than the tetrahedral (Table 2.2). Therefore, it would be reasonable that the trivalent ions such as Fe^{3+} would go into the tetrahedral sites and the divalent ions would go into the octahedral. Two exceptions are found in Zn^{2+} and Cd^{2+} which prefer tetrahedral sites because the electronic configuration is favorable for tetrahedral bonding to the oxygen ions. Thus, Zn takes preference for tetrahedral sites over the Fe^{3+} ions. Zn^{2+} and Co^{2+} have the same ionic radius but Zn prefers tetrahedral sites and Co^{2+} prefers octahedral sites because of the configurationally exception. Ni^{2+} and Cr^{3+} have strong preferences for octahedral sites, while other ions have weaker preferences.

Table 2.1 Radii of Metal Ions involved in spinel ferrites

Metal	Ionic Radius Angstrom units Å
Mg^{2+}	0.78
Mn^{3+}	0.70
Mn^{2+}	0.91
Fe^{2+}	0.83
Fe^{3+}	0.67
Co^{2+}	0.82
Ni^{2+}	0.78
Cu^{2+}	0.70
Zn^{2+}	0.82
Cd^{2+}	1.03
Al^{3+}	0.57
Cr^{3+}	0.64

Table 2.2 Radii of Tetrahedral and Octahedral Sites in Some Ferrites

Ferrite	Tetrahedral Site Radius Å	Octahedral Site radius Å
MnFe ₂ O ₄	0.67	0.72
ZnFe ₂ O ₄	0.65	0.70
FeFe ₂ O ₄	0.55	0.75
MgFe ₂ O ₄	0.58	0.78

Unit Cell Dimensions

The dimensions of the unit cell are given in Angstrom Units which are equivalent to 10^{-8} cm. Table 2.3 lists the lengths, a_0 , of some spinel unit cells. If we assume that the ions are perfect spheres and we pack them into a unit cell of measured (X-ray diffraction) dimensions we find certain discrepancies that show that the packing is not ideal. The positions of the ions in the spinel lattice are not perfectly regular (as the packing of hard spheres) and some distortion does occur. The tetrahedral sites are often too small for the metal ions so that the oxygen ions move slightly to accommodate them. The oxygen ions connected with the octahedral sites move in such a way as to shrink the size of the octahedral cell by the same amount as the tetrahedral site expands. The movement of the tetrahedral oxygen is reflected in a quantity called the oxygen parameter which is the distance between the oxygen ion and the face of the cube edge along the cube diagonal of the spinel sub cell. This distance is theoretically equal to $3/8a_0$.

Table 2.3 Unit Cell Lengths of Some Simple Ferrites

Ferrite	Unit Cell Length (Å)
Zinc Ferrite	8.44
Manganese Ferrite	8.51
Ferrous Ferrite	8.39
Cobalt Ferrite	8.38
Nickel Ferrite	8.34
Magnesium Ferrite	8.36

Crystal field splitting of energy levels and John-Teller Effect

With respect to the magnetic properties, the interest is primarily in transition metal ions particularly those of $3d^n$ group. The outer d-electrons of these ions may be regarded as practically localized in almost all oxide spinels so that the crystal (or ligand) field theory applies. This theory says that the low lying energy levels are decisive for the magnetic behaviour. The origin of the ligand field splitting of levels is attributed to both the electrostatic crystal field and the covalency between the cation and the surrounding anions (ligands). Both these effects contribute to the stabilization of cations in the given surrounding. Crystal or ligand field stabilization energy = lowering of the ground level with respect to the ground level of the free ion. In an octahedral environment, the five d orbitals on a transition metal atom are no longer degenerate but split into two groups, the t_{2g} group of lower energy and the e_g group of higher energy as shown in Figure 2.2 If possible, electrons occupy orbitals singly, according to Hund's rule of maximum multiplicity. For d^4 to d^7 atoms or ions, two possible configurations occur, giving low spin and high spin states; these are shown for a d^7 ion in Figure 2.3 In these, the increased energy, Δ , required to place an electron in an e_g orbital, and hence maximize the multiplicity, has to be balanced against the repulsive energy or pairing, P , which arises when two electrons occupy the same t_{2g} orbital. The magnitude of Δ depends upon the ligand or anion to which the metal ion is bonded: for weak field anions (ligands), Δ is small and the high spin state configuration occurs, and vice versa for strong field ligands. For magnitude of Δ , generally $\Delta(5d) > \Delta(4d) > \Delta(3d)$. Consequently the high spin behaviour is rarely observed in the 4d and 5d series.

In many transition metal compounds, the metal coordination is distorted octahedral and the distortions are such that the two axial bonds are either shorter than or longer than the other four bonds. The Jahn-Teller effect [2, 3] is responsible for these distortions in d^9 , d^7 (low-spin) and d^4 (high spin) ions. Consider the d^9 ion Cu^{2+} whose configuration is $(t_{2g})^6 (e_g)^3$. One of the e_g orbitals contains two electrons and the other contains one. The singly occupied orbital can be either d_z^2 or $d_{x^2-y^2}$ and in a free ion situation both would have the same energy. However, since the metal coordination is octahedral the e_g levels, with one doubly and one singly occupied orbitals, are no longer degenerate. The e_g orbitals are high energy orbitals (relative to t_{2g}) since they point directly towards the surrounding ligands and the doubly occupied orbital will experience stronger repulsions and hence have somewhat higher energy than the singly occupied orbital. This has the effect of lengthening of the metal-ligand bonds in the directions of the doubly occupied orbital, e.g. if the d_z^2 orbital is doubly occupied, the two metal-ligand bonds along the z axis will be longer than the other four metal-ligand bonds. The energy level diagram for this latter situation is shown in Figure 2.4. Lengthening of the metal-ligand bond along the z-axis leads to a lowering of the d_z^2 orbital. The distorted structure is stabilized by an amount $(\frac{1}{2})\delta_2$ relative to the regular octahedral arrangement and, hence, the distorted structure becomes the observed, ground state.

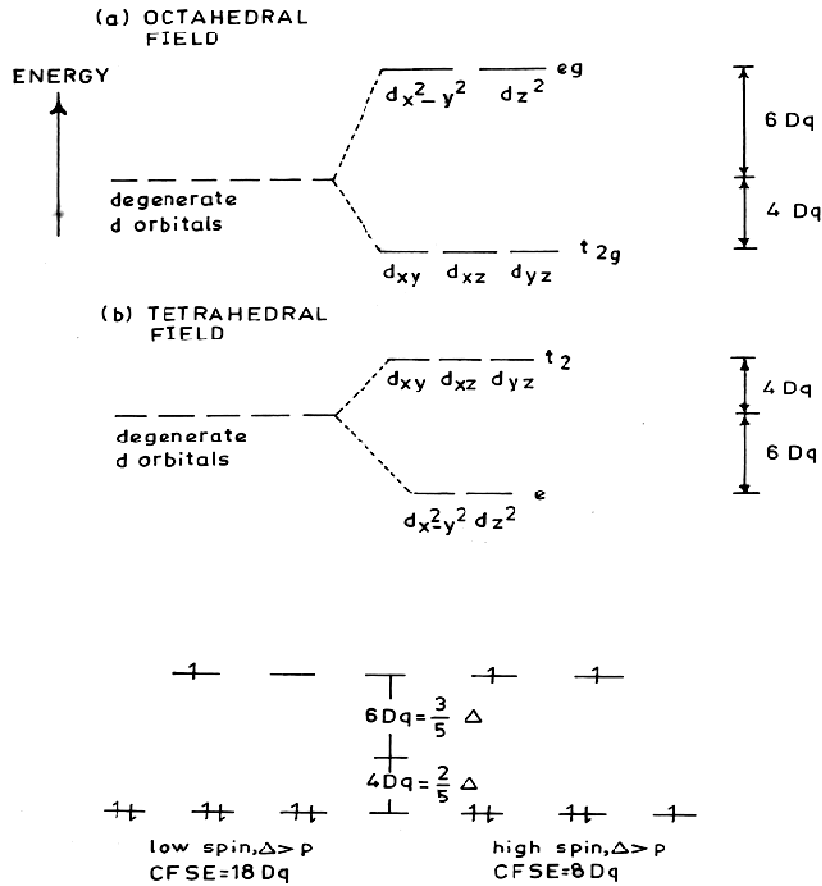


Figure 2.2 Crystal field splitting of Energy level and spin states in octahedral coordination.

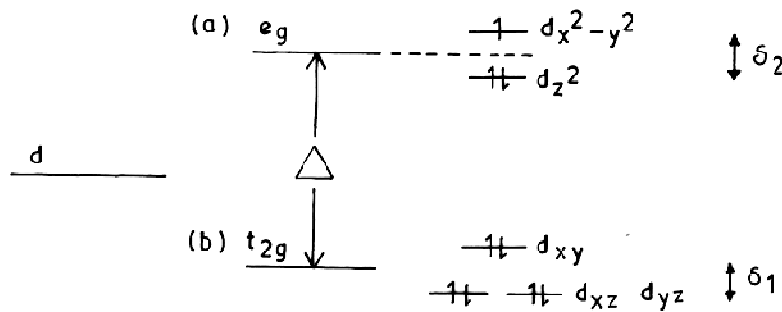


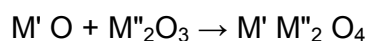
Figure 2.3 Energy level diagram for the d-levels in an ion experiencing a Jahn-Teller distortion.

In the oxide spinels, the cooperative Jahn-Teller effect is frequently encountered. The necessary condition for this to appear is the presence of transition metal ions which have an orbitally degenerate electronic ground state. The interaction between the degenerate states and the lattice vibrations

leads to an effective coupling between electronic states on different cations. When this coupling is sufficiently strong and the concentration of active cations exceeds a certain critical value, the electronic states order and simultaneously a structural phase transition from cubic to lower symmetry appears. Thus, Jahn-Teller effect refers to the condition in which a crystal lattice is distorted from the cubic to tetragonal configuration as a consequence of the possession of some 3d orbitals of fewer electrons than other orbitals. This condition results in an electrostatic imbalance that has the effect of repelling some oxygen anions more than others. In effect, these anions are pushed further away, thus producing the change from cubic to tetragonal symmetry. The phase with lower symmetry is stable only below a critical temperature. In the B-site, there are two ions, namely Mn^{3+} and Cu^{2+} both having doubly degenerate ground state of e_g type, which exhibit the Jahn-Teller effect. The corresponding distortion is always tetragonal with $c/a > 1$. The $CuFe_2O_4$ having the degree of inversion, $0.06 < \delta < 0.24$ exhibits Jahn-Teller effect with c/a ratio ~ 1.06 [4].

Chemistry of Ferrites

The oxide spinels are commonly prepared at elevated temperatures by a direct solid-state reaction between the simple oxides. The relevant temperature range is about $800^\circ C$ to $1500^\circ C$, depending on the type of cations. The thermodynamic stability of spinels compared to the constituent oxides is given by Gibbs free energy of formation (ΔG) for the reaction,



The largest contribution to the crystal energy in oxide spinels comes from the Coulomb energy of the charged ions (Madelung energy),

$$E_c = (-e^2 / a) A_M$$

where, e is the charge of electron, a is the lattice parameter and A_M the Madelung constant. The Madelung constant, A_M can be expressed as a function of the mean electric charge q_A of the cations in tetrahedral positions and of the oxygen parameter u . With increasing A_M the stability of the spinel increases. Therefore, owing to its dependence on q_A , the Coulomb energy generally plays an important role in the equilibrium distribution of cations among tetrahedral and octahedral positions, even though in some cases other energy contributions may become important.

According to the formula, $(M'_{1-\delta} M''_{\delta}) [M'_{\delta} M''_{2-\delta}] O_4$, oxide spinels may have various degrees of inversion. If the energy difference between two limiting cases $\delta = 1$ and $\delta = 0$ is not very large, we expect the distribution of cations to be random at high temperatures due to the prevailing influence of entropy term $-TS$ in the free energy. When the temperature is lowered, the spinel tends to be more or less normal or inverse depending on the sign and amount of energy corresponding to the interchange of cations M' , M'' in different sublattices. The equilibrium distribution will be given by the requirement that the Gibbs free energy is minimum, i.e.

$$dG/d\delta = \{ (dH/d\delta) - T(dS/d\delta) \} = 0$$

If one restricts to configurational entropy of cations and assumes total randomization in both sublattices, S may be approximated by,

$$S = Nk [-\delta \ln \delta + 2(\delta - 1) - (\delta + 1) \ln (\delta + 1)]$$

$$\text{Defining further } \Delta P = dH/d\delta, \text{ we find, } \delta (1 + \delta / (1 - \delta)^2) = \exp (- \Delta P / RT)$$

which determines the equilibrium value of δ at temperature T . Generally, ΔP depends on δ and frequently a linear expression $\Delta P = H_0 + H_1 \delta$ is used to

describe the experimental results. Here, H_0 and $H_0 + H_1$ may be interpreted as energies connected with interchange of ions M' , M'' from different sublattices in the case completely normal and inverse distribution, respectively.

When $\Delta P < 5$ kCal/mol, a partially inverted spinel is usually observed. Otherwise, the energy difference between the normal and inverse structures is sufficient for the spinel to attain either normal or inverse structure. Once again the main contributions to ΔP come from Madelung energy, Born repulsion energy and further from polarization and ligand field effects. On the basis of systematic studies of cation distribution in various spinels it has been recognized that some regularities exist in them pointing to the possibility to connect the distribution to individual site preference of cations. In such a case, the energy ΔP can be expressed as a difference $\Delta P = P(M') - P(M'')$, of individual preference energies P of cations M' and M'' . Once $P(M')$ and $P(M'')$ are known for all relevant cations, the distribution of ions in arbitrary spinel could be predicted. The values of $P(M)$ for different spinels are shown in Figure 2.4.

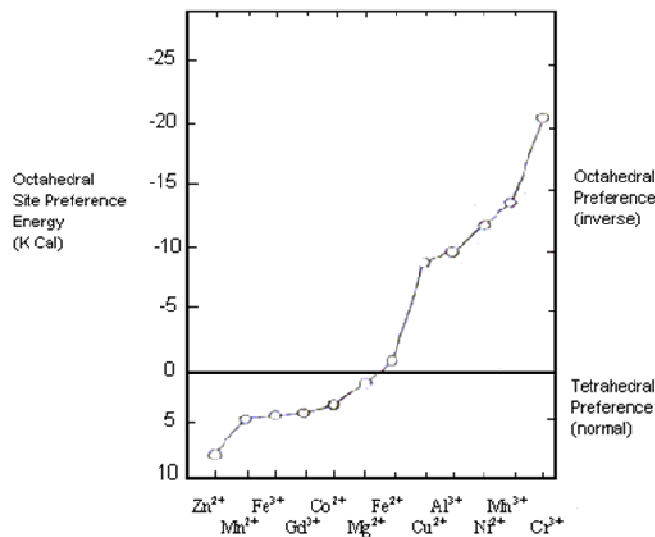


Figure 2.4 Cation site preference energy for various transition metal ions

Chemistry, crystal structure and microstructure determine the engineering material characteristics of ferrites. Many desirable combinations of chemical ingredients and basic structure cannot be obtained because some ions are incompatible with certain crystal structures despite the best efforts of materials scientists. Microstructure includes the size and number of voids, size of grains, and presence of grain boundary phases, grain shape and orientation. In essence, microstructure is the architecture of the materials that is, how the various phases and crystallites are put together, their particular patterns and arrangements, and how these are joined. Ferrite microstructures are extremely sensitive to processing because the pre-reaction and grinding of raw materials, forming technique employed, sintering time, and temperature and cooling conditions influence crystal composition and size, and also the size and volume of pores.

2.2 Magnetic interactions in spinel oxides

After having reviewed the crystallographic and some other associated aspects of spinel ferrites, we shall now review their magnetic behaviour, which is the central theme of the present work.

Atomic magnetic moment is due to the motion of electrons in their orbits and due to their spin motion. Although the orbital motion of electrons may contribute to the atomic magnetic moment when the atom is in free state, when it is a part of solids the contribution of orbital motion is often very small and negligible. For the present case of spinel ferrite, the cations are subjected to the very intense inhomogeneous electric field which influences the orbital angular momentum partly due to the large radius of 3d shell and partly due to the lack of any outer electrostatic shell to screen the 3d shell whose unpaired

electrons are responsible for net magnetic moment. The spin angular momentum is however, not affected by the influence of anion field.

The quenching of the orbital momentum can be pictured as follows: The orbital angular momentum assumes definite orientation relative to the crystal lattice under the influence of the electric field of anions which has the symmetry of crystal. This orbit-lattice coupling is so strong that the angular momentum vector direction and therefore the angular magnetic moment is locked in a particular direction and does not respond to the applied external magnetic field.

The atom with a resultant spin quantum number S gives the spin magnetic moment as follows,

$$\mu = g\sqrt{s(s+1)}\mu_B \quad g = \text{Lande's splitting factor}$$

Ferromagnetism

Oxide spinels represent a classical example of a crystal structure, which allows a special type of magnetic order called ferromagnetism. In fact, Spinel were the first materials where the existence of such magnetic ordering was recognized by Neel [5]. He coined the word ferrimagnetism and elaborated the molecular field theory to account for this type of order. Until the discovery of ferrimagnetism, the magnetic properties of the few magnetic spinels then known, such as magnetites, were classified as ferromagnetics. The difficulty, however, was to understand the low magnetic moments, the deviations from Curie-Weiss law and some other peculiarities [6, 7]. The departure from the ferromagnetic behaviour was excellently explained by Neel in his simple yet elegant theory. Ferrimagnetism can be considered as a special case of

antiferromagnetism, where at least two unequal and antiparallel systems of atomic moments exist giving rise to spontaneous magnetization.

The simplest case of ferrimagnetism is a system with two sub-lattices, where all the octahedrally coordinated sites are considered to compose one sub-lattice (B) and in similar manner all the tetrahedrally coordinated sites to compose (A) sub-lattice. These sites are crystallographically nonequivalent and when both contain paramagnetic ions in sufficiently high concentration the ferrimagnetism may occur. The ferrimagnetism, however, is a broad class and includes materials with more than two sub-lattices and other configurations of moments, rather complicated, like triangular and spiral etc.

The intense short-range electrostatic field causes the interactions, which are responsible for the magnetic ordering. These interactions are quantum mechanical in origin and are related to the overlap of the charge distributions of the atoms concerned.

The exchange interaction coupling the spins of pair of electrons is given as proportional to the scalar product of two spin vectors.

$$\varepsilon_{ij} = -2 \cdot J_{ij} S_i S_j$$

where J_{ij} is the exchange constant given as

$$J_{ij} = \int \Psi_i^*(1) \cdot \Psi_j^*(2) \cdot \left(\frac{2}{r_{12}} + \frac{2}{r_{ij}} - \frac{1}{r_{i1}} - \frac{1}{r_{j2}} - \frac{1}{r_{i2}} - \frac{1}{r_{ji}} \right) \cdot \Psi_i(2) \Psi_j(1) dv_1 dv_2$$

where, 1,2 refer to two electrons; i,j refer to two atoms; r's are the distances. The magnitude and sign of the exchange integral decide the type and strength of the magnetic ordering. The ferromagnetism results from strong parallel coupling of spins having large, positive J values. The semi empirical

calculations to decide the type of ordering depending on the type of the ions and distances between them were given by Slater [5].

The interactions causing magnetic ordering in spinels, however, are not the same as described above. In spinels the cations are situated at large distances and have anions as their nearest neighbours. These anions obscure the direct overlap of the cations' orbitals sometimes partially and at times completely. Moreover, the ratio of the distance between two cations to the diameter of the concerned electron orbit comes about 2.5 indicating a moderate to weak positive interaction favouring weak ferromagnetic type of ordering [6]. But experimental evidences favour strong interactions of negative type, as evident from the observed high magnetic transition temperatures of spinel ferrites. So it is unlikely that the interactions are dependent on direct coupling of cations spins. On the other hand since anions possess no magnetic moment the direct coupling with anions are also ruled out.

A "superexchange" mechanism was proposed by Kramer [7] for such cases and was developed by Anderson [8-11] and Van Vleck [12]. The superexchange mechanism between cations operates via the intermediate anions. The superexchange mechanism was explained by Anderson considering a simple example of MnO. In the ground state there cannot be any spin coupling of oxygen ($S = 0$) possible with cations. But in the excited state, oxygen gives a p electron from a 2p pair, which becomes a temporary part of any one of the Mn ions. The consequence of the process is the emergence of net spin on the oxygen ion due to which it can then after interact with the other Mn ion by direct exchange. If the separation is not very large the interaction will be negative favouring antiparallel arrangement of

spins in the two Mn ions. The spinel ferrites also undergo the same indirect interaction, which is responsible for the strong negative coupling of the cation spins in the above case. The p orbital of the oxygen anion overlaps with cation d orbital which accepts an electron from oxygen's p shell. The p electron will occupy the next available place in d orbital of cation according to the Hund's rule i.e. if 3d is less than half filled the p electron will be placed parallel to the electrons already present in 3d shell. But if 3d is equal to or more than half full the later will be placed antiparallel to the net magnetization. If both the cations are of same type, the Hund's rule applying to both the cations will orient the net spins on both 3d shell antiparallels since 2p electrons are paired according to Pauli Exclusion Principle.

The sign and the strength of the super exchange interactions depend, however, upon the bond angle and the bond distances involving the two cations and an intermediary anion. The bond angles are the angle formed between the bonds connecting the intervening anion with two cations. Several authors including Slater [13], Nagmiya [14], Goodenough [15] and Kanamori [16] have discussed the various types super exchange interactions considering the symmetry properties of electron orbitals. Goodenough [17] and Kanamori came up with some predictions concerning the sign and strength of super exchange interactions in their semi-empirical rules.

The magnetic orbitals involved in the super exchange interactions in spinel are the T_{2g} and E_g orbitals of 3d metal ions and P_x , P_y and P_z orbitals, which are highly directional, of intermediary anions. The T_{2g} orbitals consist of d_{xy} , d_{yz} and d_{zx} while E_g orbitals consist of d_{z^2} and $d_{x^2-y^2}$.

The semi empirical rules given by Goodenough and Kanamori (G.K.) are:

- (i) When the two cations have lobes of magnetic orbitals directed towards the anion as to involve a reasonably large overlap (i.e. the 3d orbitals are non-orthogonal with d_{z^2} type orbitals each with one d electron and pointing directly towards the legand ions in 180° configuration) the exchange is antiferromagnetic type because the antiparallel electrons gain energy by spreading into overlapping orbitals.
- (ii) When the participating cation orbitals are of the d_{xy} type, for example, each with one d electron and interacting with the P orbital of the legand in 180° configuration, the exchange interaction is antiferromagnetic type but the strength is not as large as in 1.
- (iii) In 90° configuration of the above orbitals along with d_{z^2} orbital each with one electron, the P orbital making σ bond with one cation is making π bond with another cation in this configuration. One expects strong overlapping and an antiferromagnetic exchange interaction.
- (iv) When magnetically filled cation orbital is in contact with an empty cation orbital via the intervening legand ion, the exchange is ferromagnetic. But it is not as strong as the antiferromagnetic exchange.

Few more qualitative conclusions drawn are:

- (a) From the orbital symmetry of cation-anion-cation configuration one yields $J_{d8} > J_{d5} > J_{d3}$ for 180° configuration $J_{d5} \gg J_{d8}$ for 90° configuration. J_{d3} can either be ferro or antiferro in nature.
- (b) From the valance state of the cation $J_{\text{trivalent}} > J_{\text{divalent}}$.

The higher charge on any cation increases the covalent nature of bond and results in greater overlap of orbitals giving stronger exchange interaction. The role of the legand ion is more obscure but generally it is observed that exchange interaction decreases with increasing electron negativity.

We refer now ourselves to the possible configurations in the spinel structure. We can identify basically three types of super exchange interactions to operate in the spinels:

- J_{AB} exchange interaction namely the inter sub-lattice interaction between cations on the A- and B- sub-lattices.
- J_{AA} , J_{BB} exchange interaction namely the intra sub-lattice interaction operating among the cations on the A- sites and B- sites.

Figure 2.5 gives the possible M-O-M (where M = A or B) configurations involving these three exchange interactions. Since the exchange forces are of short range in character the interactions including the next nearest are only considered. The hatched circles represent the B-site cations and small circles represent the A-site. Relative magnitude of radii and distances shown are approximately correct. We point out some configurations on the basis of our discussion so far and knowing the nature of the exchange forces. Among AB configurations only p-q-c configuration is favorable since the (M-O) distance as well as angle (M-O-M) ($\sim 126^\circ$) are favorable for having strong exchange interaction. The other AB configurations such as pre and tqe have much favorable angle ($\sim 154^\circ$ and 180° respectively) but with one very large (M-O) distance. So one cannot expect reasonable exchange interaction between them. Among the B-B configurations, the (M-O) distance is small for ppb configuration but angle (90°) is unfavorable. Other configurations are p-t-b

and p-a-b both, the angle and distance, are unfavorable. For p-t-b the angle ($\sim 126^\circ$) is favorable but one (M-O) distance is unfavorable. Thus, overall BB interactions are expected to stay lower in strength than AB interactions.

Among the AA configurations, only one configuration is shown in Figure 2.5, r-q-d, having both the (M-O) distances much larger ($\sim 3.9 \text{ \AA}$) than any BB or AB distance. Besides, for the BB interaction there is a possibility of direct exchange since B-cations direct their T_{2g} orbitals towards each other which is not the case for AA interaction. Thus AA is expected to be the weakest of all.

Now let us apply the conclusions of semi empirical rules of Goodenough and Kanamori to the configurations we have pointed out. We see that direct application is possible only for the BB interactions with M-O-M angle to be 90° . The case of A-B interaction with M-O-M angle of 126° is more complicated. The usual way is to interpolate between the 180° and 90° configurations assuming rather arbitrarily that the change is smooth. If the signs of the 180° and 90° configurations happens to be opposite than the interpolation scheme is not reliable.

The AA interaction, as we have seen, are the weakest of all and really do not influence the ordering due to another interactions. This is true, of course, only when there are sufficient numbers of magnetic ions present on both the sites and that is implied throughout in our above discussion.

Based upon the G. K. rules and the interpolation, the following tables predict the interactions between the nearest pairs in the B sub-lattice and inter-sub-lattice interactions between the A and B sub-lattices for different d electron populations.

In general for spinel we find that $|J_{AB}| \gg |J_{BB}| \gg |J_{AA}|$ with J_{AB} , J_{BB} and J_{AA} all being negative.

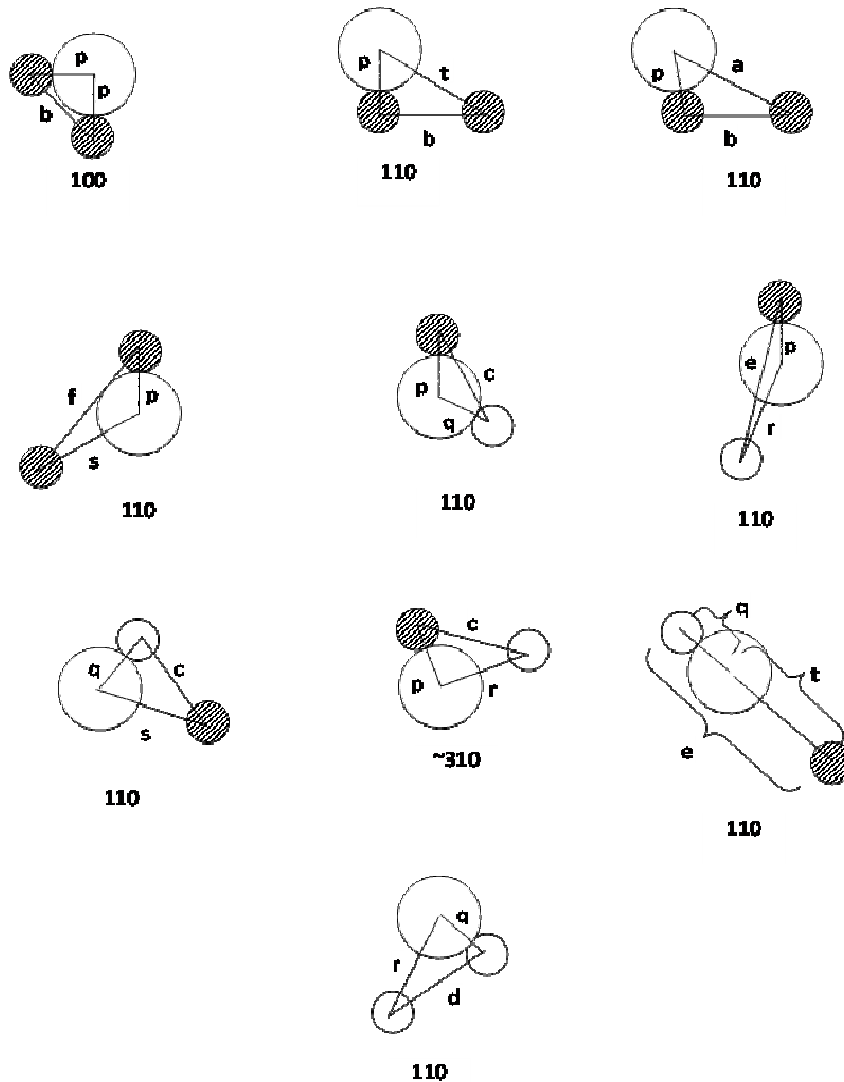


Figure 2.5 Near neighbour configuration in spinel lattice.

2.3 Magnetic ordering in a substituted ferrite

It has been shown that in ferrites, due to sublattice magnetic ordering the ferrimagnetism occurs. From the site preferences like diamagnetic cations such as Li^+ , Mg^{2+} , Al^{3+} , Ti^{4+} and Nb^{5+} are known to prefer B-site, while cations such as Zn^{2+} , Ga^{3+} and Ge^{4+} prefer A-site [18 - 22]. For example, in GeCo_2O_4 a 2-4 spinel, all Ge^{4+} ions are located at the A-site [23, 24]. Similarly in

CoFe_2O_4 an inverse spinel structure with all Co^{2+} ions at the B-site and Fe^{3+} being equally distributed over the A- and B-sites. The heat treatment given to such ferrites determines the degree of inversion [25].

The addition of extra non-magnetic substance modifies the magnetic properties giving rise to wide spectrum of magnetic structures; ferrimagnetic, antiferromagnetic, spin glass, local canting etc. In particular, models are developed to investigate magnetic properties of diluted systems like spin glass and spin canting. The highly substituted system reveal two transitions in susceptibility versus temperature curve, one at T_N (Neel temperature) for S_Z (Z component of magnetic moment) for conventional collinear order, whereas the other at T_f (freezing temperature) for S_T (the transverse component) for spin glass like ordering.

2.4 Neel theory of ferrimagnetism

Consider the simplest case of two sub-lattices, which have anti parallel and unequal magnetic moments. The inequality may be due to

- a. Different elements in different sites
- b. Same elements in different ionic states
- c. Different crystalline fields leading to different effective moments for ions having the same spin.

Neel's model is briefly outlined below which is based on a simplified model composed of identical magnetic ions divided unequally between the A and B sub-lattices.

Let there be n identical magnetic ions per unit volume with fraction λ located on the A sites and $\nu (= 1-\lambda)$ on the B sites. Let μ_A and μ_B the average moments of an A ion and B ion in the direction of field at temperature T .

Though, A- and B- sites ions are identical, μ_A and μ_B are not because they feel different fields in different sites.

Let $M_A = n\mu_A$ and $M_B = n\mu_B$

The Molecular fields acting on both sub-lattices are

$$H_{mA} = \gamma_{AB} (\lambda\alpha M_A - \nu M_B)$$

$$H_{mB} = \gamma_{AB} (\beta\nu M_B - \lambda M_A)$$

Where $\alpha = \gamma_{AA}/\gamma_{AB}$ and $\beta = \gamma_{BB}/\gamma_{AB}$

γ_{AA}, γ_{AB} and γ_{BB} are the Weiss constants

The above equations yield the expression for mass susceptibility as follows which is derived from the solving the equations above T_c

$$\frac{1}{\chi} = \frac{T}{C} + \frac{1}{\chi_0} + \frac{b}{T - \theta'}$$

$$\text{where, } \frac{1}{\chi_0} = \gamma_{AB}\rho(2\lambda\nu - \alpha\lambda^2 - \beta\nu^2)$$

$$b = \gamma_{AB}^2\rho^2 C\lambda\nu[\lambda(1+\alpha) - \nu(1+\beta)]^2$$

$$\theta' = \gamma_{AB}\rho C\lambda\nu(2+\alpha+\beta)$$

where, ρ density and C is Curie constant for the material. From equating $\chi = 0$ in the above equation for negative value of Weiss constants the Neel temperature can be given as $T_N = \gamma_{AB}\rho C/2 [\alpha\lambda + \beta\nu + \{(\alpha\lambda - \beta\nu)^2 + 4\lambda\nu\}^{1/2}]$

The equation for the mass susceptibility actually represents a hyperbola and physically meaningful part of it is shown in Figure 2.6. The curve cuts the temperature axis at θ_p which is called paramagnetic Curie point. It is in good agreement with the experimental observed susceptibility v/s temperature which differentiates ferrimagnetics from ferromagnetics.

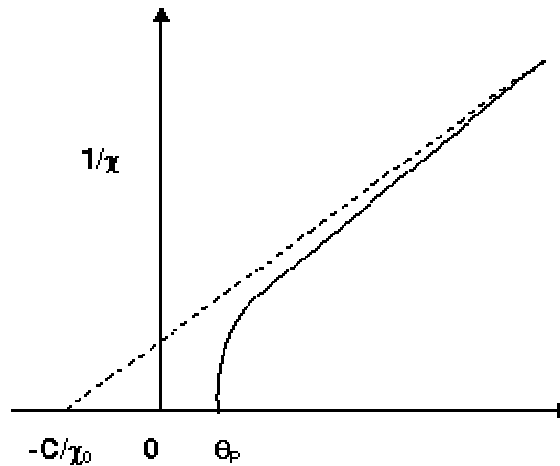


Figure 2.6 Variation of inverse susceptibility with Temperature (K) below T_c .

In the ferrimagnetic region each sub-lattice is spontaneously magnetized by the molecular field acting on it. But the two sub-lattice magnetizations are opposite to each other. The observable magnetization is

$$|M| = |M_B| - |M_A|$$

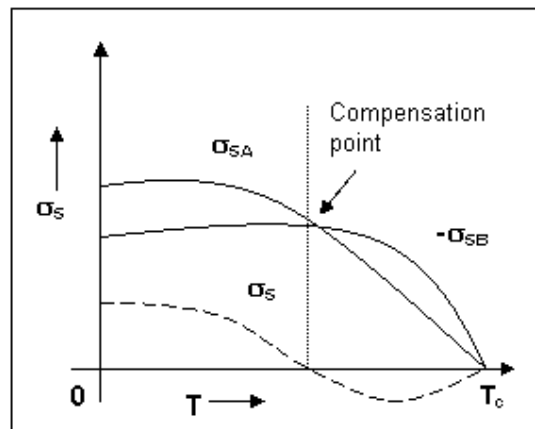


Figure 2.7 Anomalous magnetization v/s temperature curve for ferrimagnets.

Each sub-lattice magnetizations are governed by the same relation as ferromagnetics. In terms of specific magnetization, they are given by

$$\frac{\sigma_A}{\sigma_0} = B\left(J, \frac{\mu_H H_{m\Lambda}}{kt}\right)$$

$$\frac{\sigma_B}{\sigma_0} = B\left(J, \frac{\mu_H H_{mB}}{kt}\right)$$

Where, k is Boltzmann constant and B is Brillouin function.

These sub-lattice magnetizations will have different temperature response because effective molecular field acting on them are different. This suggests the possibility of having anomalous net magnetization versus temperature curves. For most ferrimagnetics the curves show simple behaviour but in few cases there may be a compensation point or a maximum in the curve at some temperature. The shape of the curve depends on γ , λ , ν and α . There is an interesting possibility of the net magnetization reversing its sign. The situation is depicted in Figure 2.7 where, at some temperature below T_c Both the $|M_B| = |M_A|$ and of opposite sign. So M disappears at that point, which is called compensation point. Gorter [26] observed these types of behaviour in Li-Cr system.

Let's see how beautifully the Neel model explains the observed features of spinel ferrite. Take the case of Nickel ferrite, where the magnetic moments of Ni and Fe are reasonably different. It gives observed magnetic moment $2.3 \mu_B$. Now let us predict the cation distribution for it.

According to Neel model, if a normal structure is assumed the moment comes out is $8 \mu_B$ as follows

$$M = |M_B| - |M_A| = [2 \times 5\mu_B (\text{Fe})] - (1 \times 2\mu_B(\text{Ni})) = 8\mu_B$$

and an inverse will give $2 \mu_B$ as follows

$$M = |M_B| - |M_A| = [1 \times 5\mu_B (\text{Fe}) + 1 \times 2\mu_B(\text{Ni})] - (1 \times 5\mu_B(\text{Fe})) = 2\mu_B$$

The later is near to observed value which allows us to term the Nickel ferrite as an inverse structure. A nominal observed difference is always present in every cases and may be ascribed to the following factors

- (1) g factor may not be exactly 2
- (2) the structure may not be completely inverse
- (3) particular ion may have different moments when in different sites.

Shortcomings of the Neel model

- (1) Saturation magnetization values in many ferrites are found to be much lower than those predicted by Neel model.
- (2) Some M v/s T curves have finite slopes at 0 K and cannot be explained by Neel model.
- (3) It is based on the assumption that strong negative AB interaction predominates over AA and BB interactions, which is not applicable to each and every case.

Random Canting of Spin Model

The non-collinear or canted spin arrangement can be explained in terms of the random canting model [27]. Substitution in one sublattice of a ferrimagnet leads to spin canting in the other sublattice. Rosencwaig [28] supposed that the nearest neighbour of the B-site can be considered to be canted with an average angle $\langle \alpha_B \rangle$ due to the A-site substitution which in the average nearest neighbour approximation estimated to the

$$\text{Cos}\langle \alpha_B \rangle = \frac{M_A}{M_B} \left(\frac{J_{AB}}{J_{BB}} \right)$$

The saturation magnetization per formula unit (Magnetron number in Bohr magneton, μ_B) is related to canting angle, $\langle \alpha_B^c \rangle$ by,

$$n_B^c = M_B \cdot \cos\langle\alpha_B^c\rangle - M_A$$

Here, M_A and M_B are sublattice magnetization of the A- and B-sites respectively, to be determined from cation distribution. The J_{AB} and J_{BB} are exchange integrals.

References

1. J. Smit and H.P.J Wijn,
Ferrites-Physical properties of Ferrimagnetic Oxides in Relation to
Their Technical Applications, (N.V. Philips Gloeilampenfabrieken,
Eindhoven, Holland, (1959) p. 136-176.
2. H. A. John and E. Teller, Proc. R. Soc., London Ser., A161 (1937)220.
3. J. B. Goodenough, Annuan Rev. Materials Science, 28 (1998)1-27.
4. H. Ohnishi and T. Teranishi, J. Phys. Soc. Japan, 16 (1961)35.
5. J. C. Slater, Phys. Rev. 35 (1930)509.
6. J. C. Slater, Phys. Rev. 36 (1930)57.
7. H. A. Kramers, Physica 1, (1934)182.
8. P. W. Anderson, Phys. Rev. 115 (1959)2.
9. P. W. Anderson, Solid State Physics 14 (1963)99.
10. P. W. Anderson, Magnetism, Eds. G. T. Rado and H Shull, 1
(Academic Press, New York, 1963)25.
11. P. W. Anderson and H. Hassgawa, Phys. Rev. 100 (1955)675.
12. J. H. Van Vleck, J. Phys. Radium 12 (1951)262.
13. J.C.Slater, Quart, Porf. Rept. M. I. T. July 15, 1, (1953) and
October 15, 1, (1953)
14. T. Nagamiya, K. Yoshida and R. Kubo, Advan. Phys. 4 (1955)1.
15. J. B. Goodenough and A. L. Loeb, Phys. Rev. 98 (1955)391.
16. J. Kanamori, J. Phys. Chem. Solids, 10 (1959)87.
17. J. B. Goodenough, Phys. Rev. 117 (1960)1442.
18. H. Knock and H. Dannheim, Phys. Status Solidi A37 (1976)K135.

19. E. De Grave, C. Druve. A. Govaert and J. De Sitter, Phys. Status Solidi B37 (1976)527.
20. S. K. Kulshreshtha, G. Ritter, J. Mat. Sci. 20 (1985)821.
21. P. Raj and S. K. Kulshreshtha, J. Appl. Phys. 42 (1971)2344.
22. M. Robbins, J. Phys. Chem. Solids 26 (1965)831.
23. F. C. Romenjn, Philips Res. Rep. 8 (1962)304.
24. G. Blasse and J. F. Fast , Philips Res. Rep. 18 (1963)393.
25. R. Plumier, J. Appl. Phys. 39 (1968)635.
26. H. W. Gorter, Philips Res. Repts. 9 (1954)295.
27. J. M. D. Coey, Can. J. Phys. 65 (1987)1210.
28. A. Rosencwaig, Can. J. Phys. 48 (1970) 2857.

Chapter 3

Synthesis and characterization techniques

3.1 Synthesis of spinel ferrites

The properties of spinel ferrite are very much sensitive to the preparation conditions. A number of novel methods have been developed since then for the preparation of homogenous, fine/coarse grained and high density spinel ferrite.

The preparation methods have been classified as:

- (i) Ceramic method
- (ii) Wet-chemical method (co-precipitation method)
- (iii) Precursor method (Combustion, Sol-gel technique etc)

(i) Ceramic method

This is the conventional powder processing method which is commercially accepted since it is possible to maintain the stoichiometry of the final product even in large scale industrial production. In this method, the preparation of spinel ferrite takes place at about 1000°C by solid state reaction. The finely grained powder of the required composition is shaped by pressing and finally sintered to obtain ceramically prepared spinel ferrite.

The appropriate metal oxides or their salts, which decompose to give metal oxides are accurately weighed in the desired proportion and mixed thoroughly. The mixing is usually carried out in liquid suspension (water, acetone, alcohol or kerosene) in agate mortar and pestle or ball mill. The slurry is dried or filtered depending upon the suspension medium and then transferred to ceramic crucibles and pre-sintered in air or oxygen atmosphere.

The pre-sintered powder contains nucleation centres that are mixed homogeneously using agate mortar and pestle or ball mill, which helps in the

distribution of nucleation centres formed during pre-sintering. The mixing at this stage determines the size as well as the grain size distribution. An organic binder like polyvinyl alcohol (PVA) or Carbon tetrachloride (CTC) is often added at this stage. The sample is then pressed in a suitable die at about 5 to 10×10^6 kg/m². The pressed material is then fired in oxygen or air between 1000° - 1300° C depending upon the substitutions in the ferrites. The completion of solid state reaction gives rise to homogeneous ferrites.

The ceramic method can be briefly described in four steps:

- (i) Initial mixing, grinding and pelletizing
- (ii) First sintering or pre-sintering
- (iii) Regrinding and re-pelletizing
- (iv) Final sintering

(ii) Co-precipitation (wet-chemical) method

The preparation of ferrites powders by the co-precipitation method consists of oxidation by bubbling oxygen gas through an aqueous suspension of hydroxides of ferrous and other di or trivalent ions after an alkaline solution has been added. Thus powders with high homogeneity and purity are obtained [1]. In this method, the starting solution is prepared by mixing required amount of aqueous solutions of corresponding sulphates/nitrates/chlorates in proper proportions. A solution of Sodium hydroxide (NaOH) of appropriate molarity (generally about 2M) is used as a precipitant. It has been suggested that the solubility product constant (K_{sp}) [2] of all the constituents is always exceeded when the starting solution is added into the precipitant. Therefore in order to achieve simultaneous precipitation of

hydroxides, the starting solution ($\text{pH} < 7$) is added to the precipitant and the suspension ($\text{pH} > 7$) is heated at about 60°C - 100°C and oxygen gas is bubbled uniformly into the suspension to promote oxidation reaction until all the precipitates change into the precipitates of ferrites. The samples are filtered, washed and dried at 200°C under vacuum.

The wet samples when annealed in air at about 1000°C , exhibit generally weight loss because of removal of water and hydroxyl ions even after the prolonged drying process.

The wet-chemical method can be briefly described in five steps:

- (i) Preparation of starting solution
- (ii) Precipitation of hydroxides
- (iii) Oxidation at $\approx 60^{\circ}\text{C}$ with stirring
- (iv) Filtering and washing the precipitate of ferrites
- (v) Drying at 100 - 200°C

(iii) Precursor method

This method involves preparing a precursor, which is a solid solution or a compound containing metal ions in the desired ratio and the decomposition of precursor to yield the ferrites. Some of the precursor methods used are:

- (a) Hydroxide precursor
- (b) Carbonate precursor
- (c) Oxalate precursor
- (d) Hydrazine carboxylate precursor

This method requires low sintering temperature and hence it is possible to maintain proper stoichiometry and obtain fine particle ferrite. The disadvantage in this method is that the hydroxides are gelatinous and therefore it is difficult to handle, filter and wash them. Sometimes the losses of ions like Cu, Ni occur on complexing with ammonia. The incomplete precipitation may result in undesired compositions [3].

3.2 Structural and micro- structural characterization

(A) Energy Dispersive Analysis of X-rays (EDAX)

EDAX stands for Energy Dispersive analysis of X-rays. It is sometimes referred to as EDS analysis. Energy dispersive X-ray spectroscopy is an analytical technique used predominantly for the elemental analysis or chemical characterization of a specimen. Being a type of spectroscopy, it relies on the investigation of a sample through interactions between electromagnetic radiation and matter, analyzing X-rays emitted by the matter in this particular case. Its characterization capabilities are due in large part to the fundamental principle that each element of the periodic table has a unique atomic structure allowing X-rays that are characteristic of an element's atomic structure to be uniquely distinguished from each other.

To stimulate the emission of characteristic X-rays from a specimen, an high energy beam of charged particles such as electrons or protons, or a beam of X-rays, is focused into the sample to be characterized. At rest, an atom within the sample contains ground state (or unexcited) electrons situated in discrete energy levels or electron shells bound to the nucleus. The incident beam may

excite an electron in an inner shell, prompting its ejection and resulting in the formation of an electron hole within the atom's electronic structure. An electron from an outer, higher-energy shell then fills the hole, and the difference in energy between the higher-energy shell and the lower energy shell is released in the form of an X-ray. The X-ray released by the electron is then detected and analyzed by the energy dispersive spectrometer. These X-rays are characteristic of the difference in energy between the two shells, and of the atomic structure of the element from which they were emitted.

Principle of EDAX

During EDAX analysis the specimen is bombarded with an electron beam inside the scanning electron microscope. The bombarding electrons collide with the specimen atoms own electrons, knocking some of them off in the process. A position vacated by an ejected inner shell electron is eventually occupied by a higher energy electron from an outer shell. To be able to do so, however the transferring outer electron must give up some of its energy by emitting an x-ray.

The amount of energy released by the transferring electron depends on which shell it is transferring from, as well as which shell it is transferring to. Furthermore, the atom of every element releases X-rays with unique amounts of energy during the transferring process. Thus, by measuring the amounts of energy present in the x-rays being released by a specimen during electron beam bombardment, the identity of the atom from which the X-rays was emitted can be established.

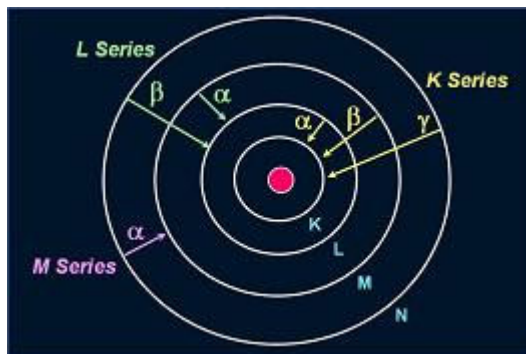


Figure 3.1 Elements in an EDX spectrum are identified based on the energy content of the X-rays emitted by their electrons as these electrons transfer from a higher-energy shell to a lower-energy one.

The output of an EDAX analysis is an EDAX spectrum. The EDAX spectrum is just a plot of how frequently an X-ray is received for each energy level. An EDAX spectrum normally displays peak corresponding to the energy levels for which the most x-rays had been received (Figure 3.2) Each of these peaks are unique to an atom, and therefore corresponds to a single element. The higher a peak in a spectrum, the more concentrated the element is in the spectrum

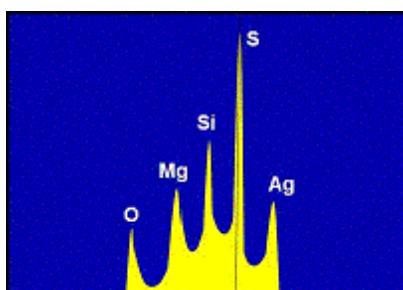


Figure 3.2 Example of an EDX spectrum.

Construction and working of spectrometer

The essential parts of the Energy Dispersive spectrometer are shown in the diagram (Figure 3.3).

The sample specimen is bombarded with x-rays of enough high energy generated from the X-ray tube. The fluorescence radiation, emitted by the sample comprising of various wavelengths according to the various elements present in the sample is analyzed and various wavelengths are separated on the basis of their energies by means of a Si (Li) counter and a multichannel analyzer (MCA).

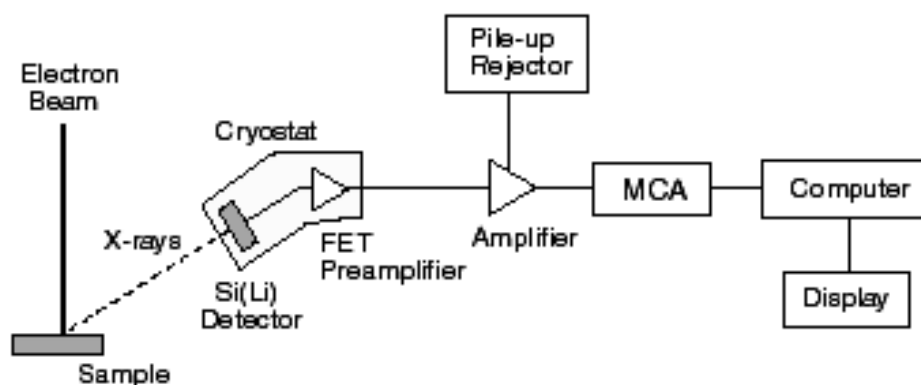


Figure 3.3 Energy Dispersive spectrometer.

The counter produces the pulses proportional in height to the energies in the incident beam and MCA sorts out the various pulse heights. The excellent energy resolution of the Si (Li) counter with FET preamplifier and the ability of the MCA to perform rapid pulse height analysis make the spectrometer to measure the intensities of all the spectral lines from the sample in about a minute, unless there are elements in very low concentration are to be determined.

(B) X-ray powder diffractometry

When X-ray radiation passes through matter, the radiation interacts with the electrons in the atoms, resulting in scattering of the radiation. If the atoms are organized in planes (i.e. the matter is crystalline) and the distances between the atoms are of the same magnitude as the wavelength of the X-rays, constructive

and destructive interference will occur. This result in diffraction where X-rays are emitted at characteristic angles based on the spaces between the atoms organized in crystalline structures called planes. Most crystals can have many sets of planes passed through their atoms. Each set of planes has a specific inter planer distance and will give rise to a characteristic angle of diffracted X-rays. The relationship between wavelength, atomic spacing (d) and angle was solved as the Bragg Equation. If the illuminating wavelength is known (depends on the type of X-ray tube used and if a monochromator is employed) and the angle can be measured (with a diffractometer) then the inter planer distance can be calculated from the Bragg equation. A set of 'd-spaces' obtained from a single compound will be represent the set of planes that can be passed through the atoms and can be used for comparison with sets of d-spaces obtained from standard compounds.

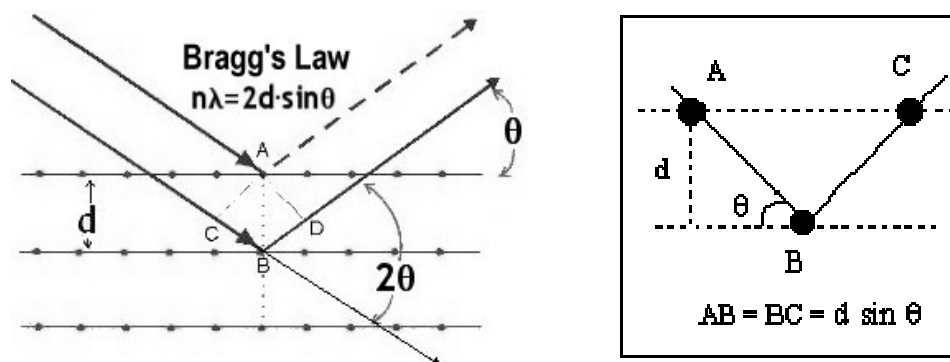


Figure 3.4 Bragg's law is satisfied when the inter planer spacing equals to $2d \sin \theta$

Diffraction of X-ray beam striking a crystal occurs because the λ of the X-ray beam is equivalent to the spacing of atoms in minerals (1-10 Å). When an X-ray beam encounters the regular, 3-D arrangement of atoms in a crystal most of the x-rays will destructively interfere with each other and cancel each other

out, but in some specific directions they constructively interfere and reinforce one another. It is these reinforced (diffracted) X-rays that produce the characteristic X-ray diffraction patterns that used for mineral identification. W.L. Bragg (early 1900's) showed that diffracted X-rays act as if they were "reflected" from a family of planes within crystals. Bragg's planes are the rows of atoms that make up the crystal structure.

These "reflections" were shown to occur under certain conditions, which satisfy the equation:

$$n\lambda = 2d\sin\theta$$

where, n is an integer (1, 2, 3,, n), λ the wavelength, d the distance between atomic planes, and θ the angle of incidence of the X-ray beam and the atomic planes. $2d\sin\theta$ is the path length difference between two incident X-ray beams where one X-ray beam takes a longer (but parallel) path because it "reflects" off an adjacent atomic plane. This path length difference must be equal to an integer value of the λ of the incident X-ray beams for constructive interference to occur such that a reinforced diffracted beam is produced. For a given λ of incident X-rays and inter planer spacing (d) in a mineral, only specific angles (θ) will satisfy the Bragg equation. For example, on focusing a monochromatic X-ray beam (X-rays with a single λ) on a cleavage fragment of calcite and slowly rotating the crystal, no "reflections" will occur until the incident beam makes an angle θ that satisfies the Bragg equation with $n = 1$. Continued rotation leads to other "reflections" at higher values of λ and correspond to when $n = 2, 3 \dots$ etc; these are known as 1st, 2nd, 3rd order, etc., "reflections".

Powder Methods: (X-ray beam focused on a powder pellet or powder smeared on a glass slide). This method is essential for minerals that do not form large crystals (i.e. clays) and eliminates the problem of precise orientation necessary in single-crystal methods with its primary application being for mineral identification. It can also be used to determine mineral compositions (if d-spacing is a function of mineral chemistry) and to determine relative proportions of minerals in a mixture. Monochromatic X-rays are focused on pellet or slide mounted on rotating stage. Since sample is powder, all possible diffractions are recorded simultaneously from hypothetical randomly oriented grains. Mount is then rotated to ensure all diffractions are obtained. Older methods used photographic techniques while most modern applications employ X-ray powder diffractometers.

X-ray powder diffractometry



Figure 3.5 Photograph of a typical X-ray diffractometer.

X-ray powder diffractometry uses monochromatic X-rays on powder mounted on glass slide that is attached to a stage which systematically rotates

into the path of the x-ray beam through $\theta = 0$ to 90° . The diffracted x-rays are detected electronically and recorded on an inked strip chart. The detector rotates simultaneously with the stage, but rotates through angles $= 2\theta$. The strip chart also moves simultaneously with the stage and detector at a constant speed. The strip chart records the intensity of X-rays as the detector rotates through 2θ . Thus, the angle 2θ at which diffractions occur and the relative intensities can be read directly from the position and heights of the peaks on the strip chart. Use is then made of the Bragg equation to solve for the inter planer spacing (d) for all the major peaks and look up a match with JCPDS cards. JCPDS = Joint Committee on Powder Diffraction Standards.

The X-ray diffractograms were recorded on Philips PW 1710 automated X-ray powder diffractometer using CuK_α radiation, graphite monochromator, and Xe-filled proportional counter with following specifications.

Scanning rate: 1 degree /minute

Chart speed : 2 cm /minute

The X-ray diffraction patterns were obtained from SICART, Vallabh Vidya nagar, Gujarat.

The procedure of indexing the X-ray diffractograms, determination of lattice parameter and X-ray intensity calculations are briefly explained below: In the case of a cubic lattice,

$$\frac{1}{d^2} = \frac{h^2 + k^2 + l^2}{a^2} \quad (1)$$

where, a = lattice parameter

d = Inter planer spacing between adjacent planes

(hkl) = Miller indices.

Using Bragg's law in Equation (1),

$$\sin^2 \theta_{hkl} = \frac{\lambda^2}{4a^2} (h^2 + k^2 + l^2) \quad (2)$$

where λ = incident wavelength.

In equation (2) the sum $(h^2 + k^2 + l^2)$ is always an integer while $\lambda^2/4a^2$ is constant for any one pattern. The equation further suggests that for a particular cubic crystal, the diffraction takes place at all possible values of Bragg's angle from the planes (hkl) .

The indices of different planes of a diffractogram for the cubic system can be derived as:

$$\frac{\sin^2 \theta}{(h^2 + k^2 + l^2)} = \frac{\lambda^2}{4a^2} \quad (3)$$

Lattice parameter ' a ' can be determined using the formula,

$$a = N^{1/2} d \quad (4)$$

where, $N = (h^2 + k^2 + l^2)$

In order to determine the cation distribution, X-ray diffraction line intensities were calculated using the formula suggested by Buerger:

$$I_{hkl} = |F_{hkl}|^2 PL_p$$

where I_{hkl} = Relative integrated intensity

F_{hkl} = Structure factor

P = Multiplicity factor

L = Lorentz-polarization factor

θ = Bragg's angle

The details are given chapter 4.

The Rietveld refinement method

There are six factors affecting the relative intensities of the diffraction lines on a powder pattern, namely, (i) Polarization factor, (ii) Structure factor, (iii) Multiplicity factor, (iv) Lorentz factor, (v) absorption factor and (vi) Temperature factor. A very important technique for analysis is powder diffraction data is the whole pattern fitting method proposed by Rietveld (1969) [4, 5]. The Rietveld method is an extremely powerful tool for the structural analysis of virtually all types of crystalline materials not available as single crystals. The method makes use of the fact that the peak shapes of Bragg reflection can be described analytically and the variations of their width (FWHM) with the scattering angle 2θ . The analysis can be divided into number of separate steps. While some of these steps rely on the correct completion of the previous one(s), they generally constitute independent task to be completed by experimental and depending of the issue to be addressed by any particular experiment, one, several of all these tasks will be encountered [6].

The parameters refined in the Rietveld method fall into mainly three classes: peak shape function, profile parameters and atomic and structural parameters. The peak shapes observed are function of the both the sample (e.g. domain size, stress/strain, defects) and the instrument (e.g. radiation source, geometry, slit sizes) and they vary as a function of 2θ . The profile parameters

include the lattice parameters and those describing the shape and width of Bragg peaks (changes in FWHM and peak asymmetry as a function of 2θ , 2θ correction, unit cell parameters). In particular, the peak widths are smooth function of the scattering angle 2θ . It uses only five parameters (usually called U, V, W, X and Y) to describe the shape of all peaks in powder pattern. The structural parameters describe the underlying atomic model include the positions, types and occupancies of the atoms in the structural model and isotropic or anisotropic thermal parameters. The changes in the positional parameters cause changes in structure factor magnitudes and therefore in relative peak intensities, whereas atomic displacements (thermal) parameters have the effect of emphasizing the high angle region (smaller thermal parameters) or de-emphasizing it (larger thermal parameters). The scale, the occupancy parameters and the thermal parameters are highly correlated with one another and are more sensitive to the background correction than are the positional parameters. Thermal parameter refinement with neutron data is more reliable and anisotropic refinement is sometimes possible. Occupancy parameters are correspondingly difficult to refine and chemical constraints should be applied whenever possible [7].

Once the structure is known and a suitable starting model is found, the Rietveld method allows the least-squares refinement [chi-squared (χ^2) minimization] of an atomic model (crystal structure parameters) combined with an appropriate peak shape function, i.e. a simulated powder pattern, directly against the measured powder pattern without extracting structure factor of integrated

intensities. With a complete structural model and good starting values of background contribution, the unit cell parameters and the profile parameters, the Rietveld refinement of structural parameters can begin. A refinement of structure of medium complexity can require hundred cycles, while structure of high complexity may easily require several hundreds. The progress of refinement can be seen from the resultant profile fit and the values of the reliability factors or R-values. The structure should be refined to convergence. All parameters (profile and structural) should be refined simultaneously to obtain correct estimated standard deviations can be given numerically in terms of reliability factors of R-values [8]. The weighted profile R value, R_{WP} is defined as,

$$R_{WP} = \left\{ \frac{\sum_i w_i \{ y_i(\text{obs}) - y_i(\text{calc}) \}^2}{\sum_i w_i y_i(\text{obs})^2} \right\}^{1/2} \times 100\%$$

Ideally, the final R_{WP} , should approach the statistically expected R Value, R_{exp} ,

$$R_{exp} = \left\{ \frac{(N - P + C)}{\sum_i w_i y_i(\text{obs})^2} \right\}^{1/2} \times 100\%$$

where, N is the number of observations and P the number of parameters and C is the number of constraints used in the refinement.. R_{exp} reflects the quality of data. Thus, the ratio between the two (goodness of fit),

$$\chi^2 = (R_{wp} / R_{exp})^2$$

An R value is observed and calculated structure factors, F_{hkl} , can also be calculated by distributing the intensities of the overlapping reflections according to the structural model,

$$R_F = \left(\frac{\sum_{hkl} |F_{hkl}(\text{obs}) - F_{hkl}(\text{calc})|}{\sum_{hkl} F_{hkl}(\text{obs})} \right) \times 100\%$$

Similarly, the Bragg-intensity R value can be given as,

$$R_I = \left(\frac{\sum_{hkl} |I_{hkl}(\text{obs}) - I_{hkl}(\text{calc})|}{\sum_{hkl} I_{hkl}(\text{obs})} \right) \times 100\%$$

R values are useful indicators for the evaluation of refinement, especially in the case of small improvements to the model, but they should not be over interpreted. The most important criteria for judging the quality of a Rietveld refinement are (i) the fit of the calculated patterns to the observed data and (ii) the chemical sense of structural model.

(C) Scanning electron microscopy(SEM)

The SEM was pioneered by Manfred von Ardenne in 1937. The instrument was further developed by Charles Oatley and first commercialized by Cambridge Instruments.



Figure 3.6 SEM opened sample chamber.

The scanning electron microscope (SEM) is a type of electron microscope that creates various images by focusing a high energy beam of electrons onto the surface of a sample and detecting signals from the interaction of the incident electrons with the sample's surface. [9, 10]

The type of signals gathered in a SEM varies and can include secondary electrons, characteristic X-rays, and back scattered electrons. In a SEM, these signals come not only from the primary beam impinging upon the sample, but from other interactions within the sample near the surface. The SEM is capable of producing high-resolution images of a sample surface in its primary use mode, secondary electron imaging. Due to the manner in which this image is created, SEM images have great depth of field yielding a characteristic three-dimensional appearance useful for understanding the surface structure of a sample. This great depth of field and the wide range of magnifications are the most familiar imaging mode for specimens in the SEM. Characteristic x-rays are emitted when the primary beam causes the ejection of inner shell electrons from the sample and are used to tell the elemental composition of the sample. The back-scattered electrons emitted from the sample may be used alone to form an image or in conjunction with the characteristic x-rays as atomic number contrast clues to the elemental composition of the sample.

In a typical SEM, electrons are thermionically emitted from a tungsten or lanthanum hexaboride (LaB_6) cathode and are accelerated towards an anode; alternatively, electrons can be emitted via field emission (FE). Tungsten is used because it has the highest melting point and lowest vapour pressure of all metals, thereby allowing it to be heated for electron emission. The electron beam, which typically has an energy ranging from a few hundred eV to 100 keV, is focused by one or two condenser lenses into a beam with a very fine focal spot sized 0.4 nm to 5 nm. The beam passes through pairs of scanning coils or pairs

of deflector plates in the electron optical column, typically in the objective lens, which deflect the beam horizontally and vertically so that it scans in a raster fashion over a rectangular area of the sample surface. When the primary electron beam interacts with the sample, the electrons lose energy by repeated scattering and absorption within a teardrop-shaped volume of the specimen known as the interaction volume, which extends from less than 100 nm to around 5 μm into the surface. The size of the interaction volume depends on the electrons' landing energy, the atomic number of the specimen and the specimen's density. The energy exchange between the electron beam and the sample results in the emission of electrons and electromagnetic radiation, which can be detected to produce an image.

Electronic devices are used to detect and amplify the signals and display them as an image on a cathode ray tube in which the faster scanning is synchronized with that of the microscope. The image displayed is therefore a distribution map of the intensity of the signal being emitted from the scanned area of the specimen. The image may be captured by photography from a high resolution cathode ray tube, but in modern machines is digitally captured and displayed on a computer monitor.

Resolution of the SEM

The spatial resolution of the SEM depends on the size of the electron spot, which in turn depends on both the wavelength of the electrons and the magnetic electron-optical system which produces the scanning beam. The resolution is also limited by the size of the interaction volume, or the extent to which the

material interacts with the electron beam. The spot size and the interaction volume both might be large compared to the distances between atoms, so the resolution of the SEM is not high enough to image individual atoms, as is possible in the shorter wavelength (i.e. higher energy) transmission electron microscope (TEM). The SEM has compensating advantages, though, including the ability to image a comparatively large area of the specimen; the ability to image bulk materials (not just thin films of foils); and the variety of analytical modes available for measuring the compositions and nature of the specimen. Depending on the instrument, the resolution can fall somewhere between less than 1nm and 20nm. The world's highest SEM resolution is obtained with the Hitachi S-5500. Resolution is 0.4 nm at 30kV and 1.6 nm at 1 kV.

3.3 Elastic properties

(A) Ultrasonic pulse echo-overlap technique

Introduction

Ultrasonic is the term used to describe the study of all sound like waves whose frequency is above the range of normal human hearing. Ultrasonic has been with the living beings from prehistoric days, though the human being had limited themselves to the primary sense of sound and hearing in the audible almost 200 years ago that dogs could hear sound at frequencies well above the audible limits (Ultrasonic Sounds) and hence the Galtoris whistle began to be used as a practical device. The clear recognition that bats use ultrasound for location, locomotion and communication was however made less than hundred years ago. The use of ultrasound as a means of locating underwater objects, started at the

time of the First World War, is the beginning of the modern phase of the subject. Here also it has been recognized that underwater animals like whales, porpoises and dolphins have been using similar techniques in nature.

Ultrasonic becomes an important tool in physics, a far ranging tool for flaw detection in engineering, a rival to the x-rays in medical and a reliable method of underwater sound signaling. Ultrasonic measurement stands as one of the primary techniques for study of properties of matter such as mechanical, electromagnetic and particle interaction. The term silent sound also has been used in the literature to denote ultrasonic waves. Ultrasound (US) is simple mechanical wave at a frequency above the limit of human hearing. It can be generated at a broad range of frequencies (20 kHz - 10 MHz) and acoustic intensities. It can be further subdivided into three frequency ranges:

Power US (20 Hz – 100 kHz)

High frequency (100 kHz - 1 MHz)

Diagnostic US (1 MHz - 10 MHz)

US application parameters are given below:

US frequency : more than 20 kHz

US intensity : Power supplied per transducer area, unit (watt/cm^2)

US density : Power supplied per sample volume, unit (watt/l)

US dose : Energy supplied per sample volume, unit (J/l)

Generation and detection of Ultrasound

Ultrasonic energy is generated and detected by devices called transducers. By definition, transducer is a device that transfers power from one system to another

one. In ultrasonic, the most typical conversions are electrical to Ultrasonic energy (transmitters) or Ultrasonic to electrical energy (receivers). Transducers most often used for generating ultrasound are piezoelectric, magnetostrictive, electromagnetic and mechanical devices. Transducers are used for generating and monitoring ultrasonic waves in different substances viz. gases, liquids and solids and are at the heart of ultrasonic instrumentation. Several methods can be used in generating and detecting ultrasonic waves in physical ultrasonic. Few methods require direct physical contact between the propagating medium and the ultrasonic source, the best example being piezoelectric transducers. At very high temperatures and materials that are highly corrosive and inaccessible, non-contact transducers are needed. Electromagnetic, Capacitive and Optical transducers come under this category.

Specimen

Since, the non-parallelism of faces of transducer causes errors in measurement of attenuation and velocity; therefore the specimen should be optically plane. If end faces of the sample are not perfectly (optically) plane and parallel, then a wave even though originally plane, when reflected, meets the transducers at an angle. Thus different surface areas of transducer detect different phases of the wave. The result will be an echo pattern with interference due to interference. Another error due to improper preparation of sample is called 'side wall effect' which results when sample cross-section is comparable to transducer diameter. This is due to beam divergence.

When ultrasonic waves are passing from liquid to metal in a short distance at the surface (due to roughness) the sound that passes through liquid lags the sound which travel through the metal because velocity of sound in liquid is less than the velocity of sound in metal. In this case the sound wave recombines inside the material so as to accommodate the difference in travel time. When this difference in travel time is equal to one half the period of sound wave, a pressure crest combines with a rarefaction through and the resultant energy is nearly zero in the metal. The average peak to valley roughness of the surface of specimen which will cause this destructive interference is called the critical roughness and is given by:

$$R_c = \lambda_1 v_2 / 2(v_2 - v_1) = \lambda_2 v_1 / 2(v_2 - v_1)$$

where , R_c = critical roughness,

λ_1 = wavelength of sound in liquid,

λ_2 = wavelength of sound in metal,

v_1 & v_2 = respective velocities.

Couplant

Though the thickness of couplant (bonding material) is very small (around 0.01 mm) for good coupling it is not entirely negligible compared to the thickness (5 - 10 mm) of many solid specimens used. The purpose of a couplant is to provide a suitable sound path between the transducer and the test surface. An ideal couplant effectively wets and totally contacts both surface of transducer and test part and expel all air between them. It also fills and smooth out irregularities on the surface of the test part and aids in the movement of the transducer over the

surface. Oil of water is commonly used as a couplant. Grease or heavy oil can be used on rough and vertical surface.

Transducer

The pulse echo method has to be refined when higher accuracy is needed in measurements. For instance, in a crystalline solid the velocity depends upon the direction of propagation. It is important therefore, to select diameter of the transducer 'D' large in comparison with a wave length of the acoustic wave, one gets a narrow beam of ultrasonic energy with an angular spread ϕ given by

$$\sin \phi = 1.2 \lambda / D$$

where, λ = wavelength of acoustic wave

It is clear that D should be large and ϕ small to keep beam divergences small. However if 'D' becomes comparable to the lateral dimensions of the specimen, reflection from the lateral walls of the specimen begin to interfere with the echo signals which create a serious problem in attenuation measurement.

The ultrasonic propagation characteristic of materials can be determined using two methods.

1. Continuous wave method and
2. Pulse echo method.

The continuous method, historically the older techniques, uses generally adopted in KHz regions. For low loss specimen it is possible to achieve high sensitivities with this method. If specimen thickness were too small to provide sufficient separation of pulse in pulse echo method, then the continuous wave

method would be better. The pulse method though generally requiring more complex instrumentation, overcomes most of the limitations of continuous wave method and have therefore come into wide spread use, the simplest pulse method is pulse echo method, where in a transducer is attached to a system (a solid or a liquid medium) in such a way that the ultrasonic energy can be clearly reflected from the opposite face and be received by transducer itself.

Ultrasonic pulse echo-overlap Technique

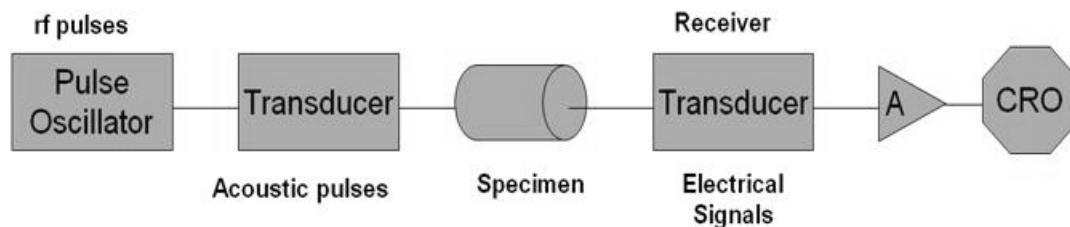


Figure 3.7 Block diagram of UPT Technique.

- Ultrasonic pulses were generated and detected by X-and Y-cut (for longitudinal and shear waves, respectively) 9 MHz PZT transducers.
- The sample was bonded to the transducer using Nonaq stopcock grease.
- The transmit time of the ultrasound was measured upto an accuracy of $1\mu\text{s}$ using a 100MHz digital storage oscilloscope
- The overall accuracy of these measurements is about 0.25% in velocity and about 0.5% in elastic moduli.

The periodic motion of a particle about its mean position in a body results in the vibrational motion of the adjacent particles due to transfer of mechanical energy. This transfer of disturbance and hence energy, is called wave motion. Out of the two possible wave motions, one is perpendicular to the direction of motion (transverse wave) while the other is parallel to it. The latter are called the

longitudinal waves, and they require a medium for their propagation. The waves falling in the range 20 – 20,000 Hz are called sonic (audible) waves and hence frequencies above this range are called ultrasonic waves. Ultrasonic waves are thus a branch of sound waves and it hence exhibits all the characteristic properties of sound waves. In nature, ultrasonic waves are mechanical vibrations with different wavelengths, when it is propagated through a medium. The change in wavelength of ultrasonic waves in different mediums is due to the elastic properties and the induced particle vibrations in the medium. Further, the wavelength of the ultrasonic waves is small and hence, exhibits some unique phenomena in addition to the properties of sound waves.

Types of ultrasonic waves

Based on the mode of propagation, the ultrasonic waves are classified into four different types that are listed below. These modes are classified according to the type of vibration of the particles in the medium with respect to the direction of propagation of the initial waves.

- (a) Longitudinal or Compressional waves
- (b) Transverse or Shear waves
- (c) Surface or Rayleigh waves and
- (d) Plate or Lamb waves

(a) Longitudinal or Compressional waves

As the name suggests, the particle motion is along the direction of propagation of the incident wave. Due to the vibrations of the particle, alternate compressional and rarefactional zones are produced. The mechanism of propagation for ultrasonic waves is same as that of ordinary sound waves in air, but instead of

the air molecules it is the atoms of the material under consideration that perform compression and rarefactions. The resulting propagation of disturbance at speeds more than that of sound is called longitudinal (compressional) ultrasonic waves. Because of the compression and rarefaction (dilation of pressure) processes present in the material, pressure is developed in the material, and hence these are also called pressure (or dilational) waves. The longitudinal waves that can propagate in solids, liquids and gases, are easy to generate, detect and convert into other modes of vibrations. The representation of longitudinal waves diagrammatically is difficult and is hence avoided. The velocity of all the types of the modes of propagation is independent of the frequency of the waves and the dimensions of the material. The velocity of the ultrasonic wave of any kind can be determined from the elastic moduli, density and Poisson's ratio of the material.

The longitudinal wave velocity (V_L) and Young's modulus (Y) of the material is related as,

$$V_L = \left[\frac{Y(1-\sigma)}{\rho(1+\sigma)(1-2\sigma)} \right]^{1/2}$$

where, ρ is the density of material (kgm^{-3}) and σ is the Poisson's ratio

(b) Transverse or Shear waves

Here the vibrations of the atoms of the material considered are perpendicular (transverse) to the direction of propagation of the ultrasound and hence the name. Here the forces generated due to propagation of the waves are transverse or shear to vibrations of the atoms and hence these are also called Shear waves.

Because of these transverse forces, the rate of energy dissipation is much more

than that for longitudinal waves. Consequently, velocity of the shear waves is approximately half as that of the longitudinal waves in the same material. Shear ultrasonic waves can pass only through solids and cannot be generated in liquids or gases. This is because, the mean distance between the atoms of liquids and gases is so large compared to solids that vibrations of one atom are not readily transferred to the neighboring atoms and hence the shear waves are attenuated exceedingly fast. For example, even for highly viscous liquids such as lubrication oils, the shear ultrasonic waves can travel a very short distance of the order of a millimeter. The expression for the velocity of transverse waves is,

$$V_T = \left[\frac{Y}{2\rho(1+\sigma)} \right] \quad V_T = \left[\frac{G}{\rho} \right]^{1/2}$$

where, G is the rigidity modulus (Nm^{-2}).

(c) Surface or Rayleigh waves

Lord Rayleigh (1885) demonstrated that waves can propagate over the plane boundary between an elastic half space and vacuum or sufficiently rarefied medium (e.g. air). The particle motion is elliptical and amplitude of the waves decays rapidly with the depth of propagation of the wave in the medium.

(d) Plate or Lamb waves

These types of waves were first described by Horace Lamb in 1916 theoretically and are hence named in his honour. Simply put, when the surface wave is introduced into a material, having thickness equal to three times the wavelength or less, a different kind of wave called plate or lamb waves. During the existence of the plate wave, the material begins to vibrate as plate i.e. the wave

encompasses the entire thickness of the material. Thus, velocity of these waves not only depends on the material type but also on the material thickness unlike the other type of waves.

Elastic Properties

Ultrasonic waves are strain waves that propagate through a solid. The velocity of longitudinal and transverse elastic waves thus produced is a characteristic feature of the solid. As discussed, in a longitudinal wave, the material is alternately compressed and rarefied as one travels along the direction of wave propagation. In a transverse wave, the material is transversely stressed or sheared in alternating directions as one travels along the direction of wave propagation. The transverse wave displaces layers of material perpendicular to the direction of propagation. The layers are displaced from side to side or they are displaced up and down.

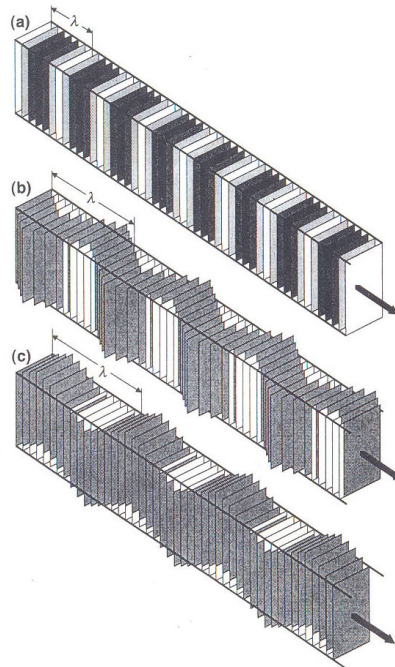


Figure 3.8 Propagation of elastic waves through materials.

The basic idea is that if there is any distortion of the solid from its equilibrium shape, (Figure 3.8) the average separation of the atoms within the solid is no longer optimal. Some atoms will be too close to their neighbours, and some too far apart. In either case there will be a restoring force, which will act to return the atoms to their equilibrium separations. The dynamics of the elastic wave will be affected by the way the solid responds to the restoring force. The two factors most critical in determining this response are the restoring force per unit displacement (the natural 'springiness' of the substance), and the density of the substance.

The restoring force on a small region of a solid depends on the type of distortion (strain) that has taken place during synthesis process. The parameters that describe the restoring force per unit strain are known as the elastic moduli of a substance. In the present work we have employed ultrasonic pulse transmission technique as a tool to get idea about such stress/strain ratio by measuring longitudinal and transverse wave velocities.

Young's modulus (E)

This characterizes the restoring forces appropriate to longitudinal extensions of a substance. In Figure 3.9 shown below, opposite shows two rigid planes of area A separated in equilibrium by a distance a and held together by 'springs' (analogous to planes within a solid held together by atomic bonds).

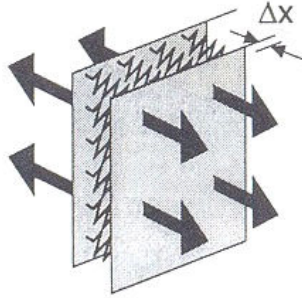


Figure 3.9 Changing length of sample due to mutually opposite forces acting on the solid.

Young’s modulus is defined by:

$$\frac{F}{A} = E \frac{\Delta x}{a}$$

where, F is the force exerted on each plane. Notice that, if a rod of material is stretched in this way, it will tend to ‘neck’ i.e. its cross-sectional area will be reduced (Figure 3.10). This tendency is characterized by the Poisson ratio, σ , of a substance. If we apply a stress S_x (force per unit area) in the x-direction, we induce stress S_y in the y-direction. The Poisson ratio is defined as:

$$\sigma = \frac{S_y}{S_x}$$

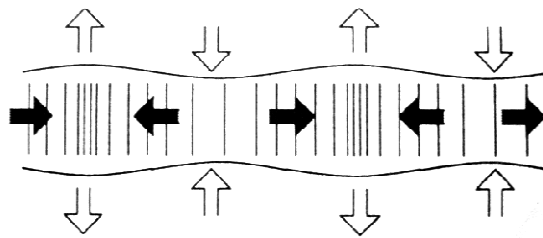


Figure 3.10 Illustration of the way in which a rod or material necks and bulges as a compressive sound wave travels along a long thin rod.

Shear or rigidity modulus (G)

This characterizes the restoring forces appropriate to shear or transverse deformations of the substance. Figure 3.11 opposite shows two rigid planes of area A held together by 'springs' (analogous to planes within a solid held together by atomic bonds). The rigidity modulus is defined by:

$$\frac{F}{A} = G\theta$$

where F is the force on each plane.

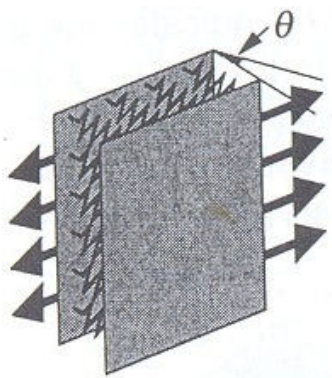


Figure 3.11 Torsion (θ) produced in the solid due to tangential forces.

Bulk modulus (B)

Here it should be noted that the bulk modulus (and its inverse, the compressibility K) describes the restoring forces appropriate to volume compressions of the substance. It is defined by:

$$B = -V \frac{\partial P}{\partial V}$$

where, P is the pressure and V is the volume of the substance.

If the material is easily compressed or easily sheared, than for a given strain, the restoring force will be small. In other words, a high modulus (E, G, or

B) indicates that the corresponding deformation of the solid is difficult and the solid has a strong tendency to 'spring' back to its equilibrium position.

Poisson's ratio (σ)

Poisson's ratio (σ) is the ratio of transverse contraction strain to longitudinal extension strain in the direction of stretching force. Tensile deformation is considered positive and compressive deformation is considered negative. The definition of Poisson's ratio contains a minus sign so that normal materials have a positive ratio.

Virtually, all common materials become narrower in cross section when they are stretched. The reason why, in the continuum view, is that most materials resist a change in volume as determined by the bulk modulus K more than they resist a change in shape, as determined by the shear modulus G . In the structural view, the reason for the usual positive Poisson's ratio is that inter-atomic bonds realign with deformation.

The theory of isotropic elasticity allows Poisson's ratios in the range from -1 to $1/2$. Physically the reason is that for the material to be stable, the stiffness must be positive; the bulk and shear stiffness are interrelated by formulae which incorporate Poisson's ratio.

Elastic Constants

Relationships between various elastic constants			
Young's Modulus	$E = \frac{G(3\lambda + 2G)}{\lambda + G}$ $E = \frac{\lambda(1+\nu)(1-2\nu)}{\nu}$ $E = \frac{9K(K-\lambda)}{3K-\lambda}$ $E = 2G(1+\nu)$ $E = \frac{9KG}{3K+G}$ $E = 3K(1-2\nu)$	Poisson's Ratio	$\nu = \frac{\lambda}{2(\lambda+G)}$ $\nu = \frac{\sqrt{(E+\lambda)^2 + 8\lambda^2} - (E+\lambda)}{4\lambda}$ $\nu = \frac{\lambda}{3K-\lambda}$ $\nu = \frac{E-2G}{2G}$ $\nu = \frac{3K-2G}{2(3K+G)}$ $\nu = \frac{3K-E}{6K}$
Shear Modulus	$G = \frac{\sqrt{(E+\lambda)^2 + 8\lambda^2} + (E-3\lambda)}{4}$ $G = \frac{\lambda(1-2\nu)}{2\nu}$ $G = \frac{3(K-\lambda)}{2}$ $G = \frac{E}{2(1+\nu)}$ $G = \frac{3EK}{9K-E}$ $G = \frac{3K(1-2K)}{2(1+\nu)}$	Bulk Modulus	$K = \frac{3\lambda+2G}{3}$ $K = \frac{\sqrt{(E+\lambda)^2 + 8\lambda^2} + (3\lambda+E)}{6}$ $K = \frac{\lambda(1+\nu)}{3\nu}$ $K = \frac{GE}{3(3G-E)}$ $K = \frac{2G(1+\nu)}{3(1-2\nu)}$ $K = \frac{2G(1+\nu)}{3(1-2\nu)}$ $K = \frac{E}{3(1-2\nu)}$

The inter relationship between various elastic constants are given above. The knowledge of any two elastic moduli will suffice to give the values of the remaining elastic constants. Here, it is important to note that Bulk modulus, rigidity modulus and Young's modulus are measure in dynes/cm² (CGS unit system), Newton/m² (MKS unit system), or Pascal (SI unit system), while ' σ ' is a unit less quantity. The values of elastic moduli for different materials taken from various sources are given in Table 3.1.

Table 3.1 Bulk modulus (B) Young's modulus (E), rigidity modulus (G) and Poisson's ratio (σ) for typical metals, materials and polycrystalline compositions.

Formula	B (GPa)	E(GPa)	G(GPa)	σ
Aluminum	75.5	69	25	0.33
Copper	137.8	110	46	0.34
Magnesium	44.7	45		
Nickel	186.0	45	17	0.31
India rubber	-	0.48-1.52	0.0016	0.46-0.49
CoFe ₂ O ₄	179.4	-	-	-
Mg Fe ₂ O ₄	110.1/149.2	190.8	74.1	-
Ni Fe ₂ O ₄	194.4	177.3	68.0	-
Cu Fe ₂ O ₄	168	174.0	66.0	0.33
Zn Fe ₂ O ₄	145	184.3	72.0	0.27
Fe Fe ₂ O ₄	177.2	-	-	
Li _{0.5} Fe _{2.5} O ₄	179.0	173	65	0.34
MgAl ₂ O ₄	-	62.7	-	-
Y ₃ Fe ₅ O ₁₂	128.99	145.09	58.33	-
YBa ₂ Cu ₃ O ₇₋₈	49.38 (205K)	92	39.85(205 K)	-

3.4 Magnetic Properties

(A) Physical Property Measurements System (PPMS)

The Quantum Design PPMS represents a unique concept in laboratory equipment: an open architecture, variable temperature-field system, designed to perform a variety of automated measurements. Use the PPMS with specially-designed measurement options, or easily adapt it to our own experiments. Sample environment controls include fields up to ± 16 Tesla and temperature range of 1.9 - 400 K

The key features of PPMS used for magnetic measurements are listed below:

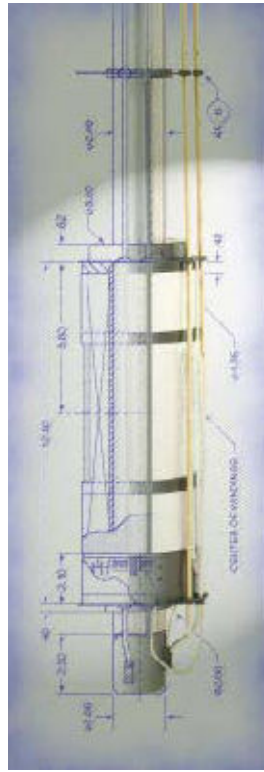
- Sealed sample chamber with 2.6 cm diameter sample access.
- Ever Cool-II – cryogen-free cooling technology.
- Versatile sample mounts couple easily to the 12 electrical leads built into the cryostat insert.
- The PPMS is controlled by the Model 6000, a sophisticated microprocessor-controlled device that eliminates the need to use or purchase external bridges, current or voltage sources, or lock-in amplifiers.
- Continuous Low-Temperature Control – maintains temperature below 4.2 K for indefinite periods of time and offers smooth temperature transitions when warming and cooling through 4.2 K.
- Temperature Sweep Mode.
- User Experiments – External instruments may be controlled automatically using an integrated Visual Basic interface within our Windows-based

MultiVu control software or by controlling external Visual C++, Delphi or Visual Basic programs. In addition, Grapher utility displays data as it is being collected.

The PPMS can be used to record various physical properties such as:

- (i) Heat Capacity
- (ii) AC resistivity
- (iii) Thermal conductivity
- (iv) Seebeck Coefficient
- (v) Thermoelectric figure of merit
- (vi) Vibrating sample magnetometer
- (vii) AC susceptibility and DC magnetization
- (viii) Torque magnetometry
- (ix) DC resistivity

Much of the versatility of the PPMS is based on the design of the PPMS probe. The probe incorporates the magnet, the temperature control, and the sample puck connector. Figure 3.12 shows typical sample / PPMS probe.



Typical Sample Probe

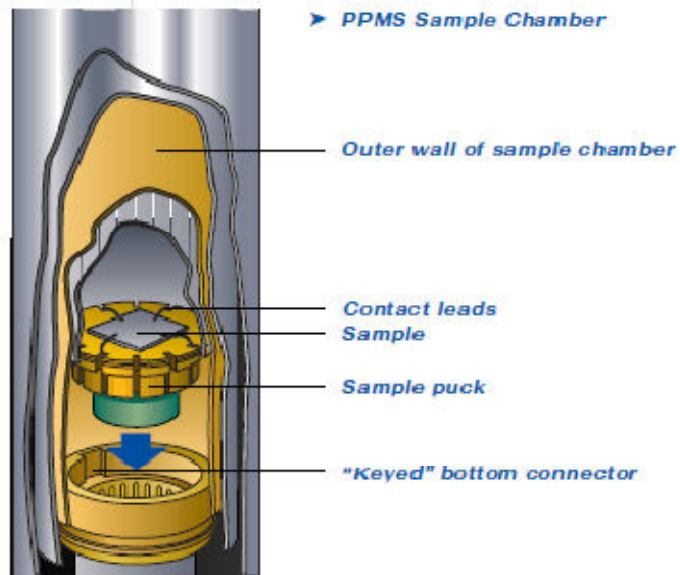


Figure 3.12 The cross-sectional enlarged PPMS sample chamber.

Sample mounting

The PPMS sample-mounting system is the most interesting and unique feature of this instrument. At the bottom of the sample chamber is a 12-pin connector pre-wired to the system electronics. This connector allows you to plug in a removable sample insert or sample “puck” (Figure 3.13) and offers convenient access to electrical leads for application hardware and electronics. This connector provides the foundation for all of the PPMS measurement inserts.



Figure 3.13 Specialized pucks, 2.4 cm in diameter, are used for different measurement applications.

Open architecture

The tremendous flexibility of the PPMS allows to interface third-party instruments to the PPMS hardware. The PPMS MultiVu software supports linking capabilities, so one can write own programs in Delphi, C++, or Visual Basic to synchronize PPMS functions with the activity of other instruments to perform custom experiment. The Model 6000 PPMS Controller houses and controls all the critical components of the instrument to provide direct communication with the application electronics for rapid data acquisition.

Temperature control operation

To control the temperature, a vacuum pump draws helium into the annular region where heaters warm the gas to the correct temperature. This design reduces thermal gradients and increases system flexibility by making the sample chamber a controllable environment.

The temperature control system offers the following features:

- Temperature sweep capability allows measurements to be taken while sweeping the temperature at a user-defined rate (0.01–6 K/min.).
- Continuous Low-Temperature Control (CLTC) ensures precise temperature control, uninterrupted operation below 4.2 K, and smooth transitions through the 4.2 K helium boiling point.
- Temperature range of 1.9–400 K accommodates many different types of measurements.

Field control

The PPMS can be configured with a 7 to 16 Tesla longitudinal magnet or a 7 Tesla transverse magnet. The low noise, bi-polar power supply allows continuous charging through zero field with current compensation and over-voltage protection.

Magnetometry

Magnetometry applications are used in conjunction with the automated temperature and field control capability of the PPMS. The result is a powerful,

fully automated Magnetic measurement workstation that includes integrated software.

AC/DC Magnetization

The AC measurement system (ACMS) provides the capability to perform both AC susceptibility and extraction DC magnetization measurements without changing hardware (Figure 3. 14)



Figure 3.14 The servo-motor, coilset, and sample rod for the ACMS.

Features

- A single automated measurement sequence can perform both AC and DC magnetization measurements.
- Direct measurement of the instrumental phase shift, not available on any other AC susceptometer: This feature uses integrated, low inductance calibration coils to measure and subtract background phase shifts prior to every AC measurement point.
- High-speed digital filtering: By using a DSP chip, the ACMS improves the signal-to-noise ratio over analog filters to offer excellent performance over a wide frequency range.

- A compensation coil reduces environmental noise in AC susceptibility measurements.

Specifications

Temperature range: 1.9-350 K

AC frequency range: 10 Hz to 10 kHz

AC field amplitude range: 2 mOe to 15 Oe

Sensitivity range: DC magnetization measurements: 2.5×10^{-5} emu to 5 emu
(2.5×10^{-8} Am² to 5×10^{-3} Am²)

AC susceptibility measurements: 2×10^{-8} emu (2×10^{-11} Am² @ 10 kHz)

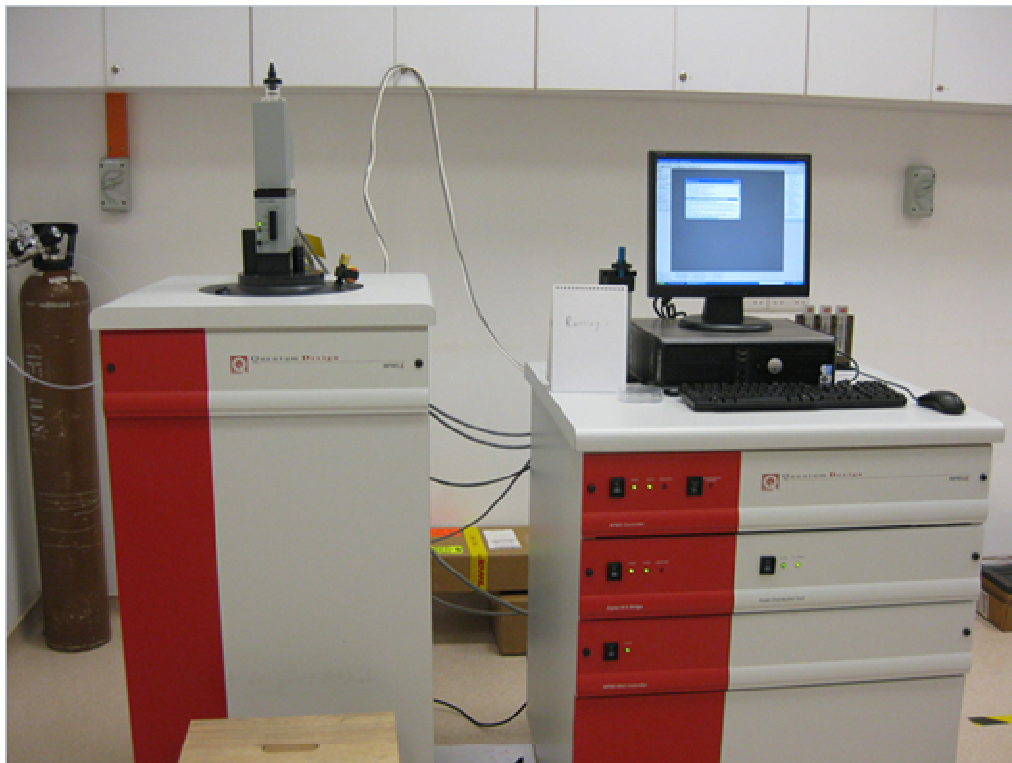


Figure 3.15 Photograph of Physical Property Measurement System.

(B) AC Susceptibility

The measurement of magnetic susceptibility is very useful technique to obtain much important information regarding physical, chemical and magnetic states of the substance.

The ratio of induced magnetization to the applied magnetic field is known as magnetic susceptibility. Therefore,

$$K = M/H \text{ emu/cm}^3$$

Since M is the magnetic moment of the material per cm^3 , H is the applied magnetic field, K also refers to unit volume and is sometimes called the volume susceptibility.

The thermal variation of low field ac susceptibility gives information regarding transition temperature, type of magnetic ordering of the substance.

The mass susceptibility related to the volume susceptibility is defined as,

$$\chi = K/\rho' = M/H\rho \quad \text{emu/g.Oe}$$

where , ' ρ' ' being the density of the material.

The thermal magnetic studies like temperature variation of low field ac susceptibility play a key role in the study of spin glass behavior. The cusp at freezing temperature T_f in the low field ac susceptibility versus temperature characterizes the spin glass behavior [11]. It is also useful to invoke grain size effects. For example, a very fine stable single domain (SD) particle becomes superparamagnetic (SP) on heating to temperature several degrees below the Curie temperature [12]. At an applied magnetic field H, the temperature at which the susceptibility becomes infinite (i.e. the sample has spontaneous

magnetization), is known as Curie or Neel temperature. At the transition (ferrimagnetic to paramagnetic) tailing effect is observed, which is due to the short range spin ordering (spin clusters).

It is obvious that the susceptibility (χ) is directly proportional to the magnetic moment M and inversely proportional to coercivity H_C when the thermal energy equals to the volume energy of a single domain (SD) particle it becomes super paramagnetic (SP) and spontaneously fluctuate between their easy directions yields zero coercivity and as a result the peak is observed in the low field χ versus T curve [13].

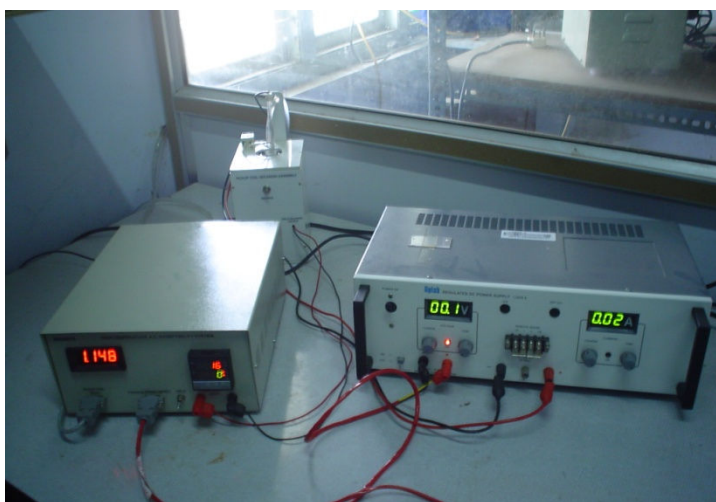


Figure 3.16 Photograph of AC Susceptibility measurement setup.

The ac susceptibility measurements of powdered samples were obtained using the instrument which consists of (i) magnetic field unit , (ii) magnetization unit and (iii) temperature unit (Figure 3.16) supplied by Magneta, Mumbai, India [14]. The block diagram of the susceptibility instrument is shown in (Figure 3.17). The double coil set-up (Halmholtz coil,) operating at a frequency of 263 Hz produced magnetic field between 0 to 10 kOe. The two coils are oppositely

wound relative to each other producing uniform magnetic field along the axis perpendicular to the coils. A pick-up coil is provided at the center of Helmholtz coil for the magnetization measurements.

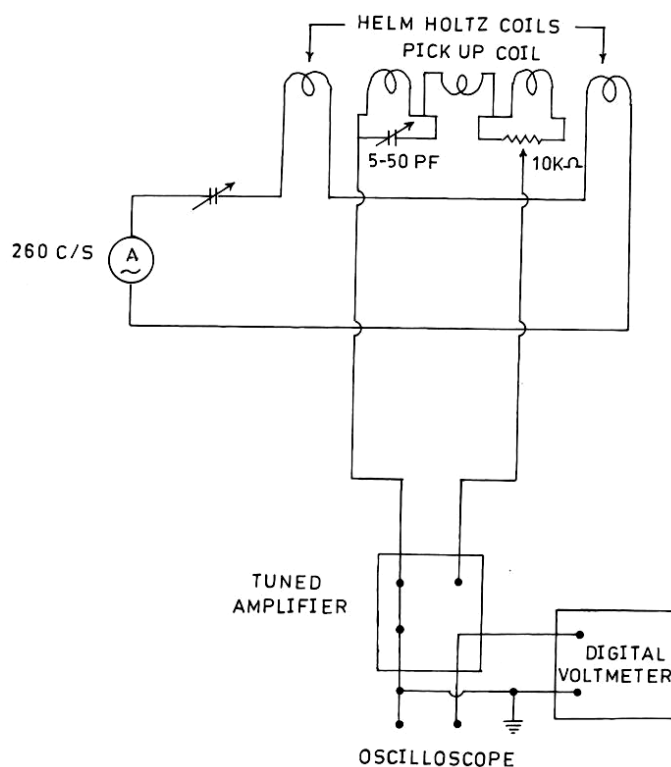


Figure 3.17 Block cum circuit diagram of susceptibility set-up.

A furnace, platinum wire wound on a silica tube, was used to heat the sample. A glass jacket with a provision of water circulation is used to avoid overheating of the coils. The furnace is inserted in a glass jacket and the glass jacket is placed in the center of the pick-up coil. The temperature was sensed by Platinum-Rhodium thermocouple calibrated against the current in the heating element. Variable current was provided to the heating element by a variable power supply.

The sample tube is held in the middle of the pick-up coil to sense minor change in magnetization of the sample. By applying the current to the Helmholtz

coil, the change in magnetization of the sample producing emf in the pick-up coil. The signal is then digitized by an analog to digital converter and then fed to a digital power meter.

Merits

- (1) This instrument can measure at room temperature magnetization of 10 Oe. This means that this even weakest paramagnetic sample in 100 mg quantity can be measured with an accuracy of 2%.
- (2) This instrument can be used to determine Curie temperature.
- (3) The electronic unit of this instrument can be used to measure permeability or hysteresis loops of soft ferrites.

3.5 Electrical Properties

(A) DC Resistivity

Introduction

There is a sense in which every property of a solid can be considered an electrical property. This is because the particles that make up solids are fundamentally electrical in nature. The response of solids to externally applied electric fields is referring to as electrical properties.

When any substance is subject to an applied electric field E , a current of electronic charge flows through the substance. The magnitude of the resultant current density, j , is characterized by the electrical resistivity ρ or the electrical conductivity ($\sigma = 1/\rho$) of the substance. The electrical resistivity and conductivity are determined by:

$$j = \sigma E \text{ and } E = \rho j$$

If the current density is measured in Am^{-2} and electric field (E) in Vm^{-1} , then the units of σ are $\Omega^{-1} \text{m}^{-1}$ or S m^{-1} . The SI symbol of S stands for Siemens not to be confused with 's' for second. The units of resistivity are Ωm . for a example of cross sectional area A and length L , the resistivity is related to the electrical resistance R by $\rho = RA / L \Omega \text{m}$

Electrical Resistivity

The range of resistivity values of ferrite and garnet materials is wide ranging from 10^{-4} to $10^9 \Omega \cdot \text{m}$ at room temperature [15]. In ferrites, the high value of resistivity is associated with the simultaneous presence of ferrous (Fe^{2+}) and ferric (Fe^{3+}) ions on equivalent lattice sites (usually the octahedral (B-) sites). The value

of resistivity in magnetite, $\text{Fe}^{2+}\text{Fe}_2^{3+}\text{O}_4$ (Fe_3O_4), is of the order of 10^{-4} or $10^{-5} \Omega\cdot\text{m}$. In nickel-zinc ferrite it was found that the resistivity was about $10 \Omega\cdot\text{m}$ when the material contained 0.42 percent by weight of ferrous oxide but this resistivity increased approximately one thousand fold when the specimen was more completely oxidized.

A mechanism of conduction is known which covers the situation cited above. The extra electron on a ferrous ion requires little energy to move to a similarly situated adjacent ferric ion. The valence states of the two ions are interchanged. Under the influence of an electric field, these extra electrons can be considered to constitute the conduction current, jumping or hopping from one iron ion to the next.

Since the materials are semiconductors, their resistivity ρ should decrease with increase in temperature according to a relation of the form:

$$\rho = \rho_0 \exp (E_p/kT)$$

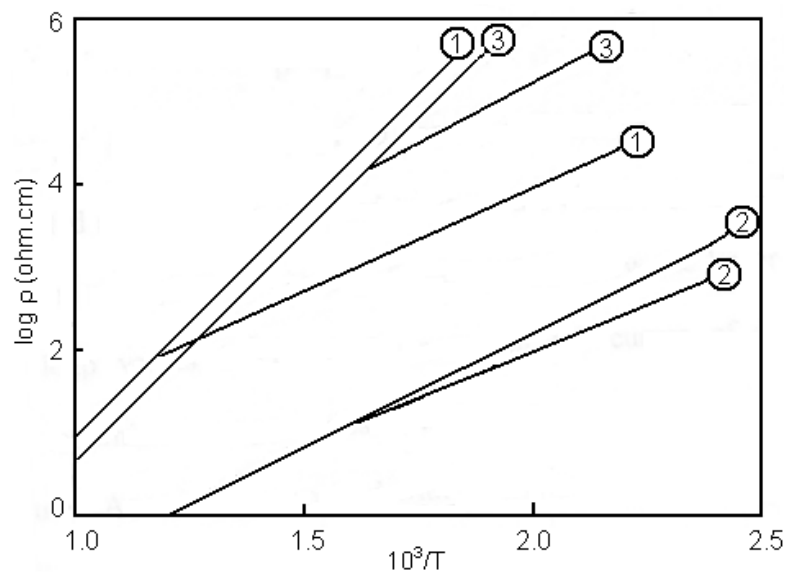


Figure 3.18 The variation of resistivity (1) Nickel ferrite, (2) Copper ferrite and (3) Magnesium ferrite, with temperature.

This relation is indeed often observed and the activation energy E_p can then be interpreted as the energy required to cause the electron jump referred to above. Some examples are given in Figure 3.18 which show the linear relation between $\log \rho$ versus $10^3/T$. Breaks occur in the curves of Figure 3.18 at temperatures which correspond closely with the observed ferrimagnetic Curie temperatures. As would be expected with such a conduction mechanism, the high activation energy is associated with a high resistivity at room temperature.

In the electrical resistivity measurement a typical sample holder shown in Figure 3.19 specially designed and fabricated for the resistivity measurement was used. It consists of two ceramic beads with supporting metal rods. The electrodes E_1 and E_2 are also shown in this figure. The spring loaded brass electrode (E_2) is introduced into the ceramic beads and it pressed hard against the surface of the pellets. The brass electrode E_1 is fixed at the other end.

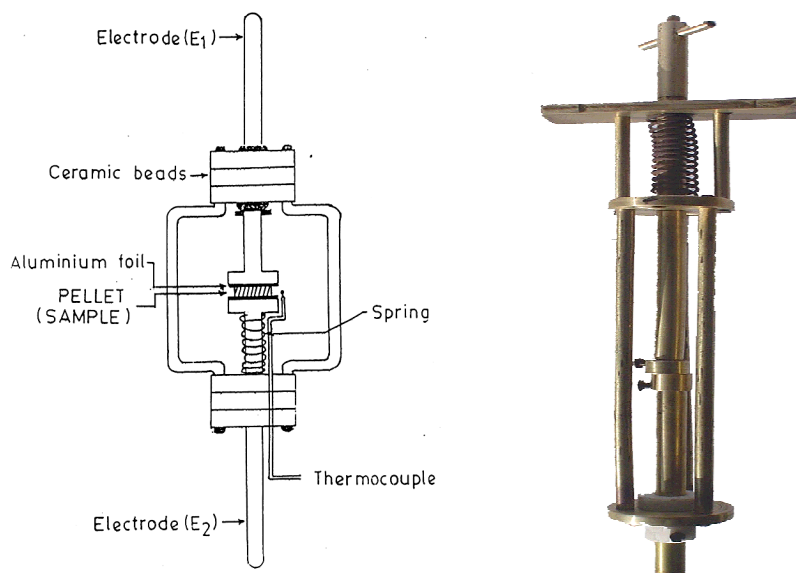


Figure 3.19 Sample holder for two-probe resistivity measurement.

The resistance of a pellet was measured by two terminal method using meg-ohm meter. The sample surfaces were rubbed by graphite and thin aluminium foils were placed between the terminals of sample holder and the pellet surfaces for the proper contacts. The sample holder with the pellet was placed in a horizontal electric furnace to study the change in resistivity with temperature. The temperature of the furnace was controlled by maintaining the current passing through the heater by means of current controller. The temperature of the sample was measured with Cr-Al thermocouple. Experimental set-up is shown in the Figure 3.20. The resistance of the each pellet was measured for raising and falling of temperature at the gap of 20°C. The thickness (l) and diameter of the pellets were measured by digital vernier calipers. From these observations the resistivity (ρ) was found us. Logarithm of resistivity was plotted against reciprocal of temperature ($10^3/T$). The activation energies for the ferrimagnetic region (E_f) and paramagnetic region (E_p) in electron volt (eV) were determined from the slopes of these plots.

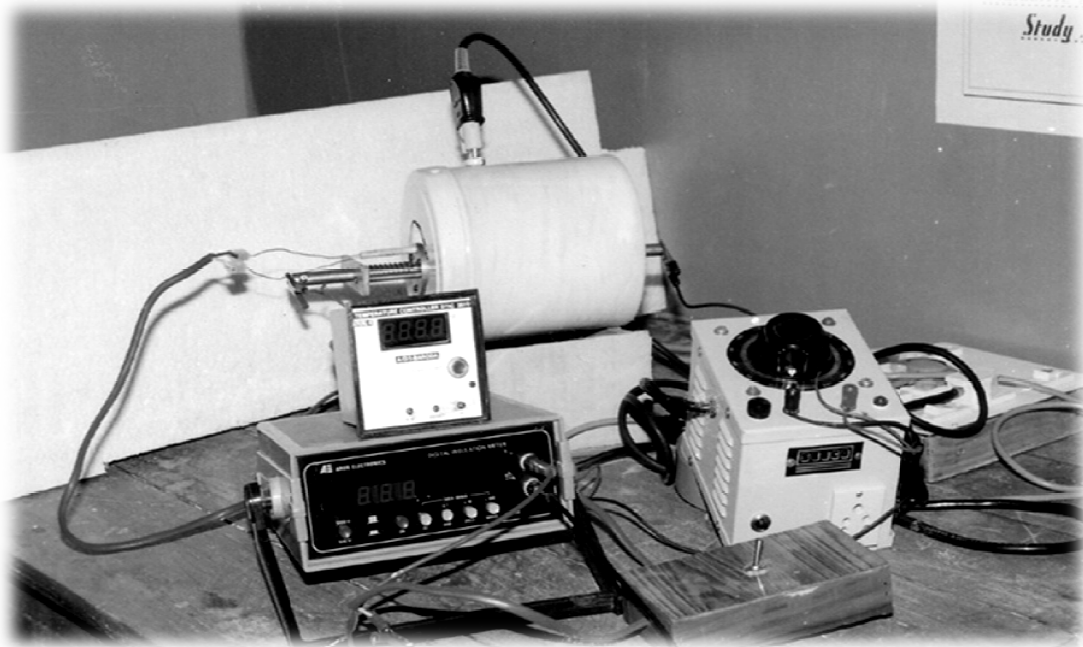


Figure 3.20 Experimental set-up for dc resistivity measurement.

Hopping model of electrons

Jonker has observed in cobalt ferrites that the transport properties differ considerably from those of normal semiconductors, as the charge carriers are not free to move through the crystal lattice but jump from ion to ion. It was also noted that in this type of materials the possibility exists of changing the valency of a considerable fraction of metal ions and especially that of iron ions [16].

Assuming the number of electrons contributing to be equal to the number of Fe^{2+} ions and the number electron holes to be equal to the number of Co^{3+} ions Jonker has calculated from the resistivity data extremely low values of mobilities $\mu_1 = 10^{-4} \text{ cm}^2/\text{Vsec}$ for electrons and $\mu_2 = 10^{-8} \text{ cm}^2/\text{V sec}$ for holes. Further, even for samples with a large concentration of Fe^{2+} or Co^{3+} ions, a fairly strong exponential dependence of resistivity on temperature was found. From the ordinary band theory of conduction one would expect metallic behaviour for such

high concentration, i.e. a high mobility with only slight temperature dependence. In cobalt ferrite compounds the behaviour is similar to NiO and Fe₂O₃ and the ordinary theory based on simple band picture does not apply. The activation energy does not belong to the energy picture of electrons but to the crystal lattice around the site of electrons. The general expression for the total conductivity where we have two types of charge carriers can be given as [17]

$$\sigma = n_1 e \mu_1 + n_2 e \mu_2$$

The temperature dependence of conductivity arises only due to mobility and not due to the number of charge carriers in the sample.

Thus, we can conclude that, for the hopping conduction mechanism

1. Low value of mobility.
2. Independence of Seebeck coefficient on temperature. This property is due to the fact that in hopping model the number of charge carriers is fixed.
3. Thermally activated process with activation energy E_a called the hopping activation energy.
4. Occurrence of n-p transition with changes in the Fe²⁺ or oxygen concentration in the system.

Small polaron model

A small polaron is a defect created when an electronic carrier becomes trapped at a given site as a consequence of the displacement of adjacent atoms or ions. The entire defect (carrier plus distortion) then migrates by an activated hopping mechanism. Small polaron formation can take place in materials whose

conduction electrons belong to incomplete inner (d or f) shells which due to small electron overlap; tend to form extremely narrow bands. The possibility for the occurrence of hopping conductivity in certain low mobility semiconductors, especially oxides, has been widely recognized for some time.

The polaron comprises the electron plus its surrounding lattice deformation. (Polaron can also be formed from holes in the valence band). If the deformation extends over many lattice sites, the polaron is “large”, and the lattice can be treated as a continuum. Charge carriers inducing strongly localized lattice distortions form “small” polarons. The concept of large polaron is most useful when the carrier mobility is high and the carrier density and temperature both are low [18].

For a small polaron the spatial extent of its self-trapped charge is comparable to or smaller than interatomic distances. In particular atoms surrounding an excess charge are displaced to new equilibrium positions and produce a potential well which traps the excess particles. Small polaron formation is typically associated with the interaction of the excess charge with the atoms in its immediate vicinity. Thus, unlike the case of the large polaron, the self-trapping is not primarily associated with the long range interaction of an excess charge with the dipolar fields of polar materials. Hence, the name polaron, coined to reflect this latter situation, is a misnomer for the small polaron. Electron and hole small polarons are found in both polar and non-polar semiconductors and insulators. This includes numerous oxides and molecular solids.

Small polaron motion proceeds relatively slowly via a succession of phonon-assisted hopping events. As a result, the small polaron drift mobility increases as a thermal agitation of the solid increases. Above a temperature comparable to the solid's phonon temperature, the diffusivity increases in an Arrhenius manner with reciprocal temperature.

The migration of small polaron requires the hopping of both the electron and the polarized atomic configuration from one site to an adjacent one [16]. For fcc lattice the drift mobility takes the form

$$\mu = (1 - c) e a^{2\Gamma/kT}$$

where, e is the electronic charge, a the lattice parameter, c is the fraction of sites which contain an electron ($c=n/N$), n is the number of electrons and N the number of available sites per unit volume. The quantity Γ is the jump rate of the polaron from one site to a specific neighbouring site.

The small polaron model also explains the low value of mobility, temperature independent Seebeck coefficient and thermally activated hopping. In addition to these properties if the hopping electron becomes localized by virtue of its interaction with phonons, then a small polaron is formed and the electrical conduction is due to hopping motion of small polarons.

(B) Thermo electric power measurement

Introduction

The temperature difference between the two ends of a semiconductor gives rise to an electro motive force (emf) known as thermo emf (∇V). It is found that the

generated thermo emf is proportional to the temperature difference (ΔT) and is given by the relation

$$\nabla V = \alpha \Delta T \quad (1)$$

where, α is the Seebeck coefficient also often known as the thermo-electric power.

Hall effect and thermo-electric power study are widely used in the interpretation of the conduction mechanism in semiconductors. The interpretation of the Hall effect is more straight forward, and it also gives precise results. However, in the case of low mobility materials such as ferrites, garnets and perovskites, it is sometimes difficult to measure the Hall effect; in such cases the thermo-electric power measurement is the only alternative. The measurement of thermo-emf is simple and its sign gives vital information about the type of conduction (p-type or n-type) or charge carriers (electrons or holes) responsible for the electrical conduction in semiconductors. Another important significance of thermo-emf is that, it enables one to calculate the values of Fermi energy and carrier concentration. A knowledge of Fermi energy helps in the determination of the various regions viz. impurity conduction, impurity exhaustion and intrinsic conduction regions of a semiconductor.

In the case of a n-type semiconducting material, the hot surface becomes positively charged, as it loses some of its electrons. The cold surface of the semiconductor becomes negatively charged due to the diffusion of free electrons from the hot portion. Conversely, in a p-type semiconducting material, the hot surface becomes negative, and the cold one positive. Thus the type of

conduction in a given semiconducting material can readily be determined from the sign of the thermo-emf.

Theory

The Fermi energy in the case of a semiconductor can be obtained from the relation

$$\alpha T = (E_G - E_F) + 2kT \quad (2)$$

for n-type semiconductors and

$$\alpha T = E_F + 2kT \quad (3)$$

for p-type semiconductors.

where, E_G = Energy gap of the ferrite semiconductor,

E_F = Height of the Fermi energy level from the top of the filled Valence band

$2kT$ = the term which accounts for the transfer of kinetic energy of the carriers in moving from the hot region of the ferrite to a cold one.

While discussing the electrical properties of $\alpha - \text{Fe}_2\text{O}_3$, for which the mobility of the charge carrier is low, Morin [19] assumed that the conduction is occurring in exceedingly narrow bands or in localized levels. This assumption leads to the result that the kinetic energy term in the Seebeck effect can be neglected, so that for electrons alone,

$$\alpha T = E_G - E_F \quad (4)$$

while, for holes alone,

$$\alpha T = E_F \quad (5)$$

Experimental procedure

The experimental set-up to determine thermo-emf of ferrite samples is shown in Figure 3.21. It consists of a point contact probe, which acts as a hot junction and a base which acts as a cold junction. Between the two junctions a sample is kept. The temperature of the hot probe is raised to a maximum of around 473K with the help of an electric heater, which is wound round the hot probe.

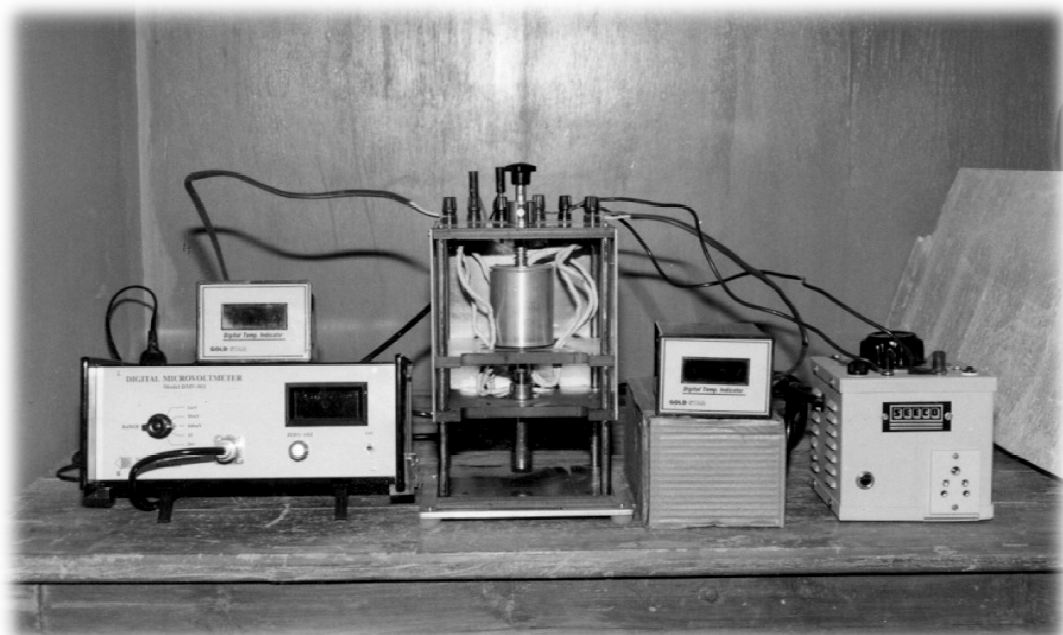


Figure 3.21 Photograph of thermo electric power measurement set up.

A thermoelectric power study was carried out over a temperature range 300–473 K by the differential method. The temperature gradient was measured by two chromel-alumel thermo-couples that were kept very close to the sample while the thermo-emf was measured with the help of a digital micro voltmeter with an accuracy of $\pm 3\%$. In order to achieve good thermal stability, the values of the thermo-emf have been recorded while cooling. The sample is maintained at a given temperature for about 5-10 minutes.

A pointed hot probe is used here since ferrite samples are very good thermal conductors; if a pointed probe is not used to upper and the lower surfaces of the samples will attain almost the same temperature and no temperature gradient will be maintained between them.

References

1. S. T. Alone and K. M. Jadhav
Parmana J. Phys. 70(1) (2008) 173.
2. R C Weast (Ed.) and M J Astle (Assoc. Ed.)
Handbook of Chemistry and Physics CRC Press Inc. (Florida) 1981.
3. A. Verma, T. C. Goel, R. G. Mendiratta and R. G. Gupta, J. Magn. and
Magn. Mater. 192(2)(1999) 271.
4. H. M. Rietveld, J. Appl. Cryst. 2 (1969) 65.
5. H. M. Rietveld, Acta, Cryst 22 (1967) 151.
6. J. Rodriguez-Cravajal, Physica B, 192 (1993) 55.
7. L. B. McCusker, R. B. Von Dreele, D. E. Cox, D. Louer and P. Scardi,
J. Appl Cryst. 32 (1999) 36.
8. R. A. Young, "The Rietveld Method", Oxford University Press Inc (1993).
9. Ian. M. Watt, "The Principles & Practice of Electron Microscopy", 2nd Ed.,
Cambridge University Press (1997)89.
10. Elton. N. Kaffmann, "Characterization of Materials", John Wiley & Sons,
Inc., Hoboken, New Jersey, Vol. 2 (2003).
11. A. P. Murani, J Magn. Magn. Mater., 5 (1977) 95.
12. K. J. Standley, "Oxide Magnetic Materials", Clarendon Press, Oxford,
(1962).
13. C. Radhakrishnamurthy, S. D. Likhite, E. R. Deutsch and G. S. Murthy,
Phys. Earth and planetary Interiors, 26 (1981) 37.

14. C. Radhakrishnamurthy S. D. Likhite and S. P. Sastry, "Philosophical Magazine", 23 (1971) 503.
15. K.J. Standly, "Oxide Magnetic Materials", Oxford, (1962).
16. G. H. Jonker, J.Phys,Chem. Solids,9 (1959)165.
17. B. Vishwanathan and V.R.K. Murthy, Ferrite materials: Science and Technology, 29 (1990).
18. S. L. Kakani and C. Hemrajani, Text book of Solid State Physics, Sultan Chand (1997).
19. F. J. Morin, Phys. Rev., 93(1953)1195.

Chapter 4

Slow cooled $\text{CuAl}_x\text{Fe}_{2-x}\text{O}_4$ system

4.1 Structural parameters and x-ray Debye temperature determination study on copper-ferrite-aluminates

(A) Introduction

The Cu-Fe-O system is of long standing interest in solid state physics, mineralogy, ceramics and metallurgy. By virtue of magnetic and semiconducting properties, copper ferrite (CuFe_2O_4) and its solid solutions with other ferrites are widely used in the electronic industry [1]. It has been reported that copper ferrite (CuFe_2O_4) is a unique spinel because (i) due to a relatively small energy difference between Cu^{2+} - ions reside at the tetrahedral (A-) and octahedral (B-) sites, cation redistribution is possible and strongly dependent upon the annealing temperature, cooling rate, microstructure etc. [1] (ii) the presence of Cu^{2+} - ions can provoke a collective Jahn-Teller distortion which is associated with the alignment of the Cu^{2+} - ions occupying the tetragonally distorted octahedral spinel lattice formed by the oxygen ions [2] (iii) it has two crystallographical spinel structures, the high temperature cubic phase with a lattice parameter of 8.380 Å and the low temperature tetragonal phase with lattice parameters of $a = b = 8.216\text{Å}$ and $c = 8.709\text{Å}$ [1].

Till today, there arose considerable interest in the synthesis and characterization of pure and substituted copper ferrite systems. The Al^{3+} - ion possesses noble gas outer electron shell structure; it is less compressible than ions with a full or half filled d-shell (Zn^{2+} , In^{3+} , Sn^{4+} etc.) [3], thus it cannot easily accommodate in the A-sites but statistically distributed among the available A- and B-sites.

The studies on magnetic, electrical, dielectric and elastic properties of typical compositions of the ferrite system: $\text{CuAl}_x\text{Fe}_{2-x}\text{O}_4$, have been carried out by different workers [4-8]. A perusal of literature indicates that these particular aspects i.e. effect of Al^{3+} -substitution on structural properties and Debye temperature of CuFe_2O_4 have not been investigated in detail, though all other physical properties are decisively dependent on structural parameters. The Debye temperature is an important parameter in solid state and materials science problems involving lattice vibrations. Various physical parameters such as the mean square displacements, the elastic constants, sound velocities, lattice instabilities etc., are known to depend upon the Debye temperature of a solid. It has been shown that Debye temperatures obtained from different experimental methods (e.g. measurements of elastic constant, specific heat and infrared spectroscopy) will not, in general, be equal [9]. To the best of our knowledge, very scant attention has been paid to x-ray Debye temperatures for ferrite materials in general, except on Ni-Li-Fe-O, Zn-substituted CuFeCrO_4 and mechanically milled $\text{Ni}_{0.5}\text{Zn}_{0.5}\text{Fe}_2\text{O}_4$ systems [10, 11, 12] and $\text{CuAl}_x\text{Fe}_{2-x}\text{O}_4$ spinel ferrite system in particular. We feel that this study will provide new direction in the area of structure - property co-relationship.

(B) Experimental details

According to the $\text{CuO} - \text{Fe}_2\text{O}_3$ phase diagram, CuFe_2O_4 is formed between 1000°C and 1100°C . The samples sintered below 1000°C or above 1100°C were of mixed-phase [13]. Aluminum (Al^{3+}) - modified copper ferrite ceramics with a general formula of $\text{CuAl}_x\text{Fe}_{2-x}\text{O}_4$ ($x = 0.0, 0.2, 0.4$ and 0.6) were synthesized from

high purity ingredients, namely CuO , Al_2O_3 and Fe_2O_3 all 99.9% pure supplied by Sigma Aldrich. The oxides were mixed thoroughly in stoichiometric proportions to yield the desired composition and then wet - ground. The mixture was dried and pressed into pellets. These pellets were pre-sintered at 1100°C for 24 hours and, slowly cooled to room temperature. The samples were again powdered, pressed in to pellets, sintered at 1100°C for 24 hours and then slowly furnace cooled to room temperature at the rate of $2^\circ\text{C}/\text{min}$. The phase identification was carried out using x-ray powder diffractometer with $\text{CuK}\alpha$ radiation at 300K.

(C) Results and discussion

(a) Energy dispersive analysis of x-rays (EDAX)

High temperature prolonged sintering may result in the loss of ingredients, which leads to non-stoichiometry in composition. This, in turn, shows unexpected behavior; which cannot be explained on the basis of normal stoichiometry. Thus, it was essential to check the chemical stoichiometry of each composition. A representative Energy dispersive analysis of x-rays, (EDAX) pattern for typical composition $x = 0.4$ is shown in Figure 1.

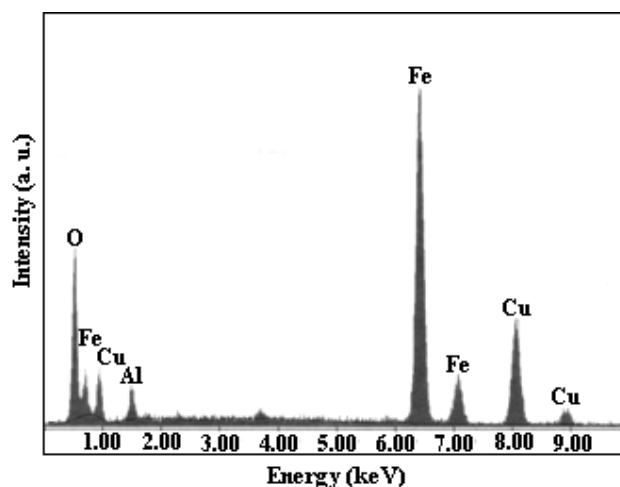


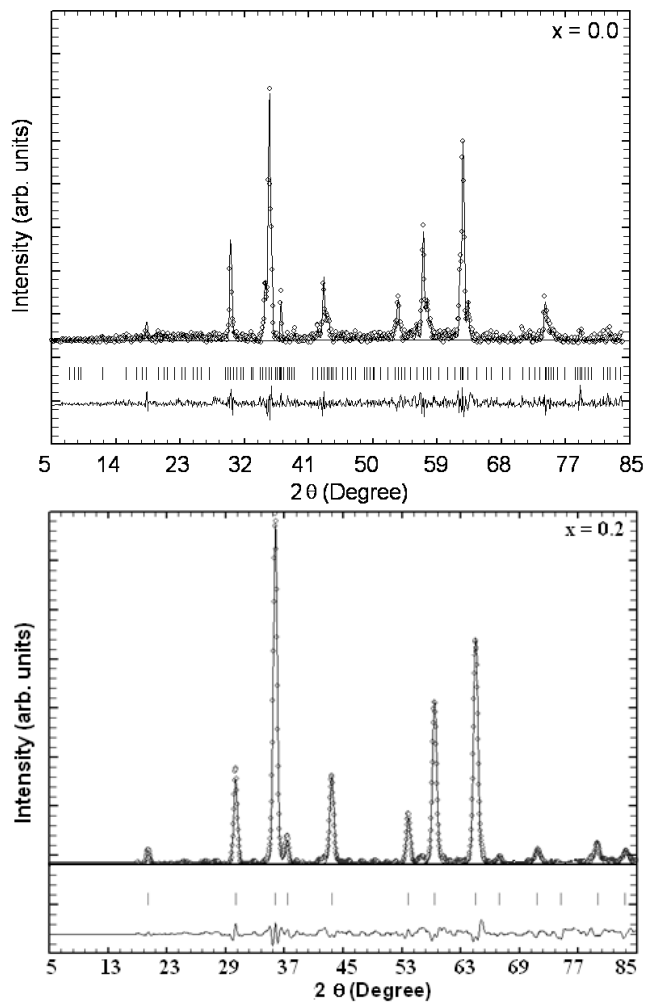
Figure 1. EDAX pattern of $\text{CuAl}_{0.4}\text{Fe}_{1.6}\text{O}_4$ ($x = 0.4$) composition.

The results of EDAX confirm the expected stoichiometry, with small oxygen deficiency. No trace of any impurity was found indicating the purity of the samples. It is also clear that there is no loss of any ingredient after high temperature sintering. EDAX results suggest that the precursors have fully undergone the chemical reaction to form the expected ferrite composition. The reason for making EDAX characterization was to ratify the purity and surety of the chemical composition.

(b) X-ray powder diffraction patterns analysis

The room temperature (300K) x-ray diffraction patterns of the samples were obtained by x-ray powder diffractometry. Indexing and Rietveld refinement using general scattering analysis software (GSAS) of x-ray diffraction (XRD) patterns revealed that these are single-phase compounds, crystallizing in a fcc structure (space group $Fd\bar{3}m$). No peaks from impurity phases could be detected within the limits of x-ray detection, which is typically 5%. Figure 2 displays Rietveld fitted XRD patterns for the compositions with $x = 0.0, 0.2, 0.4$ and 0.6 . In Rietveld analysis, we fit a model to the data. If the model is correct then it will predict what the true intensity values should be. One of the most important Rietveld error indices or discrepancy values is that of “Chi-squared” or χ^2 [14]. It is found that χ^2 for different compositions lie in the range $1.2 - 1.4$. It should be noted that χ^2 should never drop below one. If a refinement results in $\chi^2 < 1$, which means that one of the two things is true: (i) the standard uncertainties for the data must be overestimated or (ii) so many parameters have been introduced that the model is adjusting to fit noise which should be unlikely in powder diffraction. On the other

hand if at the end of a refinement $\chi^2 \gg 1$, then either: (i) the model is reasonable but the standard uncertainty values are underestimated, (ii) the model is incomplete because there are systematic effects (errors) in the data that are not expressed in the model, or (iii) the model is wrong. The χ^2 values obtained in the present analysis suggest good refinement of the data.



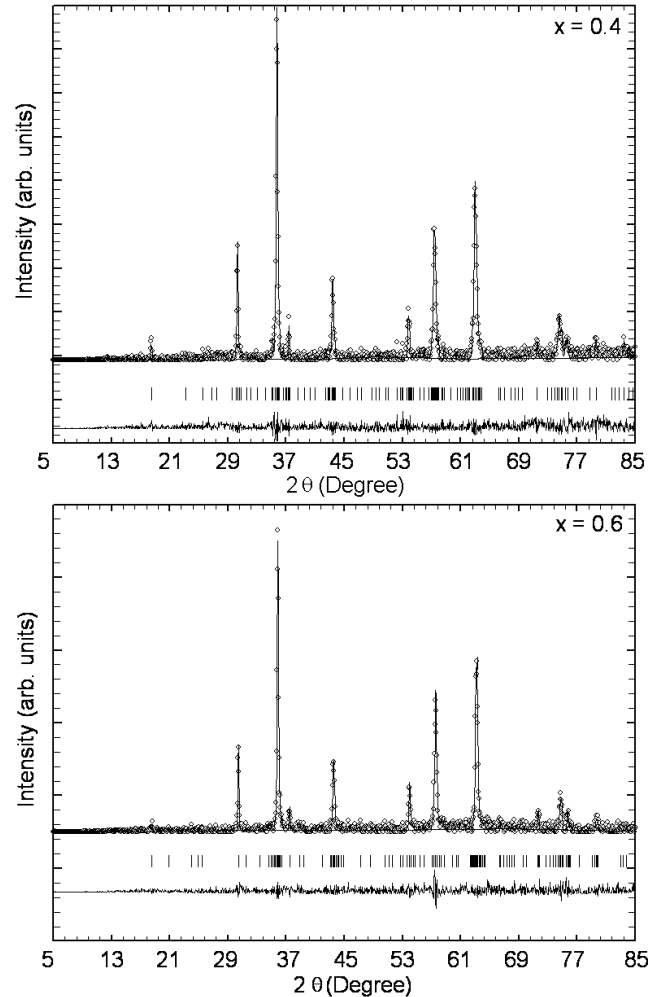


Figure 2. Rietveld –fitted XRD patterns for Cu-Fe-Al-O system.

It has been reported that slow cooled samples of $\text{CuAl}_x\text{Fe}_{2-x}\text{O}_4$ system possess tetragonal distortion ($c/a > 1$) [15] while samples quenched from 1000°C to liquid nitrogen temperature exhibit cubic spinel structure [4]. On the other hand $x = 0.6$ ($\text{CuAl}_{0.6}\text{Fe}_{1.4}\text{O}_4$) and $x = 1.0$ (CuFeAlO_4) compositions of the system: $\text{CuAl}_x\text{Fe}_{2-x}\text{O}_4$, prepared by usual double sintering ceramic technique, have shown fcc spinel structure [6, 7]. It has been found for a tetragonal deformed spinel stretched along the $\langle 0\ 1\ 1 \rangle$ direction (i. e. $c/a > 1$) that for all such compositions Cu^{2+} ions concentration on B-sites is $\geq 85\%$ [2, 4, 16 - 20]. The c/a ratio can be changed via decreasing the copper concentration or alternatively, by temperature

treatment. In the present case for $x = 0.0, 0.2$ and 0.4 compositions, Cu^{2+} - ion concentration on the octahedral (B-) sites is lower than 85% while for $x = 0.6$ composition it is on the verge of this limit. A deficit of Cu^{2+} cations in the B-sublattices leads to the absence of co-operative active Jahn-Teller distortion and the crystal cell retains into cubic.

(c) Structural parameters and cation distribution determination

The lattice constant values obtained from the above mentioned refinement, are given in Table 1, from which it is seen that the lattice constant decreases with increasing Al^{3+} - content (x) in the system. Usually in a solid solution of ferrites within the miscibility range, a linear change in lattice constant with concentration of the components is observed [21]. The linear decrease in lattice constant is due to the replacement of larger Fe^{3+} - ions (0.645 \AA) by smaller Al^{3+} ions (0.535 \AA) in the system.

The x-ray density (ρ_x) of the samples was determined using relation given by Smith and Wijn [22]:

$$\rho_x = \frac{8M}{N_A a^3} \quad (1)$$

where, M is the molecular weight of the composition, N_A the Avogadro's number and 'a' is the lattice constant. As there are 8 formula unit in the unit cell so 8 is included in the formula. The ρ_x is inversely proportional to the lattice constant, which decreases with increasing Al^{3+} - concentration; ρ_x is expected to increase with increasing (x). The x-ray density (ρ_x) decreases with Al^{3+} - ion concentration, because the decrease in molecular weight overtakes the decrease in volume of the unit cell. Bulk density (ρ) of the samples was determined by employing the

Archimedes principle using xylene ($\rho = 0.87 \text{ gcm}^{-3}$) as the buoyant to obtain fairly good results. It is observed that ρ_x of each sample is greater than the corresponding sintered density (ρ). This may be due to the existence of pores in the samples. Pore fraction (f) was calculated using the relation $f = (1 - \rho / \rho_x)$ and percentage porosity was calculated using the relation $P = f * 100\%$. The variation of porosity (P) with Al^{3+} content (x) is a result of the interplay between ρ and ρ_x .

Table 1. Lattice constant (a), molecular weight (M), x-ray density (ρ_x), bulk density (ρ), pore fraction (f) and porosity (P) for Cu-Fe-Al-O system.

Al-content (x)	a(Å) ±0.002Å	M(kg) x 10 ⁻³	ρ_x kg/m ³ x 10 ³	ρ	f	P (%)
0.0	8.389	239.23	5.385	4.736	0.1205	12.05
0.2	8.365	233.46	5.300	4.572	0.1374	13.74
0.4	8.342	227.69	5.212	4.370	0.1616	16.16
0.6	8.319	221.92	5.122	4.619	0.0982	9.82

The various physical properties of ferrites are sensitive to the nature, the valence state and distribution of cation over the tetrahedral (A-) and octahedral (B-) sites of spinel lattices. Therefore, the knowledge of cation distribution is essential to understand the structural, magnetic, electrical and infrared spectral properties of spinel ferrites.

Cation arrangements are not unique in spinel ferrites. Each spinel compound possesses at least three degree of freedom, which it uses in its search for an equilibrium structure: oxygen positional parameter (u), lattice constant (a) and cation inversion parameter. The parameter ' u ' varies, primarily, in accordance with the radius ratio between the A - and B – sites cations, r_A/r_B (or r_B/r_A). This is to say, the A – and B – sites bond lengths adjust themselves by

variation in 'u' until the A- and B- sites volumes "best – fit" the cations. The parameter 'a' varies in accordance with the average of the A – and B- sites cationic radii (i.e. with $0.33 r_A + 0.67 r_B$). The entire frame work of the unit cell swells or contracts to accommodate the size of the cations. The cation inversion parameter varies based on a much more complex set of factors. Some of the principal factors that influence cation inversion include [23]: (i) temperature (ii) the electrostatic contribution to the lattice energy (iii) cationic radii (iv) cationic charge and (v) crystal – field effects.

Precise knowledge of the cation distribution over crystallographic sites in magnetic oxides is crucial for understanding their physical properties. In order to determine the cation distribution, x-ray diffraction line intensity calculations were made using the formula suggested by Buerger [24]:

$$I_{hkl} = |F_{hkl}|^2 \cdot P \cdot L_p \quad (2)$$

where, I_{hkl} is the relative integrated intensity, F_{hkl} is the structure factor, P is the multiplicity factor and L_p is the Lorentz polarization factor = $[(1 + \cos^2 2\theta)/\sin^2 \theta \cdot \cos \theta]$. According to Ohnishi and Teranishi [25], the intensity ratios of planes $I(220) / I(440)$, $I(400) / I(422)$ and $I(220) / I(400)$ are considered to be sensitive to the any change in cation distribution. The intensities of (220) and (422) planes are mostly sensitive to cations on the tetrahedral sites [26], while the intensity of (400) plane depends on cations on both the sites. There is good contrast in the atomic scattering factor of Al^{3+} to that of Fe^{3+} and Cu^{2+} , but the scattering factor of Cu^{2+} is close to that of Fe^{3+} [26]. We had estimated the amount of Fe^{3+} ions on the tetrahedral (A-) and octahedral (B-) sites, through

Mossbauer spectral intensity calculations by considering the integrated areas under the Lorentzians corresponding to the A- and B- sites, which were taken as proportional to the amount of Fe^{3+} ion on these sites. The details are given elsewhere [27]. Any alternation in the distribution of cations causes a significant change in the theoretical values of x-ray diffraction line intensity ratio. Therefore, in the process of arriving at the final cation distribution the site occupancy of all the cations was varied for many combinations and those that agree well with the experimental intensity ratios, the fitting of the magnetization data at 10K [28] and Mossbauer data analysis [27], were taken into consideration. The comparison of x-ray diffraction line intensity ratios for various possible cation distributions for the studied compositions is shown in Table 2.

Table 2. Comparison of X-ray diffraction line intensity ratios, Seebeck coefficient (α) and oxygen deficiency (δ) for Cu-Fe-Al-O system.

Al-content (x)	Cation distribution		$\frac{I(400)}{I(422)}$		$\frac{I(220)}{I(400)}$		α ($\mu\text{V/K}$) (323K)	Oxygen deficiency (δ)
	A-site	B-site	Obs.	Cal.	Obs.	Cal.		
0.0	$\text{Cu}_{0.22}\text{Fe}_{0.78}$	$\text{Cu}_{0.78}\text{Fe}_{1.22}$	1.765	1.959	1.361	1.495	+ 64.74	0.075
	$\text{Cu}_{0.21}\text{Fe}_{0.79}$	$\text{Cu}_{0.79}\text{Fe}_{1.21}$		1.965		1.238		
	$\text{Cu}_{0.20}\text{Fe}_{0.80}$	$\text{Cu}_{0.80}\text{Fe}_{1.20}$		1.865		1.236		
0.2	$\text{Cu}_{0.22}\text{Fe}_{0.70}\text{Al}_{0.08}$	$\text{Cu}_{0.78}\text{Fe}_{1.10}\text{Al}_{0.12}$	1.922	2.076	1.417	1.418	+ 8.42	0.060
	$\text{Cu}_{0.20}\text{Fe}_{0.72}\text{Al}_{0.08}$	$\text{Cu}_{0.80}\text{Fe}_{1.08}\text{Al}_{0.12}$		1.865		1.579		
	$\text{Cu}_{0.18}\text{Fe}_{0.74}\text{Al}_{0.08}$	$\text{Cu}_{0.82}\text{Fe}_{1.06}\text{Al}_{0.12}$		1.676		1.757		
0.4	$\text{Cu}_{0.18}\text{Fe}_{0.64}\text{Al}_{0.18}$	$\text{Cu}_{0.82}\text{Fe}_{0.96}\text{Al}_{0.22}$	1.772	1.952	1.051	1.461	- 24.71	0.215
	$\text{Cu}_{0.17}\text{Fe}_{0.65}\text{Al}_{0.18}$	$\text{Cu}_{0.83}\text{Fe}_{0.95}\text{Al}_{0.22}$		1.847		1.544		
	$\text{Cu}_{0.16}\text{Fe}_{0.66}\text{Al}_{0.18}$	$\text{Cu}_{0.84}\text{Fe}_{0.94}\text{Al}_{0.22}$		1.748		1.632		
0.6	$\text{Cu}_{0.14}\text{Fe}_{0.58}\text{Al}_{0.28}$	$\text{Cu}_{0.86}\text{Fe}_{0.82}\text{Al}_{0.32}$	1.647	1.787	0.908	1.571	- 16.84	0.175
	$\text{Cu}_{0.16}\text{Fe}_{0.58}\text{Al}_{0.26}$	$\text{Cu}_{0.84}\text{Fe}_{0.82}\text{Al}_{0.34}$		1.890		1.488		
	$\text{Cu}_{0.17}\text{Fe}_{0.59}\text{Al}_{0.24}$	$\text{Cu}_{0.83}\text{Fe}_{0.81}\text{Al}_{0.36}$		1.888		1.494		

It is evident that the Cu^{2+} ions preferentially occupy B-sites than A-sites and Al^{3+} -ions replace Fe^{3+} -ions from both the sites. It is important to note that the average percentage disagreement between observed and calculated intensities of the diffracted beam increases as well as the integrated intensity of the diffracted beam in general decreases with increasing Al^{3+} - substitution (x). These systematic changes for Rietveld fitted single phase compositions can be explained on the basis of following effects.

- (i) The formation and presence of Cu^{2+} and Fe^{3+} ions in other oxidation states having different scattering factor [26].
- (ii) Preferred orientation: From the way in which the $\cos\theta$ portion of the Lorentz factor has been determined [26], it follows that equation (2) is valid only when the crystals making up the specimen are randomly oriented in space preferred orientation of the crystal grains causes radical disagreement between calculated and observed intensities and when such disagreement exists, preferred orientation should be the first possible cause to be suspected [26, 29]. It is relatively easy to prepare powder-compact specimen from ground powders so that the ideal of perfect randomness of orientation is closely approached, but virtually all polycrystalline specimens of manufactured ceramics will exhibit more or less preferential orientation of the grains.
- (iii) Extinction: it is known that real crystals, whether single crystals or individual grains in a polycrystalline aggregate are imperfect in the sense that they have a mosaic structure and the degree of imperfection can vary greatly from one crystal to another. Equation (2) is derived on the basis of the so-called

ideally imperfect crystal, one in which the mosaic blocks are quite small (of the order of 10^{-4} cm to 10^{-5} cm in thickness) and so disoriented that they are all essentially non-parallel, such a crystal has maximum reflecting power. A crystal made up of large mosaic blocks, some or all of which are accurately parallel to one another, is more nearly perfect and has a lower reflecting power. The decrease in the integrated intensity of the diffracted beam as the crystal becomes more nearly perfect is called extinction. The extinction effect can operate not only in single-crystal specimens, but also in the individual grains of polycrystalline specimens [30].

In practice, it is more appropriate to characterize the changes in the cations occupancies by considering the intensity ratio of the two reflecting planes rather than the change in the intensity of individual plane. This is due to the fact that the intensity ratio will not be affected by the preferred orientation of the sample [31]. Recently, the effects of La and oxygen deficiency in $\text{La}_{1-x}\text{MnO}_{3-\delta}$ perovskite structured manganite on the intensity ratio of (024) and (012) reflections have been studied by Zuo et al [31]. They have shown that the measured intensity ratio increases with increasing x until $x \approx 0.09$, while for x larger than ~ 0.09 , the intensity ratio levels off. On the other hand it is found that the intensity ratio is decreased with increasing oxygen vacancies (δ).

Our recent thermoelectric power measurements have shown that for $x = 0.0$ and 0.2 compositions majority charge carriers are holes or p-type conduction is dominated while for the compositions with $x = 0.4$ and 0.6 , n-type conduction is dominant or electrons are majority charge carriers [32]. It has been

also established that the probable conduction mechanisms in the system are: $\text{Fe}^{2+} \leftrightarrow \text{Fe}^{3+} + e^-$ (n-type) at the B-sites and $\text{Cu}^{2+} \leftrightarrow \text{Cu}^{1+} + e^+$ (p-type) at the A-sites. The near room temperature (323K) Seebeck coefficient value (α) has been used to determine the cationic concentration of Cu^{2+} , Cu^{1+} , Fe^{2+} and Fe^{3+} for different compositions using Heikes formula [33] and procedure suggested by Byeon et al. [34].

The small amount of Cu^{1+} and / or Fe^{2+} formation diminish the positive charge which is compensated by oxygen vacancies [35]. The Seebeck coefficient value and oxygen deficiency (δ) for each composition thus determined, are summarized in Table 2. The details are given elsewhere [32].

The decrease of oxygen deficiency (δ) can be thought of simplistically as applying a “chemical pressure” to the unit cell [36], as a result inter ionic distances decrease and the strength of bonding is expected to increase or vice versa. From Fig 3, it can be seen that the oxygen deficiency (δ) and intensity ratios of planes ($I(400)/I(422)$ and $I(220)/I(400)$) have expected inverse trend with each other [31], as a function of Al- content (x).

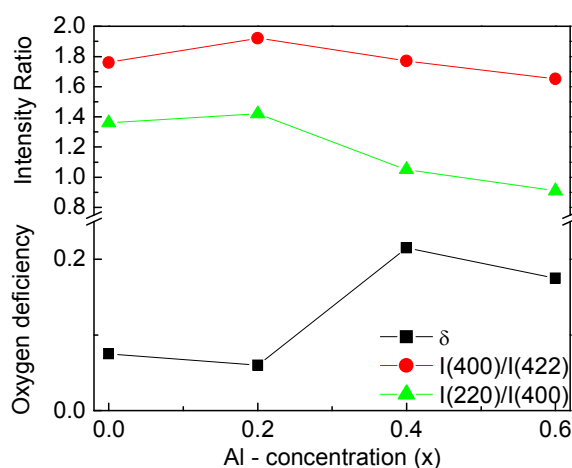


Figure 3 Compositional dependence of oxygen deficiency and intensity ratios of planes for Cu-Fe-Al-O system

Besides using experimentally found value of lattice constant and oxygen positional parameter (u), it is possible to calculate the value of the mean ionic radius per molecule of the tetrahedral and octahedral sites, r_A and r_B , respectively, based on the cation distribution for each composition using the relation [21]:

$$r_A = [f_c(\text{Cu}^{2+}) \cdot r(\text{Cu}^{2+}) + f_c(\text{Al}^{3+}) \cdot r(\text{Al}^{3+}) + f_c(\text{Fe}^{3+}) \cdot r(\text{Fe}^{3+})]$$

$$r_B = \frac{1}{2} [f_c(\text{Cu}^{2+}) \cdot r(\text{Cu}^{2+}) + f_c(\text{Al}^{3+}) \cdot r(\text{Al}^{3+}) + f_c(\text{Fe}^{3+}) \cdot r(\text{Fe}^{3+})] \quad (3)$$

where f_c and r , are the fractional concentration and ionic radius of respective cation on respective site. The ionic radius of Cu^{2+} (0.73Å), Al^{3+} (0.535 Å) and Fe^{3+} (0.645 Å) ions are taken with reference to coordination 6. Using these formulae, the mean ionic radius of the tetrahedral (A-) sites (r_A) and of the octahedral (B-) sites (r_B) have been calculated and are listed Table 3.

It can be seen that r_B decreases slowly while r_A decreases rapidly with increasing Al^{3+} - content (x) in the system, which in turn causes the lattice constant 'a', to decrease with x . It can be concluded that the tetrahedral sites substitution plays a dominant role in influencing the variation of 'a' with concentration (x).

It is known that there is a correlation between the ionic radius and the lattice constant. The radii of the tetrahedral and octahedral sites in a spinel ferrite can be calculated using the formulae given by [37]:

$$r_A = \sqrt{3} \left(u - \frac{1}{4} \right) a - R_0 \quad (4)$$

$$r_B = \left(\frac{5}{8} - u \right) a - R_0 \quad (5)$$

where R_0 represents the radius of the oxygen ion (taken as 1.32\AA) and u is the oxygen positional parameter. These relationships are further used to calculate the lattice parameter theoretically ' a_{th} ' [38].

From equation (5), one can write:

$$u = \frac{5}{8} - \frac{r_B + R_0}{a} \quad (6)$$

By substituting the value of ' u ' from equation (6) into equation (4) and rearranging the terms,

$$\begin{aligned} a &= \frac{r_A + R_0}{\sqrt{3} \left[\left(\frac{5}{8} - \frac{(r_B + R_0)}{a} \right) - \frac{1}{4} \right]} \\ &= \frac{8a(r_A + R_0)}{\sqrt{3}(5a - 8r_B - 8R_0 - 2a)} \\ \frac{\sqrt{3}a}{8a} &= \frac{r_A + R_0}{3a - 8(r_B + R_0)} \\ 3\sqrt{3}a - 8\sqrt{3}(r_B + R_0) &= 8(r_A + R_0) \\ a_{\text{th}} &= \frac{8}{3\sqrt{3}} \left[(r_A + R_0) + \sqrt{3}(r_B + R_0) \right] \quad (7) \end{aligned}$$

It has been observed that the theoretically calculated values of lattice constant follow the same trend as that obtained experimentally, although the values are generally smaller than the experimental ones [38 - 40]. Theoretical calculations presume an ideal close packed structure and valence state of the cations and thus corresponding values of ionic radii have to be taken into consideration. It is found that ' a_{th} ' as well as previously reported experimental

lattice constant values of 8.347 Å [41], 8.220 Å [42], 8.370 Å [43], 8.255 Å [44], 8.225 Å [44], 8.250 Å [44], 8.240 Å [44], for $x = 0.0$ composition and 8.280 Å [6] for $x = 0.6$ composition are much smaller than presently found experimental values of lattice constant. This may be due to the presence of larger Fe^{2+} (0.74Å) and / or Cu^{1+} (0.96Å) in the system. The formation of ferrous ion and Cu^{1+} ion are quite probable in such systems [13, 43].

The oxygen positional parameter or anion parameter (u) for each composition was calculated using the formulae available in the literature [23].

$$u_{\bar{3}m} = \frac{\frac{1}{4}R^2 - \frac{2}{3} + \left(\frac{11}{48}R^2 - \frac{1}{18}\right)^{\frac{1}{2}}}{2R^2 - 2} \quad (8)$$

$$u_{\bar{4}3m} = \frac{\frac{1}{2}R^2 - \frac{11}{12} + \left(\frac{11}{48}R^2 - \frac{1}{18}\right)^{\frac{1}{2}}}{2R^2 - 2} \quad (9)$$

$$u_{\bar{4}3m} = \frac{r_A + R_0}{a\sqrt{3}} + \frac{1}{4} \quad (10)$$

$$u_{\bar{4}3m} = 0.3876 \left(\frac{\langle r_B \rangle}{\langle r_A \rangle} \right)^{-0.07054} \quad (11)$$

where, $R = (B-O) / (A-O)$. The bond lengths, $B - O$ and $A - O$ are average bond lengths calculated based on the cation distribution listed in Table 2; where, $B-O = \langle r_B + R_0 \rangle$ and $A-O = \langle r_A + R_0 \rangle$. Equation (8) gives 'u' assuming centre of symmetry at (1/4, 1/4, 1/4) for which $u_{\text{idea}} = 0.250$ (origin at B-site), while equations (9) – (11) give 'u' assuming centre of symmetry at (3/8, 3/8, 3/8) for which $u_{\text{idea}} = 0.375$ (origin at A-site). The values of $u_{\bar{4}3m}$ determined from different formulae are in agreement with each other (Table 3). To convert origin

from A-site to B-site, $u^{\bar{4}3m} = u^{\bar{3}m} + 1/8$ [23], relationship has been used. In an ideal fcc structure $u^{\bar{4}3m} = 0.375$; $u^{\bar{3}m} = 0.250$.

Table 3 Ionic radius (r), lattice constant (a) and oxygen positional parameter (u) for Cu-Fe-Al-O system.

Al^{3+} - content(x)	r_A (Å)	r_B (Å)	a_{th} (Å)	$u^{\bar{3}m}$ (1/4,1/4,1/4)	$u^{\bar{4}3m}$ (3/8, 3/8, 3/8)		
					Eq.(9)	Eq.(10)	Eq.(11)
0.0	0.6637	0.6782	8.3826	0.2618	0.3868	0.3865	0.3870
0.2	0.6549	0.6716	8.3514	0.2617	0.3867	0.3863	0.3869
0.4	0.6405	0.6678	8.3191	0.2613	0.3863	0.3857	0.3865
0.6	0.6261	0.6640	8.2868	0.2608	0.3858	0.3851	0.3860

Although, most ferrites generally have 'u' greater than this ideal value [39, 45], it is slightly larger in the present series (Table 3), implying that the oxygen ions are displaced in such a way that in the A-B interaction, the distance between A and O ions and between B - O ions decreased. This leads to an increase in the A - A and B - B interactions. As 'u' increases from its ideal value, anions move away from the tetrahedrally coordinated A - site cations along the $\langle 111 \rangle$ directions, which increase the volume of each A - site interstice while the octahedral B -sites become correspondingly smaller. The Fe^{2+} - ion is one of the largest divalent ions found in spinels, whereas the Al^{3+} ion is the smallest of the trivalent spinel cation: thus the $r(\text{Fe}^{2+}) / r(\text{Al}^{3+})$ ratio is large, which favours large u values [23]. The small deviation of 'u' parameter from its ideal value (Table 3) combined with positive values of quadrupole shift, determined from Mossbauer spectral analysis for cubic phase $x = 0.0 - 0.6$ compositions of $\text{CuAl}_x\text{Fe}_{2-x}\text{O}_4$

system [4] suggest absence of oblate type deformation of $3d^5$ shell that prevents canting of Fe^{3+} on the B-sites. They have observed Neel's collinear ferrimagnetic structure for these compositions [4], as predicted.

Using the experimental values of 'a' and anion parameter (u) of each composition in equations [23, 39, 46, 47], interatomic distances have been calculated.

$$\begin{aligned}
 d_{\text{AE}} &= a(2)^{1/2} \left(2u^{\bar{4}3m} - \frac{1}{2} \right) && \text{Shared tetrahedral edge} \\
 d_{\text{BE}} &= a(2)^{1/2} \left(1 - 2u^{\bar{4}3m} \right) && \text{Shared octahedral edge} \\
 d_{\text{BEu}} &= a \left[4 \left(u^{\bar{4}3m} \right)^2 - 3u^{\bar{4}3m} + \frac{11}{16} \right]^{1/2} && \text{Unshared octahedral edge} \\
 d_{\text{AL}} &= a\sqrt{3} \left(u^{\bar{4}3m} - \frac{1}{4} \right) && \text{Tetrahedral bond length} \\
 d_{\text{BL}} &= a \left[3 \left(u^{\bar{4}3m} \right)^2 - \frac{11}{4} u^{\bar{4}3m} + \frac{43}{64} \right]^{1/2} && \text{Octahedral bond length} \quad (12)
 \end{aligned}$$

Table 4. Edge length and bond length for Cu-Fe-Al-O system

Al^{3+} - content(x)	d_{AE} (Å)	d_{BE} (Å)	d_{BEu} (Å)	d_{AL} (Å)	d_{BL} (Å)
0.0	3.2470	2.6850	2.9726	1.9883	2.0028
0.2	3.2352	2.6797	2.9640	1.9811	1.9979
0.4	3.2148	2.6838	2.9553	1.9686	1.9960
0.6	3.1945	2.6880	2.9467	1.9561	1.9942

The calculated values of edge lengths and bond lengths are given in Table 4. It is found that with an increase in Al^{3+} - concentration, shared tetrahedral and octahedral, unshared octahedral edge lengths and tetrahedral as well as

octahedral bond lengths decrease. These may be due to the replacement of larger Fe^{3+} -ions by smaller Al^{3+} ions in the system.

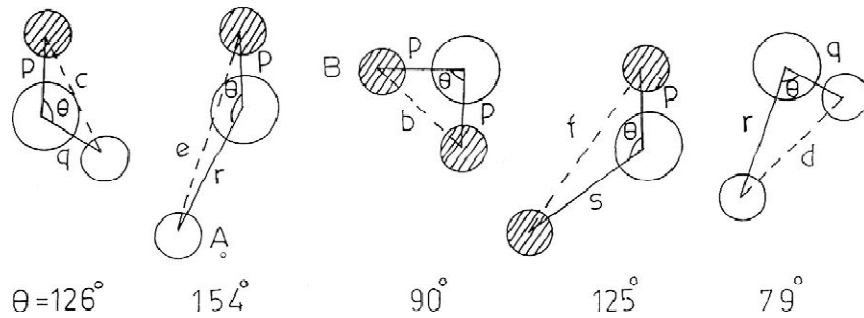


Figure 4 Configuration of ion pairs in spinel ferrites with favorable distances and angles for effective magnetic interactions.

The configuration of ion pairs in spinel ferrites with favorable distances and angles for magnetic interactions are shown in Fig. 4. The interionic distances between the cations (Me-Me) (b, c, d, e, and f) and between the cation and anion (Me-O) (p, q, r and s) were calculated using the experimental values of lattice constant (a) and oxygen positional parameters (u^{3m}) (Tables 1 and 3) by the relations [48, 49]:

$\text{M}_e - \text{O}$

$$p = a \left(\frac{1}{2} - u^{3m} \right)$$

$$q = a \left(u^{3m} - \frac{1}{8} \right) 3^{1/2}$$

$$r = a \left(u^{3m} - \frac{1}{8} \right) 11^{1/2}$$

$$s = \frac{a}{3} \left(u^{3m} + \frac{1}{2} \right) 3^{1/2}$$

$M_e - M_e$

$$b = \left(\frac{a}{4}\right) 2^{1/2}$$

$$c = \left(\frac{a}{8}\right) 11^{1/2}$$

$$d = \left(\frac{a}{4}\right) 3^{1/2}$$

$$e = \left(\frac{3a}{8}\right) 3^{1/2}$$

$$f = \left(\frac{a}{4}\right) 6^{1/2} \quad (13)$$

The overall strength of the magnetic interactions (A-B, B-B and A-A) depend upon the bond length and bond angles between the cations and cation - anion. The strength is directly proportional to bond angle but inversely proportional to bond length. It is seen from Table 5, that both interatomic distances between the cation - anion (p, q, r and s) and between the cations (b, c, d, e and f) decrease with increasing Al^{3+} concentration (x). These results are accordance with decrease in unit cell volume. The bond angles (θ_1 , θ_2 , θ_3 , θ_4 and θ_5) (Fig.4) were calculated by simple trigonometric principle using the interionic distances with the help of following formulae:

$$\theta_1 = \cos^{-1} \left[\frac{p^2 + q^2 - c^2}{2pq} \right]$$

$$\theta_2 = \cos^{-1} \left[\frac{p^2 + r^2 - e^2}{2pr} \right]$$

$$\theta_3 = \cos^{-1} \left[\frac{2p^2 - b^2}{2p^2} \right]$$

$$\theta_4 = \cos^{-1} \left[\frac{p^2 + s^2 - f^2}{2ps} \right]$$

$$\theta_5 = \cos^{-1} \left[\frac{r^2 + q^2 - d^2}{2rq} \right]$$
(14)

Table 5 Interionic distances (b, c, d, e, f and p, q, r, s) and bond angles (θ) for Cu-Fe-Al-O system

Al ³⁺ - content (x)	0.0	0.2	0.4	0.6
b	2.9659	2.9574	2.9493	2.9412
c	3.4779	3.4679	3.4584	3.4489
d	3.6324	3.6220	3.6121	3.6021
e	5.4487	5.4331	5.4181	5.4032
f	5.1370	5.1223	5.1082	5.0941
p	1.9979	1.9930	1.9916	1.9902
q	1.9883	1.9811	1.9686	1.9561
r	3.8074	3.7937	3.7697	3.7458
s	3.6898	3.6787	3.6663	3.6538
θ_1	121.50	121.63	121.68	121.84
θ_2	137.41	137.54	138.11	138.71
θ_3	95.85	95.79	95.54	95.28
θ_4	126.56	126.55	126.50	126.44
θ_5	69.69	69.77	70.15	70.54

(Distances in Å and angles in degrees)

It is found that angles θ_1 , θ_2 and θ_5 increase while θ_3 and θ_4 decrease with increase in Al³⁺- content (x). The observed increase in θ_1 , θ_2 and θ_5 suggest strengthening of the A – B and A – A interactions while decrease in θ_3 and θ_4 indicative of weakening of the B-B interaction on Al³⁺-substitution in the system. These results are consistent with relative strength of exchange integrals,

J_{AB} / J_{BB} , determined from high field magnetization data [15]. It has been found that for $x = 0.0 - 0.2$ compositions of $\text{CuAl}_x\text{Fe}_{2-x}\text{O}_4$ system, ratio J_{AB} / J_{BB} varies from 1.39 to 1.42 on increasing Al-concentration.

(d) Debye temperature determination

A method which depends on the principle of measuring the integrated intensities of a large number of Bragg reflections at a fixed temperature was first outlined by Buerger [24] and later described in detail by Walford et al. [50], for the determination of x-ray Debye temperature. The details of method can be found from refs. [24, 50], however, we briefly present here.

The average vibrational amplitudes are related to the Bragg intensities, within the quasi harmonic approximation, through the Debye-Waller theory. The integrated intensity, I_{hkl} , from a cubic structured material can be expressed as follows:

$$I_{hkl} = L_p P_m |F_{hkl}|^2 \quad (15)$$

where F_{hkl} is the modulus of the structure factor, P_m the multiplicity factor and L_p is the Lorentz polarization factor = $(1 + \cos^2 2\theta / \sin^2 \theta \cos \theta)$.

The structure factor for present system can be written as :

$$F_{hkl} = (1.0) f_{\text{Cu}} F_{\text{Cu}} e^{-M_{\text{Cu}}} + (x) f_{\text{Al}} F_{\text{Al}} e^{-M_{\text{Al}}} + (2-x) f_{\text{Fe}} F_{\text{Fe}} e^{-M_{\text{Fe}}} + 4 f_{\text{O}} F_{\text{O}} e^{-M_{\text{O}}} \quad (16)$$

The exponential terms in equation (16) represent the temperature factor in terms of Debye-Waller factors for the four constituent atoms of copper, aluminum, iron and oxygen, 'f' and 'F' are their respective atomic scattering factor and structure factor, which are sine and cosine functions of the hkl values.

The Debye-Waller factor is defined as [51]:

$$M(T) = \frac{6h^2T}{mk\theta_M^2} \left\{ \varphi(x) + \frac{x}{4} \right\} \frac{\sin^2\theta}{\lambda^2} \quad \text{or}$$

$$M(T) = B_M \frac{\sin^2\theta}{\lambda^2}, \quad \text{where } B_M = \frac{6h^2T}{mk\theta_M^2} \left\{ \varphi(x) + \frac{x}{4} \right\} \quad (17)$$

Here m is the mass of the vibrating atom given by A/N_A , where A is the atomic weight taken as the mean atomic weight (molecular weight of the composition / number of atoms in formula unit i.e./ 7), N_A is the Avogadro's number, h is the Planck's constant, k is the Boltzmann constant, θ_M is the x-ray Debye temperature, T is the temperature (300K), θ is the Bragg angle, λ is the wavelength of the x-rays (for CuK_α radiation $\lambda=1.5405\text{\AA}$), $x = \theta_M/T$, and function $(\Phi(x) + x/4)$ is calculated by the procedure described by James et al. [51].

As the atomic masses of copper and iron are nearly equal (atomic mass of aluminum is much lower), the respective Debye-Waller factors (M_{Cu} and M_{Fe}) will also be approximately equal in $\text{CuAl}_x\text{Fe}_{2-x}\text{O}_4$. To the first approximation, let M_{Cu} , M_{Al} , M_{Fe} , and M_{O} be equal to each other, equation (16), therefore becomes:

$$F_{hkl} = \sum f \cdot e^{-M}$$

where, $\sum f = [(1.0)f_{\text{Cu}} F_{\text{Cu}} + (x)f_{\text{Al}} F_{\text{Al}} + (2-x) f_{\text{Fe}} F_{\text{Fe}} + 4 f_{\text{O}} F_{\text{O}}]$ (18)

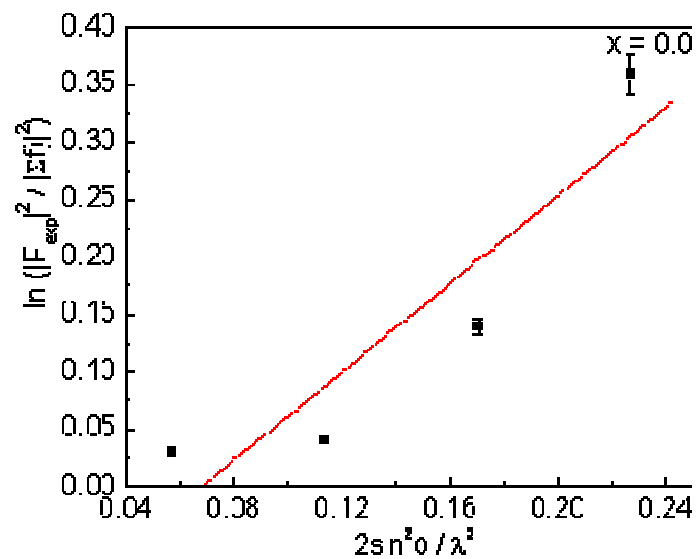
Equation (15) may be written using equations (16) and (17) as:

$$I_{hkl} = L_p \cdot P_m \cdot \left| \sum f \right|^2 e^{-\frac{2B_M \sin^2\theta}{\lambda^2}} \quad (19)$$

The experimental structure factor, F_{exp} , may be obtained from equation (19) using experimentally measured integrated intensity I as :

$$\left| F_{\text{exp}} \right|^2 = \frac{1}{L_p \cdot P_m} \left| \sum f \right|^2 e^{-\frac{2B_M \sin^2\theta}{\lambda^2}} \quad (20)$$

The measured intensities were corrected for thermal diffuse scattering (TDS) using the correction for cubic structure powders [52]. In addition to the TDS correction, intensities were also corrected for Lorentz polarization and absorption. The even-even ($h+k = 2n$, $l+k = 2n$), even-odd ($h+k = 2n$, $l+k = 2n+1$), odd-even ($h+k = 2n+1$, $l+k = 2n$), odd-odd ($h+k = 2n+1$, $l+k=2n+1$), reflections lie on the same straight line indicates that $M_{\text{Cu}} \sim M_{\text{Al}} \sim M_{\text{Fe}} \sim M_{\text{O}}$. Thus the experiment has not distinguished between the individual Debye temperature or mean square atomic displacements appropriate to the atoms of copper, aluminum, iron and oxygen in the system.



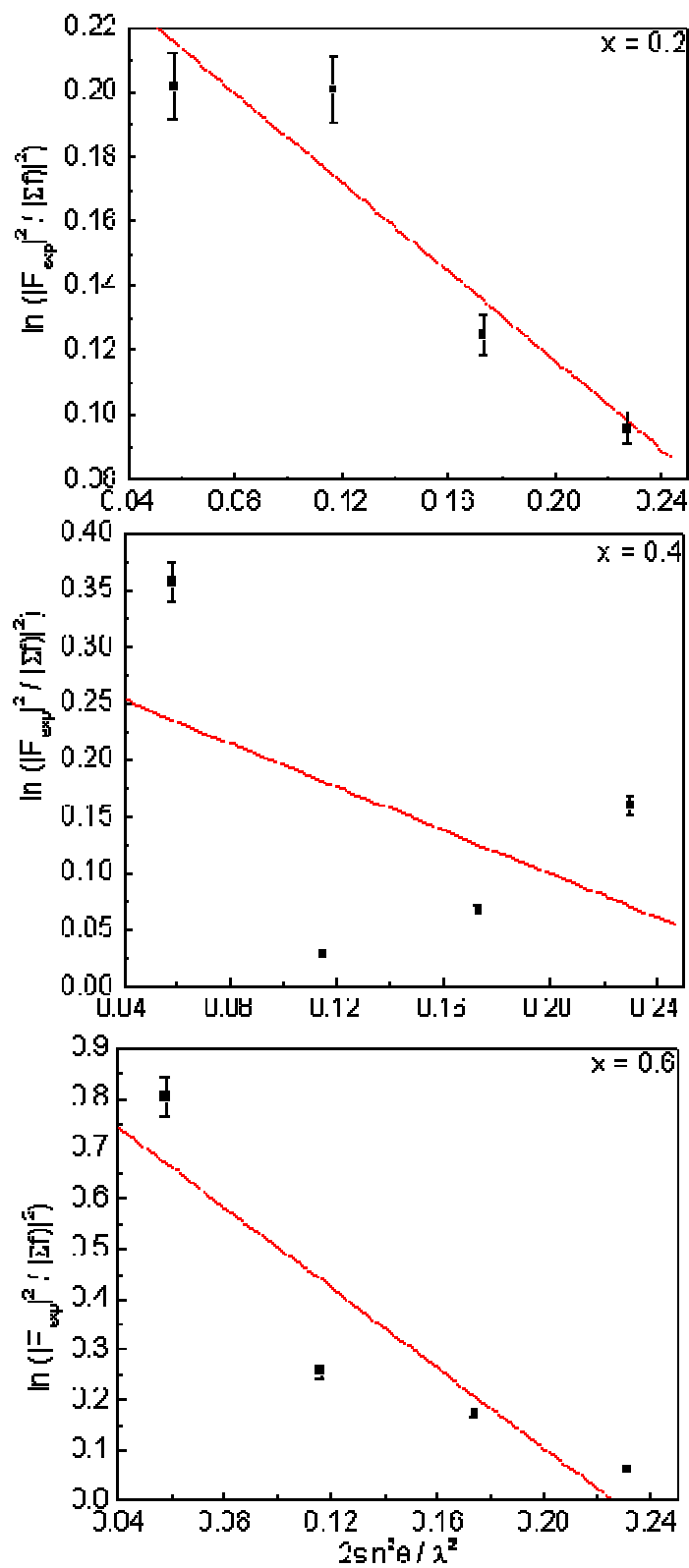


Figure 5. Plots of $\ln(|F_{\text{exp}}|^2 / |\Sigma f|^2)$ against $2\sin^2\theta/\lambda^2$ for different compositions of Cu-Fe-Al-O system.

The solid lines in Fig. 5 are least squares fit to the experimental data points. This validates the approximation made for θ_M determination. It follows from equation (20) that the slope of $\ln(|F_{exp}|^2/|\Sigma f|^2)$ against $2\sin^2\theta/\lambda^2$ plot yields the Debye-Waller parameter (B_M) and hence θ_M can be obtained from equation (17), by substituting the value of various parameters. The equation for θ_M in its simplified form is given by:

$$\theta_M = \left[\frac{345 \times 10^4}{A \cdot B_M} \left\{ \varphi(x) + \frac{x}{4} \right\} \right]^{1/2} \quad (21)$$

Table 6: Plane (hkl), Bragg angle (θ), integrated intensity (I), Lorentz polarization factor (L_p), multiplicity factor (P_m), slope (B_M), Debye temperature (θ) and structure factor (F) for CuAl_xFe_{2-x}O₄ spinel ferrite system.

Plane (hkl)	2 θ (Degree)	I_{hkl}^* (%)	I^* (%)	L_p	P_m	B_M	θ_M (K) \pm 2K	θ_D (K) \pm 2K	Structure factor (F)
x = 0.0 (Cu_{0.22}Fe_{0.78})^A[Cu_{0.78}Fe_{1.22}]^BO₄									
220	30.06	40.70	32.54	26.89	12	0.489	472.2	512.4	-8f _a
400	43.18	20.97	26.32	12.15	6				8(-f _a +2f _b +4f ₀)
422	53.51	13.90	14.11	7.47	24				8f _a
440	62.56	52.37	77.27	5.26	12				8(f _a +2f _b +4f ₀)
x = 0.2 (Cu_{0.22}Fe_{0.70}Al_{0.08})^A[Cu_{0.78}Fe_{1.10}Al_{0.12}]^BO₄									
220	30.14	36.96	30.20	26.75	12	0.692	397.7	430.0	-8f _a
400	43.66	26.06	21.32	11.86	6				8(-f _a +2f _b +4f ₀)
422	53.86	12.56	11.09	7.36	24				8f _a
440	62.54	56.83	62.58	5.26	12				8(f _a +2f _b +4f ₀)
x = 0.4 (Cu_{0.18}Fe_{0.64}Al_{0.18})^A[Cu_{0.82}Fe_{0.96}Al_{0.22}]^BO₄									
220	30.35	38.60	27.00	26.36	12	0.957	338.3	330.5	-8f _a
400	43.43	26.43	25.70	12.00	6				8(-f _a +2f _b +4f ₀)
422	53.86	13.54	14.50	7.36	24				8f _a
440	63.02	57.06	68.98	5.17	12				8(f _a +2f _b +4f ₀)
x = 0.6 (Cu_{0.14}Fe_{0.58}Al_{0.28})^A[Cu_{0.86}Fe_{0.82}Al_{0.32}]^BO₄									
220	30.46	41.40	18.54	26.15	12	1.390	282.0	259.4	-8f _a
400	43.54	26.35	20.42	11.93	6				8(-f _a +2f _b +4f ₀)
422	53.98	14.75	12.40	7.33	24				8f _a
440	63.19	59.19	55.64	5.14	12				8(f _a +2f _b +4f ₀)

* Relative intensity with respect to 100% intensity of (311) plane.

The experimental values of Bragg angle (θ), Debye-Waller parameter (B_M) (i.e. slope of the $\ln(|F_{\text{exp}}|^2/|\Sigma f|^2)$ versus $2\sin^2\theta/\lambda^2$ plot) and the Debye temperature (θ_M) along with other structural parameters used in the calculation for selected planes, (220), (400), (422) and (440) for different samples are summarized in Table 6. The Debye temperature, θ_M obtained at 300K from x-ray data analysis, lies in the range between 475 - 280 K, in consistent with the Debye temperature, θ_D , obtained from ultrasonic pulse echo-overlap technique, ranging from 510 - 260 K for $x = 0.0$ to $x = 0.6$ compositions [53]. This is in accordance with the assertion of Salter et al.[9].

The Debye temperature is the temperature at which maximum lattice vibrations take place. The observed decrease in θ_M with Al^{3+} - content (x) suggested that the lattice vibrations are enhanced due to Al - substitution. The enhancement in lattice vibrations reduces the elastic wave velocities that result in decrease in magnitude of elastic moduli with Al^{3+} - substitution, as observed [53].

(D) Conclusions

In summary (i) The cubic phase spinel ferrite structure for all the compositions of $\text{CuAl}_x\text{Fe}_{2-x}\text{O}_4$ system is mainly due to deficit of Cu^{2+} - ions in the octahedral sites that leads to the absence of co-operative active Jahn-Teller distortion. (ii) The preferred orientation and extinction effects are responsible for the observed variation and disagreement between experimental and calculated intensities of the diffracted beam with Al^{3+} - substitution. (iii) Various structural parameters can be determined from x-ray powder diffraction pattern analysis and are found useful to explain other physical properties. (iv) The strength of the A - B interaction increase while B - B interaction decreases with Al^{3+} - substitution for Fe^{3+} in the system. (iv) The Debye temperature decreases with increasing Al-content (x) suggests enhancement of lattice vibrations.

References

- [1] G. F. Goya, H. R. Rechenberg, J. Z. Jiang
J. Appl. Phys. 84(2)(1998)1101-1108.
- [2] I. Nedkov, R. E. Vandenberghe, Ts. Marinova, Ph. Thailhades, T. Merodiiska, I. Avramova
Appl. Surf. Sci. 253(2006)2589-2596.
- [3] F. C. Romeijn
Philips. Res. Rep. 8 (1953)304-321.
- [4] R. G. Kulkarni, B. S. Trivedi, H. H. Joshi, G. J. Baldha
J. Magn. Mater. 159(1996)375-380.
- [5] B. S. Trivedi, N. N. Jani, H. H. Joshi, R. G. Kulkarni
J. Mater. Sci. 35(3)(2000)5523-5526.
- [6] S. S. Ata-Allah, M. Kaiser
J. Alloys Compd. 471(2009)303-309.
- [7] S. S. Ata-Allah, M. F. Fayek, H. S. Refai, M. F. Mostafa
J. Solid State Chem. 149(2000)434-442.
- [8] S. S. Ata-Allah
Mat. Chem. Phys. 87(2004)378-386.
- [9] L. S. Salter
Adv. Phys. 14(53) (1965)1-5.
- [10] S. S. Bhatu, V. K. Lakhani, A. R. Tanna, N. H. Vasoya, J. U. Buch, P. U. Sharma, U. N. Trivedi, H. H. Joshi, K. B. Modi
Ind. J. Pure Appl. Phys. 45(2007)596-608.

- [11] K. B. Modi
J. Mater. Sci. 39(2004)2887-2890.
- [12] K. B. Modi, T. K. Pathak, N. H. Vasoya, V. K. Lakhani, G. J. Baldha,
P. K. Jha
Ind. J. Phys. 85(3) (2011) 411-420.
- [13] V.V.Parfnov, R.A.Nazipov
Inorg. Mater. 38(1) (2002) 78-82.
- [14] B. H. Toby
Powder Diff. 21(1) (2006)67-70.
- [15] B. S. Trivedi, Ph.D. thesis, Saurashtra University, Rajkot, India (1995).
- [16] H. M. Zaki, S. F. Mansour
J. Phys. Chem, Solids. 67 (2006)1643-1648.
- [17] U. N. Trivedi, K. B. Modi, D. C. Kundaliya, A. G. Joshi, H. H. Joshi, S. K.
Malik
J. Alloys Compd. 369(2004)58-61.
- [18] S. S. Ata-Allah, M. K. Fayek, M. Yehia
J. Magn. Magn. Mater. 279(2004)411-420.
- [19] S. S. Ata-Allah, M. Yehia
Physica B 404(2009)2382-2388.
- [20] S. S. Ata-Allah, A. Hashhash
J. Magn. Magn. Mater. 307(2006)191-197.
- [21] C. G. Whinfrey, D. W. Eckart, A. Tauber
J. Am. Chem. Soc. 82(1960)2695-2699.

- [22] J. Smith, H. P. J. Wijn
Ferrites, John Wiley, New York, 1959.
- [23] K. E. Siokafus, J. M. Wills, N. W. Grimes
J. Am. Ceram. Soc. 82 (12) (1999)3279-3291.
- [24] M. J. Buerger
Crystal Structure Analysis, Wiley, NY, 1960.
- [25] H. Ohinishi, T. Teranishi
J. Phys. Soc. Jpn. 16(1961)35-43.
- [26] B. D. Cullity
Elements of x-ray diffraction, 2nd Edn. Addison Wesley Pub. Co. Reading MA 1978.
- [27] V. K. Lakhani, K. B. Modi, (unpublished work).
- [28] V. K. Lakhani, Bangchuan Zhao, Lan Wang, U. N. Trivedi, K. B. Modi,
J. Alloys Compd. 509(2011)4861-4867
- [29] N H Vasoya, L H Vanpariya, P N Sakariya, M D Timbadiya, T K Pathak,
V K Lakhani, K B Modi, Ceram. Int. 36(2010)947-954.
- [30] A. Globus, H. Pascard , V. Cagan,
J. Phys. Suppl. 438 (C-1) (1977) 163-168.
- [31] Yanbo Zuo, Jianheng Li, Jianxin Yi, Zhongbing Wang, Chusheng Chen,
J. Solid State Chem, 18 (2008)700-704.
- [32] V. K. Lakhani, K. B. Modi, J. Phys. D:Appl. Phys. 44 (2011)
- [33] R. R. Heikes, in Thermo electricity (eds) R. R. Heikes, R. W. Ure, 45 (NY: Wiley Inter Science (1961)).

- [34] S. C. Byeon, K. S. Hong, J. G. Park, W.N. Kang, J. Appl. Phys. 81(12) (1997) 7835-7841.
- [35] J. Zhang, Y. Zhao, H. Xu, B. Li, D. J. Weidner, A. Navrotsky, Appl. Phys. Lett. 90(2007)161903, 1-3.
- [36] Q. Wang, G. A. Saunders, D. P. Almond, M. Cankurtaran, K. C. Goretta, Phys. Rev. B. 52 (1995) 3711-3726.
- [37] K. J. Standly
Oxide magnetic materials, Clarendon Press, Oxford, 1972.
- [38] S. A. Mazen, M. H. Abdallah, B. A. Sabrah, H. A. M. Hasham
Phys. Status. Solidi A 134 (1992)263-271.
- [39] R. K. Sharma, Varkey Sebastain, N. Lakshmi, K. Venugopalan, V. R. Reddy, Ajay Gupta
Phys. Rev. B. 75(2007)144419-1-6.
- [40] H. Bhargava, N. Lakshmi, V. Sebastina, V. R. Reddy, K. Venugopalan, Ajay Gupta
J. Phys D: Appl. Phys. 42(2009)245003-245010.
- [41] B. J. Evans, S. S. Hafner
J. Phys. Chem. Solidi. 29(1968) 1573-1588.
- [42] R. G. Kulkarani, V. G. Panicker
J. Mater. Sci. 19(1984)890-894.
- [43] M. Ajmal, A. Maqsood
J. Alloys Compd. 460(2008)54-59.

- [44] D. Ravinder, K. V. Kumar, B. S. Boyanov
Mater. Lett. 38(1999)22-27 and references their in.
- [45] K. H. Jani, M. C. Chhanbar, H. H. Joshi
J. Magn. Magn. Mater. 18(2008)2208-2214.
- [46] C. Arena, J. Blanco, J. Gonzalez, M. Fernandez
J. Math. Psychol. 9(1990)229-233.
- [47] T. Abbas, Y. Khan, M. Ahmad, S. Anwar
Solid State Commun. 82(9)(1992)701-703.
- [48] J. B. Goodenough
J. Phys. Chem. Solids. 6(1958)287-297.
- [49] J. Kanamori
J. Phys. Chem. Solids. 10(2-3)(1959)87-98.
- [50] L K Walford, J. A. Schoffel,
Philos. Mag. 21(1970) 375-384.
- [51] R W James, The optical principles of the diffraction of x-rays, Bell,
London, (1967) p.216.
- [52] D. R. Chipman, A. Paskin,
J.Appl.Phys. 30(1959)1998-2001.
- [53] V. K. Lakhani, K. B. Modi,
Solid State Sci. 12(2010)2134-2143.

4.2 Effect of Al^{3+} - substitution on the transport properties of copper ferrite

(A) Introduction

Copper ferrite (CuFe_2O_4) is one of the most investigated ferrite by various experimental techniques. Due to a relatively small energy difference between Cu^{2+} - ions at the tetrahedral (A-) and octahedral (B-) sites, cation redistribution is possible and strongly dependent on the annealing temperature, cooling rate, microstructure, and other parameters [1]. At certain technological conditions, the Cu^{2+} and Mn^{3+} ions in substituted spinels can lead to severe Jahn-Teller distortion of sites [2], which is associated with the alignment of the Cu^{2+} ions occupying the tetragonally distorted octahedral spinel lattice formed by the oxygen ions. Copper ferrite has two crystallographical spinel structures, the high temperature cubic phase with a lattice parameter of 8.380 Å and a low-temperature tetragonal phase with lattice parameters of $a = 8.216$ Å and $c = 8.709$ Å [1]. It is ferrimagnetic at room temperature with Neel temperature of 780K [1], although lower values down to 710K have been reported [3]. Copper ferrite crystallizes mostly in the inverse spinel structure. Statistically, 6 % - 24 % of Cu^{2+} ions occupy the A-sites depending on the sample preparation [3], allowing engineering of the electrical and magnetic properties of CuFe_2O_4 possible. [1, 4, 5]. The Al^{3+} - ion possess noble-gas structure, being less compressible than ions with full or half filled d-shell as in Co^{2+} , Mn^{2+} , Fe^{3+} , Zn^{2+} , In^{3+} and Sn^{4+} ions [6]. Thus Al^{3+} cannot be easily accommodated in the A-sites, but statistically distributed among the available A- and B- sites. The system

under investigation $\text{CuAl}_x\text{Fe}_{2-x}\text{O}_4$ belongs to a large class of compounds having general formula $\text{A}^{2+}\text{B}_2^{3+}\text{O}_4^{2-}$ and crystallizing in a spinel structure.

A precise knowledge of the cation distributions in ferrites over the crystallographic sites plays an important role in understanding their physical properties. The magnetization and magnetic transition temperature are known to depend not only on the composition of these materials but also on the cation distributions. As a result, ferrites identical in composition may differ in Neel temperature and magnetic moment by $\pm 10\%$. The effect of cation distribution on the electrical properties of ferrites is one of the important performance parameters of these materials as they play a key role in determining their magnetic losses at high frequencies. The conduction in ferrites takes place via electron jumps between differently charged ions of the same metal residing in equivalent crystallographic sites. The hopping transport in ferrites is mostly due to the presence of Fe^{2+} and Fe^{3+} ions, contribution from the Mn^{3+} and Mn^{2+} , Co^{3+} and Co^{2+} , Ni^{2+} and Ni^{3+} , Cu^{1+} and Cu^{2+} and other cations may also be significant. Mixed – valence cations are often associated with cation non-stoichiometry. The generation of anion vacancies during sintering or the incorporation of excess oxygen during synthesis in an oxidizing atmosphere [4] can also be a cause.

To best of the authors' knowledge, few reports are available on structural, magnetic, electrical, and dielectric properties of typical compositions of $\text{CuAl}_x\text{Fe}_{2-x}\text{O}_4$ spinel ferrite system [7 - 12]. No efforts have been made to investigate the effect of Al^{3+} - substitution on transport properties and conduction mechanism of CuFe_2O_4 in the light of cationic distribution and the role of Cu^{2+}

and Fe^{3+} ions in other oxidation states (i.e. Cu^{1+} and $\text{Fe}^{2+}/\text{Fe}^{4+}$ respectively). No systematic study on Cu^{1+} and Fe^{2+} ions concentration and oxygen content determination by thermoelectric power measurements have been reported. The structural and magnetic properties of $\text{CuAl}_x\text{Fe}_{2-x}\text{O}_4$ system over a wide range of compositions ($x = 0.0 - 1.6$) have been reported by Baldha et al [8].

It is well known fact that the thermal history and heat treatment employed, affect the structural parameters and other physical properties to large extent for any ferrite system in general, but pure and substituted copper ferrite systems in particular [7, 13, 14]. The structural characteristics play very important role in governing and understanding the various physical properties. It has been found that experimental lattice constant values of 8.385 Å [7, 8], 8.347 Å [15], 8.220 Å [16], 8.370 Å [17], 8.225 Å [18], 8.250 Å [18], 8.240 Å [18], for $x = 0.0$ (CuFe_2O_4) and 8.280 Å [10] for $x = 0.6$ ($\text{CuAl}_{0.6}\text{Fe}_{1.4}\text{O}_4$) are much smaller than the presently found experimental values of lattice constant. The lattice constant value for $\text{CuAl}_{0.6}\text{Fe}_{1.4}\text{O}_4$ ($x = 0.6$) is reported to be 8.334 Å [8], which is larger than the presently found value of lattice constant ($a = 8.319$ Å) (Table 1).

The slow cooled samples of $\text{CuAl}_x\text{Fe}_{2-x}\text{O}_4$ system possess tetragonal distortion ($c/a > 1$) [7] while samples quenched from 1000°C to liquid nitrogen temperature exhibit cubic spinel structure [7, 8]. On the other hand, $x = 0.6$ and $x = 1.0$ compositions of the $\text{CuAl}_x\text{Fe}_{2-x}\text{O}_4$ system prepared by the usual double sintering ceramic technique, have shown fcc spinel structure [10 - 12]. In short, the structural properties are sensitive to preparation conditions (sintering

temperature, cooling rate, gaseous environment, starting-mixture composition etc.) and influence the physical properties.

The present investigation reports the transport properties and conduction mechanisms of copper-ferri-aluminates $\text{CuAl}_x\text{Fe}_{2-x}\text{O}_4$ ($x = 0.0, 0.2, 0.4$ and 0.6) by means of compositional and temperature dependence of the thermoelectric power and dc resistivity measurements.

(B) Experimental details

From the $\text{CuO} - \text{Fe}_2\text{O}_3$ phase diagram, copper ferrite (CuFe_2O_4) is formed between 1000°C and 1100°C . The samples sintered below 1000°C or above 1100°C were of mixed-phase [4]. Aluminum (Al^{3+}) - substituted copper ferrite ceramics with a general chemical formula of $\text{CuAl}_x\text{Fe}_{2-x}\text{O}_4$ ($x = 0.0, 0.2, 0.4$ and 0.6) were synthesized from high purity chemicals CuO , Al_2O_3 and Fe_2O_3 of 99.9% purity supplied by Sigma Aldrich. The oxides were mixed thoroughly in appropriate stoichiometry to yield the desired composition and then wet – ground by blending with acetone in an agate mortar and pestle for 4 hours. The mixture was dried and pressed into pellets at a pressure of 2 MPa using Hydraulic Press (BIMPEX machines International, Mumbai, India). The pellets were pre-sintered at 1100°C for 24 hours and slowly cooled to room temperature. The samples were again powdered, pressed into pellets, sintered at 1100°C for 24 hours, and then slowly cooled to room temperature at the rate of $2^\circ\text{C}/\text{min}$. The pre-sintering and sintering processes were carried out under atmospheric conditions. Room temperature (300K) X-ray powder diffraction patterns were recorded with a Philips, Holland, Xpert MPD automated x-ray powder diffractometer using $\text{CuK}\alpha$.

radiation ($\lambda = 0.15405$ nm), graphite monochromater, and Xe-filled proportional counter. Data were collected in a 2θ range of $5-85^\circ$ at a scan speed of $2^\circ/\text{min}$.

The discs - shaped ferrite samples with 10 mm diameter and 3mm thickness were polished using zero grade emery paper, washed in dilute HCL and acetone to obtain clean, flat and parallel faces. The electrical measurements were done on samples covered with graphite and aluminium foil for good electrical contacts.

The dc electrical resistivity was measured by the two terminal pressure contact method. A BPL meg-ohm meter was used to measure the resistance directly. The variation of resistance with temperature was obtained by placing sample holder containing a pellet in a horizontal electric furnace. Chromel-alumel thermo couple measured temperature of the pellet. The resistance was measured during cooling cycle at intervals of 20°C .

Thermoelectric power (α) measurement studies were carried out over a temperature range 300 - 475 K by the differential method. According to the relation: $\alpha = \nabla V (\mu\text{V})/\Delta T (\text{K})$, the thermo emf (∇V) was measured with the help of a digital micro voltmeter (KUSAM - MECO 306) with an accuracy of $\pm 3 \%$ while the temperature gradient (ΔT) was measured by two chromel-alumel thermocouples which were kept very close to the sample. The temperature difference between two ends of the sample was kept at 10 K throughout the temperature range studied. In order to achieve good thermal stability, the values of the thermo emf were recorded while cooling and the sample was maintained at a given temperature for about five minutes.

(C) Results and discussion

(a) X-ray powder diffraction patterns analysis

The room temperature (300K) x-ray diffraction (XRD) patterns of the system $\text{CuAl}_x\text{Fe}_{2-x}\text{O}_4$ with $x = 0.0, 0.2, 0.4$ and 0.6 were obtained by x-ray powder diffractometry. Indexing and Rietveld refinement using general scattering analysis software (GSAS) [19] of XRD patterns revealed that these are single phase compounds, crystallizing in a fcc structure (space group O_h^7 Fd3m).

In Rietveld analysis, we fit a model to the data. If the model is correct then it will predict what the “true” intensity values should be. The refinement of the data was started using a model in which the space group is Fd3m; its origin is at $\bar{3}m$ at $1/8, 1/8, 1/8$ from the centre $\bar{4}3m$, in which, the oxygen atom occupies the 32e position with fractional coordinates, $1/4, 1/4, 1/4$; A-site at 8f and B-site at 16c positions. The experimental profile was fitted using a multiterm Simpson’s rule integration of the pseudo-Voigt function [20]. In the first and second refinement cycles of process, the global parameters (2θ -zero, instrumental profile, profile asymmetry, background, specimen displacement) and structural parameter (atomic coordinates, specimen profile breadth parameters, lattice parameter, preferred orientation, and site occupancy) were refined in sequence mode. The site occupancy of the cations in the A- and B-sites were constrained in order to keep the sum of the particular cation in the two sites always have its stoichiometric value. In the last cycle, when the discrepancy factor R_{wp} has reached its minimum values, the parameters were refined simultaneously giving the goodness-of-fit (χ^2).

Although a difference profile plot is probably the best way of following and guiding a Rietveld refinement, the fit of the calculated pattern to the observed data can also be given numerically. The fitting quality of the experimental data were checked by using the various Rietveld discrepancy values, i.e., the weighted profile R-factor (R_{wp}), the expected R factor (R_{exp}) and the goodness-of-fit ($\chi^2 = (R_{wp}/R_{exp})^2$) [21]. It should be noted that χ^2 should never drop below one. If a refinement results in $\chi^2 < 1$, which means that one of the two things is true: (i) the standard uncertainties for the data must be overestimated or (ii) so many parameters have been introduced that the model is adjusting to fit noise, which should be unlikely in powder diffraction. On the other hand, if at the end of a refinement $\chi^2 \gg 1$, then either: (i) the model is reasonable but the standard uncertainty values are underestimated (ii) the model is incomplete because there are systematic effects (errors) in the data that are not expressed in the model, or (iii) the model is wrong [21].

It is found that “Chi squared” or χ^2 for different compositions lie in the range 1.2 -1.4. The χ^2 values obtained in the present analysis suggest good refinement of the data. The Rietveld agreement factors for $x = 0.0, 0.2, 0.4$ and 0.6 are summarized in Table 1. Figure 1 displays Rietveld fitted XRD patterns for $x = 0.0, 0.2$ and 0.6 .

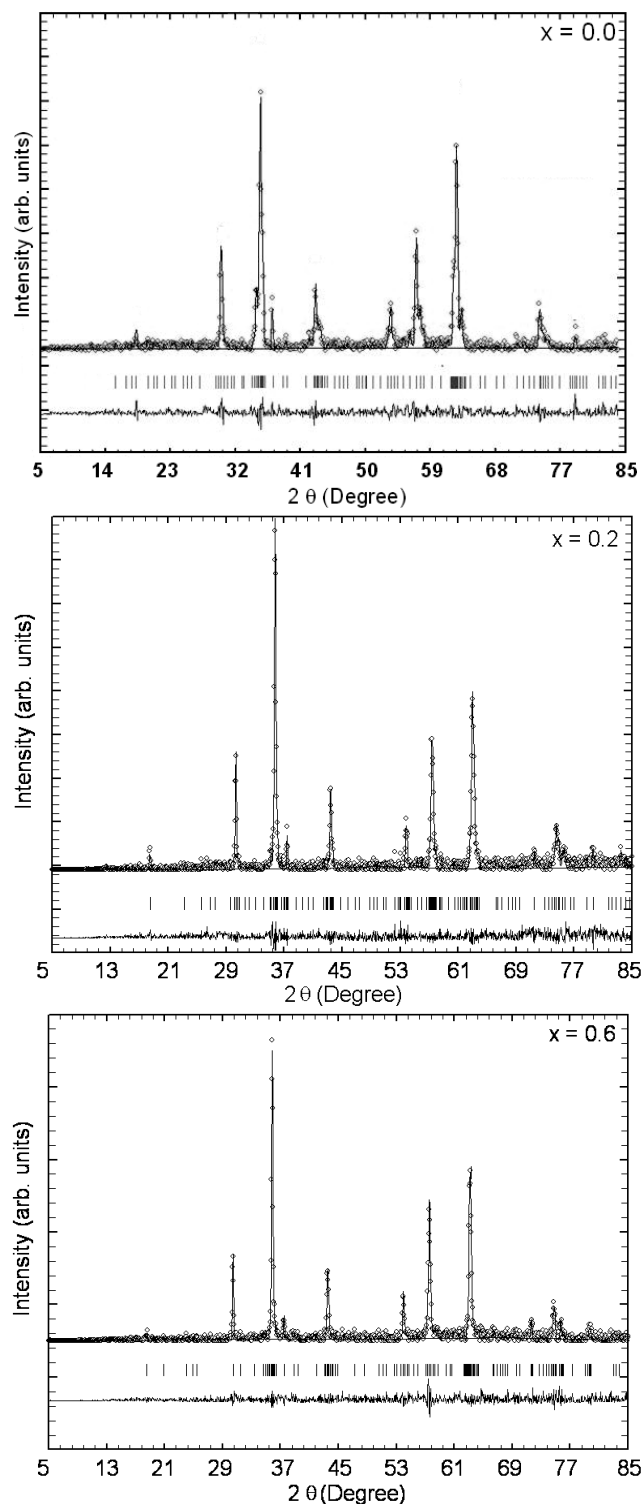


Figure 1. Observed (Solid Circles) and calculated (Solid line) x-ray powder diffraction patterns for the $\text{CuAl}_x\text{Fe}_{2-x}\text{O}_4$ ($x = 0.0, 0.2$ and 0.6) system at 300K. The difference between the observed and calculated spectra is plotted at the bottom. The ticks indicate allowed Bragg peaks positions.

The lattice constant values obtained from the above mentioned refinement, along with x-ray density (ρ_x), bulk density (ρ), pore fraction (f) ($f = 1 - \rho/\rho_x$) and average grain size (D) determined from SEM analysis are given in Table 1 in order to facilitate the discussion.

Table 1. Rietveld agreement factors, lattice constant (a), x-ray density (ρ_x), bulk density (ρ), pore fraction (f) and average grain size (D) for Cu-Fe-Al-O system.

Al-content (x)	R_{wp}	R_{exp}	χ^2	a(Å) $\pm 0.002\text{Å}$	ρ_x kg/m ³ x 10 ³	ρ kg/m ³ x 10 ³	f	D (μm)
0.0	5.11	4.50	1.29	8.389	5.385	4.736	0.1205	12
0.2	6.32	5.23	1.46	8.365	5.300	4.572	0.1374	9
0.4	4.48	3.81	1.38	8.342	5.212	4.370	0.1616	6.5
0.6	4.04	3.50	1.33	8.319	5.122	4.619	0.0982	4

A precise knowledge of the distribution of cations among the available crystallographic sites (A- and B-sites) of the spinel lattice is essential to understand the various physical properties of ferrites. The x-ray diffraction line intensity calculations were carried out using a computer program based on Buerger formula [22] given by:

$$I_{hkl} = |F_{hkl}|^2 \cdot P_m \cdot L_p$$

where, I_{hkl} is the relative integrated intensity, F_{hkl} the structure factor, P_m the multiplicity factor and L_p is the Lorentz polarization factor.

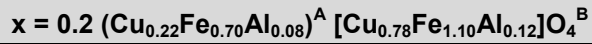
The details regarding x-ray diffraction line intensity calculation and cation distribution determination can be found from our recent work [23, 24], however, we briefly present here.

The calculations are most readily carried out in tabular form as in Table 2. Table 2(a) demonstrates illustrative intensity calculation for particular plane (here

(220)), considering corresponding Bragg angle (θ) obtained from the x-ray diffraction pattern analysis and atomic scattering factors (f) for different elements taken from the literature [25]. It should be noted that in cubic crystals, for example, Miller indices hkl stands for such indices as (311) or (422) for which $P_m = 24$, $0kk$ for such indices as (220) or (440) for which $P_m = 12$, $00l$ for indices such as (400) for which $P_m = 6$ [25]. The Lorentz-polarization factor, $L_p = (1 + \cos^2 2\theta) / (\sin^2 \theta \cdot \cos \theta)$ [25] for different planes is calculated from the corresponding Bragg angle (θ).

The calculated (I_{hkl}) and experimental (I) relative integrated intensity of different planes for the typical composition with $x = 0.2$ are shown in Table 2(b). The experimental intensities of different planes are directly deduced from the x-ray powder diffraction patterns analysis.

The intensity ratios of planes $I(220) / I(440)$, $I(400) / I(422)$ and $I(220) / I(400)$ are considered to be sensitive to the any change in cation distribution [26]. The intensities of (220) and (422) planes are mostly sensitive to cations on the A-sites, while the intensities of (400) and (440) are depend on cations on both the sites [25] (Table 2(b)). In practice, it is more appropriate to characterize the changes in the cations occupancies by considering the intensity ratio of the two reflecting planes rather than the change in the intensities of individual plane. This is due to the fact that the intensity ratio will not be affected by the preferred orientation of the sample [27].

Table 2.
(a) Plane (hkl), Bragg angle (θ), atomic scattering factor (f), structure factor (F), Lorentz-polarization factor (L_p), multiplicity factor (P_m) and Intensity (I) for $\text{CuAl}_x\text{Fe}_{2-x}\text{O}_4$ system.


Plane (hkl)	θ (Degree)	$\text{Sin}\theta/\lambda$	Atomic scattering factor			f_a	$ F_{\text{hkl}} ^2$	L_p	P_m	I_{hkl}
			f_{Cu}	f_{Fe}	f_{Al}					
220	15.07	0.1686	22.95	20.22	9.59	19.97	25523.77	26.75	12	81.93×10^5

 Atomic Scattering factor of the A-site, $f_a = 0.22 f_{\text{Cu}} + 0.70 f_{\text{Fe}} + 0.08 f_{\text{Al}}$

 Structure factor for (220) plane, $F_{\text{hkl}} = (-8f_a) \Rightarrow |F_{\text{hkl}}|^2 = 64(f_a)^2$
(b) Plane (hkl), Bragg angle (θ), integrated intensity (I), Lorentz-polarization factor (L_p), multiplicity factor (P_m), and structure factor (F) for $\text{CuAl}_x\text{Fe}_{2-x}\text{O}_4$ spinel ferrite system.

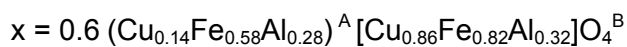
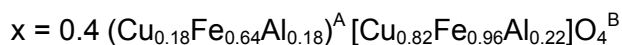
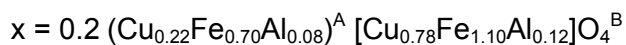
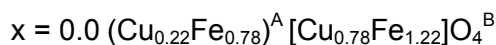
Plane (hkl)	θ (Degree)	$I_{\text{hkl}}^{\text{a}}$ (%)	I^{a} (%)	L_p	P_m	Structure factor (F)
220	15.07	36.96	30.20	26.75	12	$-8f_a$
400	21.83	26.06	21.32	11.86	6	$8(-f_a + 2f_b + 4f_0)$
422	26.93	12.56	11.09	7.36	24	$8f_a$
440	31.27	56.83	62.58	5.26	12	$8(f_a + 2f_b + 4f_0)$

^a Relative intensity with respect to 100% intensity of (311) plane.

(c) Comparison of x-ray diffraction line intensity ratios for Cu-Fe-Al-O system.

Al-content (x)	Cation distribution		$\frac{I(400)}{I(422)}$		$\frac{I(220)}{I(400)}$	
	A-site	B-site	Obs.	Cal.	Obs.	Cal.
0.0	$\text{Cu}_{0.22}\text{Fe}_{0.78}$	$\text{Cu}_{0.78}\text{Fe}_{1.22}$	1.765	1.959	1.361	1.495
	$\text{Cu}_{0.21}\text{Fe}_{0.79}$	$\text{Cu}_{0.79}\text{Fe}_{1.21}$		1.965		1.238
	$\text{Cu}_{0.20}\text{Fe}_{0.80}$	$\text{Cu}_{0.80}\text{Fe}_{1.20}$		1.865		1.236
0.2	$\text{Cu}_{0.22}\text{Fe}_{0.70}\text{Al}_{0.08}$	$\text{Cu}_{0.78}\text{Fe}_{1.10}\text{Al}_{0.12}$	1.922	2.076	1.417	1.418
	$\text{Cu}_{0.20}\text{Fe}_{0.72}\text{Al}_{0.08}$	$\text{Cu}_{0.80}\text{Fe}_{1.08}\text{Al}_{0.12}$		1.865		1.579
	$\text{Cu}_{0.18}\text{Fe}_{0.74}\text{Al}_{0.08}$	$\text{Cu}_{0.82}\text{Fe}_{1.06}\text{Al}_{0.12}$		1.676		1.757
0.4	$\text{Cu}_{0.18}\text{Fe}_{0.64}\text{Al}_{0.18}$	$\text{Cu}_{0.82}\text{Fe}_{0.96}\text{Al}_{0.22}$	1.772	1.952	1.051	1.461
	$\text{Cu}_{0.17}\text{Fe}_{0.65}\text{Al}_{0.18}$	$\text{Cu}_{0.83}\text{Fe}_{0.95}\text{Al}_{0.22}$		1.847		1.544
	$\text{Cu}_{0.16}\text{Fe}_{0.66}\text{Al}_{0.18}$	$\text{Cu}_{0.84}\text{Fe}_{0.94}\text{Al}_{0.22}$		1.748		1.632
0.6	$\text{Cu}_{0.14}\text{Fe}_{0.58}\text{Al}_{0.28}$	$\text{Cu}_{0.86}\text{Fe}_{0.82}\text{Al}_{0.32}$	1.647	1.787	0.908	1.571
	$\text{Cu}_{0.16}\text{Fe}_{0.58}\text{Al}_{0.26}$	$\text{Cu}_{0.84}\text{Fe}_{0.82}\text{Al}_{0.34}$		1.890		1.488
	$\text{Cu}_{0.17}\text{Fe}_{0.59}\text{Al}_{0.24}$	$\text{Cu}_{0.83}\text{Fe}_{0.81}\text{Al}_{0.36}$		1.888		1.494

There is an excellent contrast in the atomic scattering factor of Al^{3+} to that of Fe^{3+} and Cu^{2+} , but the scattering factor of Cu^{2+} is close to that of Fe^{3+} [25]. Thus, the amount of Fe^{3+} - ions on the A- and B-sites was estimated through Mossbauer spectral intensity calculation by considering the integrated areas under the Lorentzians corresponding to the A- and B-sites, which were taken proportional to the amount of Fe^{3+} - ion on these sites. The details are given elsewhere [28]. Any alternation in the distribution of cations causes a significant change in the theoretical values of x-ray diffraction line intensity ratio. Therefore, in the process of arriving at the final cation distribution, the site occupancy of all the cations was varied for many possible combinations and those that agree well with the experimental intensity ratios, the fitting of the magnetization at 10K [29] and Mossbauer data analysis [28] were taken into consideration. The comparison of x-ray diffraction line intensity ratios for various possible cation distribution for $x = 0.0, 0.2, 0.4$ and 0.6 is shown in Table 2(c). The final cation distributions thus arrived for different compositions are given by:



(b) Thermoelectric power study

In order to understand the mechanisms responsible for electrical conduction, Seebeck coefficient measurements and Hall effect measurements are used. In the case of low mobility materials such as spinel ferrites, garnets and perovskites

it may be difficult to measure the Hall effect. In such circumstances, the thermoelectric power measurement is the only alternative. The Seebeck coefficient measurement is straightforward and its sign gives vital information regarding the type of charge carriers (electrons or holes) responsible for the conduction process. It enables one to calculate the Fermi energy, charge carrier concentration, mobility of charge carrier etc. [30-33].

The values of Seebeck coefficient, α , does not depend significantly upon heating and cooling cycles and we have obtained repeatable values within the accuracy of $\pm 10\%$ in successive observations. The variation of α with hot junction temperature (T) for the studied compositions is depicted in Figure 2.

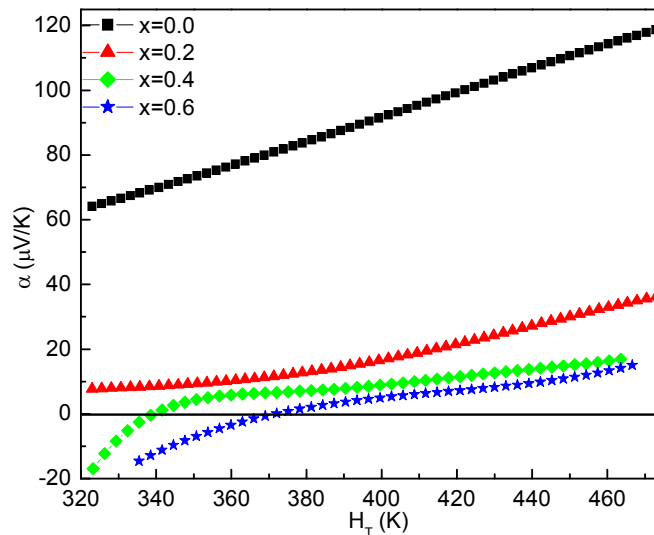


Figure 2. Thermoelectric power versus hot junction temperature for Cu-Fe- Al-O system.

The first observation suggests that for $x = 0.0$ and 0.2 α is positive. That means majority charge carriers are holes or p-type conduction is dominant. For the compositions with $x = 0.4$ and 0.6 , α is negative in low temperature range (300 - 340K for $x = 0.4$ and 300 - 370 K for $x = 0.6$). That means in this

temperature range n-type conduction is dominant or majority charge carriers are electrons. Beyond these temperature ranges both the compositions show p-type conduction.

According to Nazipov et al [4], copper ferrite (CuFe_2O_4) prepared without special measures (synthesis in an oxygen atmosphere at an elevated pressure) contains oxygen vacancies, which lead to partial reduction of Fe^{3+} ion to Fe^{2+} ion and Cu^{2+} ion to Cu^{1+} ion in the system. The presence of Cu^{2+} and Fe^{3+} in other oxidation state (Cu^{1+} and Fe^{2+} respectively) entails important modifications to the electrical properties of ferrites [4, 34, 35]. The hopping of electron between Fe^{2+} and Fe^{3+} as well as between Cu^{1+} and Cu^{2+} at the octahedral sites of the spinel lattice takes place by the mechanism: $\text{Fe}^{2+} \leftrightarrow \text{Fe}^{3+} + e^-$ or $\text{Cu}^{1+} \leftrightarrow \text{Cu}^{2+} + e^-$. On the other hand, hole (e^+) is involved in hopping process between Cu^{1+} and Cu^{2+} at the tetrahedral sites by the hopping mechanism: $\text{Cu}^{2+} \leftrightarrow \text{Cu}^{1+} + e^+$.

It is important to note that p-type conduction can also be explained based on hole exchange between Fe^{4+} and Fe^{3+} according to: $\text{Fe}^{4+} \leftrightarrow \text{Fe}^{3+} + e^+$, but Fe^{4+} ions do not occur in spinel ferrites [4]. Similarly, holes can transfer between Fe^{2+} and Fe^{3+} as: $\text{Fe}^{3+} \leftrightarrow \text{Fe}^{2+} + e^+$. In this case, the amount of Fe^{2+} would then exceed the amount of Fe^{3+} , which is necessary for p-type conductivity; the corresponding oxygen non-stoichiometry is too large for ferrites [4]. On the other hand, Cu^{1+} ions cannot be formed on the B-sites. Based on above discussion, the probable conduction mechanisms in the system are: $\text{Fe}^{2+} \leftrightarrow \text{Fe}^{3+} + e^-$ (n-type) at the B-sites and $\text{Cu}^{2+} \leftrightarrow \text{Cu}^{1+} + e^+$ (p-type) at the A-sites of the spinel lattice.

Based on the assumption that two hopping mechanisms are involved, the pre-dominance of one over the other depends upon the concentration of substituted cation(x) and temperature (T). If the hole exchange mechanism ($\text{Cu}^{2+} \leftrightarrow \text{Cu}^{1+} + e^+$) dominates to the electron exchange mechanism ($\text{Fe}^{2+} \leftrightarrow \text{Fe}^{3+} + e^-$), the spinel ferrite composition might conduct as a p-type semiconductor (or vice versa).

The second observation is that, Seebeck coefficient increases with increasing temperature for $x = 0.0$, while for $x = 0.4$ and 0.6 , initially α increases rapidly within small range of temperature (300 - 370K) while for further increase in temperature α increases slowly. This variation of α with temperature can be explained based on the fact that in the case of n-type semiconducting material ($x=0.4, 0.6, T = 300 - 370\text{K}$) the hot surface becomes positively charged, as it loses some of its electrons. The cold surface of the semiconductor becomes negatively charge due to the diffusion of free electrons from the hot portion. On increasing temperature conduction mechanism $\text{Fe}^{2+} \leftrightarrow \text{Fe}^{3+} + e^-$ becomes more probable which generates electrons. These electrons are accumulating on the cold surface and as a result, potential difference (∇V) developed increases α in the temperature range 300 - 370K. Further increases in temperature shows a small change in α conjuring (i) saturation in the electron generation, (ii) recombination of liberated electrons with holes, produced due to $\text{Cu}^{2+} \leftrightarrow \text{Cu}^{1+} + e^+$ transition in the system. For $x = 0.4$ and 0.6 , the increase of temperature tends to oxidize Fe^{2+} ions. In turn, the negativity of the Seebeck coefficient might decrease, i.e. the positivity increases, as tentatively obtained.

It is observe from Figure 2 that α in the temperature range studied is dependent upon temperature. Based on the classifications suggested by Bashikiriv and Liberman [36], these ferrites are classified as non-degenerate semiconductor as Seebeck coefficient (α) is temperature dependent.

In the case of hopping conduction, the Seebeck coefficient (α) is given by the Heikes formula [37]:

$$\alpha = -\frac{k}{e} \left[\frac{S_T}{k} + \ln \frac{1-c}{c} \right]$$

where, S_T is the effective entropy transport by the charge carriers which is temperature independent. The S_T/k is generally very small in oxides / ferrites and it contributes less than 10 $\mu\text{V}/\text{K}$ [38], thus neglected. Here, c is given by n/N , where, N is the number of available states and n is the number of carriers in the states. Neglecting the term S_T/k from the above relation gives:

$$\alpha = -\frac{k}{e} \left[\ln \frac{1-c}{c} \right]$$

Doumerc et al [39] have derived a more general formula for systems containing mixed valency cations, $M^{n+} / M^{(n+1)+}$, accordingly:

$$\alpha = -\frac{k}{e} \ln \frac{1-c}{c} = \frac{k}{e} \ln \frac{1-c_h}{c_h}$$

where, c_h , the hole concentration (number of holes per active transport site) defined as $c_h = 1-c = p/N$ (p -number of holes).

Assuming that N is equal to the total number of Cu^{1+} and Cu^{2+} or Fe^{2+} and Fe^{3+} ions on the A- and B-sites respectively and n to the number of Cu^{2+} or Fe^{3+} ions on these sites respectively, we obtain:

$$\alpha = -\frac{k}{e} \ln\left(\frac{\text{Cu}_A^{2+}}{\text{Cu}_A^{1+}}\right) = \frac{k}{e} \ln\left(\frac{\text{Cu}_A^{1+}}{\text{Cu}_A^{2+}}\right)$$

$$\left[\frac{\text{Cu}_A^{2+}}{\text{Cu}_A^{1+}}\right] = \exp\left(-\frac{\alpha \cdot e}{k}\right)$$

OR

$$\left[\frac{\text{Fe}_B^{2+}}{\text{Fe}_B^{3+}}\right] = \exp\left(-\frac{\alpha \cdot e}{k}\right)$$

where, k is the Boltzmann constant and e is the electronic charge. Above equations contain no adjustable parameter and can be used to test various distribution models. This has been shown to be a suitable way for some spinels, such as ferrites [40, 41], magnetite [42], hausmannite [43] and manganite perovskites [33]. The subscripts A and B represent the tetrahedral sublattice and octahedral sublattice of the spinel structure.

The cationic concentration of Cu^{1+} , Cu^{2+} , Fe^{2+} and Fe^{3+} ions calculated using the near room temperature (323K) Seebeck coefficient values (α) have been used to determine the actual cation distribution and oxygen deficiency (δ) for each composition and are summarized in Table 3.

Table 3. Cation distribution and oxygen deficiency (δ) for Cu-Fe-Al-O system at 323K.

Al ³⁺ - content (x)	Actual cation distribution	Oxygen deficiency (δ)
0.0	$(\text{Cu}^{1+}_{0.15}\text{Cu}^{2+}_{0.07}\text{Fe}^{3+}_{0.78})^A[\text{Cu}^{2+}_{0.78}\text{Fe}^{3+}_{1.22}]^B\text{O}^{2-}_{3.925}$	0.075
0.2	$(\text{Cu}^{1+}_{0.12}\text{Cu}^{2+}_{0.10}\text{Fe}^{3+}_{0.70}\text{Al}^{3+}_{0.08})^A[\text{Cu}^{2+}_{0.78}\text{Fe}^{3+}_{1.10}\text{Al}^{3+}_{0.12}]^B\text{O}^{2-}_{3.940}$	0.060
0.4	$(\text{Cu}^{2+}_{0.18}\text{Fe}^{3+}_{0.64}\text{Al}^{3+}_{0.18})^A[\text{Cu}^{2+}_{0.82}\text{Fe}^{2+}_{0.43}\text{Fe}^{3+}_{0.53}\text{Al}^{3+}_{0.22}]^B\text{O}^{2-}_{3.785}$	0.215
0.6	$(\text{Cu}^{2+}_{0.14}\text{Fe}^{3+}_{0.58}\text{Al}^{3+}_{0.28})^A[\text{Cu}^{2+}_{0.86}\text{Fe}^{2+}_{0.35}\text{Fe}^{3+}_{0.47}\text{Al}^{3+}_{0.32}]^B\text{O}^{2-}_{3.825}$	0.175

The high temperature (403K) Seebeck coefficient values, which are positive for all the compositions have been used to determine the relative concentration of $\text{Cu}^{2+}/\text{Cu}^{1+}$, the absolute concentration of Cu^{1+} ion, and the product of $(\text{Cu}^{1+})(\text{Cu}^{2+})$ ions residing at the A- sites of the spinel lattice (Table 4). These are used to explain the variation and origin of dc resistivity with Al^{3+} - content (x).

Table 4. Seebeck coefficient (α) and cationic concentration for Cu-Fe-Al-O system at 403K.

Al^{3+} - content (x)	α ($\mu\text{V}/\text{K}$) (403K)	$\frac{(\text{Cu}_A^{2+})}{(\text{Cu}_A^{1+})} 10^{-2}$	$(\text{Cu}_A^{1+})(\text{wt}\%)$	$(\text{Cu}_A^{1+})(\text{Cu}_A^{2+}) 10^{-3}$
0.0	94.22	16.50	2.31	5.7
0.2	17.72	12.12	1.69	4.0
0.4	9.61	9.50	1.09	3.2
0.6	4.55	7.18	0.64	1.3

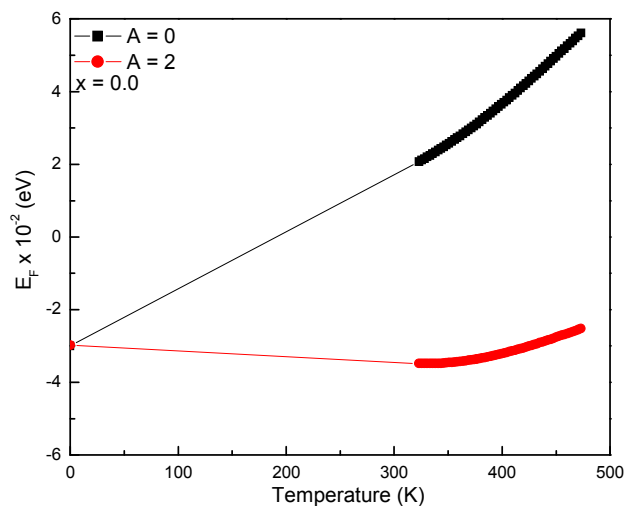
The percentage variation of the Cu^{1+} - concentration and the product of $(\text{Cu}^{1+})(\text{Cu}^{2+})$ ions on the A-sites for the compositional range studied is $\sim 77\%$. This means that, the variation of electrical resistivity cannot exceed by 77%, if the variation originates from the change in these two parameters.

(c) Fermi energy determination

The energy corresponding to the highest filled state in energy band structure of solids at 0K is called the Fermi energy, $E_F(0)$. An attempt has been made to determine $E_F(0)$ by extrapolating values of $E_F(T)$ to 0K. According to Bosman and Crevecoem et al [44], in the region where conduction is due to either holes or electrons (not both), the relation between α and E_F is given by:

$$E_F(T) = e\alpha T - AkT$$

where, e , k and T are charge of carrier, Boltzmann constant (1.38×10^{-23} J/K = 8.62×10^{-5} eV/K) and hot junction temperature in Kelvin, respectively. Here, A is a dimension-less constant connected with the kinetic energy of charge carrier. The plots of thermal variation of E_F for two values of A , ($A = 0$ and 2), for the compositions with $x = 0.0, 0.2, 0.4$ and 0.6 are shown in Figure 3. The extrapolation of the two series of E_F for $A = 0$ and $A=2$ intercept at one point on y-axis at $T = 0\text{K}$. The values of E_F (T) extrapolated to 0K yield the value of $E_F(0)$ (Table 5). The interception point lies below zero (negative value), but we have to consider its magnitude only, as $E_F(0)$ cannot be negative [45].



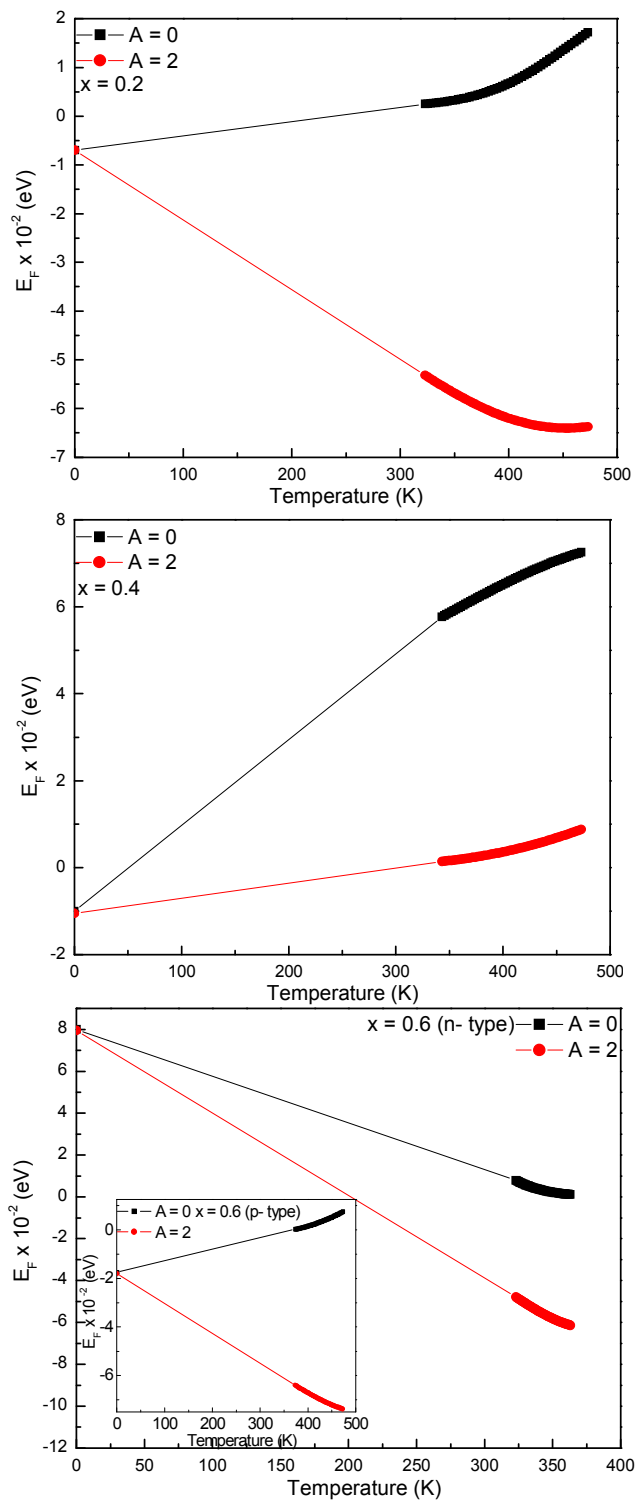


Figure 3. The variation of Fermi energy with temperature for Cu-Fe-Al-O system. The high temperature region where α is positive is shown in the inset.

Table 5 shows the values of $E_F(0)$ for the different compositions. It is seen that $E_F(0)$, in general, increases with Al^{3+} - substitution (x). Such behavior of $E_F(0)$ can be attributed to the contribution of Cu^{1+} in the system. It is important to note that for $x = 0.4$, only high temperature region where α is positive has been taken into consideration. On the other hand, for $x = 0.6$ low temperature region where α is negative and high temperature region where α is positive are treated separately.

The variation of compensation temperature ($T_{\text{comp.}}$) against Al-content (x) is shown in Figure 4. The compensation temperature is the temperature at which the Seebeck coefficient (α) changes its polarity from n- to p-type. The values of $T_{\text{comp.}}$ obtained from Seebeck coefficient (α) versus temperature (T) curves for $x = 0.4$ and 0.6 have been used to estimate the $T_{\text{comp.}}$ for $x = 0.0$ and 0.2 . From the extrapolation of the line, it can be concluded that the un-substituted ferrite (CuFe_2O_4) changes polarity from n- to p-type at temperature as low as 274K. This transition temperature is in good agreement to that reported by Mazen et al. for CuFe_2O_4 [30]. On the other hand, for $x = 0.2$, $T_{\text{comp.}}$ is found to be $\sim 306\text{K}$.

Table 5. Experimental values of $E_F(0)$, $T_{\text{comp.}}$, η_i and H_i for Cu-Fe-Al-O system.

Al-content(x)	$ E_F(0) \cdot 10^{-2}$ eV	$T_{\text{comp.}}$ (K)	$\eta(\text{V}) \pm 0.002\text{V}$	$H(\mu\text{V/K})$
0.0	1.9	274	0.37	-56
0.2	1.0	306	L 0.05	-7
			H 0.25	-83
0.4	4.0	338	L 0.52	-190
			H 0.15	-56
0.6	L 7.0	370	L 1.03	-360
	H 2.7		H 0.11	-38

L: Low temperature region, H: High temperature region

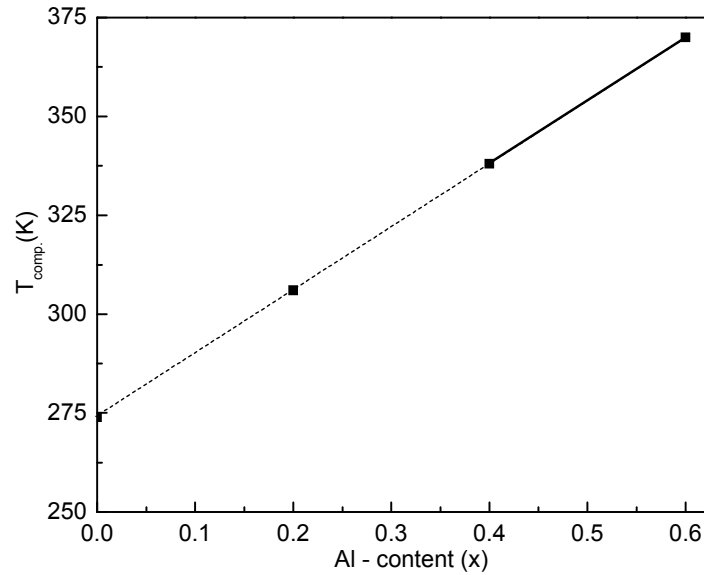


Figure 4. Compositional dependence of $T_{\text{comp.}}$ (transition from n- to p- type) for Cu-Fe-Al-O system.

At the compensation temperature ($T_{\text{comp.}}$), the heat exchange by holes equalizes that transferred by electrons. Accordingly, the emf produced due to electrons equals and opposes that due to holes. Thus, complete compensation occurs at $T_{\text{comp.}}$.

Within the experimental accuracy, the variation of α with temperature (T) can be represented by the following equation:

$$\alpha = \eta_i T^{-1} + H_i$$

where, $i = 1, 2$ represent the first and second temperature range, beginning from lower temperature side, T is the absolute temperature, η_i is the slope and H_i is the intercept of the curve with α -axis (Y-axis). The results are summarized in Table 5. The values of η_i and H_i have been obtained by the least square method.

(d) Charge carrier concentration determination

Thermal variation of charge carrier concentration (n_c) per unit volume can be calculated using the corresponding values of Seebeck coefficient (α) by the Heikes formula [37]:

$$n_c = \frac{N}{V} \left[\frac{1}{1 + \exp(\alpha / k / e)} \right]$$

where, V is the volume of the sample under investigation and N is the density of states or the concentration of electronic levels involved in the conduction process. The value of ' N ' can be taken as $10^{22} / \text{cm}^3$ for low mobility semiconductors like spinel ferrites and garnets having exceedingly narrow bands or localized levels [46].

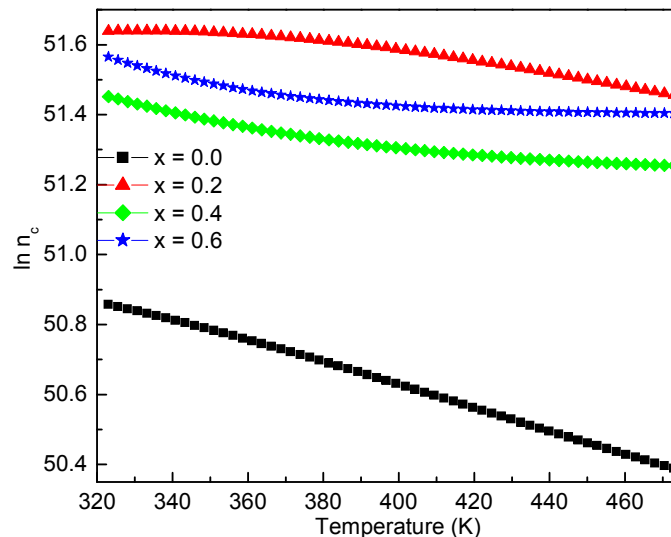


Figure 5. Temperature dependence of charge carrier concentration for Cu-Fe-Al-O system.

Figure 5 shows that the thermal variation of charge carrier concentration behaves inversely as compared with the variation of Seebeck coefficient (Figure 2). In the determination of n_c , the absolute magnitude of α should be

taken into consideration, irrespective of the positive or negative signs which indicate charge carriers are holes or electrons. From figure 5, for $x = 0.0, 0.2, 0.4$ and 0.6 , n_c decreases continuously with temperature. On increasing temperature, holes, which are the majority charge carriers are compensated by thermally generated electrons, thus, n_c decrease slowly with increasing temperature.

(e) Compositional and thermal variation of dc resistivity

Table 1, shows that the highest observed value of bulk density (ρ) remains lower than the corresponding x-ray density (ρ_x) of the material. This suggests that even highly pressed and sintered pellets contain pores. The presences of pores are unavoidable and they enter into the material through fabrication process. A correction for the pore-fraction to obtain the crystalline values of electrical resistivity has been applied using the relation [47]:

$$\rho_{dc} = \rho_p \left[1 + f \left(1 + f^{2/3} \right)^{-1} \right]^{-1}$$

where, ρ_{dc} is the corrected value, ρ_p is measured value of dc resistivity and f is pore fraction (Table 1). The equation seems to hold well for $f < 0.4$. In the present studies 'f' is much less than 0.4.

The variation of dc resistivity (ρ_{dc}) as a function of Al^{3+} - content (x) at 403 K is shown in Table 6. It is found that the ρ_{dc} values increase with increase in Al^{3+} - concentration in the system. This is rather expected because the substitution of non-magnetic Al^{3+} - ions replaces magnetic Cu^{2+} - ions ($1\mu_B$) from the A-sites to the B-sites in the system $\text{CuAl}_x\text{Fe}_{2-x}\text{O}_4$ (Table1). This reduces conduction through the tetrahedral sites. The incorporation of Al^{3+} - ions do not

participate in the conduction process, limits the degree of Cu^{1+} - Cu^{2+} conduction that occurs at the tetrahedral sites of the spinel lattice. Thus, the efficient method of curtailing the conduction process is the replacement of effective magnetic ions by less effective nonmagnetic ions in the system. Similar trend for ρ_{dc} with content (x) for the $\text{MgAl}_x\text{Fe}_{2-x}\text{O}_4$ system was observed [48].

Thermoelectric power measurements have shown that for ferrite compositions under study, at low temperatures, conduction is due to electron exchange between ferrous (Fe^{2+}) and ferric (Fe^{3+}) ions at the B-sites, while at high temperatures conduction is due to the hopping of hole between Cu^{2+} and Cu^{1+} at the A-sites. Thus, observed increase in dc resistivity value (ρ_{dc}) with Al^{3+} - substitution (x) is also due to decrease in total concentration of Fe^{3+} at the octahedral sites (Table 3).

The near room temperature dc electrical resistivity values for different ferrite compositions lie in the range 10^3 - $10^4 \Omega \cdot \text{cm.}$, suggesting that they are good insulators at room temperature (300K).

In Figure 6, the variation of dc resistivity ($\log_{10}\rho_{\text{dc}}$) against reciprocal of temperature ($10^3/T$) for $x = 0.0, 0.2, 0.4,$ and 0.6 is shown. It is observed that the resistivity values for a particular ferrite composition do not differ much from sample to sample as well as no significant difference in resistivity values during heating and cooling cycles occurs. All the samples show typical semiconducting behavior that is, the resistivity decreases with increasing temperature. Observations suggest three distinct regions and two breaks in ρ_{dc} versus temperature plots for all the compositions. The temperature marked as T_1

corresponds to transition from region I to region II, while temperature marked as T_2 , corresponds to transition from region II to region III. The transition temperature T_2 is nearly equal to the Neel temperature deduced from the low field ac susceptibility measurements and those calculated theoretically based on modified molecular field theory for $x = 0.0$ and 0.2 [29]. The observed change in the slope in vicinity to Neel temperature strongly supports the influence of magnetic ordering upon the conduction process [49]. Another transition around $T_1 \sim 410\text{K}$ for all the compositions has been observed. Based on the work of Parfenov and Nazipov on the transport properties of copper ferrites [4] it seems likely that the compositions are stable above 410K . Ghani et al [50] have attributed conduction in the first region to the presence of impurities, in the second region to the phase transition and in the third region to magnetic disorder.

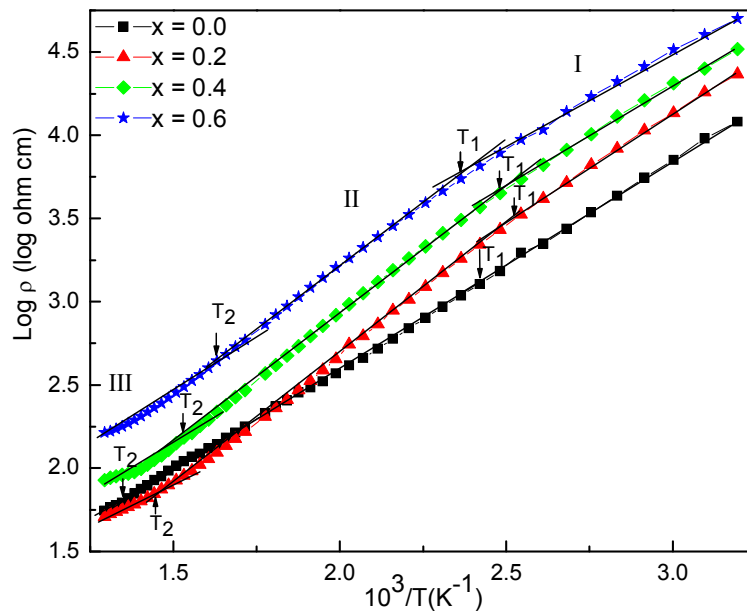


Figure 6. Arrhenius plots of resistivity for Cu-Fe-Al-O system.

Table 6. DC resistivity (ρ_{dc}), transition temperature (T) and activation energy (E) for Cu-Fe-Al-O system.

Al ³⁺ - content (x)	$\rho_{dc} * 10^3$ (Ω cm) (403K)	T_2 (K) T_1 (K) ± 2 K (Resistivity)		Activation Energy (eV)		
				E_I	E_{II} (E_f)	E_{III} (E_p)
0.0	1.53	733	413	0.48	0.22	0.18
0.2	2.71	693	394	0.50	0.24	0.21
0.4	4.49	704	408	0.49	0.30	0.27
0.6	7.81	669	416	0.23	0.33	0.28

As discussed earlier, the $\log_{10}\rho_{dc}$ versus $10^3/T$ plots consist of three straight-line portions; hence, there are three activation energies. The activation energy for the three different regions can be calculated from the well-known Arrhenius equation given by:

$$\rho = \rho_0 \exp\left(\frac{\Delta E}{k \cdot \Delta T}\right)$$

where, k is the Boltzmann constant, ΔE is the activation energy and T is the absolute temperature.

The activation energies thus calculated are shown in Table 6. Based on the theory of magnetic semiconductors, the activation energy in the paramagnetic state (E_p) should be greater than the activation energy in the ferrimagnetic state (E_f), because the ferrimagnetic state is an ordered one while the paramagnetic state is a disordered one. Thus, charge carriers require more energy for the conduction in the paramagnetic state as compared to the ferrimagnetic state.

In the present system, E_p is found to be smaller than E_f for all the compositions (Table 6). In general, on increasing temperature an expansion of the unit cell volume is expected. If, however, the system transfers from the cubic to the tetragonal phase at high temperatures ($T > T_N$), a contraction of the unit cell volume takes place resulting in a lower value of the activation energy in the paramagnetic state.

The activation energies of ferrimagnetic region for all the four compositions are much higher than the ionization energy of donors or acceptors (i.e. 0.1 eV) and thus one can rule out possibility of band type conduction. On the other hand, these values are also higher than the electron transition energy (0.2 eV) but smaller than the small polaron hopping energy (≥ 0.5 eV). Thus, hole hopping between Cu^{1+} and Cu^{2+} in tetrahedral coordination of the spinel lattice is quite probable.

The decrease in the lattice constant value (Table 1) manifests itself as decrease in the interionic distances and consequently decreases in barrier height encounter by the hopping charge carriers. Therefore, one can expect decrease in the activation energy with Al^{3+} - substitution. The activation energy in the ferrimagnetic region (E_f) is found to increase with Al^{3+} - substitution (x) in the system. This can be explained as follows.

In the present case, this effect is dominated by decrease in Fe^{3+} ion concentration from the system as well as from the octahedral (B-) sites on Al^{3+} - substitution. On the other hand, decrease in concentration of Cu^{2+} and Cu^{1+} ions at the tetrahedral (A-) sites results in increase of resistivity and activation energy

values with Al^{3+} -substitution (x). In other words, charge carrier jumps between differently charged ions of the same metal residing on equivalent crystallographic sites get restricted and as a result, activation energy increases with increasing (x).

The activation energy is also influenced by the grain size. Bigger grain size implies increased grain-to-grain contact area for the charge carrier to flow and therefore a lower barrier height. Since, in the present system grain size is found to decrease with Al^{3+} - substitution (x) (Table 1), the activation energy is expected to increase. This explains increase in the activation energy on Al^{3+} - substitution.

The activation energy of ferrimagnetic region (E_f) is found higher than the Fermi energy at 0 K ($E_F(0)$) for $x = 0.0, 0.2, 0.4$ and 0.6 (Tables 5 and 6). The observed difference between the two values ($E_f - E_F(0)$) can be attributed to the activation energy associated with the drift mobility of charge carriers. This suggests that the activation energy consists of two parts, one part is associated with the generation of charge carriers and other part is associated with the hopping of charge carriers (holes).

(f) Thermal variation of charge carrier mobility

It has been reported by Tuller et al [51] that in iron-excess manganese-zinc ferrites, ($\text{Mn}_{1-y}\text{Fe}_{2+y}\text{O}_4$), the electrical conduction arises from the small polaron hopping between Fe^{2+} and Fe^{3+} ions present at the B-sites of the spinel lattice. Based on this model, the electrical resistivity (ρ) for the present system is given

$$\text{by [36, 37]: } \sigma = \frac{1}{\rho} = \text{const} * (\text{Cu}^{1+})(\text{Cu}^{2+}) \exp \frac{(-E/kT)}{T}$$

where, E is the activation energy, k the Boltzmann constant, and T the absolute temperature. Based on above equation, it is clear that for electrical conductivity the product of Cu^{1+} and Cu^{2+} ions concentration is of importance not the total concentration of Cu^{1+} - ions at the A-sites of the spinel lattice. A correlation of the variation of ρ_{dc} with the $(\text{Cu}^{1+})(\text{Cu}^{2+})$ ions concentration for the compositional range studied is seen . The variation in the values of $(\text{Cu}^{1+})(\text{Cu}^{2+})$ ions concentration is about 77% (Table 4) while the variation in ρ_{dc} values is about 80% (Table 6) for $x = 0.0 - 0.6$. Thus, $(\text{Cu}^{1+})(\text{Cu}^{2+})$ ions concentration is the main factor that governs conduction in ferrites while other factors such as oxygen content, grain size, grain boundary resistivity, pore etc. play less significant role.

The drift mobility (μ_{d}) of the charge carriers has been calculated from the experimental values of the dc electrical resistivity (ρ_{dc}) and charge carrier concentration (n_{c}), using the relation [46].

$$\mu_{\text{d}} = 1/\rho_{\text{dc}} \cdot n_{\text{c}} \cdot e$$

where, e is the electronic charge of the carrier

Thermal variation of charge carrier mobility for different compositions is shown in Figure 7 as a plot of $\log \mu_{\text{d}}$ versus temperature (T). It is found that the mobility increases with increasing temperature for all the compositions. Such a trend has also been observed before in many ferrites [30]. On increasing temperature, holes are thermally activated and as a result mobility of holes increases; on the other hand, holes interact with the lattice ions and distort the surroundings in such a way that the potential well generated, is deep enough to introduce localization and so the mobility value is small.

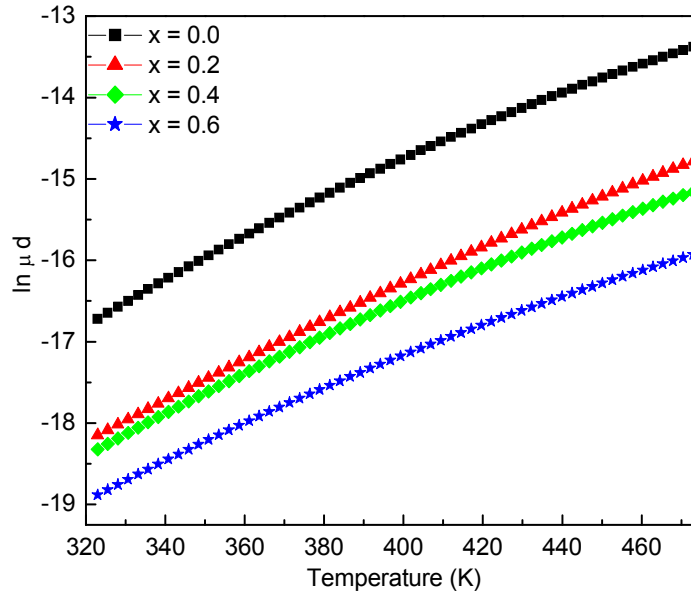


Figure 7. Thermal variation of charge carrier mobility for Cu-Fe-Al-O system.

The magnitude of the mobility is found in the range $10^{-6} - 10^{-9} \text{ cm}^2/\text{V s}$ ($T = 300 - 475\text{K}$) for different compositions. This range is consistent with the mobility value suggested in the literature for holes ($10^{-8} \text{ cm}^2/\text{V s}$) [52]. These values are much smaller than that suggested for electrons ($10^{-4} \text{ cm}^2/\text{V s}$).

An examination of thermal variation of charge carrier concentration (n_c) and mobility of charge carrier (μ_d) revealed that the rate of change of μ_d is greater than that of n_c for a given range of temperature. This suggests that the observed decrease in resistivity with temperature is essentially influenced by the μ_d rather than the n_c . This could be due to the localization of charge carriers at vacant sites or ions. The ions occasionally come close enough due to the lattice vibrations that allow the transfer of charge carrier and conduction may take place. As a result, mobility of charge carriers shows exponential temperature dependence with the activation energy.

(D) Conclusions

Using a combination of thermoelectric power and dc resistivity measurements as a function of composition and temperature, the transports properties of $\text{CuAl}_x\text{Fe}_{2-x}\text{O}_4$ ($x = 0.0 - 0.6$) spinel ferrite system have been studied.

In summary (i) It has been shown that the dominant conduction mechanism is hole exchange between Cu^{1+} and Cu^{2+} ions at the tetrahedral sites in the system.

(ii) The absolute concentration of Cu^{1+} , Cu^{2+} , Fe^{2+} , Fe^{3+} ions and oxygen deficiency can be determined from Seebeck coefficient values. (iii) The

$(\text{Cu}^{1+})(\text{Cu}^{2+})$ ions concentration is the main factor that governs conduction in ferrites while other factors play less significant role. (iv) The thermal variation of dc resistivity is essentially influenced by the mobility of charge carriers rather than the charge carrier concentration.

References

- [1] Goya G F, Rechenberg H R and Jaing J Z 1998 J. Appl. Phys. **84(2)** 1101
- [2] Nedkov I, Vandenberghe R E, Marinova Ts, Thailhades Ph, Merodiiska T and Avramova I 2006 Appl. Surf. Sci. **253** 2589
- [3] Krupicka S and Novak P 1982 "Oxide Spinel" in Ferroelectric Materials, edited by Wohlforth EP, North-Holland, Amsterdam, Vol.3
- [4] Parfnov V V and Nazipov R A 2002 Inorg. Mater. **38(1)** 78
- [5] Yang A, Chen Z, Islam S M, Vittoria C and Harris V G 2008 J. Appl. Phys. **103** 07E509
- [6] Romeijn F C, Philips 1953 Res. Rep. **8** 304
- [7] Trivedi B S 1995 Ph.D. Thesis, Saurashtra University, Rajkot, India
- [8] Kulkarni R G, Trivedi B S, Joshi H H and Baldha G J, 1996 J. Magn. Mater. **159** 375
- [9] Trivedi B S, Jani N N, Joshi H H and Kulkarni R G 2000 J. Mater. Sci. **35(21)** 5523
- [10] Ata-Allah S S and Kaiser M, 2009 J. Alloys Compd. **471** 303
- [11] Ata-Allah S S, Fayek M F, Refai H S and Mostafa M F 2000 J. Solid State Chem. **149** 434
- [12] Ata-Allah S S 2004 Mater. Chem. Phys. **87** 378
- [13] Trivedi U N, Modi K B, Kundaliya D C, Joshi A G, Joshi H H and Malik S K 2004 J. Magn. Mater. **369 (1-2)** 58
- [14] Dubrovina I N, Balakirev V F and Antonov A V 2001 Inorg. Mater. **37(1)** 76
- [15] Evans B J and Hafner S S 1968 J. Phys. Chem. Solidi. **29** 1573
- [16] Kulkarni R G and Panikar V G 1984 J. Mater. Sci. **19** 890

- [17] Ajmal M and Maqsood A 2008 J. Alloys Compd. **460** 54
- [18] Ravinder D, Kumar K V and Boyanov B S 1999 Mater. Lett. **38** 22 and references there in
- [19] Rietveld H M 1969 J. Appl. Cryst. **2** 65
- [20] Games J A, Sousa M H, Tourinho F A, Mestnik-Filho J, Itri R and Depeyrot J 2005 J. Magn. Magn. Mater. **289** 184
- [21] Toby B H 2006 Powder Diff. **21** 67
- [22] Buerger M J 1960 Crystal Structure Analysis, Wiley, NY
- [23] Lakhani V K, Pathak T K, Vasoya N H and Modi K B 2011 Solid State Sci. **13** 539
- [24] Modi K B, Pathak T K, Vasoya N H, Lakhani V K, Baldha G J and Jha P K 2011 Ind. J. Phys. **85(3)** 411
- [25] Cullity B D 1978 Elements of x-ray diffraction, Addison-Wesley
- [26] Ohinishi H and Teranishi T 1961 J. Phys. Soc. Jpn. **16** 35
- [27] Yanbo Zuo, Jianheng Li, Jianxin Yi, Zhongbing Wang and Chusheng Chen 2008 J. Solid State Chem., **181 (4)** 700
- [28] Lakhani V K and Modi K B, (unpublished work).
- [29] Lakhani V K, Zhao Bangchuan, Wang Lan, Trivedi U N and Modi K B 2011 J. Alloys Compd. **509** 4861
- [30] Mazen S A and Zaki H M 2002 J. Magn. Magn. Mater. **248** 200 and references there in
- [31] Mazen S A and Elfalaky 1999 J. Magn. Magn. Mater. **195** 148
- [32] Lakhani V K, Sharma P U, Saija K G, Zankat K B and Modi K B 2006 Ind. J. Phys. **80(8)** 789
- [33] Buch J J U, Pathak T K, Lakhani V K, Vasoya N H and Modi K B 2007 J. Phys. D: Appl. Phys. **40** 5306

- [34] Mazen S A 2003 Mater. Chem. Phys. **62 (2)** 131
- [35] Mazen S A, Elfalaky A and Hashem H A 1995 Appl. Phys. A. **61 (5)** 557
- [36] Bashikirov S S, Liberman A B and Parfenov V V 1979 Inorg. Mater. **15** 404.
- [37] Heikes R R in Thermoelectricity eds.1961Heikes R R and Ure R W 45 (NY: Wiley Interscience)
- [38] Goodenough J B 1971 Prog. Solid State Chem. **5** 145
- [39] Doumerc J P 1994 J. Solid State Chem. **109(2)** 419
- [40] Topfer J, Feltz A, Dordor P and Doumerc J P 1994 Mater. Res. Bull. **29** 225
- [41] Vasoya N H, Lakhani V K, Sharma P U, Modi K B, Ravi Kumar and Joshi H H 2006 J. Phys: Condens. Mater. **18** 8063
- [42] Wu C C and Mason T O 1981 J. Am. Ceram. Soc. **64** 520
- [43] Dorris S E and Mason T O 1988 J. Am. Ceram. Soc. **71** 379
- [44] Bosman A J and Crevecoeur C 1966 Phys. Rev. **144** 763
- [45] Morin F J 1954 Phys. Rev. **93** 1199
- [46] Morin F J and Geballe T H 1955 Phys. Rev. **99(2)** 467
- [47] Russel H W 1935 J. Am. Ceram. Soc. **18** 1
- [48] Modi K B, Joshi H H and Kulkarni R G 1996 J. Mater. Sci. **31(5)** 1311
- [49] Mazen S A and Subrah B A 1986 Thermochim. Acta **105** 1
- [50] Ghani A A, Eatah A and Mohanad A A 1980 Int. Conf. on Ferrites – 3 (Tokyo -Japan) 216
- [51] Tuller H L and Nowick A S 1977 J. Phys. Chem. Solids **38** 859

- [52] Ahmed M A, Tawfik A, El-Nimr M K and El-Haseb A A 1991 J. Mater. Sci. Lett. **10(9)** 549

4.3 Al^{3+} - modified elastic properties of copper ferrite

(A) Introduction

It has been reported that copper ferrite (CuFe_2O_4) is an unique spinel because (i) due to a relatively small energy difference between Cu^{2+} - ions in the tetrahedral (A-) and octahedral (B-) sites, cation redistribution is possible and strongly dependent upon the annealing temperature, cooling rate, microstructure etc [1] (ii) the presence of Cu^{2+} - ions can provoke a collective Jahn-Teller distortion which is associated with the alignment of the Cu^{2+} - ions occupying the tetragonally distorted octahedral spinel lattice formed by the oxygen ions [2] (iii) it has two crystallographical spinel structure, the high temperature cubic phase and the low temperature tetragonal phase [1].

Various test techniques (destructive, semi-destructive and non-destructive) are available for complete characterization of the material. Among the various non-destructive techniques, Ultrasonic non-destructive testing and evaluation plays a key role in materials characterization [3]. Ultrasonic waves are important in research and applications. By employing coherent ultrasonic phonons of carefully controlled frequency and polarization several basic properties of solids have been investigated.

The study of propagation of ultrasonic waves in materials determines the elastic constant, which provides better understanding of the behaviour of the engineering materials. Elastic constants relate closely to many physical properties of solids, such as acoustic-phonon frequencies, internal stress, Debye

temperature etc. Furthermore, they provide a sensitive probe of phase transitions and an indication of the nature of interatomic binding forces in the material [4].

During the last decade (2000 – 2010) there has been an upsurge in the study of various physical properties including elastic properties of the single [5-13] and double layered [14-16] perovskite structured manganites in polycrystalline form. The reports mainly focus on study of elastic anomalies associated with magnetic phase transition near the temperature of the charge-ordering transition and antiferromagnetic transition or structural phase transition as a function of temperature. The results have been explained in the light of spin-phonon interaction, different types of antiferromagnetic phase transition or mean field theory and the Jahn-Teller phenomenon.

There have been few research reports on other class of perovskite like ferrites: SrFeO_3 and LaFeO_3 [17], SrZrO_3 [18], single crystal of $\text{Na}_{0.5}\text{Bi}_{0.5}\text{TiO}_3$ [19], ferrite - perovskite composites of (x) $\text{Ni}_{0.4}\text{Zn}_{0.6}\text{Fe}_2\text{O}_4$ - (1-x) $\text{Pb}_{0.95}\text{Sr}_{0.05}\text{Zr}_{0.53}\text{Ti}_{0.47}\text{O}_3$ [20], perovskite $\text{La}_{0.67}\text{Ca}_{0.33}\text{MnO}_3:\text{ZrO}_2$ composites [21] and brownmillerite ($\text{Ca}_2\text{Fe}_2\text{O}_5$) -a stoichiometric defect perovskites structure [22].

On the other hand limited number of research articles describing elastic properties of superconducting systems such as $\text{RuSr}_2\text{GdCu}_2\text{O}_8$, $\text{YBa}_2\text{Cu}_3\text{O}_{7-x}$, $(\text{Er}_{1-x}\text{Pr}_x)\text{Ba}_2\text{Cu}_3\text{O}_{6.9}$, $\text{EuBa}_2\text{CuO}_{7-\delta}$, $\text{TlSr}_2(\text{Sr}_{0.5}\text{Y}_{0.5})\text{Cu}_2\text{O}_7$, $\text{DyBa}_{2-x}\text{Sr}_x\text{Cu}_3\text{O}_{7-x}$ are available in the literature [23- 27].

Recent research reports on elastic properties of mixed spinel ferrite systems [28-33] just discuss the variation of elastic moduli as a function of

substitution at 300K. The variation has been explain on the basis of increase or decrease of strength of interatomic bonding without any emphasis on other structural and microstructural parameters like porosity, grain size, interionic distances, type of bonding, microcracks, oxygen vacancies etc.

Earlier, an excellent work has been carried out by Wang et al. [34] on elastic properties of $\text{YBa}_2\text{Cu}_3\text{O}_{7-x}$ ceramics with different oxygen contents. Zero porosity corrections of elastic moduli have been carried out by several methods for the effects of porosity and micro cracking on the elastic properties. The correction methods were mainly based on the shape, size and distribution of the voids (pores) and cracks. They have clearly demonstrated that on increasing oxygen content ultrasonic wave velocities and elastic moduli increase to greater extent. The relationship between the porosity and elastic moduli of the Bi-Pb-2212 high Tc-superconductors has been studied by Reddy et al. [35]. They have employed eight theoretical models for calculating elastic moduli in void free state. They have found ~37% variation in the magnitude of nonporous value of Young's modulus determined from different semi-empirical relations. The origin, formation, types of micro cracks and the factors that affect the micro cracks characteristics have been studied by many workers for single phase polycrystalline ceramics, granite and concrete. The various methods for micro cracks evaluation and detection have been suggested [36-38].

To our knowledge very few research reports are available on elastic properties of trivalent cation substituted ferrite systems [39-41]. In the case of Al^{3+} substituted Mg-Cu mixed ferrites [39], it is found that the magnitude of elastic

moduli decreases with increase in Al^{3+} - content(x) for Fe^{3+} in the system. While in the case of substitution of Al^{3+} or Cr^{3+} for Fe^{3+} in $\text{Ni}_{1.05}\text{Sn}_{0.05}\text{Fe}_{1.9-x}(\text{Cr or Al})_x\text{O}_4$ system [41] enhances the magnitude of Young's modulus, rigidity modulus, bulk modulus and Debye temperature. These lead to conclude that the Al^{3+} -substitution plays crucial role in influencing the elastic properties. Till today, there arose considerable interest in the synthesis and characterization of pure and substituted copper ferrite systems. The structural, magnetic, electrical and dielectric properties of typical compositions of the ferrite system $\text{CuAl}_x\text{Fe}_{2-x}\text{O}_4$ have been carried out by different workers[42-47], but no efforts have been made to investigate the elastic behaviour of Al^{3+} - substituted CuFe_2O_4 in particular, the present work is important from fundamental research point of view. The Al^{3+} - ion possesses noble gas outer electron shell structure; it is less compressible than ions with a full or half filled d-shell (Zn^{2+} , In^{3+} , Sn^{4+} etc.) [48], thus it cannot easily accommodate in A-sites but statistically distributed among the available A- and B-sites.

(B) Experimental details

Copper oxide (CuO), ferric oxide (Fe_2O_3) and aluminium oxide (Al_2O_3), all 99.9% pure were procured from Sigma Aldrich India, Mumbai. Polyvinyl alcohol (PVA) and acetone, analytical reagent (AR) grade, were purchased from Rankem (RFCL Ltd., New Delhi) used as the binder to make the pellets and cleaning purpose, respectively.

According to the $\text{CuO-Fe}_2\text{O}_3$ phase –diagram, CuFe_2O_4 is formed between 1000°C and 1100°C . The samples sintered below 1000°C or above 1100°C were

mixed-phase [49]. Aluminum (Al^{3+}) – modified copper ferrite ceramics with a general formula of $\text{CuAl}_x\text{Fe}_{2-x}\text{O}_4$ ($x = 0.0, 0.2, 0.4$ and 0.6) were synthesized from high purity ingredients, namely CuO , Al_2O_3 and Fe_2O_3 . The oxides were mixed thoroughly in stoichiometric proportions to yield the desired composition and then wet – ground by blending with an acetone in an agate mortar and pestle for 4hrs. The mixture was dried and pressed into pellets under a pressure of $2 \times 10^7 \text{ kg/m}^2$ using Hydraulic press (BIMPEX machines international, Mumbai, India). These pellets, were pre-sintered at 1100°C for 24 hours and slowly cooled to room temperature. The samples were again powdered, pressed in to pellets sintered in a muffle furnace (Therelek, India) at 1100°C for 24 hours and then slowly furnace cooled to room temperature at the rate of $2^\circ\text{C}/\text{min}$. The pre-sintering and sintering processes were carried out under an air atmosphere.

Room temperature (300K) X-ray powder diffraction patterns were recorded with a Philips, Holland, Xpert MPD automated x-ray powder diffractometer using $\text{CuK}\alpha$ radiation ($\lambda=0.15405 \text{ nm}$), graphite monochromater, and Xe-filled proportional counter. Data were collected in a 2θ range of $5-85^\circ$ at a scan speed of $2^\circ/\text{min}$. The elemental analysis of the powder samples was checked by energy dispersive analysis of x-rays (EDAX). The grain size determination and grain morphology of powdered samples were studied by scanning electron microscopy (SEM) (model: Philips, Holland, ESEM EDAX XL-30).

The important aspect of ultrasonic velocity and attenuation measurement in a material is the specimen preparation. Longitudinal and transverse wave

velocity measurements were undertaken by the ultrasonic pulse echo-overlap technique (UPT). The radio frequency (rf) pulses generated by the pulse oscillator were applied to transmitting transducer, which converts them into acoustic pulses; these in turn, after propagating through the test samples, were converted into electrical signals by the receiving transducer. The amplified output signal was then displayed on a storage oscilloscope. The cuboids-shaped ferrite samples with 10 mm diameter and 3-4 mm thickness were polished to have flat and parallel faces. Ultrasonic pulses were generated and detected by an X-cut (longitudinal waves) and Y-cut (transverse waves) transducer with the carrier frequency of 9 MHz. The sample was bound to the quartz transducer using Nonaq stopcock grease so that intimate contact (no air gap) was established. A transducer correction was applied to the ultrasonic wave velocities. In all the cases, measurements were made on both sides of the specimen. The transit time of ultrasound was measured up to an accuracy of 1 μs using a digital storage oscilloscope (Matec 7700 system). The overall accuracy of these measurements is about 0.25% in velocity and about 0.5% in elastic moduli.

(C) Results and discussion

(a) EDAX and XRD studies on the $\text{CuAl}_x\text{Fe}_{2-x}\text{O}_4$ system

High temperature prolong sintering may result in the loss of ingredients, which leads to non-stoichiometry in composition. This in turn shows unexpected behavior; which cannot be explained on the basis of normal stoichiometry. Thus, it was essential to check the chemical stoichiometry of each composition. A

representative Energy dispersive analysis of x-rays, (EDAX) pattern for typical composition $x = 0.4$ is shown in Figure 1.

The results of EDAX confirm the expected stoichiometry, with small oxygen deficiency. No trace of any impurity was found indicating the purity of the samples. It is also clear that there is no loss of any ingredient after high temperature sintering. EDAX results suggest that the precursors have fully undergone the chemical reaction to form the expected ferrite composition. The reason for making EDAX characterization was to ratify the purity and surety of the chemical composition.

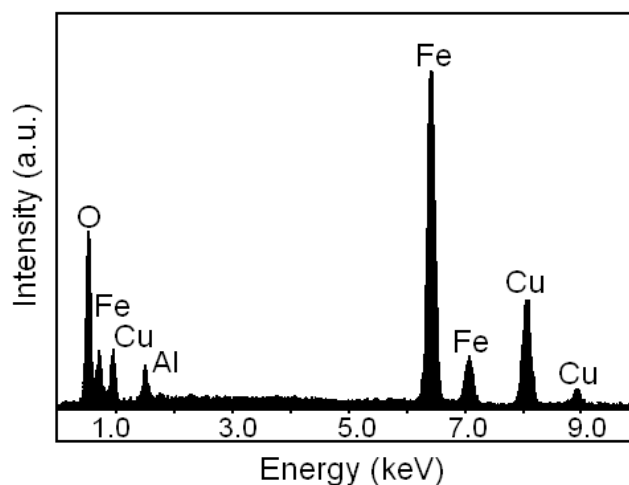


Figure 1. EDAX pattern of $\text{CuAl}_{0.4}\text{Fe}_{1.6}\text{O}_4$ ($x = 0.4$) composition.

The room temperature (300K) x-ray diffraction (XRD) patterns of the samples were obtained by x-ray powder diffractometry. Indexing and Rietveld refinement using general scattering analysis software (GSAS) of XRD patterns of all the compositions revealed that these are single-phase compounds, crystallizing in a fcc structure (space group $\text{Fd}\bar{3}\text{m}$). No peaks from impurity

phases could be detected within the limits of x-ray detection, which is typically 5%.

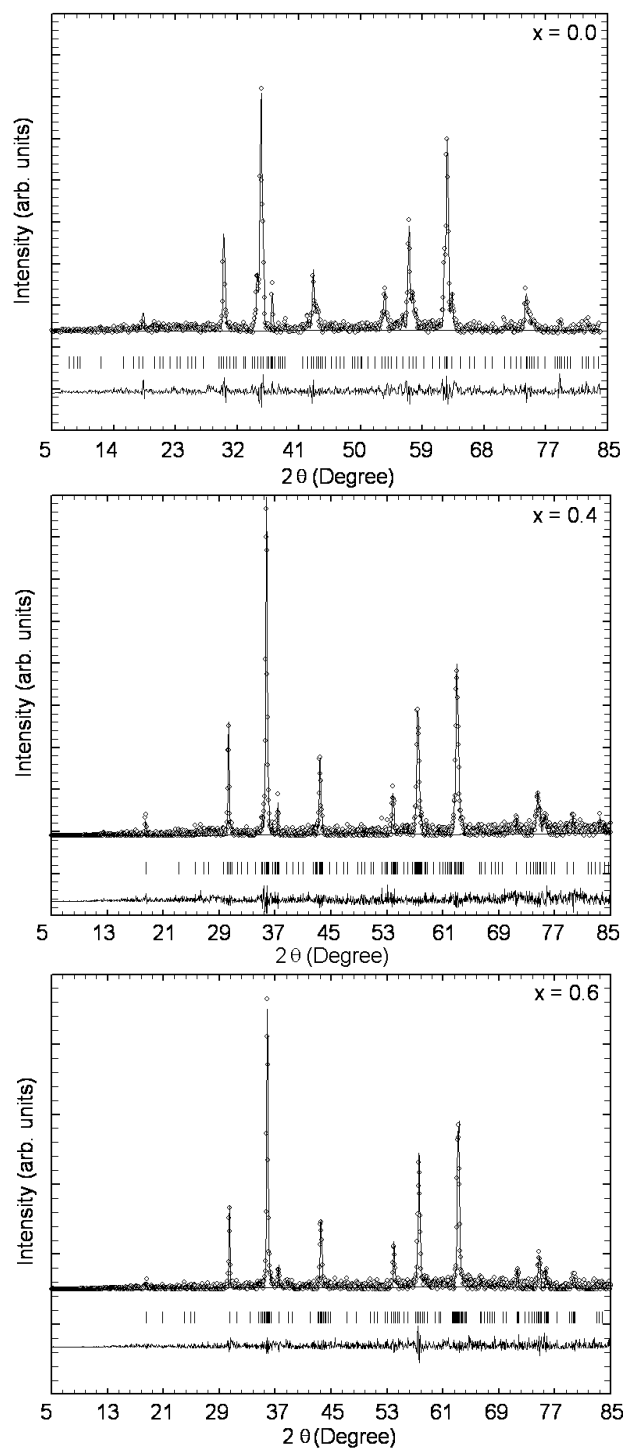


Figure 2. Rietveld – fitted XRD patterns for Cu-Fe-Al-O system.

Figure 2 displays Rietveld fitted XRD patterns for $x = 0.0, 0.4$ and 0.6 compositions. In Rietveld analysis, we fit a model to the data. If the model is correct then it will predict what the true intensity values should be. One of the most important Rietveld error indices or discrepancy values is that of “Chi-squared” or χ^2 [50]. It is found that χ^2 for different compositions lie in the range $1.2 - 1.4$. It should be noted that χ^2 should never drop below one. If a refinement results in $\chi^2 < 1$, which means that one of the two things is true: (i) the standard uncertainties for the data must be overestimated or (ii) so many parameters have been introduced that the model is adjusting to fit noise which should be unlikely in powder diffraction.

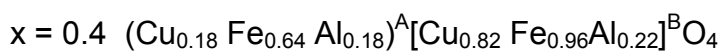
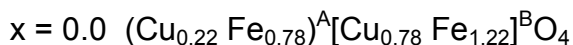
On the other hand if at the end of a refinement $\chi^2 \gg 1$, then either: (i) the model is reasonable but the standard uncertainty values are underestimated, (ii) the model is incomplete because there are systematic effects (errors) in the data that are not expressed in the model, or (iii) the model is wrong. The χ^2 values obtained in the present analysis suggest good refinement of the data.

Precise knowledge of the cation distribution over crystallographic sites in magnetic oxides like spinel ferrites and garnets is crucial for understanding their physical properties. In order to determine the cation distribution, x-ray diffraction line intensity calculations were made using the formula suggested by Buerger [51]:

$$I_{hkl} = |F_{hkl}|^2 \cdot P_m \cdot L_p$$

where I_{hkl} is the relative integrated intensity, F_{hkl} is the structure factor, P_m is the multiplicity factor and L_p is the Lorentz polarization factor.

In the process of arriving at the final cation distribution, the site occupancy of all the cations was varied for many combinations and those that agree well with the experimental intensity of the diffracted beam were taken into consideration. The final cation distribution thus arrived for $\text{CuAl}_x\text{Fe}_{2-x}\text{O}_4$ system can be given by:



The details are given elsewhere [52].

The lattice constant values obtained from the above mentioned refinement, are given in Table 1, from which it is seen that the lattice constant decreases with increasing Al^{3+} - content (x) in the system. Usually in a solid solution of ferrites within the miscibility range, a linear change in lattice constant with concentration of the components is observed [53]. The linear decrease in lattice constant is due to the replacement of larger Fe^{3+} - ions (0.645 Å) by smaller Al^{3+} ions (0.535 Å) in the system.

The x-ray density (ρ_x) of the samples was determined using relation given by Smith and Wijn [54]:

$$\rho_x = \frac{8M}{N_A a^3}$$

where M is the molecular weight of the composition, N_A the Avogadro's number and 'a' is the lattice constant. As there are 8 formula unit in the unit cell so 8 is included in the formula. The ρ_x is inversely proportional to the lattice constant,

which decreases with increasing Al^{3+} - concentration; ρ_x is expected to increase with increasing (x). The x-ray density (ρ_x) decreases with Al^{3+} - ion concentration, because the decrease in molecular weight overtakes the decrease in volume of the unit cell. Bulk density (ρ) of the samples was determined by employing the Archimedes principle using xylene ($\rho = 0.87 \text{ g.cm}^{-3}$) as the buoyant to obtain fairly good results. It is observed that ρ_x of each sample is greater than the corresponding sintered density (ρ). This may be due to the existence of pores in the samples. Pore fraction (f) was calculated using the relation $f = (1 - \rho / \rho_x)$ and percentage porosity was calculated using the relation $P = f \times 100\%$. The variation of porosity (P) with Al^{3+} content (x) is a result of the interplay between ρ and ρ_x .

Table 1. Lattice constant (a), molecular weight (M), x-ray density (ρ_x), bulk density (ρ), pore fraction (f) and porosity (P) for Cu-Fe-Al-O system.

Al-content (x)	a(Å) $\pm 0.002\text{Å}$	M(kg) $\times 10^{-3}$	ρ_x $\text{kg/m}^3 \times 10^3$	ρ $\text{kg/m}^3 \times 10^3$	f	P (%)
0.0	8.389	239.23	5.385	4.736	0.1205	12.05
0.2	8.365	233.46	5.300	4.572	0.1374	13.74
0.4	8.342	227.69	5.212	4.370	0.1616	16.16
0.6	8.319	221.92	5.122	4.619	0.0982	9.82

(b) Scanning electron microscopy (SEM)

The scanning electron micrographs for x = 0.0, 0.2, 0.4 and 0.6 compositions are shown in Figure 3. It is seen that grain morphology; grain size, uniformity, homogeneity are highly influenced by Al^{3+} -substitution. We have observed well define grain structure for un-substituted copper ferrite (x = 0.0), on Al^{3+} -substitution grain size is found to decrease. With small amount of Al^{3+} -substitution (x = 0.2) grain morphology is found to change completely. The sample with x = 0.4 possesses the most compact and uniform microstructure in

all samples. The sample with $x = 0.6$ shows small grains stuck to each other in a regular and uniform manner to form a network like structure or diffused grain structure.

In general with Al^{3+} -substitution, average grain size reduces from about 12 μm for $x = 0.0$ composition to about 4 μm for $x = 0.6$ composition, as well as uniformity and homogeneity of grains also found to increase. The decrease in grain size with Al^{3+} - substitution is attributed to the fact that as a consequence of deviation from the stoichiometric state, a small amount of aluminum oxide can be segregated at grain boundaries [55]. The boundary movement can be inhibited by aluminum oxide as the second phase particle in the final sintering stage; consequently, grain size decreases. The reduction in grain growth and lower density of Al in comparison with Fe and Cu are the main reasons for the reduction in the ferrite density [55].

The decrease in grain size may be due to the surface tension in the samples. It has been reported by Hoque et al. [56] that grains having fewer than six sides will have boundaries which are concave when observed out word from the centre of the grain. To decrease their total area, boundaries will move toward their centers of curvature. Thus grains having less than six sides will grow smaller. In the present case for un-substituted ferrite (i.e. CuFe_2O_4), grains with less than six sides are clearly observed. The Al^{3+} - substitution may be the driving force that leads to the above discussed grain reduction mechanism. The observed grain size reduction with Al^{3+} - substitution is consistent with Al-substituted NiFe_2O_4 system [55].

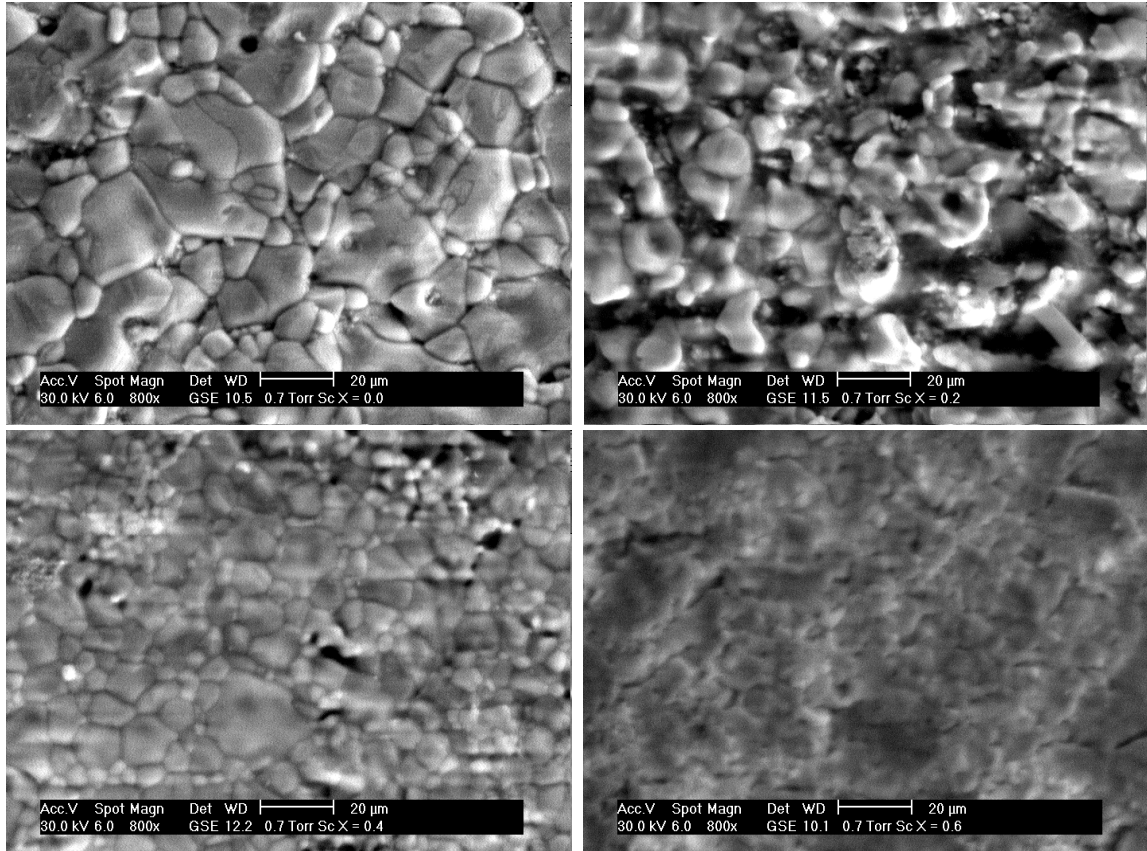


Figure 3. Scanning electron micrographs of various compositions of Cu-Fe-Al-O system.

(c) Ultrasonic study of Al^{3+} - substituted CuFe_2O_4

An ultrasonic wave is a strain wave, which produces longitudinal and transverse elastic waves while propagating through a solid. The velocity of such waves is a characteristic feature of a solid. The fundamental idea is that if there is distortion of the solid from equilibrium shape, the average separation of atoms within the solid is no longer optimal; some atoms will be too close to their neighbor and some too far apart. In either case there will be a restoring force, which will act to return the atoms to their equilibrium separations. The dynamics of the elastic wave will be affected by the way in which the solid responds to the restoring forces the natural 'Springiness' of the substance and the density of the substance

are critical parameters that determine this response. On the other hand, the restoring force on the small region of the solid depends on the type of distortion (strain) that has taken place during the synthesis process. Parameters that describe the restoring force per unit strain are known as elastic moduli of the substance. In the present work, we have employed the ultrasonic pulse echo-overlap technique (UPT) as a tool to obtain an idea about such a stress/strain ratio. When we think about the application of any polycrystalline material, in addition to knowledge of its magnetic and electrical/dielectric responses, elastic moduli help in deciding the suitability of the material for a specific application.

The experimental values of longitudinal wave velocity (V_l) and transverse wave velocity (V_s) determined by the ultrasonic pulse echo-overlap technique and the bulk density (ρ) for different compositions are used to calculate longitudinal modulus (L), rigidity modulus (G), bulk modulus (B), Poisson's ratio (σ), Young's modulus (E), mean sound velocity (V_m), Debye temperature (θ) and Lamé's constant (λ_L) using the following formulae [3]:

$$\text{Longitudinal modulus (L)} = \rho(V_l)^2$$

$$\text{Rigidity modulus (G)} = \rho (V_s)^2$$

$$\text{Bulk modulus (B)} = L - \left(\frac{4}{3}\right)G$$

$$\text{Poisson's ratio } (\sigma) = \left(\frac{3B - 2G}{6B + 2G}\right)$$

$$\text{Young's modulus (E)} = (1 + \sigma)2G$$

$$\text{Mean sound velocity } (V_m) = \left[\frac{3(V_l^3 \cdot V_s^3)}{(V_s^3 + 2V_l^3)} \right]^{1/3} \text{ and}$$

$$\text{Debye temperature}(\theta) = \frac{h}{k} \left[\frac{3N_A}{4\pi\pi_A} \right]^{1/3} \cdot V_m$$

$$\text{Lame's constant } (\lambda_L) = (V_l^2 - 2V_s^2)\rho$$

Where, h and k are Planck's and Boltzmann constants respectively, N_A is Avogadro's number and V_A is mean atomic volume given by $(M/\rho)/q$, where M is the molecular weight and q is the number of atoms in the formula unit (in the present case $q=7$).

The polycrystalline ceramics under study can be treated as an isotropic elastic medium, because the grain size estimated from the SEM study for different composition is much smaller from the ultrasonic wavelength. For example, a 9 MHz longitudinal ultrasonic wave travelling with a velocity of about 4500 ms^{-1} has a wave length of $500 \mu\text{m}$, which is much greater than the grain size of the samples. Here, it is should be noted that the adiabatic (ultrasonic) and isothermal moduli differ much less for solids than for gases; thus generally it is not stated which value is presented. If the data are derived at high pressure, than generally it is possible to determine only the isothermal modules. If the data are determined by using the speed of sound (as in the present case), the approximate modulus to use is the adiabatic modulus [57].

The velocity of transverse waves is approximately half that of longitudinal waves (Table 2). This is due to the reduction in the energy of transverse waves, i.e. when a wave travels through a material, due to transfer of energy, it makes the particle vibrate and hence the vibrating particle incident on the neighboring particles causes it to vibrate and so on. In case of transverse waves, the particle in a medium vibrates perpendicular to the direction of propagation of wave

motion, and hence it requires a larger energy to make the neighboring particle vibrate. This results in reduction in the energy of ultrasonic waves, and hence the velocity of the transverse waves is about half that of longitudinal waves.

The value of Poisson's ratio (σ) is found in the range of 0.23-0.25 for different compositions. These values lie in the range from -1 to 0.5, which are in conformity with the theory of isotropic elasticity. The acoustic Debye temperature (θ), at which nearly all modes of vibrations in solid are excited, plays an important role in the study of a large number of solid state problems involving lattice vibrations. The observed decrease in θ with Al^{3+} - content (x) suggests that lattice vibrations are enhanced due to Al^{3+} - substitution. The parameter λ_L has no physical interpretation, but it serves to sampling the stiffness matrix in Hooke's law. The two parameters (λ_L and G) together constitute a parameterization of the elastic moduli for homogeneous isotropic media and are thus related to the other elastic moduli.

Table 2. Elastic wave velocity (V), elastic moduli, Poisson's ratio, Debye temperature (θ) and Lamé's constant (λ_L) for the Cu-Fe-Al-O system.

Al^{3+} - content (x)	$\frac{V_l}{V_s} \quad V_m$ (m/s)			$\underline{L} \quad G \quad B \quad E$ (GPa)				σ	θ (K)	λ_L ($\text{kg}/\text{m}\cdot\text{s}^2$)* 10^9
	V_l	V_s	V_m	\underline{L}	G	B	E			
0.0	5650	3362	3722	151.80	53.53	79.81	131.26	0.226	484.5	44.09
0.2	4830	2810	3117	106.66	36.10	58.53	89.82	0.244	404.4	34.47
0.4	3710	2152	2388	60.15	20.24	33.16	50.54	0.246	307.6	19.66
0.6	2890	1676	1860	38.58	12.97	21.29	32.35	0.247	248.2	12.61

At this juncture, it would be interesting to correlate the variation of elastic moduli values with porosity rather than with composition. The presence of pores is unavoidable and they enter into the material through fabrication routes. Pores are of different sizes and shapes. Their magnitudes and distributions are

different. These parameters decide the overall strength of a material. In most of the solids, the velocity decreases linearly with increase in porosity and increase in porosity decreases the density [3], which in turn reduces the magnitude of the elastic moduli and vice-versa. It is found that the variation of elastic moduli with porosity does follow this general trend as discussed (Table 2). The magnitude of elastic moduli decreases with increasing porosity; this is rather expected.

(d) Zero porosity correction to elastic moduli

Though, from applications point of view elastic moduli; Young's modulus, rigidity moduli and Poisson's ratio of the bulk porous materials are important but from the point of view fundamental research, the measured elastic moduli do not have much significance unless they are corrected to a void-free state. As the ferrites under study are porous (Table 1), the values of elastic moduli have been corrected to zero porosity. The basic purposes behind zero porosity correction to elastic moduli are that (i) it gives an idea about the maximum strength of the material that can be achieved by controlling porosity (ii) in compositional dependent study, based on the magnitude of void-free moduli, one can have an insight about relative change in the strength of the material as a function of substitution (iii) one can approximate the magnitude of elastic moduli, elastic constants, elastic compliances and magnetostriction constants for single crystalline counterpart [58], which are important from the applications point of view. Thus, it is common and often required practice for polycrystalline materials that certain parameters such as resistivity [59-60], permeability [61, 62], including elastic moduli [34, 63-65] to be corrected for zero porosity.

In the literature various theoretical models and empirical relations such as the Hasselmann and Fulrath model [66], the Ledbetter and Datta model [67], elastic theory [68], powder metallurgy model, Mackenzie's wave-propagation theory, particle-reinforced composites, theory of potential energy change [34] etc. are available for the determination of elastic moduli in a void-free state. The correction methods commonly used are those developed for pores of cracked bodies, such as ceramics and rocks, or those for a composite with inclusions. Different methods based on distinct approaches that restrictively account for one or a few factors (porosity, dimensions, distribution, shape of the cracks etc) can give different values for the corrected elastic moduli. We have employed here three different approaches for the determination of zero porosity corrected elastic moduli.

(d) 1. Hasselmann and Fulrath model

The basic assumption in their treatment is that pores are spherical and distributed in a material having homogeneous (independent of position) and isotropic (independent of direction) elastic properties. According to the Hasselmann and Fulrath model, elastic moduli have been corrected to the void-free state using empirical relations:

$$\frac{1}{E_0} = \frac{1}{E} \left[1 - \frac{3f(1-\sigma)(9+5\sigma)}{2(7-5\sigma)} \right]$$

$$\frac{1}{G_0} = \frac{1}{G} \left[1 - \frac{15f(1-\sigma)}{(7-5\sigma)} \right]$$

$$\sigma_0 = \left(\frac{E_0}{2G_0} - 1 \right)$$

$$B_0 = \left[\frac{E_0 G_0}{3(3G_0 - E_0)} \right]$$

$$L_0 = B_0 + \frac{4}{3}G_0$$

The corrected values of Young's modulus (E_0), rigidity modulus, Poisson's ratio (σ_0), bulk modulus (B_0) and longitudinal modulus (L_0) for the different compositions are given in Table 3.

Table 3. Elastic data corrected to zero porosity. Longitudinal modulus (L_0), Rigidity modulus (G_0), Bulk modulus (B_0), Young's modulus (E_0) and Poisson's ratio (σ_0); (Hasselmann and Fulrath model) for the Cu-Fe-Al-O system.

Al ³⁺ - content (x)	$\frac{L_0 \quad G_0 \quad B_0 \quad E_0}{\text{(GPa)}}$				σ_0	θ_0 (K)
	0.0	200.95	70.28	107.24		
0.2	149.97	49.42	84.08	123.97	0.254	430.0
0.4	91.23	29.62	51.74	74.62	0.260	330.5
0.6	48.70	16.06	27.29	40.28	0.254	259.4

(d) 2. Ledbetter and Datta model

Ledbetter and Datta assumed that the randomly distributed spherical voids possess zero resistance to both dilation and shear. The modified equations thus arrived at, incorporating these assumptions, are given by:

$$G_0 = \left(\frac{1}{2A_1} \right) \left[-A_2 + (A_2^2 - 4A_1A_3)^{1/2} \right]$$

$$B_0 = \frac{(4G_0B)}{[4(1-f)(G_0 - 3fB)]}$$

$$E_0 = \frac{9B_0G_0}{3B_0 + G_0}$$

where,

$$A_1 = \left(\frac{8}{3}\right)(1-f)$$

$$A_2 = (3-2f)B - \left(\frac{8}{3} + 4f\right)G$$

$$A_3 = -3(1+f)BG$$

The void-free values of Young's modulus (E_0), rigidity modulus (G_0) and bulk modulus (B_0) for all the compositions are summarized in Table 4.

Table 4. Longitudinal modulus (L_0), Rigidity modulus (G_0), Bulk modulus (B_0), Young's modulus (E_0) and Poisson's ratio (σ_0) (Ledbetter and Datta model) for the Cu-Fe-Al-O system.

Al ³⁺ - content (x)	L_0 G_0 B_0 E_0 (GPa)				σ_0	A_1	A_2	A_3
	0.0	193.87	68.01	103.19				
0.2	142.73	47.34	79.61	118.53	0.252	2.300	43.39	-7209.75
0.4	84.90	27.85	47.77	69.95	0.256	2.236	21.70	-2338.85
0.6	47.51	15.73	26.54	39.41	0.253	2.405	20.00	-909.74

(d) 3. Elastic theory

Based on elastic theory, the linear relation between elastic moduli as a function of porosity as a lower range of porosity ($f < 0.2$) can be written as:

$$V_l = V_{l0} (1-C_l f)$$

$$V_s = V_{s0} (1-C_s f)$$

$$E = E_0 (1-C_E f)$$

$$G = G_0 (1-C_G f)$$

$$\sigma = \sigma_0 (1-C_\sigma f)$$

where C_1 , C_s , C_E , C_G and C_σ are constants of the material. The subscription '0' denotes the non-porous elastic moduli of the material. Exact expressions for the constants are as follows:

$$C_1 = \frac{1}{2} \left\{ \frac{[C_E + 2C_\sigma \sigma^2 (2 - \sigma_0)]}{(1 - \sigma_0)(1 + \sigma_0)(1 - 2\sigma_0) - 1} \right\}$$

$$C_s = \frac{1}{3}$$

$$C_E = \left(\frac{1}{18} \right) (29 + 11\sigma_0)$$

$$C_G = \frac{5}{3}$$

$$C_\sigma = \left(\frac{5}{9} \right) + \left(\frac{11}{18} \sigma \right) - \left(\frac{1}{18} \sigma \right)$$

The above relations are used to determine the elastic moduli for non-porous material and the results are shown in Table 5.

Table 5. Elastic wave velocity (V), Rigidity modulus (G_0), Young's modulus (E_0) Poisson's ratio (σ_0) (Elastic theory) for the Cu-Fe-Al-O system.

Al^{3+} - content (x)	$\frac{V_{l0} \quad V_{s0} \quad V_{m0}}{\text{(m/s)}}$			$\frac{E_0 \quad G_0}{\text{GPa}}$		σ_0	C_1	C_E	C_σ
0.0	7239.4	3502.7	3936.5	166.63	66.99	0.2462	1.8220	1.7616	0.6800
0.2	6304.4	2944.7	3315.3	118.81	48.82	0.2696	1.7021	1.7759	0.6904
0.4	5080.2	2274.4	2565.4	70.95	27.70	0.2770	1.6690	1.7804	0.6916
0.6	3436.9	1732.7	1942.8	39.17	15.51	0.2650	1.6200	1.7731	0.6922

(d) 4. Ishani and Cohen's equation

In 1967, a representative model was proposed by Cohen et al assuming the shape of the pore as a cube and derived a relation [35]:

$$M = M_0 (1 - f^{2/3})$$

where, M is the effective elastic modulus and M_0 is the zero porosity corrected elastic modulus.

Using the above power-law equation, non-porous values of elastic moduli have been calculated and are presented in Table 6.

Table 6. Zero porosity corrected elastic moduli (Ishani and Cohen equation) for the Cu-Fe-Al-O system.

Al ³⁺ - content (x)	$\frac{L_0 \quad G_0 \quad B_0 \quad E_0}{\text{(GPa)}}$			
	0.0	200.33	70.64	105.32
0.2	145.02	49.08	79.58	122.12
0.4	85.31	28.70	47.03	71.68
0.6	48.91	16.44	26.99	41.01

(d) 5. Jones equation

Jones et al has also suggested another equation for the evaluation of zero-porosity corrected elastic moduli and it is given by [35]:

$$M = M_0 (1 - f)^3$$

They have successfully obtained the non-porous elastic moduli for Y-123 superconducting system. On the other hand, for Bi-2212 samples the corrected values were found very high [35] as compared to standard value of Young's modulus for single crystalline counterpart.

The elastic moduli values in void-free state calculated from this relation for the present system are included in Table 7.

Table 7. Elastic modulus in void free state (Jones et al) for the Cu-Fe-Al-O system.

Al ³⁺ - content (x)	$\frac{L_0 \quad G_0 \quad B_0 \quad E_0}{\text{(GPa)}}$			
	0.0	223.13	78.68	117.31
0.2	166.18	56.24	91.19	139.94
0.4	102.07	34.34	56.27	85.76
0.6	52.61	17.69	29.03	44.11

It has been found that the zero porosity corrected values of elastic moduli obtained by applying different models differ by about 37% in the case of Bi-2212 and Bi(Pb) – 2212 superconducting systems [35]. These models are based on shape and distribution of pores without considering micro cracks in the polycrystalline ceramics. On the other hand, elastic moduli values obtained in void free state by considering shape, size and distribution of pores as well as micro cracks differ by about 10% only in the case of Y-123 superconducting system [34]. In the present case of polycrystalline spinel ferrite system $\text{CuAl}_x\text{Fe}_{2-x}\text{O}_4$, elastic moduli values obtained by various models differ by less than 10%. These suggest that, though pore fraction plays very important role in governing magnitude of elastic moduli but its shape, size and the way in which they are distributed play less significant role in spinel ferrite system under investigation as compared to various superconducting systems [34, 35]. The role of micro cracks is significant in both the type of systems.

It can be seen from Tables 3 - 7 that the magnitude of elastic moduli decreases with increasing Al^{3+} -content (x) in $\text{CuAl}_x\text{Fe}_{2-x}\text{O}_4$ system for $x = 0.0 - 0.6$, which suggests that the corresponding deformation of the solid is easy and the solids have a weak tendency to spring (analogous to planes within a solid held together by an atomic bond) back to its equilibrium position. Following the Wooster's work, the observed variation of elastic moduli may be interpreted in terms of change in the strength of interionic bonding [69].

The strength of interionic bonding is expected to change:

1. If interionic distances get changed by the substitution of larger or smaller cations in the system [70-72].

In the present system, as discussed above, lattice constant and as a result interionic distances decrease with increasing Al^{3+} - substitution (Table 1). The observed reduction in interionic distances enhanced the strength of bonding and as a result the magnitude of elastic moduli is expected to increase. On the other hand, the variation of elastic moduli with dopant concentration (x) may be explained on the basis of a model, according to which the general relationship between elastic constant and interionic distance of a solid is given by

$$C_{ij} = F_{ij} \left[\frac{(Ze)^2}{r^4} \right]$$

where C_{ij} is the elastic constant Z is the valency, e is the electronic charge, r is the interionic distance and F_{ij} is a tensor that has a constant value for a particular crystallographic structure. All the samples in the study are of fcc structure and as

such F_{ij} , Z and e can be considered as constant so that the above relationship reduces to

$$C_{ij} \propto \left(\frac{1}{r^4} \right)$$

As discussed, since interionic distances decrease with increasing Al^{3+} - content (x) in the system, the increase in the magnitude of the elastic moduli with increasing x is quite expected.

2. Change in the electronic configuration and as a result the nature of the bond formation between cations and cation-anion by cationic substitution in the structure [72-74].

It is well known that cations with a completely filled outermost orbit are more stable than cations with a half-filled outermost orbit or a incomplete outermost orbit. In the system under investigation, $\text{CuAl}_x\text{Fe}_{2-x}\text{O}_4$, Fe^{3+} ions having a half filled ($3d^5$) outermost orbit is replaced by Al^{3+} ions with a completely filled outermost orbit, which do not contribute to the bond formation. Thus, on increasing Al^{3+} - substitution for Fe^{3+} , strength of bonding and magnitude of moduli are expected to decrease.

3. Occupancy of the substituted cation along the grain boundary instead of the interstitial structural position [75].

In the present case in either situation magnitude of elastic moduli is expected to increase. The mechanical properties of polycrystalline powder are influenced by the size of the grains or grain structure in nano regime. Adjacent grains normally have different crystallographic orientation and of course a common grain boundary. The grain boundary acts as a barrier to strain motion. In the present

case, small amount of substituted Al^{3+} - ions reside at grain boundaries and likely to impede dislocation motion (strain). This enhances the magnitude of elastic moduli with Al^{3+} -substitution. Here, from x-ray data refinements it is clear that there is a systematic decrease in lattice parameters that suggests occupancy of Al^{3+} -ions at the interstitial structural position.

4. Grain size effect and change in micro-structure with composition [72, 76, 77].

It is seen from SEM images that the average grain size of $\sim 12 \mu\text{m}$ for $x = 0.0$ composition decreases to $\sim 4 \mu\text{m}$ for $x = 0.6$ composition (Figure 3). The elastic moduli could be greatly influenced by the presence of porosity, second phase, impurities, but not by the grain size in the micron range as in the present case. As compared with grain size, the geometry and distribution of pores also exert a greater influence on wave propagation in polycrystalline ferrites and thus the elastic properties thereof. A decrease in elastic moduli values with increased pore fraction just hints that pore fraction might be the dominant factor in determining elastic moduli.

Contrary to the above facts, we have observed a rapid decrease in the magnitude of elastic moduli with Al^{3+} -substitution (Tables 3 - 5). These decrease in magnitude of elastic moduli may be due to the Al^{3+} -substitution that do not contribute to the active bond formation as well as increase in pore fraction value with Al^{3+} - content (x) in the system, that dominant the effect of reduction of length of inter ionic bonding. We feel that these two factors can not lead to the 75% of reduction of elastic moduli values for only 30% ($x = 0.6$) of Al^{3+} -substitution in the

system. There may be other factors that are responsible for the low apparent stiffness.

Our recent thermoelectric power measurements have shown that for $x = 0.0$ and 0.2 compositions majority charge carriers are holes or p-type conduction is dominated while for the compositions with $x=0.4$ and 0.6 , n-type conduction is dominant or electrons are majority charge carriers [78]. It has been also established that the probable conduction mechanisms in the system are: $\text{Fe}^{2+} \leftrightarrow \text{Fe}^{3+} + e^-$ (n-type) at the B-site and $\text{Cu}^{2+} \leftrightarrow \text{Cu}^{1+} + e^+$ (p-type) at the A-site [78]. The near room temperature (323K) Seebeck coefficient value (α) has been used to determine the cationic concentration of Cu^{2+} , Cu^{1+} , Fe^{2+} and Fe^{3+} for different compositions using Heikes formula [79] and procedure suggested by Byeon et al. [80]. The details are given elsewhere [78]. The actual cation distribution and oxygen deficiency (δ) for each composition thus determined are summarized in Table 8.

Table 8. Seebeck coefficient(α), actual cation distribution and oxygen deficiency (δ) for Cu-Fe-Al-O system at 323K

Al^{3+} - content (x)	$\alpha(\mu\text{V/K})$ (323K)	Actual cation distribution	(δ)
0.0	+64.74	$(\text{Cu}^{1+}_{0.15}\text{Cu}^{2+}_{0.07}\text{Fe}^{3+}_{0.78})^A[\text{Cu}^{2+}_{0.78}\text{Fe}^{3+}_{1.22}]^B\text{O}^{2-}_{3.925}$	0.075
0.2	+8.42	$(\text{Cu}^{1+}_{0.12}\text{Cu}^{2+}_{0.10}\text{Fe}^{3+}_{0.70}\text{Al}^{3+}_{0.08})^A[\text{Cu}^{2+}_{0.78}\text{Fe}^{3+}_{1.10}\text{Al}^{3+}_{0.12}]^B\text{O}^{2-}_{3.940}$	0.060
0.4	-24.71	$(\text{Cu}^{2+}_{0.18}\text{Fe}^{3+}_{0.64}\text{Al}^{3+}_{0.18})^A[\text{Cu}^{2+}_{0.82}\text{Fe}^{2+}_{0.43}\text{Fe}^{3+}_{0.53}\text{Al}^{3+}_{0.22}]^B\text{O}^{2-}_{3.785}$	0.215
0.6	-16.84	$(\text{Cu}^{2+}_{0.14}\text{Fe}^{3+}_{0.58}\text{Al}^{3+}_{0.28})^A[\text{Cu}^{2+}_{0.86}\text{Fe}^{2+}_{0.35}\text{Fe}^{3+}_{0.47}\text{Al}^{3+}_{0.32}]^B\text{O}^{2-}_{3.825}$	0.175

The fluctuating valences of the cations like Cu^{2+} and Fe^{3+} in the present system have pronounced effects on their elastic properties. The small amount of Cu^{1+} and / or Fe^{2+} formation diminish the positive charge which is compensated

by oxygen vacancies [81]. It is known that the compounds with vacant sites are known to be elastically softer [82-83] than those with compounds with filled sites. In the samples of the present investigation since there are number of oxygen vacant sites, their presence must have given rise to a lower elastic moduli than otherwise.

The increase of oxygen content ($4 - \delta$) (or decrease of oxygen deficiency (δ)) can be thought of simplistically as applying a “chemical pressure” to the unit cell [34], as a result inter ionic distances decrease and the strength of bonding and the magnitude of elastic moduli are expected to increase or vice a versa.

Also, it may result from micro cracks, which reduce elastic stiffness without lowering mass density. During the synthesis process, micro cracks occur due to anisotropic thermal stresses. This probability cannot be neglected. In single phase polycrystalline ceramics, thermal expansion anisotropy of the grains gives rise to residual stresses during cooling from the synthesis temperature and these residual stresses can result in spontaneous cracking, primarily along grain boundaries [38]. It has been shown that such cracking is grain size dependent [84-85]. Fine grained materials do not crack, whereas some cracks are observed when the grains reach a certain critical size range, and for larger grains of micron range, cracking is more severe. The reduction of the effective elastic moduli resulting from micro cracking, and partly due to the volume expansion arising from the release of residual stresses when micro crackes are formed [38]. In the present case of single phase polycrystalline ferrite compositions, Al^{3+} -substitution leads to the nucleation and development micro cracks (interior cracks), that result

in weakening the strength of the material i.e. reduction in the effective elastic moduli with Al^{3+} -substitution (Tables 3 - 5). Crack growth in crystalline ceramics is usually through grains, i.e. trans-granular and along specific crystallographic planes of high atomic density.

In the literature, for polycrystalline MgFe_2O_4 the magnitude of E and G is reported to be 190.8 GPa and 74.1 GPa respectively [86], while it is found to be 62.7 GPa and 22.59 GPa respectively for MgAl_2O_4 [87]. These results are consistent with the present findings. On the other hand for single crystalline Al^{3+} -substituted CoFe_2O_4 and ZnFe_2O_4 [88, 89] spinel ferrites, enhancement in elastic stiffness constants ($C_{11} = 257.1$ GPa, $C_{12} = 150$ GPa for CoFe_2O_4 and $C_{11} = 290.5$ GPa, $C_{12} = 170.3$ GPa for CoAl_2O_4) and elastic moduli ($G = 65$ GPa, $B = 179.6$ GPa for ZnFe_2O_4 and $G = 102$ GPa, $B = 209.2$ GPa for ZnAl_2O_4) values has been observed for 100% replacement of Fe^{3+} by Al^{3+} in the system, which is rather expected based on the first probability discussed above and due to the fact that for single crystalline materials grain size, oxygen vacant sites, micro cracks, porosity etc. are not the factors that affect the magnitude of elastic moduli as in the case of polycrystalline materials. Earlier, such softening of elastic moduli has been observed for the substitution of Al^{3+} into Mg-silicate perovskites (MgSiO_3) [81]. These results have recently received considerable attention in computational and mineral physics communities, not only because such elastic weakening is fundamentally important for the study of condensed matters but also because it can lead to important geophysical consequences for the dynamics and rheology of the Earth's interior.

(e) Relationship between M/q and V_l/ρ_x , V_s/ρ_x

In 1961, Birch [90] showed that the longitudinal velocity (V_l) is approximately a linear function of x-ray density (ρ_x) in the case of Silicates and oxides having the same atomic weight (M/q). Subsequently, Simmons [91] confirmed these results and extended the applicability of such a linear relationship to transverse wave velocity (V_s) also. Anderson [92] further observed that whenever there is a variation in the values of V_l/ρ_x and V_s/ρ_x , a corresponding variation in the values of mean atomic weight is expected because the product of M/q with V_l/ρ_x and V_s/ρ_x should be constant. A similar relationship was arrived at by Reddy et al [93], Ravinder et al. [94] and Kumar et al [95] in the case of some mixed ferrites and by Buch et al. [72] for manganite perovskites. As such, an attempt has been made to establish a relationship between V_l/ρ_x , V_s/ρ_x and M/q of the sample of the present investigation and is given Table 9. It can be seen from Table 9 that the values of V_l/ρ_x and V_s/ρ_x decrease with decreasing mean atomic weight, thus the products ($M/q * V_l/\rho_x$ and $M/q * V_s/\rho_x$) do not remain constant. These observations establishing the fact that these materials do not behave like other oxide materials described in the literature.

Table 9. Experimental data of Al^{3+} -substituted CuFe_2O_4 ferrites.

Al^{3+} - content (x)	M/q (kg)* 10^{-3}	V_l / ρ_x ($\text{m}^4/\text{kg} \cdot \text{sec}$)* 10^{-3}	V_s / ρ_x	$(M/q)(V_l / \rho_x)$ (m^4/s)* 10^{-3}	$(M/q)(V_s / \rho_x)$
0.0	34.18	1049.21	624.33	35.86	21.34
0.2	33.35	911.32	530.19	30.39	17.68
0.4	32.53	711.82	412.89	23.16	13.43
0.6	31.70	564.23	327.22	17.89	10.37

(f) Lattice energy determination

The lattice energy of ionic solids is a measure of the strength of bonds in that compound. We have employed here Kudriavtsev's approach [96] for lattice energy determination of polycrystalline Cu-Fe-Al-O ferrites. According to this approach, the velocity of sound waves (V) in liquids as well as in solids, assuming the additivity of internal energy and making use of the standard thermodynamic formula expressed as:

$$V^2 = -\frac{nm\gamma}{U_0} + \frac{\gamma RT}{M}$$

where n and m are constants defining the potential energy function, γ is the ratio of specific heats (C_p/C_v), R , T (K), M (kg) and U_0 (eV) represent the gas constant, temperature of the substance, molecular weight and potential energy of the substance occupying an equilibrium volume at the specified temperature respectively.

In the above equation, (i) for ionic solids, U_0 can be replaced by the lattice energy of the solid U_{Lp} , (ii) for most of the ionic solid γ is nearly equal to 1 and (iii) the value of $n = 3$ is found suitable to many spinel ferrites, crystal with garnet structure and various ionic solid [97-99].

Based on the above considerations, the equation for lattice energy (U_{Lp}) in its simplified form is given by

$$U_{Lp} = -3.108 (MV_{mo}^2) * 10^{-5}$$

where, V is replaced by zero porosity corrected mean sound velocity (V_{mo}) of the elastic wave (Table 5). The lattice energy values for all the compositions are summarized in (Table 10)

Table 10. Lattice energy (U) for the Cu-Fe-Al-O system.

Al ³⁺ - content (x)	$\frac{r^+}{r^-}$ (Å)		z^+	z^-	$\frac{U_{\text{LD}}}{U_{\text{LS}}}$ (eV)		U _L (eV)		
	Compound	Present work			Catlow et al. Ref. [101]				
0.0	0.673	1.32	2.67	2.0	115.22	192.9	YFeO ₃	-149.82	-142.5
0.2	0.666	1.32	2.67	2.0	79.75	193.7	Y ₄ Fe ₄ O ₁₂	-599.27	-567.6
0.4	0.659	1.32	2.67	2.0	46.57	194.3			
0.6	0.651	1.32	2.67	2.0	26.03	194.9			

It is found that lattice energy decreases with increasing Al³⁺-content (x) in the system, suggests a weakening of the strength of bonding and results in a reduction in magnitude of elastic moduli; as observed.

Lattice energy is dependent on ionic charge and ionic radius: as the charge of the ions increase the magnitude of the lattice energy increases (becomes more negative) and as the ionic radius decreases lattice energy increases. An attempt has been made to calculate the lattice energy (U_{LS}) for all the compositions using the Kapustinkii equation [100] for lattice energy determination of ionic crystals:

$$U_{\text{LS}} = -1202.5 \frac{\nu |z^+| |z^-|}{r^+ + r^-} \left(1 - \frac{0.345}{r^+ + r^-} \right)$$

In this formula ν is the number of ions in the empirical formula (i.e. 7 in the present case) z^- and z^+ are anionic and cationic charge, respectively, while r^- and r^+ are the radii of the anion and cation, respectively. It is important to remember that the units of radii in this equation are in angstrom and lattice

energy is given in kJ. mole^{-1} (for the comparison purpose it is converted into eV (Table 8)). For the calculation of z^+ and r^+ , we have taken the weighted average of ionic charge and ionic radii while z^- and r^- , ionic charge and ionic radius, of the oxygen anion are taken to be (-2) and 1.32 (Å) respectively (Table 10). The calculated values of z^+ , r^+ and U_{LS} are given in the Table 8. For the sake of comparison the lattice energy value for the other class of ferrite materials, single crystalline yttrium orthoferrite (YFeO_3) and yttrium substituted yttrium iron garnet ($\text{Y}_4\text{Fe}_4\text{O}_{12}$), based on the weighted average of charge and ionic radii have been included in the Table 10. It is found that there is fairly good agreement between the calculated values and those determined from atomistic computer simulations [101], thus validating the present approach.

It is found that in the present system, the lattice energy value (U_{LS}) increases with increasing Al^{3+} -substitution. The observed increase in lattice energy value with Al^{3+} -substitution as well as the magnitude of lattice energy value for pure and substituted copper ferrite compositions ($x = 0.0 - 0.6$) contradict the trend observed and the magnitude determined from Kudriavtsev's approach. This leads one to conclude that, for polycrystalline materials, lattice energy is not only a function of ionic charge and ionic radii as in the case of single crystalline materials.

The lower value of lattice energy (U_{LP}) for polycrystalline material can be explained as follows. Polycrystalline materials are composed of a collection of many small crystals or grains. Adjacent grains with different crystallographic orientation are separated by a grain boundary. Within the boundary region, which

is probably, just several atomic distances wide, there is some atomic mismatch in a transition from the crystalline orientation of one grain to that of an adjacent one. Various degrees of crystallographic misalignment between adjacent grains are possible. The atoms are bounded less regularly along a grain boundary as bond angles are longer and consequently there is grain boundary energy. The magnitude of this energy is a function of the degree of disorientation, being larger for high angle boundaries [102]. These grain boundaries prevent long-distance interactions. As a result, the strength or lattice energy of polycrystalline material is smaller than its single crystalline counterpart. In the present case, Al^{3+} -substitution further restricts these interactions and may result in an increased degree of disorientation at the grain boundary. This further reduces the lattice energy value for compositions with higher Al^{3+} -concentration.

(D) Conclusions

In the present study we have determine the elastic moduli by ultrasonic pulse echo-overlap technique and their variation with Al^{3+} - concentration (x) for the $\text{CuAl}_x\text{Fe}_{2-x}\text{O}_4$ system has been investigated, it is concluded that:

- (i) Contrary to expectation substitution of Al^{3+} for Fe^{3+} in the system, results in a weakening of the elastic stiffness of the material as reflected by a 75% decrease in the magnitude of elastic moduli with 30% of Al^{3+} -substitution.
- (ii) Structural and microstructural parameters are found to be less effective in governing the magnitude of elastic moduli. Reduction of effective elastic moduli is not only due to substitution of Al^{3+} - ions, that do not contribute to the active bond formation and increase in pore fraction value, but also due to anisotropic thermal stress-induced occurrence and development of micro cracks as well as oxygen vacant sites in the samples with Al^{3+} - substitution.
- (iii) The lowering of lattice energy values of polycrystalline materials as compared to their single crystalline counterparts is due to grain and grain boundary contribution to polycrystalline materials.

References

- [1] G. F. Goya, H. R. Rechenbery, J. Z. Jiang, J. Appl. Phys. 84(2)(1998)1101-1108
- [2] I. Nedkov, R. E. Vandenberghe, Ts. Marinova, Ph. Thailhades, T. Merodiiska, I. Avramova, Appl. Surf. Sci. 253(2006)2589-2596
- [3] R. Baldev, V. Rajendran, P. Palanichamy, Science and Technology of Ultrasonics (New Delhi: Norosa Publishing House) (2004) p.250
- [4] Lin Sihan, He Yusheng, Wei Chongde, Shen Zhaohui, Supercond. Sci. Technol. 2(1989)145-148
- [5] Y. S. Reddy, V. P. Kumar, P. Kistaiah, C.V. Reddy, J. Alloys Comps. 424 (2006) 46-50
- [6] G. Lalitha, P. V. Reddy, J. Phys.: Condens. Matter, 21 (2009) 056003-056009
- [7] S. Sankarrajan, S. Aravindan, R. Yuvakkumar, K. Sakthipandi, V. Rajendran, J. Magn. Magn. Mater, 321 (2009) 3611-3620
- [8] Y. S. Reddy, V. P. Kumar, M. V. R. Reddy, P. Veerasomaiah, C. V. Reddy, Inv. J. Sci. Tech. 1(3) 2007 236-240
- [9] N. G. Bebenin, R. I. Zainullina, V. V. Ustinov, J. Magn. Magn. Mater, 321 (2009) 682- 685
- [10] Changfei Zhu, Renkui Zheng, J. Appl. Phys. 87 (7) (2000) 3579-3581
- [11] C. X. Chen, G. S. Jeiang, J. L. Jiang, Q. L. Zhang, R. K. Zheng, J. Magn. Magn. Mater, 308 (2007) 71-73
- [12] Nor Azah Nik Jaafar, R. Abd-Shukor, Physica B 334 (2003) 425-431

- [13] G. Lalitha, P. V. Reddy, J. Phys. Chem. Solids 70 (6) (2009) 960-966
- [14] Y. S. Reddy, V. P. Kumar, E. Nagabhushanam, P. Kistaiah, C. V. Reddy, J. Alloys. Comps., 440 (2007) 6-12
- [15] Y. S. Reddy, P. Kistaiah, C. V. Reddy, Mater. Chem. Phys., 102(2007)171-175
- [16] Y. S. Reddy, M. V. R. Reddy, P. Veerasomaiah, C. V. Reddy, Mater. Sci (Poland) 25 (3) (2007) 619-626
- [17] I. R. Shein, K. I. Shan, V. L. Kozhevnikov, A. L. Ivanovskii, Phys. Solid state, 47(11)(2005) 2082-2088
- [18] R. E. A. Mcknight, C. J. Howard, M. A. carpenter, J. Phys. Condens. Matter, 21(2009) 015901-015914
- [19] J. Suchanicz, J. Mater. Sci., 37 (2002) 489-497
- [20] S. A. Gridnev, A. G. Gorshkov, O. N. Korolevskays, Phys. Solid State, 51(8)(2009) 1553-1556
- [21] G. Lalitha, D. Das, D. Bahadur, P. V. Reddy, J. Alloys. Comps. 464 (1-2) (2008) 6-8
- [22] N. L. Ross, R. J. Angel, F. Seifert, Phys. Earth Planet. Inter. 129(1-2) (2002)
- [23] Z. R. Hassan, R. Abd-Shkor, H. A. Alwi, Supercond. Sci. Technol. 15(2002) 431-434
- [24] A. K. Yahya, J. Phys. Conf. Series 153 (2009) 012037 (6pp)
- [25] Nor Azah Nik Jaafar, S. A. Halim, R Abd- Shukor, Supercond. Sci. Technol. 18 (2005) 1365-1369

- [26] M. F. Bakar, A. K. Yahya, *Solid State Sci. Tech.* 17 (1) (2009) 50-56
- [27] N. A. Rasih, A. K. Yahya, *J. Alloys Comps.* 480 (2) (2009) 777-781
- [28] Y. C. Venudhar, K. S. Mohan, *Mater. Lett.* 55(3)(2002) 196-199
- [29] D. Ravinder, T. Alivelumanga, *Mater. Lett.* 49 (1)(2001) 1-6
- [30] D. Ravinder, *Mater. Lett.* 45(2)(2000)68-70
- [31] D. Ravinder, *Mater. Lett.* 47(1-2)(2001)35-39
- [32] V. G. Patil, S. E. Shirsath, S. D. More, S. J. Shukla, K. M. Jadhav, *J. Alloys Comps.* 488(1)(2009)199-203.
- [33] D. Ravinder, B. Ravi Kumar, *Mater. Lett.* 57 (28)(2003)4471-4473
- [34] Q. Wang, G. A. Saunders, D. P. Almond, M. Cankurtaran, K. C. Goretta, *Phys. Rev. B.* 52 (1995) 3711-3726
- [35] R. Ravinder Reddy, M. Murlidhar, V. Hari Babu, P. V. Reddy, *Supercond. Sci. Technol.*, 8 (1995) 101-107
- [36] Y. H. Loo, *Mater. Stru.* 25(1992) 573-578 and references therein
- [37] Paul Tapponnier, W. F. Brace, *Int. J. Rock Mech. Min. Sci. Geomech. Abstr.*, 13 (1976)103-112
- [38] V. Tvenggaard , J. W. Hutchinson, *J. Am. Ceram. Soc.* 71, (3)(1988) 157-166
- [39] P. V. Reddy, V. N. Mulay, K. B. Reddy, Y. V. Ramana, *Solid State Commun.* 67 (4) (1988) 449-452
- [40] S. Srinivas Rao, D. Ravinder, *Mater. Lett.* 57(24-25)(2003)3802-3804
- [41] K. Vishnu Prasad Rao , Y. Purushotham , J. S. Chandel, *Cryst. Res. Tech.* 31(3)(1996)329-333

- [42] B. S. Trivedi, Ph.D. Thesis, Saurashtra University, Rajkot, India (1995)
- [43] R. G. Kulkarni, B. S. Trivedi, H. H. Joshi, G. J. Baldha, J. Magn. Magn. Mater. 159(1996)375-380
- [44] B. S. Trivedi, N. N. Jani, H. H. Joshi, R. G. Kulkarni, J. Mater. Sci. 35(21)(2000)5523-5526
- [45] S. S. Ata-Allah, M. Kaiser, J. Alloys. Comps. 471(2009)303-309
- [46] S. S. Ata-Allah, M. F. Fayek, H. S. Refai, M. F. Mostafa, J. Solid. State. Chem. 149(2000)434-442
- [47] S. S. Ata-Allah, Mater. Chem. Phys. 87(2004)378-386
- [48] F. C. Romeijn, Philips Res. Rep. 8 (1953)304-320
- [49] K.S.R.C. Murthy, S. Mahanty, J. Ghose, Mater. Res. Bull. 22(11)(1987)1665-1675
- [50] B. H. Toby, Powder Diff. 21(2006)67-70
- [51] M. J. Buerger, Crystal Structure Analysis, Wiley, N. Y. (1960)
- [52] V. K. Lakhani, T. K. Pathak, N. H. Vasoya, K. B. Modi, Solid State Sciences 13 (2011) 539-547
- [53] C. G. Winfrey, D. W. Eckart, A. Tauber, J. Am. Chem. Soc. 82(1960)2695-2697
- [54] J. Smith, H. P. J. Wijn, Ferrites, John Wiley & Sons, New York, 1959
- [55] I. Maghsoudi, M. I. Hadianfard, H. Shokrollahi, J. Alloys. Comps. 481 (2009)539-542
- [56] S. M. Hoque, Md. A. Choudhary, Md. F. Islam, J. Magn. Magn. Mater. 251(2002)292-303

- [57] M. de Podesta, Understanding the properties of matter 2nd edn. (London: Taylor and Francis) (220) p. 182.
- [58] A. E. Clark, R. E. Strakna, J. Appl. Phys. 32(1961)1172-1180
- [59] V. R. Yadav, H. B. Lal, Canad. J. Phys. 57(1979)1204
- [60] M. P. Pandya, K. B. Modi, H. H. Joshi, J. Mater. Sci. 40(2005)52235232
- [61] A. D. P. Rao, B. Ramesh, P. R. M. Rao, S. B. Raja, J. Alloys. Comps. 282(1999)268-273
- [62] A. M. Sankpal, S. V. Kakatkar, V. D. Chaudari, R. S. Patil, S. R. Swant, S. S. Suryanvansi, J. Mater. Sci. 9(1998)173-179
- [63] S. Yamanaka, K. Kurosaki, T. Maekawa, T. Matsuda, S. Kobayashi, M. Uno,
J. Nucl. Mater. 344(2005)61-66
- [64] K. Ganesh, R. J. Topare, S. S. Shah, P. V. Reddy, J. Alloys. Comps. 230 (1995) 23-29
- [65] P. U. Sharma, K. B. Modi, Phys. Scr. 81(2010) 015601, 1-9
- [66] D. P. H. Hasselmann, R. M. Fulrath, J. Am. Ceram. Soc. 47(1964)52-53
- [67] H. Ledbetter, S. K. Datta, J. Acoust. Soc. Am., 79(1986)239-248
- [68] R. W. Rice, Treatise on Material Science and technology ed. R. K. Mac Crane (New York: Academic) 11(1977)199-381
- [69] W. A. Wooster, Rep. Prog. Phys. 16(1953)62-82
- [70] M. B. Solunke, P. U. Sharma, M. P. Pandya, V. K. Lakhani, K. B. Modi, P. V. Reddy, S. S. Shah, Pramana – J. Phys. 65 (2005)481-490

- [71] M. B. Solunke, P. U. Sharma, V. K. Lakhani, M. P. Pandya, K. B. Modi, P. V. Reddy, S. S. Shah, *Ceram. Int.* 33(2007)21-26
- [72] J. J. U. Buch, G. Lalitha, T. K. Pathak, N. H. Vasoya, V. K. Lakhani, P. V. Reddy, Ravi Kumar, K. B. Modi, *J. Phys. D: Appl. Phys.* 41(2008)025406, 1-10
- [73] K. B. Modi, M. C. Chhantbar, H. H. Joshi, *Ceram. Int.* 32(2006)111-114
- [74] S. S. Bhatu, V. K. Lakhani, A. R. Tanna, N. H. Vasoya, J. J. U. Buch, P. U. Sharma, U. N. Trivedi, H. H. Joshi, K. B. Modi, *Ind. J. Pure. Appl. Phys.* 45(2007)596-608
- [75] M. B. Solunke, K. B. Modi, V. K. Lakhani, K. B. Zankat P. U. Sharma, P. V. Reddy, S. S. Shah, *Ind. J. Pure Appl. Phys.* 45(2007)764-766
- [76] K. B. Modi, U. N. Trivedi, P. U. Sharma, V. K. Lakhani, M. C. Chhantbar, H. H. Joshi, *Ind. J. Pure Appl. Phys.* 44(2006)165-168
- [77] T. K. Pathak, J. J. U. Buch, U. N. Trivedi, H. H. Joshi, K. B. Modi, *J. Nano Sci. Nano Tech.* 8 (2008)4181-4187
- [78] V. K. Lakhani, K. B. Modi, *J. Phys. D: Appl. Phys.* 44 (2011)
- [79] R. R. Heikes, in *Thermo electricity* (eds) R. R. Heikes and R. W. Ure, 45 (NY: Wiley Inter Science (1961))
- [80] S. C. Byeon, K. S. Hong, J. G. Park, W.N. Kang, *J. Appl. Phys.* 81(12) (1997) 7835-7841
- [81] J. Zhang, Y. Zhao, H. Xu, B. Li, D. J. Weidner, A. Navrotsky, *Appl. Phys. Lett.* 90(2007)161903, 1-3
- [82] G. A. Saunders, T. Seddars, *J. Phys. Chem. Solids.* 37(1976)873-882

- [83] T. Hailing, G. A. Saunder, W. A. Lambson, Phys, Rev. B. 26(1982)
5786-5797
- [84] J. A. Kuszyk, R. C. Bradt, J. Am. Ceram. Soc. 56(8) (1973)420-423
- [85] R. W. Rice, R. C. Pohanka, J. Am. Ceram. Soc. 62(11-12)(1979)559-563
- [86] S. R. Murthy, P. V. Reddy, T. S. Rao, J. Mater. Sci. Lett. 3(7)(1984)
647-650
- [87] www. Ceramics. nist. gov/srd. summary
- [88] H. J. Reichmann, S. D. Jacobsen, Am. Geo. Phys. Union, Fall Meeting
(2004)
- [89] Z. Li, E. S. Fisher, J. Z. Liu, M. V. Nevitt, J. Mater. Sci. 26(10)(1991)2621-
2624
- [90] F. Birch, J. Geophys. Res., 69(20)(1964)4377-4388
- [91] G. Simmons, J. Geophys. Res. 69(6)(1964)1123-1130
- [92] O. L. Anderson, Phys. Acoust. Vol. 3B ed. W. P. Mason (New York:
Academic) (1965) p. 43
- [93] P. V. Reddy, M. B. Reddy, V. N. Mulay, Y. V. Ramana, J. Mater. Sci. Lett.
7(11)(1988)1243-1244
- [94] D. Ravinder, K. Vijaya Kumar, B. S. Boyanov, Mater. Lett. 38(1999)22-27
- [95] N. Kumar, Y. Purushottam, P. V. Reddy, Z. H. Zaidi, P. Kishan, J. Magn.
Magn. Mater. 192(1999)116-120
- [96] B. B. Kudriavtsev, Soviet Phys. Acoust. 2(1956)172-177
- [97] B. Komalamba, K. V. Sivakumar, V. R. K. Murthy, Acoust lett.
19(1996)163-166

- [98] B. Komalamba, K. V. Sivakumar , V. R. K. Murthy, Acoust lett.
85(1999)433-435
- [99] M. Subrahmanyam, E. Rajagopal, N. M. Murthy, S. V. Subrahmanyam,
J. Acoust. Soc. India, 14(1986)54-58
- [100] A. F. Kapustinskii, Quart-Rev. Chem. Soc. 10(1956)283-294
- [101] H. Donnerberg, C. R. A. Catlow, J. Phys. Condens. Matter.
5(18)(1993)2947-2960
- [102] W. D. Callister, Materials Science and Engineering: An Introduction
(New York:Wiley) (2000) p.166

4.4 Negative magnetization, magnetic anisotropy and magnetic ordering studies on Al^{3+} -substituted copper ferrite

(A) Introduction

Copper ferrite (CuFe_2O_4) is one of the most investigated ferrite by various experimental techniques. Due to a relatively small energy difference between Cu^{2+} - ions at the tetrahedral (A-) and octahedral (B-) sites, cation redistribution is possible and strongly dependent on the annealing temperature, cooling rate, microstructure and other parameters. [1]. Copper ferrite is mostly an inverse spinel. Statistically, 6 % - 24 % of Cu^{2+} ions occupy the A-sites depending on the preparative parameters [2]. The corresponding magnetization is about 1.48 - 2.92 μ_B per chemical formula. On the other hand, copper ferrite is ferrimagnetic at room temperature with Neel temperature of 738K [3], although lower values down to 290K have also been reported [2]. Thus, tailoring of the magnetic and electrical properties of CuFe_2O_4 is possible with ease [1, 4-5]. On the spin structure, as the t_{2g} bands of Cu^{2+} on the B-sites are fully occupied; the inter-site direct hopping is absent and results in a ferromagnetic or weak anti-ferromagnetic exchange coupling between the B-sites which stabilize the Neel configuration (collinear spin arrangement). However, as Cu^{2+} is redistributed on the A-sites, Fe^{3+} occupies the B-sites and results in an anti-ferromagnetic exchange coupling between the B-sites, which frustrates the Neel configuration. If the exchange coupling between Cu^{2+} on the A-sites and Fe^{3+} on the B-sites is weak enough, the redistribution may result in spin canting, or other complex

structures. In addition, redistribution of Cu^{2+} from the B- to A-sites alters the ground multiple from doublet to triplet. This effect, combined with the large spin-orbital coupling constant, may result in different magnetocrystalline anisotropy [6].

In particular, copper ferrite (CuFe_2O_4) in bulk polycrystalline [7-8] and thin film [5, 9-12] forms have shown very interesting multifunctional properties upon the application of external stimuli. On the other hand, nano particles of CuFe_2O_4 have been shown to be useful as a catalyst for CO_2 decomposition, hydrogen production and as a gas sensor [13]. In the literature, wide varieties of experimental techniques have been employed for the synthesis and characterization of nanocrystalline copper ferrite [14 - 19].

The substitution of Al^{3+} - ions have some beneficial effects on power handling capability [20]. The addition of Al^{3+} - ions have shown to modify the structural properties [21], electrical properties [22-23] including switching characteristics [7, 24], magnetic properties [22, 25-29], dielectric properties [30, 31], and elastic properties [32] of spinel ferrite materials in an interesting manner.

The system under investigation, copper ferrite aluminates, $\text{CuAl}_x\text{Fe}_{2-x}\text{O}_4$, belong to a large class of compounds having the general formula $\text{A}^{2+}\text{B}_2^{3+}\text{O}_4^{-2}$ and crystallize in the spinel structure.

Magnetic systems undergoing transitions to ordered ferromagnetic, anti-ferromagnetic and ferrimagnetic states are reported to show irreversibility, indicated by the difference between their field cooled (FC) and zero-field cooled (ZFC) magnetization [33-34]. The irreversible FC and ZFC magnetic behaviour is

one of the characteristic features of a spin glass [35-36], other characteristic properties of a spin glass include the relaxation of magnetization (i.e. the aging effect) and the presence of a cusp in the low field ZFC magnetization as well as in the thermal variation of ac susceptibility curves. The spins are frozen in random directions due to lack of long-range magnetic interactions. Spin-glass-like properties have been reported for magnetic systems [37-38] for which neutron diffraction studies indicate long range magnetic ordering. These results contradict each other. On the other hand, low field magnetic behaviour of some ferromagnetic and ferrimagnetic oxides indicated that their spin-glass-like magnetic properties originate from the magnetocrystalline anisotropy [33, 39]. In other words, the magnetic behaviour similar to that of cluster spin glass could also be explained based on the magneto- crystalline anisotropy of the compound. Though, conventional spin glasses and materials showing spin-glass-like features such as superparamagnetic systems, cluster spin glass systems, superconducting oxides, the ordered magnetic system, etcetera show thermomagnetic irreversibility between the FC and ZFC magnetization and cusp in their ZFC susceptibilities, the origin of such a behavior is not yet properly understood [33].

Recently, Sundaresan et al. [40] have demonstrate that in certain ferrimagnetic materials, small negative trapped field in the sample space as well as large coercive fields are responsible for the observed negative magnetization under ZFC process. The negative values of magnetization measured in low applied fields for double perovskite composition: LaSrCoRuO_6 , have been

interpreted to be due to disorder in site occupancy of Co and Ru leading to octahedral distortions and formation of Ru-O-Ru ferromagnetic linkages. It is mentioned that below 150K these ferromagnetic Ru spins polarize the Co-spins in a direction opposite to that of the applied field resulting in observed negative magnetization [41]. In short, there still exists large controversy regarding the origin of the phenomenon. A microscopic understanding of this phenomenon can be effectively utilized to tailor the magnetic properties for various applications. This would facilitate the design of various magnetic memories, thermo magnetic switches and magnetic cooling/heating devices [42]. The authors have observed a crossover of the ZFC magnetization from positive to negative for the $\text{CuAl}_{0.6}\text{Fe}_{1.4}\text{O}_4$ ($x = 0.6$) composition, below their magnetic ordering temperature.

The thermomagnetic irreversibility ($M_{\text{FC}} > M_{\text{ZFC}}$) below a certain temperature has been observed for many ferrite system in nano regime [43-44]. The results are explained based on the blocking of the magnetic moment of nano particles and the superparamagnetic behavior of the studied system. It may also be due to the large anisotropy barrier for the studied compositions. On the other hand, the observed non-coincidence of the FC-ZFC curves for nanosized nickel ferrite with grain size of 51nm, has been explained based on the distribution of particle size in the sample [45]. We have observed that for $x = 0.0, 0.4$ and 0.6 compositions of $\text{CuAl}_x\text{Fe}_{2-x}\text{O}_4$ system, the ZFC and FC curves bifurcate at about 276K, 310K and 278K respectively, while for $x = 0.2$ composition, ZFC-FC curves do not coincide throughout the temperature range studied. Nanosized ferrite particles exhibit unusual magnetic properties which are not observed in the

bulk material, such as, single domain behavior, superparamagnetism, and reduced magnetization. Similarly, the mechanisms responsible for such magnetic behavior of ferrite nanoparticles are not directly applicable to coarse grained (micron size particles) polycrystalline ferrite material.

In the present communication, it clearly demonstrates that the observed features of the FC - ZFC magnetization and ac susceptibility curves arise due to the low magnetocrystalline anisotropy, but not due to the cluster-spin-glass like phase in the system. To our knowledge, no work has been reported on the role of magnetocrystalline anisotropy in governing the magnetic properties of the coarse grained ferrite materials in general, except for an excellent work by Joy et al. [33,46] on Ni-Zn ferrite, $\text{Ni}_{0.8}\text{Zn}_{0.2}\text{Fe}_2\text{O}_4$. Recently, the role of anisotropy ion, Fe^{2+} , in enhancing and tailoring the magnetization of CuFe_2O_4 nanoparticles has been discussed by Thapa et al. [13], while the observed large magnetic moment ($80 \text{ Am}^2/\text{kg}$) for nanosized $\text{Cu}_{0.25}\text{Co}_{0.25}\text{Zn}_{0.5}\text{Fe}_2\text{O}_4$ has been explained in terms of the enhancement in the B-B interaction because of the distortion in the B-sites due to the presence of the Jahn-Teller cation Cu^{2+} at this site [47].

To our knowledge few research reports are available on various physical properties of $\text{CuAl}_x\text{Fe}_{2-x}\text{O}_4$ spinel ferrite system including our recent work on the system [21, 25, 26, 30, 32, 48-51].

In the view of above facts, the effect of Al^{3+} substitution on magnetic properties of CuFe_2O_4 with general chemical formula: $\text{CuAl}_x\text{Fe}_{2-x}\text{O}_4$ ($x = 0.0, 0.2, 0.4$ and 0.6) have been studied by means of field cooled and zero field

cooled magnetization, magnetic hysteresis and low field ac susceptibility measurements.

(B) Experimental details

From the $\text{CuO-Fe}_2\text{O}_3$ phase – diagram, CuFe_2O_4 is formed between 1000°C and 1100°C . The samples sintered below 1000°C or above 1100°C were of mixed-phase [4]. Aluminum (Al^{3+}) - modified copper ferrite ceramics with a general formula of $\text{CuAl}_x\text{Fe}_{2-x}\text{O}_4$ ($x = 0.0, 0.2, 0.4$ and 0.6) were synthesized from high purity chemicals, namely CuO , Al_2O_3 and Fe_2O_3 , of 99.9% purity supplied by Sigma Aldrich. The oxides were mixed thoroughly in stoichiometric proportions to yield the desired composition and then wet-ground. The mixture was dried and pressed into pellets. These pellets were pre-sintered at 1100°C for 24 hours and slowly cooled to room temperature. The samples were again powdered, pressed into pellets, sintered at 1100°C for 24 hours and then slowly furnace cooled to room temperature at the rate of $2^\circ\text{C}/\text{min}$. The stoichiometry of the powder samples was checked by energy dispersive analysis of x-rays (EDAX). The samples were characterized for single phase formation and the determination of cation distributions by x-ray powder diffractometry using $\text{CuK}\alpha$ radiation at 300K.

Magnetic measurements (field-cooled (FC) and zero-field-cooled (ZFC) magnetization and magnetic hysteresis) were performed using the physical property measurement system (PPMS, Quantum Design). The low field ac susceptibility measurements for powdered samples were made in the temperature range 300K to 750K using double coil set-up [52], operating at a frequency of 263Hz with r.m.s. field of 40 A/m.

(C) Results and discussion

High temperature prolonged sintering may result in the loss of ingredients, which leads to non-stoichiometry in composition. This, in turn, shows unexpected behaviour which cannot be explained based on normal stoichiometry. Thus, it was essential to check the chemical stoichiometry of each composition. A representative energy dispersive analysis of x-rays (EDAX) pattern for typical composition with $x = 0.4$ is shown in Fig. 1.

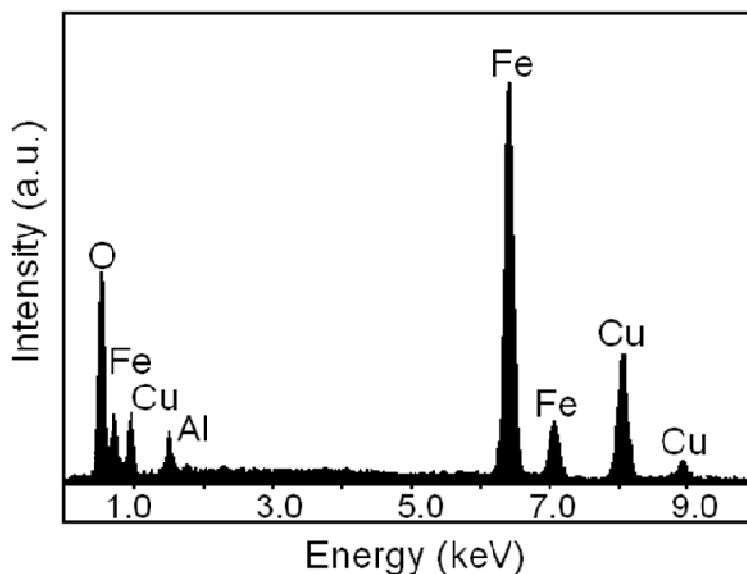


Figure 1. EDAX pattern of $\text{CuAl}_{0.4}\text{Fe}_{1.6}\text{O}_4$ ($x = 0.4$) composition.

The results of EDAX confirm the expected stoichiometry, with small oxygen deficiency. No trace of any impurity was found indicating the purity of the samples. It is also clear that there is no loss of any ingredient after high temperature sintering. EDAX results suggest that the precursors have fully undergone the chemical reaction to form the expected ferrite composition. The reason for making EDAX characterization was to verify the purity and the chemical composition.

The room temperature (300K) x-ray diffraction (XRD) patterns of the samples were obtained by x-ray powder diffractometry. Indexing and Rietveld refinement using general scattering analysis software (GSAS) of XRD patterns for $x = 0.0, 0.2, 0.4$ and 0.6 compositions of $\text{CuAl}_x\text{Fe}_{2-x}\text{O}_4$ system, revealed that these are single-phase compounds, crystallizing in a face centered cubic (fcc) structure (space group O_h^7 Fd3m). No peaks from impurity phases could be detected within the limits of x-ray detection, which is typically 5%. Figure 2 displays Rietveld fitted XRD patterns for the typical compositions with $x = 0.2$ and 0.6 . One of the most important Rietveld error indices or discrepancy values is that of “Chi-squared” or χ^2 [53]. It is found that χ^2 for different compositions lie in the range 1.2-1.4. The χ^2 values obtained in the present analysis suggest good refinement of the data.

The distribution of the cations among the available tetrahedral (A-) and octahedral (B-) sites of the spinel lattice have been determined by comparing experimental and calculated intensities of the diffracted beam. The x-ray diffraction line intensities of various Bragg's planes were calculated for different combinations of the cations in the A- and B- sites using a computer program based on the Buerger formula [54]. In the process of arriving at the final cation distribution, the site occupancy of all the cations was varied for many possible combinations and those that agree well with the experimental intensities of various Bragg's planes were taken into consideration. The cation distributions obtained for $\text{CuAl}_x\text{Fe}_{2-x}\text{O}_4$ system are represented as:

$x = 0.0$	$(\text{Cu}_{0.22}\text{Fe}_{0.78})[\text{Cu}_{0.78}\text{Fe}_{1.22}]\text{O}_4$
$x = 0.2$	$(\text{Cu}_{0.22}\text{Fe}_{0.70}\text{Al}_{0.08})[\text{Cu}_{0.78}\text{Fe}_{1.10}\text{Al}_{0.12}]\text{O}_4$
$x = 0.4$	$(\text{Cu}_{0.18}\text{Fe}_{0.64}\text{Al}_{0.18})[\text{Cu}_{0.82}\text{Fe}_{0.96}\text{Al}_{0.22}]\text{O}_4$
$x = 0.6$	$(\text{Cu}_{0.14}\text{Fe}_{0.58}\text{Al}_{0.28})[\text{Cu}_{0.86}\text{Fe}_{0.82}\text{Al}_{0.32}]\text{O}_4$

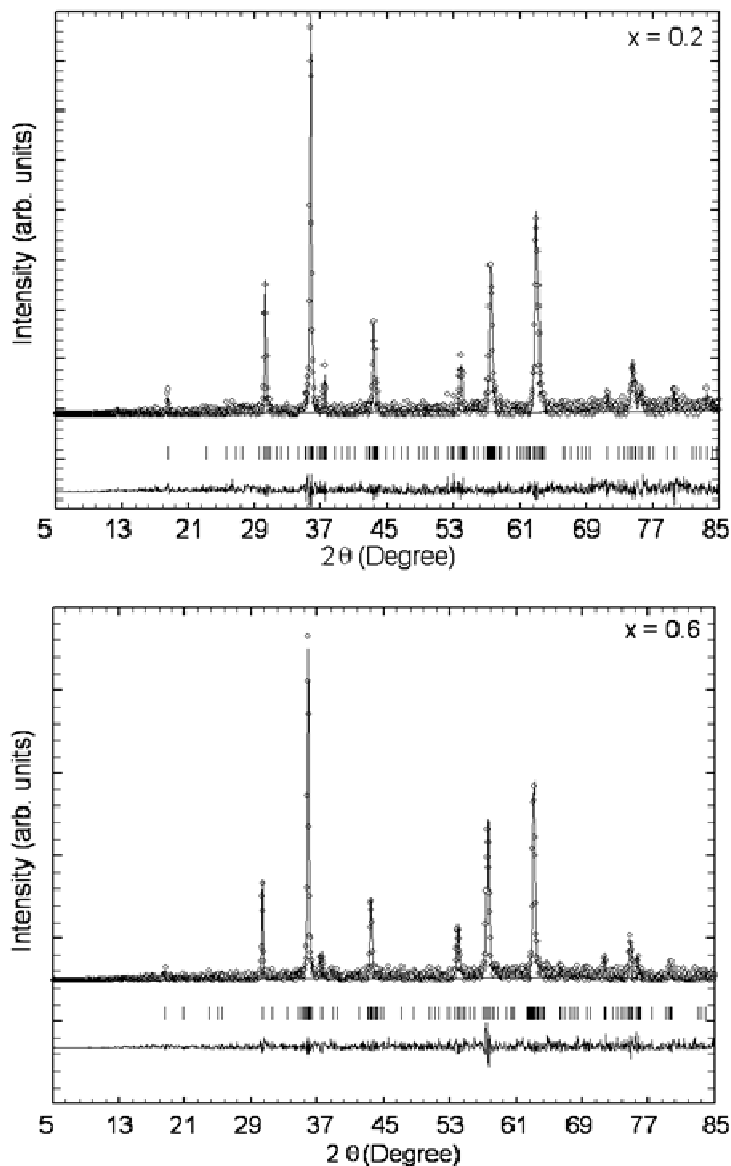
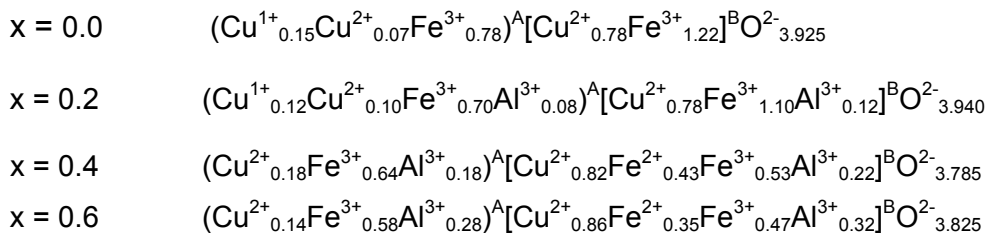


Figure 2. Observed (Solid Circles) and calculated (Solid line) x-ray powder diffraction patterns for the $\text{CuAl}_x\text{Fe}_{2-x}\text{O}_4$ ($x = 0.2$ and 0.6) system at 300K. The difference between the observed and calculated spectra is plotted at the bottom. The ticks indicate allowed Bragg peaks positions.

Near room temperature (323K) Seebeck coefficient values (α) have been used to determine the cationic concentration of Cu^{1+} , Cu^{2+} , Fe^{2+} and Fe^{3+} ions using the Heikes formula [55]. The details of this are given elsewhere [51]. The actual cation distributions thus derived for different compositions are summarized below, which, in turn, are used to explain the magnetic properties.



The main plot of Fig. 3 shows the magnetization (M) versus applied magnetic field (H) curves, measured at 10K for $x = 0.0 - 0.6$ compositions. The hysteresis loops recorded at 300K are shown in the inset. The values of saturation magnetization (σ_s), and the magneton number (saturation magnetization per formula unit in Bohr magneton (μ_B)) at 10K for each composition are listed in Table 1. Figure 3 demonstrates that there is a high field slope to magnetization $M(H)$ curves for $x = 0.0 - 0.6$, compositions which exhibit strong evidence for a canted spin structure, and canting angle varies with applied field. The high field slope has been established as due to the high magnetic anisotropy [56]. This fact does not apply here since all the compositions have very low concentration of magnetic anisotropy ion (Fe^{2+}), and therefore, the observed features may be thought of arising from canting of spins. From the field dependence of magnetization, and observed magnetic moment, it is clear that

the samples with $x = 0.0 - 0.6$ show ferrimagnetic behavior, which decreases with increasing x values.

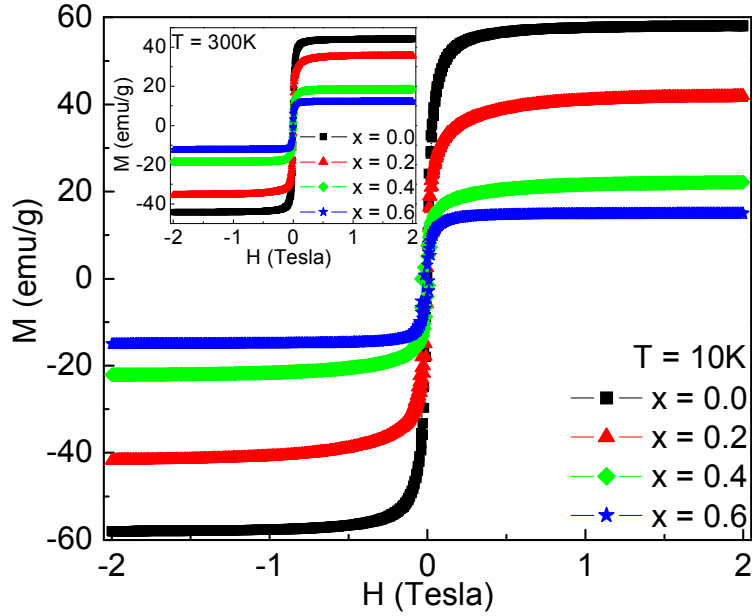


Figure 3. Magnetic field dependence of magnetization at 10K; main panel, inset at 300K, for Cu-Fe-Al-O samples.

A very important characteristic of the $M(H)$ curves is the negligible coercivity and remanence for all the compositions, which are often found in magnetic cluster system [57]. The negligible coercivity for different compositions also suggests that these are low anisotropic compounds [46].

According to the Neel's two sub lattice model of ferrimagnetism [58], Neel's magnetic moment per formula unit in μ_B , n_B^N , is expressed as:

$$n_B^N = M_B(x) - M_A(x) \quad (1)$$

where, M_B and M_A are the octahedral (B-) and tetrahedral (A-) sub lattice magnetization to be determined from the cation distributions and the free-ion magnetic moments of the cations involved: $m(\text{Fe}^{3+}) = 5\mu_B$, $m(\text{Fe}^{2+}) = 4\mu_B$,

$m(\text{Cu}^{2+}) = 1\mu_B$, $m(\text{Cu}^{1+}) = 0\mu_B$ and $m(\text{Al}^{3+}) = 0\mu_B$. It is clear from the Table 1, that the observed values of magneton number do not agree with the Neel's moment (n_B^N) found from the Neel's formula for collinear spin arrangement. This indicates significant canting of the B-site moments. The substitution of non-magnetic Al^{3+} ions in CuFe_2O_4 may lead to collapse of long range magnetic ordering in the system. Therefore, it was thought appropriate to apply random canting of spins (RCS) model. Since, the actual spin canting depends upon a number of non-magnetic nearest neighbours and their spatial arrangement, the statistical model like RCS proposed by Rosencwaig [59] should be used. According to this model, the B-sites magnetic ions can be considered to be canted with an average angle $\langle\theta_{\text{RCS}}\rangle$ due to non-magnetic substitution (Al^{3+}) which, in the average nearest neighbour approximation is estimated to be:

$$\cos \langle\theta_{\text{RCS}}\rangle = \left(\frac{M_A}{M_B} \right) \left(\frac{J_{AB}}{J_{BB}} \right) \quad (2)$$

Here, J_{AB} and J_{BB} are exchange integrals.

The net magnetization per formula unit (magneton number), n_B , is related to canting angle, $\langle\theta_{\text{RCS}}\rangle$, by:

$$n_B = M_B(x)\cos \langle\theta_{\text{RCS}}\rangle - M_A(x) \quad (3)$$

The experimental values of canting angle, $\langle\theta_{\text{RCS}}\rangle$ have been obtained from equation (3), using measured n_B values (Table 1), and the same are also listed in Table 1.

As the Al^{3+} - content increases in the system, the magnetic coupling, J_{AB}/J_{BB} , remains nearly constant for $x = 0.0$ to 0.2 and thereafter it is getting

weakened for $x > 0.2$, indicates change in the magnetic structure (increase frustration and disorder).

Table 1. Magnetic parameters for $\text{CuAl}_x\text{Fe}_{2-x}\text{O}_4$ system.

Al-content (x)	σ_s (emu/gm)	$n_B(\mu_B)$	n_B^N (μ_B)	$\langle\theta_{RCS}\rangle$ (Degree)	J_{AB} / J_{BB}	T_{cusp} (K)	T_{irr}
0.0	58.07	2.49	2.91	20.1	1.63	60	276
0.2	41.71	1.74	2.68	31.8	1.48	65	-
0.4	22.61	0.92	1.81	34.1	1.27	61	310
0.6	15.22	0.61	1.57	37.7	1.20	75	287

Further, studies on magnetic properties using dc magnetization measurements were carried out. Figure 4 shows plots of magnetization versus temperature (M - T) recorded in zero- field cooled (ZFC) and field cooled (FC) modes in an external magnetic field of 10mT for the samples with $x = 0.0, 0.2, 0.4$ and 0.6 . The ZFC magnetization was recorded by first cooling the sample from 325 to 4K in zero magnetic fields, then applying the magnetic field and warming the sample up to 325K in the presence of the field and recording the moment during the warming cycle. Field cooled patterns were obtained by first cooling the sample from 325K down to 4K in the external field and then warming it up to 325K and recording the moment. The plots of ZFC-FC magnetization show thermo-magnetic irreversibility (TMI) (divergence between FC and ZFC magnetization). This is the property of all magnetic systems exhibiting magnetic hysteresis behaviour. For the compositions with $x = 0.0, 0.4$ and 0.6 the ZFC and FC curves bifurcate at about 276K, 310K and 287K respectively. This temperature is referred to as the temperature of irreversibility above which $[(M_{\text{FC}}/M_{\text{ZFC}})-1]$ is less than 1%. The behaviour of $x = 0.2$ composition is

particularly interesting of which ZFC and FC curves show bifurcation at the whole temperature range, which indicates that the system is not magnetically homogeneous although the material is chemically homogeneous. This may indicate the existence of magnetic cluster phase in the sample [57].

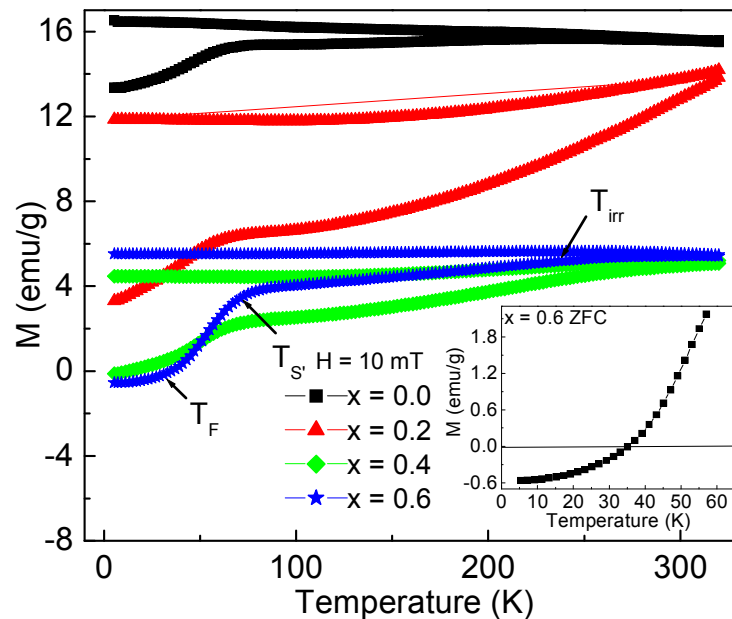


Figure 4. Temperature dependence of M_{FC} and M_{ZFC} of Cu-Fe-Al-O system. Inset shows the expanded version of the ZFC mode near the magnetic transition.

During both the FC and the ZFC processes, the anisotropy field plays an important role in determining the magnetization at a given field strength. Magneto crystalline anisotropy aligns the spins in a preferred direction. As mentioned earlier, during the process of zero-field cooling (ZFC) magnetization measurement, no magnetic field is applied while cooling the sample through the ordering temperature. At the lowest temperature when a small magnetic field is applied, the magnitude of resultant magnetization will depend on the magnetic anisotropy of that material. If the system is low anisotropic, as in the present

case, the small applied magnetic field will be sufficient to rotate the spins in the direction of the applied field and therefore the magnetization will be very large i.e. difference in the FC and ZFC magnetization will be small. If the anisotropy of the sample is very low, the FC magnetization will remain almost constant, while the FC magnetization increases with decreasing temperature for highly anisotropic materials [33]. The observed flat response of FC magnetization with temperature confirms that all the ferrite compositions studied are low anisotropy materials.

We have observed a very broad hump in the ZFC magnetization (M_{ZFC}) for $x = 0.0, 0.4$ and 0.6 compositions in vicinity to bifurcate temperature between the FC and ZFC curves. The sharp peak in M_{ZFC} is observed at a temperature where the coercivity is larger than the applied field and a broad maximum is observed when coercivity is comparable or smaller than the applied field. This observation suggests that in the present case coercivity for different compositions is much less than the 10mT and materials under study are low anisotropy compounds.

The TMI between the M_{FC} and M_{ZFC} and a very broad maximum in the ZFC magnetization of the ferrite compositions are due to their magnetic anisotropy and not due to any spin-glass-like behavior as reported for many ordered magnetic systems [46].

A careful examination of Fig. 4, reveals two interesting features (i) for $x = 0.6$ composition ZFC magnetization decreases slowly with decrease in temperature, shows cusp centered around 75K, then decreases rapidly, passes through a zero value of magnetization ($M = 0$) at the compensation temperature

($T \sim 35\text{K}$). Below this temperature, the magnetization is negative, down to the lowest temperature (4K).

Negative magnetization was observed more than five decades ago in spinels like Co_2VO_4 [60], and more recently in natural ferrites such as magnetite and maghemite [61] spinels like CoCr_2O_4 and MnCr_2O_4 [62], ferrite like $\text{Fe}_2\text{Mo}_{0.6}\text{Ti}_{0.4}\text{O}_4$ [63], perovskites like $\text{NdMnO}_{3+\delta}$ $\text{La}_{0.75}\text{Nd}_{0.25}\text{CrO}_3$ [64], molecular magnets [65], other oxides [66], double perovskites $\text{Sr}_2\text{YbRuO}_6$ [67], Cu, Mn and Fe based prussian blue analogues [42], Co_2CrAl type Heusler alloy, inorganic compounds [68] and CuFe_2O_4 thin film [69]. A number of mechanisms and new models have been proposed to explain the phenomenon of negative magnetization [64]. Usually, negative magnetization appears in complex ferri or canted antiferromagnetic systems or two phase magnetic system.

Since, a non-zero, but negative residual field of the superconducting magnet during cooling is another possible reason for the observed diamagnetism, we have checked the residual field. It was +2.5 Oe, which is positive. Therefore, the observed negative magnetization is not due to the residual field of SQUID magneto meter during cooling. Furthermore, the investigated sample is ferrite sample; we can safely exclude superconductivity as the origin for the observed negative magnetization down to $\sim 35\text{K}$.

Reports of materials exhibiting asymmetry along the magnetization axis have been limited to a two-phase magnetic system [60]. In this case, the hysteresis loop was explained as a symmetrical $\alpha\text{-Fe}_2\text{O}_3$ loop superimposed upon a very hard magnetization in one direction. This explanation cannot be

applied indiscriminately to our sample because it is essentially a single phase material.

However, $\text{CuAl}_{0.6}\text{Fe}_{1.4}\text{O}_4$ ($x= 0.6$) composition represents a complicated magnetic system. Magnetic interactions of the A-sites cations with the B-sites cations (A - B interactions) and of the B-sites cations among themselves (B - B interactions) give rise to five distinct interactions. The effects of $\text{Fe}_B - \text{Cu}_B$ and $\text{Fe}_B - \text{Fe}_B$, B - B interactions have been ignored. These interactions make it possible to obtain the multiple magnetic effects required to understand the experimental results. In copper-ferri-aluminates the $\text{Fe}^{3+} - \text{O}^{2-} - \text{Fe}^{3+}$, A - B interaction is the strongest single interaction and will give rise to a net magnetic moment whether or not a canted spin arrangement of the Fe^{3+} - ions exists. In addition, a weaker A - B, $\text{Fe}^{3+} - \text{O}^{2-} - \text{Cu}^{2+}$ interaction exists as well as a direct B - B, $\text{Cu}^{2+} - \text{Cu}^{2+}$ interaction. If these latter two interactions are of comparable magnitude, the Cu^{2+} ions will have a canted spin arrangement with a net magnetic moment. This copper moment, with a net effect antiparallel to that of the Fe^{3+} ions but with different temperature dependence, could give rise to a compensation effect. However, despite the simplifications, the above description should be illustrative of the true behaviour of the sample. As discussed earlier, for $\text{NiAl}_x\text{Fe}_{2-x}\text{O}_4$ spinel ferrite system annealed at the rate of $1^\circ/\text{min}$, compositions with $x \geq 0.63$ have shown reversal in the direction of the resultant magnetization [70]. These results are consistent with present findings. The possibility of the presence of uncompensated spins at grain boundaries of polycrystalline sample

[71], or the crystallographic imperfections cannot be neglected as a possible cause for negative magnetization.

(ii) for all the four compositions, $x = 0.0, 0.2, 0.4$ and 0.6 , as the temperature decreases, the ZFC curve splits from the FC one below T_{irr} , abruptly falls below T_s' and finally saturates at T_F (Figure 4). Such anomaly at T_s' and T_F on the ZFC curve was observed earlier in CoCr_2O_4 and MnCr_2O_4 spinels [60]. On the similar line of argument in copper - ferrite - aluminates, magnetic order consists coexistence of a ferrimagnetic long range order and short range order [70], at all temperatures below the Neel temperature (T_N) up to T_{irr} . The short range order transforms into long-range at T_s' while below T_F the ferrimagnetic long – range order and the short range order coexist. The low temperature neutron scattering, specific heat and dielectric measurements are essential to understand the low temperature anomaly in the system.

The temperature dependence of relative ac susceptibility, $\chi_{\text{ac}}(T)/\chi_{\text{ac}}(R_T)$ ($\chi_{\text{ac}}(T)$) for all the four compositions is shown in Fig. 5. For $x = 0.0, 0.2$ and 0.4 compositions, the $\chi_{\text{ac}}(T)$ displays two peaks. The first asymmetric peak at a high temperature corresponds to ferrimagnetic to paramagnetic transition temperature. The emergence of the peak just below the transition temperature can be explained based on the fact that, at lower temperature a higher value of magnetization is expected in ferrimagnetic system due to an ordering of spins within the domains. On the other hand, magnetic hardness also increases because of domain wall pinning mechanism at lower temperature. Both the competing agencies result in a peak near the transition temperature. The second

lower temperature peak has the shape, which is rather like a hump, which is an indication of some degree of magnetic ordering or net result of competing anisotropies. Such a 'cusp' in susceptibility resembles the feature shown by spin glasses [72-73] and spin-glass-like phases. However, such a feature also arises due to locally canted spins system [74 - 76]. The second peak arises where magneto crystalline anisotropy constant changes its sign. The temperature at which the sign reversal occurs is referred to as an isotropic point. Below this temperature shape anisotropy dominates and coercive force increases rapidly resulting in a rapid diminution of susceptibility.

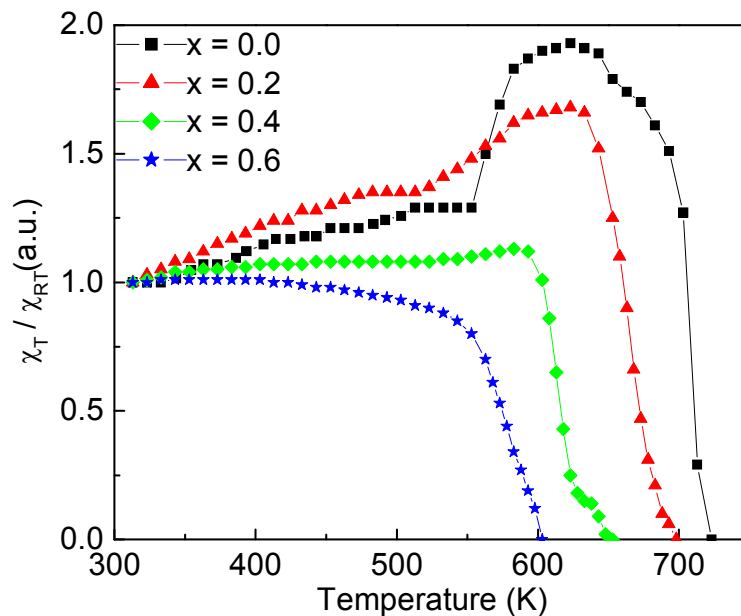


Figure 5. Temperature dependence of ac susceptibility $\chi_{ac}(T)/\chi_{ac}(R_T)$ for different compositions of $\text{CuAl}_x\text{Fe}_{2-x}\text{O}_4$ system.

We see that the ferrimagnetic peak gradually diminishes on Fe- dilution indicating shift towards lower temperature and decrease in T_N . However, low temperature broad hump appears around the same temperature for $x = 0.0, 0.2$

and 0.4 compositions. The sample with $x = 0.6$ shows normal ferrimagnetic behavior.

In general, the observed features of ac susceptibility curves arise in the systems with high concentration of anisotropy ions like Co^{2+} , Mn^{3+} , Fe^{2+} as they can give rise to a local induced anisotropy. It has been shown that the system under investigation possesses small concentration of anisotropy ion Fe^{2+} .

The possibility of any spin-glass-like phase is thus ruled out based on the above discussion and the following facts:

(i) It is well known that when ferrites are sufficiently diluted with non-magnetic cations they can show a wide spectrum of magnetic structure [74]. According to Scholl and Binder [77] if the magnetic ion concentration on the A-sites and B-sites is lower than the A-sub lattice percolation threshold (0.429) and the B-sub lattice percolation threshold (0.390) respectively, no long range ordering is possible in the system. However, if we assume that the short range interactions are present and these are limited to the first neighbours, then according to mean field theory, the interacting spins form clusters which behave as single entities below a certain temperature. These clusters may not have the collinear spin configuration within, as the nearest neighbours are at random.

In the present system, magnetic ion concentration on both the sites is well above the percolation threshold limits thus; spin glass like phases cannot be expected.

(ii) If the canting angle is greater than 60° , it is expected that a transverse component is much larger than a longitudinal component. As a result there is a

gradual increase of spin-spin correlation as the temperature is lowered and that favours cluster spin glass type magnetic ordering [78-79].

The canting angle is much smaller than 60° , (Table 1) that prevents formation of spin glass like phases in the system.

(iii) On increasing the applied frequency, peak and hump temperatures should shift towards lower temperature side, which is a general feature of the cluster spin glass type of magnetic ordering.

No such shifting in peak and hump temperatures have been observed on increasing the frequency to ~ 1300 Hz (not shown). Thus, the possibility of spin glass type of magnetic ordering is ruled out.

(iv) If the system approaching the cluster spin glass type of magnetic ordering, sudden rise in $\chi_{ac}(T)$ with magnetic dilution has been observed [80-81], this is because of the inter-cluster interaction comparable to the thermal energy. As a result, there may be a rapid increase in magnetic viscosity resulting in the freezing of clusters.

The system studied shows no sudden rise in $\chi_{ac}(T)$ curves on magnetic dilution by replacing of magnetic (Fe^{3+}) ions by non-magnetic (Al^{3+}) ions. This further supports the absence of spin glass type magnetic ordering.

(v) If the observed magnetic moment is much lower than the spin only moments of constituent cations, one can expect that no long range ordering contributes to transverse component but it exists only for the longitudinal component. This supports the random freezing of 'spin clusters' in the system,

rather than freezing of individual spins as in the case of conventional spin glass [82].

The present system showed magnetic moment for different compositions not very much lower than the Neel's moment. Thus, the possibility of spin glass type magnetic ordering is ruled out.

The magnetic transition temperature, i.e. Neel temperature (T_N), at which the magnetic susceptibility vanishes, is determined from the thermal variation of ac susceptibility measurements for different compositions as listed in Table 2. Copper ferrite is ferrimagnetic at room temperature with Neel temperature of 738 K [3], although lower values down to 290K have also been reported [2]. The Neel temperature $\sim 733\text{K}$ found for CuFe_2O_4 ($x = 0.0$) (Table 2) lies in the expected range.

Table 2. Neel temperature (T_N) for $\text{CuAl}_x\text{Fe}_{2-x}\text{O}_4$ system.

Al ³⁺ -content (x)	Neel temperature, $T_N(\text{K})$,	
	ac susceptibility $\pm 2\text{K}$	Theoretical
0.0	733	-
0.2	693	698
0.4	653	654
0.6	613	610

Table 2 shows the Neel temperature decreases with increasing Al³⁺ - content (x) in the system. The Neel temperature depends on the active magnetic linkages per magnetic ion per formula unit. The substitution of non-magnetic Al³⁺ ions ($0\mu_B$) for magnetic Fe³⁺ ions ($5\mu_B$) in the system weakens the Fe³⁺ - O²⁻ - Fe³⁺ super exchange linkages and hence the Neel temperature.

The Neel temperatures have also been calculated theoretically for $x = 0.0 - 0.6$ compositions, applying the modified molecular field theory [83] and using the cation distribution found from x-ray diffraction line intensity calculations. The average number of magnetic interactions, $n(x)$, for a ferrite with non-magnetic substitution (x) is given by:

$$n(x) = \frac{1}{N} [f_t f_o (Z_{BA} C_o + Z_{AB} C_t)] \quad (4)$$

Where, f_t and f_o are the fractions of magnetic concentration with respect to un-substituted ferrite and C_t and C_o are the number of metal ions at the tetrahedral and octahedral sites respectively, Z_{BA} and Z_{AB} denote the A-site nearest neighbours to the B-site, and the B-site nearest neighbour to the A-site respectively. N is the total number of magnetic ions in a substituted ferrite. In CuFe_2O_4 , each iron ion at the A-site is surrounded by twelve octahedral ions (Z_{AB}) on the other hand, each iron ion at the B-site has only six A-nearest neighbours (Z_{BA}). Thus, equation (4) reduces to:

$$n(x) = \frac{24}{N} (f_t f_o) \quad (5)$$

The influence of Al^{3+} -ion substitution upon Neel temperature of un-substituted ferrite CuFe_2O_4 may be approximated through its effect upon the average number, $n(x)$ of the super exchange interactions per magnetic ion per formula unit. In the case of $\text{M}'_{1-x}\text{M}''_x\text{Fe}_2\text{O}_4$ (where M' and M'' are non-magnetic divalent cations), there are $24/2$ interactions per magnetic ion Fe^{3+} which is denoted by $n(x = 0)$. In the present case, the un-substituted ferrite possesses three magnetic cations ($\text{Cu}^{2+} + 2\text{Fe}^{3+}$) with magnetic moment; Cu^{2+} ($1\mu\text{B}$) and

Fe^{3+} ($5\mu\text{B}$). The introduction of non-magnetic Al^{3+} - ions into CuFe_2O_4 will reduce $n(x = 0)$, which is expressed by general chemical formula of spinel ferrite system under investigation: $\text{CuAl}_x\text{Fe}_{2-x}\text{O}_4$ and equation (5), as:

$$n(x) = \frac{24}{1 + 5(2 - x)} [f_t f_0]$$

Therefore, the Neel temperature of Al^{3+} - substituted CuFe_2O_4 , $T_N(x)$, will vary approximately as $n(x)$, so that it can be related to the Neel temperature of CuFe_2O_4 , $T_N(x = 0)$, by:

$$T_N(x) = \frac{n(x)}{n(x = 0)} T_N(x = 0) \quad (6)$$

The Neel temperatures estimated using equation (6) for $x \leq 0.6$ compositions are in good agreement with the measured values and given in Table 2. The difference observed between measured and calculated Neel temperature values is due to the random variation of number of super exchange interactions per magnetic ion because of the random distribution of Al^{3+} - ions at the A- and B-sites.

(D) Conclusions

From the aforementioned x-ray powder diffraction, field dependent magnetization $M(H)$, dc magnetization ($M(T)$) and ac susceptibility $\chi_{ac}(T)$ measurements on $\text{CuAl}_x\text{Fe}_{2-x}\text{O}_4$ spinel ferrite system, several important experimental conclusions are listed below:

- (1) $M(H)$ curves show high field slope, negligible coercive field and remanence. These results suggest that the materials under study are low anisotropic materials with canted spin structure.
- (2) The flat response of the FC magnetization with temperature, relatively small difference in the FC and ZFC magnetization, a very broad maximum in vicinity to bifurcate temperature and a broad hump in ac susceptibility curves are characteristic features of a low anisotropy material. The observed features in ac susceptibility and dc magnetization may arise in locally canted spins system from magnetic domain effect but not due to cluster spin glass phase in the system.
- (3) The composition with $x = 0.2$ shows a bifurcation between the FC and ZFC curves for the whole temperature range which indicates that the composition is not magnetically homogeneous although the material is chemically homogeneous. The negative magnetization below 35K for $x = 0.6$ composition is due to the copper ion moment, with a net effect antiparallel to that of the Fe^{3+} ions with different temperature dependence giving rise to a compensation effect.

(4) The anomaly at T_s' and T_F on the ZFC curves for all the compositions is due to coexistence and interplay between the ferrimagnetic long range ordering and short range ordering in the system.

References

- [1] G. F. Goya, H. R. Rechenberg, J. Z. Jiang, J. Appl. Phys. 84(2)(1998)1101-1108.
- [2] M. U. Rana, M. Ul. Islam, T. Abbas, Solid State Commun. 126 (2003)129-133.
- [3] Ch. Venkateshwarlu, D. Ravinder, J. Alloys Compd. 426(2006)4-6.
- [4] V. V. Parfnov, R. A. Nazipov, Inorg. Mater. 38(1) (2002)78-82.
- [5] A. Yang, Z. Chen, S. M. Islam, C. Vittoria, V. G. Harris, J. Appl. Phys. 103(2008) 07E509(1-3).
- [6] Xu. Zuo, A. Yang, C. Vittoria, V. G. Harris, J. Appl. Phys. 99(2006)08M909 (1-3).
- [7] K. G. Saija, U. S. Joshi, V. K. Lakhani, K. B. Modi, J. Phys. D: Appl. Phys. 42 (2009) 165402 (5pp)
- [8] J. Darul, Z. Kristallogr. Suppl. 30(2009)335-340.
- [9] A. Yang, Z. Chen, Xu. Zuo, D. Arena, J. Kirkland, C. Vittoria, V. G. Harris, J. Appl. Phys. 86(2005) 252510(1-3).
- [10] M. M. Ibrahim, M. S. Seehra, G. Srinivasan, J. Appl. Phys. 75(1994)6822-6824.
- [11] M. Desai, S. Prasad, N. Venkataramani, I. Samajdar, A. K. Nigam, R. Krishan, J. Appl. Phys. 91(4)(2002)2220-2227.
- [12] M. Sultan, R. Singh, Mater. Lett. 63(21)(2009)1764-1766.
- [13] D. Thapa, N. Kulkarni, S. N. Mishra, P. L. Paulose, P. Ayyub, J. Phys.D.: Appl.Phys. 43 (2010) 195004 (5pp).

- [14] M. A. Gabal, Mater. Lett. 64(17)(2010)1887-1890.
- [15] S. A. Mazen, N. I. Abu-Elsaad, J. Magn. Magn. Mater. 36(5)(2010)1597-1601.
- [16] B. S. Randhawa, H. S. Dosanjh, M. Kaur, Ceram. Int. 35(3)(2009)1045-1049.
- [17] N. M. Deraz, J. Alloys Compd. 501(2)(2010)317-325.
- [18] T. G. Altincekic, I. Boz, A. Baykal, S. Kazan, R. Topkaya, M. S. Toprak, J. Alloys Compd. 493(1-2)(2010)493-498.
- [19] P. P. Kankare, M. R. Kadam, R. P. Patil, K. M. Garadkar, R. Sasikala, A. K. Tripathi, J. Alloys Compd. 501(1)(2010)37-41.
- [20] P. V. Reddy, J. Appl. Phys. 63 (1998) 3783-3785.
- [21] V. K. Lakhani, T. K. Pathak, N. H. Vasoya, K. B. Modi, Solid State Sci. 13 (2011) 539-547.
- [22] K. B. Modi, H. H. Joshi, R. G. Kulkarni, J. Mater. Sci. 31 (1996) 1311-1317.
- [23] U. V. Chhaya, R. G. Kulkarni, Mater. Lett. 39 (1999) 91-96.
- [24] K. G. Saija and K. B. Modi, Unpublished work.
- [25] M. Almokhtar, A. M. Abdalla, M. A. Gaffar, J. Magn. Magn. Mater. 272-276(2004)2216-2218.
- [26] R. G. Kulkarni, B. S. Trivedi, H. H. Joshi, G. J. Baldha, J. Magn. Magn. Mater. 159(1996)375-380.
- [27] I. Maghsoudi, M. J. Hadianfard, H. Shokrollahi, J. Alloys Compd. 481(1-2) (2009)539-542.

- [28] B. S. Trivedi, R. G. Kulkarni, *Solid State Commun.* 86(1993)327-331.
- [29] M. M. Eltabey, K. M. El-Shokrofy, S. A. Gharbia, *J. Alloys Compd.* 509(5) (2011)2473-2477.
- [30] S. S. Ata-Allah, M. Kaiser, *J. Alloys Compd.* 74(2009)303-309.
- [31] S. M. Patange, S. E. Shirsath, K. S. Lohar, S. S. Jadhav, N. Kulkarni, K. M. Jadhav, *Physica B: Condens. Matt.* 406(3)(2011)663-668.
- [32] V. K. Lakhani, K. B. Modi, *Solid State Sci.* 12(2010)2134-2143 and references there in.
- [33] P. A. Joy, P. S. Anil Kumar, S. K. Date, *J. Phys. Condens. Matter* 10(1998)11049-11054.
- [34] J. Perez, J. Garcia, J. Blasco, J. Stankiewicz, *Phys. Rev. Lett.* 80(1998)2401-2404.
- [35] K. Binder, A.P. Young, *Rev. Mod. Phys.* 58(1986)801-976.
- [36] J.A. Mydosh, *Spin glasses: (London: Taylor and Francis)1993*
- [37] J.E. Gareedan, N. P. Raju, A. Maigna, Ch. Simon, J. S. Pederson, A. M. Niraimathi, E. Gmelin, M. A. Subramaniam, *Phys. Rev. B.* 54 (1996)7189-7200.
- [38] S. Pechev, B. Chevalier, D. Lattargne, B. Darriet, T. Roisnel, J. Etourneau, *J. Magn. Magn. Mater.* 191(1999)282.
- [39] P. S. Anil Kumar, P. A. Joy, S. K. Date, *J. Phys. Condens. Matter* 10(1998) L487-L493.
- [40] N. Kumar, A. Sundarsen, *Solid State Commun.* 150(25-26)(2010)1162-1164.

- [41] P. S. R. Murthy, K. R. Pirolkar, P. A. Bhoose, A. Das, P. R. Sarode, A. K. Nigam, *J. Magn. Mater.* 322(22)(2010)3704-3709.
- [42] Amit Kumar, S. M. Yusuf, L. Keller, J. V. Yakhmi, *Phys. Rev. Lett.* 101 (2008) 207201(1-4)
- [43] S. N. Dolia, *J. Phys.:Conf. Seri.* 200(2010)072026(1-4).
- [44] N. Novosel, D. Pajje, A. T. Raghavender, K. Zadro, K. M. Jadav, *J. Phys.:Conf. Seri.* 200(2010)072070(1-4).
- [45] John Jacob, M. Abdul Khadar, *J. Appl. Phys.* 107(2010)114310-1 - 114310-10.
- [46] P. S. Anil Kumar, P. A. Joy, S. K. Date, *Bull. Mater. Sci.* 23(2) (2000)97-101.
- [47] H. Bhargava, N. Lakshmi, V. Sebastian, V. R. Reddy, K. Venugoplan, Ajay Gupta, *J. Phys. D: Appl. Phys.* 42(2009)245003(8pp).
- [48] B.S. Trivedi, N. N. Jani, H. H. Joshi, R.G. Kulkarni, *J. Mater. Sci.* 35(2000)5523-5526.
- [49] S. S. Ata-Allah, *Mater. Chem. Phys.* 87 (2004)378-386.
- [50] S. S. Ata-Allah, M. K. Fayek, H. S. Refai, M. F. Mostafa, *J. Solid State Chem.* 149 (2000)434-442.
- [51] V. K. Lakhani, K. B. Modi, *J. Phys. D: Appl. Phys.* 44 (2011)
- [52] C. R. K. Murthy, S. D. Likhite, P. Sashrabudhe, *Proc. Ind. Acad. Sci.* 87A(1978)245.
- [53] B. H. Toby, *Powder diff.* 21(1) (2006) 67-70.
- [54] M. J. Buerger, *Crystal Structure Analysis*, Wiley, N. Y., 1960.

- [55] R. R. Heikes, in *Thermoelectricity* (eds), Heikes RR and Ure RW, New York: Wiley International, 1961.
- [56] R. M. Persoons, E. de Grave, P.M.A. de Bakker, R. E. Vandenberghe, *Phys. Rev. B.* 47(1993)5894-5905.
- [57] B. C. Zhao, H. W. Hu, B. Xia, L. H. Tan, A. C. Huan, L. Wang, *Appl. Phys. Lett.* 93(2008)222506-222509.
- [58] L. Néel, *Ann. Phys.* 3(1948)137-142.
- [59] A. Rosencwaig, *J. Phys.* 48(1970) 2857-2867.
- [60] N. Menyuk, K. Dwight, D. G. Wickham, *Phys. Rev. Lett.* 4(3) (1960)119-120.
- [61] V. I. Trukhin, V. I. Maksimochkin, Yu. A. Elesin, V. A. Zhilyaeva, *Moscow Uni. Phys. Bull.* 62 (1) (2007)51-57.
- [62] K. Tomiyasu, J. Fukunaga, H. Suzuki, *Phys. Rev. B.* 70 (2004)214434(1-12).
- [63] L. Wang, J. Ding, A. Roy, J. Ghose, Y. Li, Y. P. Feng, *J. Phys. Condens. Matter* 12(2000) 9963-9972.
- [64] V. A. Khomchenko, I. O. Troyanchuk, R. Szymczak, *J. Mater. Sci.* 43 (2008)5662-5665.
- [65] O. Kahn, *Nature (London)* 399(1999)21-22.
- [66] Yu. G. Chukalkin, V. R. Shtirts, *Phys. Stat. Sol. A* 173(2) (1999) 459-465.
- [67] R. P. Singh, C. V. Tomy, *J. Phys. Condens. Matter* 20 (2008) 235209 (7pp).

- [68] C. Mathoniere, C. J. Nuttall, S. G. Carling, Day Peter, *Inorg. Chem.* 35 (5) (1996) 1201-1206.
- [69] M. M. Ibrahim, M. S. Seehra, *J. Appl. Phys.* 75(10) (1974)6822- 6824.
- [70] L. R. Maxwell, S. J. Pickart, *Phys. Rev.* 92(5) (1953)1120-1126.
- [71] G. Lawes, B.Melot, K.Page, C.Ederer, M.A.Hayward, Th.Proffen,R.Seshadri, *Phys. Rev. B.* 74 (2006)024413(1-6).
- [72] C. Y. Huang, A review, *J. Magn. Magn. Mater.* 51 (1985)1-74.
- [73] J. L. Soubeyroux, D. Fiorani, E. Agostinelli, *J. Magn. Magn. Mater.* 54 (1986) 83-84.
- [74] J. L. Dormann, M. Nogues, *J. Phys. Condens. Matter* 2 (1990)1223-1237.
- [75] S. M. Yusuf, V. C. Sahni, L. Madhav Rao, *J.Phys. Condens. Matter* 7 (1995) 873-881.
- [76] S. M. Yusuf, L. Madhav Rao, *PRAMANA-J.Phys.* 47 (1996) 171-182.
- [77] F. Scholl, K. Binder, *J. Phys. B.* 39(1980)239-247.
- [78] R. B. Jotania, R. V. Upadhyay, R. G. Kulkarni, *IEEE Trans. Magn.* 28(4) (1992)1889-1894.
- [79] J. Nogues, T. Puig, R. B. Jotania, R. V. Upadhyay, R. G. Kulkarni, K. V. Rao, *J. Magn. Magn. Mater.* 99(1991)275-279.
- [80] B. S. Trivedi, Ph.D. thesis, Saurashtra University Rajkot, India, 1993.
- [81] K. B. Modi, Ph.D. thesis, Saurashtra University Rajkot, India, 1996.
- [82] K. B. Modi, H. H. Joshi, R. G. Kulkarni, *Ind. J. Pure Appl. Phys.* 34 (1996) 92-95.
- [83] G. J. Baldha,R. V. Upadhyay, R. G. Kulkarni, *J.Mater. Sci.* 23 (1988) 3357-3361.

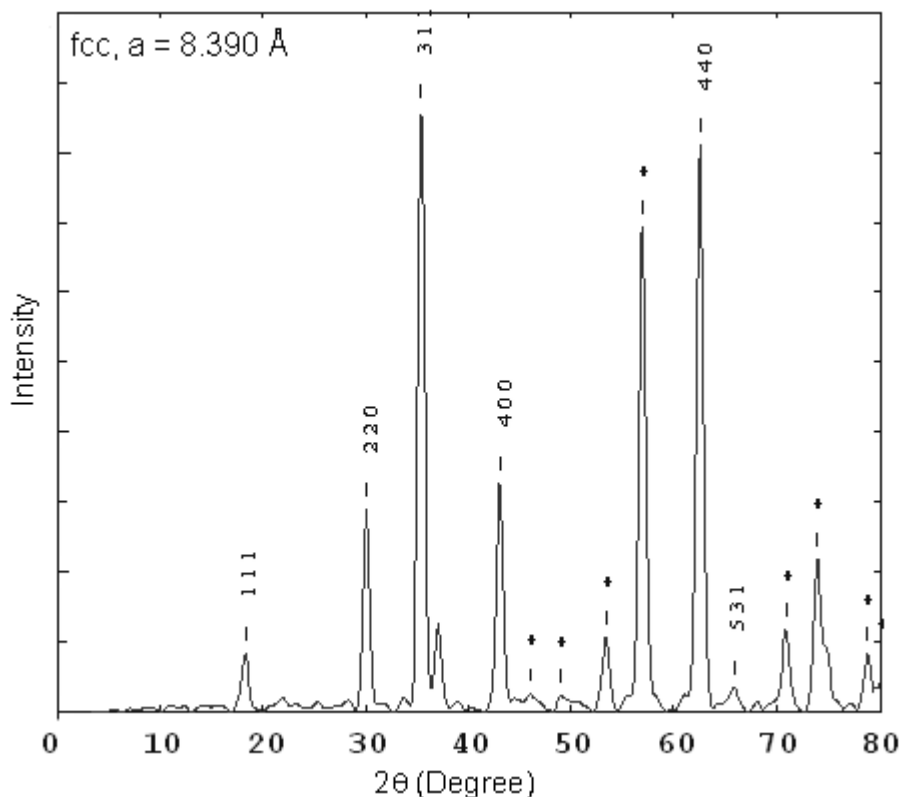
Chapter 5

Quenched $\text{CuAl}_x\text{Fe}_{2-x}\text{O}_4$ system

5.1 Structural analysis, cation distribution and structural parameters determination.

(A) X-ray powder diffraction patterns analysis

The room temperature (300K) x-ray diffraction (XRD) patterns of the samples were obtained by x-ray powder diffractometry. Indexing and refinement of XRD patterns were carried out using powder-X software [1]. An attempt to fit the XRD spectra in a single phase fcc spinel structure (space group $O_h^7 Fd\bar{3}m$) or single phase tetragonal spinel with space group $I4_1/amd$, fail to large extent. Figure 5.1 shows x-ray powder diffraction patterns for un-substituted CuFe_2O_4 ($x = 0.0$) fitted assuming (a) fcc spinel structure, with lattice constant value, $a = 8.390 \text{ \AA}$ (b) tetragonal structure, with lattice parameters values $a = b = 5.945 \text{ \AA}$, $c = 8.225 \text{ \AA}$ and $c/a = 1.38$ by keeping 2θ error, 0.05.



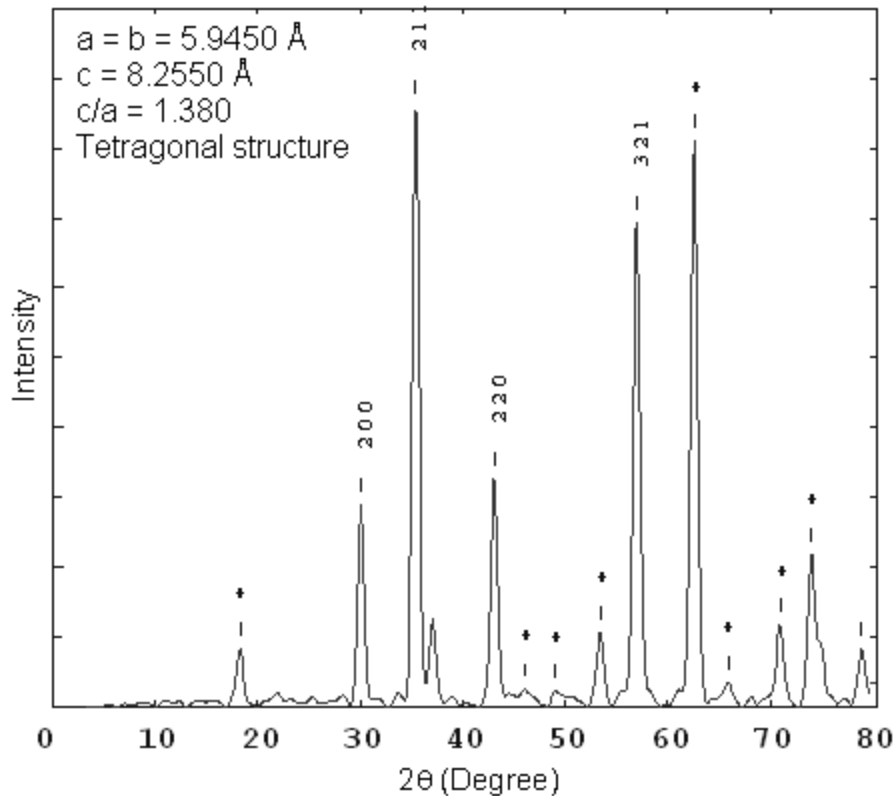


Figure 5.1 X-ray powder diffraction patterns for copper ferrite (*indicates un-indexed diffraction peak).

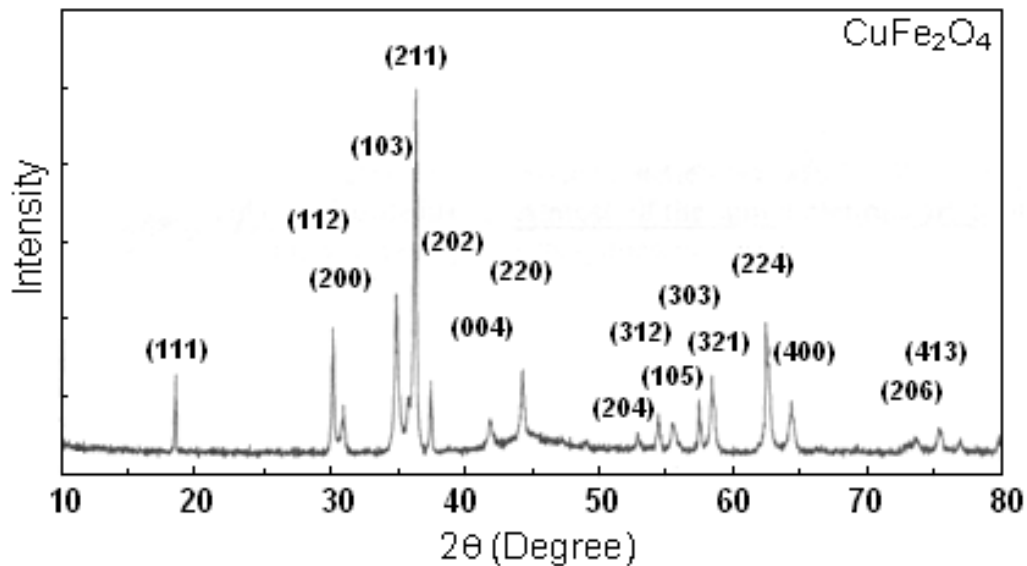
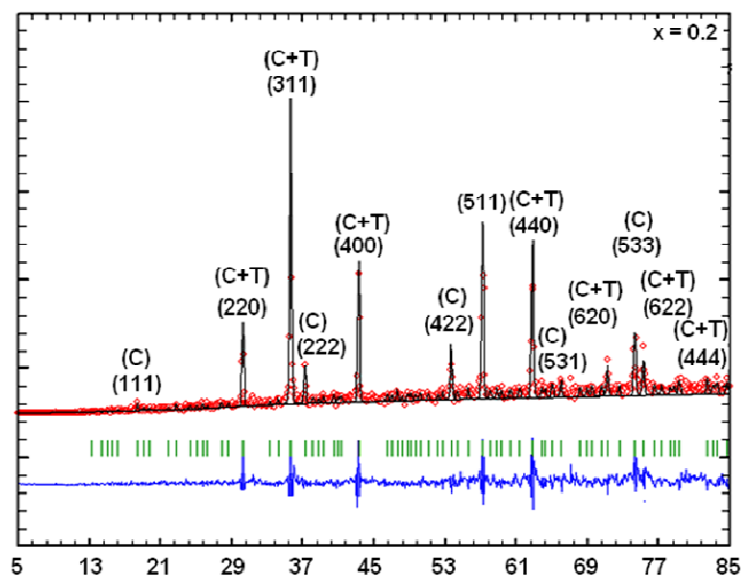


Figure 5.2 X-ray powder diffraction pattern at room temperature for CuFe_2O_4 .

For the sake of comparison, x-ray diffraction pattern of tetragonal structured (space group $I4_1/amd$) and $c/a \sim 1.449$ [2] CuFe_2O_4 , is shown in Figure 5.2. In spite of the fact that a quench cooling process usually leads to the cubic structure of CuFe_2O_4 [3], from structural analysis results based on the powder diffraction data we confirmed that the rapidly quenched samples of the system $\text{CuAl}_x\text{Fe}_{2-x}\text{O}_4$ ($x = 0.0, 0.2, 0.4$ and 0.6) possess a tetragonally distorted spinel structure with non-standard face-centered space group $F4_1/ddm$. Figure 5.3 displays Rietveld fitted (using general scattering analysis software (GSAS) [4]) XRD patterns for the selected compositions with $x = 0.2, 0.6$. One of the most important Rietveld error indices is that of χ^2 [5].



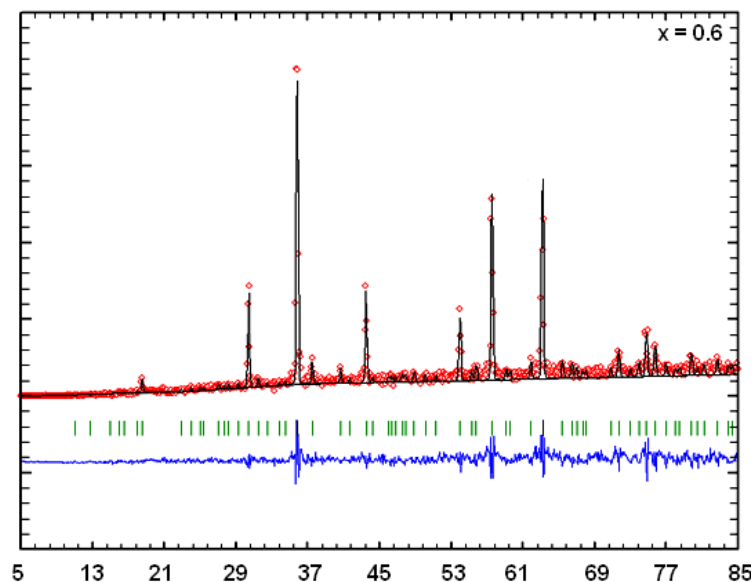


Figure 5.3 Rietveld – fitted XRD patterns for quenched Cu-Fe-Al-O system for $x = 0.2$ and 0.6 compositions at 300K.

The χ^2 values (1.3 - 1.6) obtained in the present analysis suggest good refinement of the data. The samples showed a dominant cubic phase with a minor tetragonal component. The lattice parameters obtained from the above mentioned refinements are given in Table 5.1, from which it is seen that the lattice parameters ($a = b$ and c) decrease with increasing Al^{3+} - concentration (x) in the system. The linear decrease in lattice constants is due to the replacement of larger Fe^{3+} - ions with ionic radius of 0.645 \AA by smaller Al^{3+} - ions with ionic radius of 0.535 \AA in the system.

The axial ratio (c/a) for $\text{CuAl}_x\text{Fe}_{2-x}\text{O}_4$ ($x = 0.0$) is found to be 1.037 and it increases to 1.050 for $x = 0.6$ composition, suggests enhancement of tetragonal distortion with increasing Al- content (x). The JCPDS card gives $c/a = 1.06$ for CuFe_2O_4 while Naik et al. [6] have reported values ranging between 1.01 and 1.06. According to other authors [7], crystal cell parameters may vary from $a = b =$

8.20 to 8.30 Å and $c = 8.544$ to 8.692 Å, but axial ratio (c/a) remains almost constant (1.03 – 1.05). The axial ratio ($c/a = 1.037$) found for CuFe_2O_4 (Table 5.1) lies in the expected range. The c/a ratio can be changed via decreasing the copper concentration, or alternatively, by heat treatment temperature and cooling rate [8]. The structure of pure CuFe_2O_4 ($x = 0.0$) and Al^{3+} substituted CuFe_2O_4 ($x = 0.2 - 0.6$) is considered as that of a tetragonally deformed spinel stretched along the $\langle 011 \rangle$ direction. According to theorem of Jahn-Teller (JT), molecules with orbitally degenerate electronic ground state are unstable in the symmetric configuration. The molecule will always find at least one vibrational coordinate along which it can distort to split the degeneracy and lower its energy. The transition metal ions having one, two, four, six, seven and nine 3d-electrons will have orbitally degenerate ground state, but only for the Cr^{2+} , Mn^{3+} , Fe^{4+} ($3d^4$) and Cu^{2+} ($3d^9$) configurations the degeneracy occurs in the strongly anti bonding orbits and the distortion are large unless the long-range elastic coupling between the sites clearly favours another [9]. The commonly observed distortions are of the prolate tetragonal type i.e. octahedraon is elongated so that four ligands lie close to the cation while two are further removed as shown in Figure 5.4.

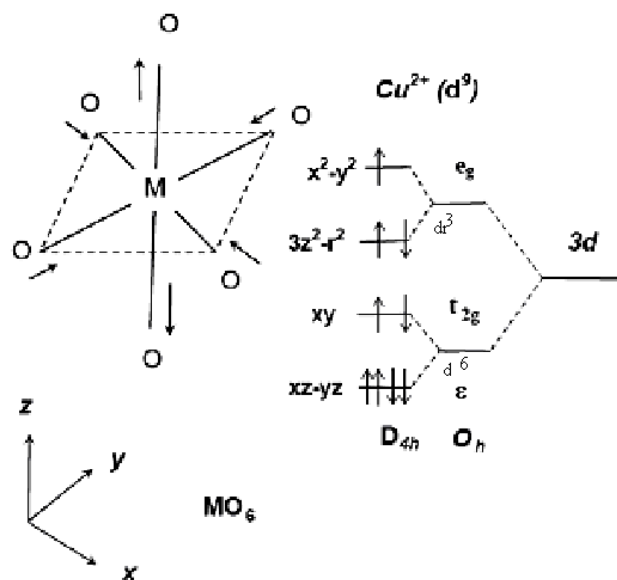


Figure 5.4 Tetragonal distortion of MO_6 octahedron and the 3d orbital energy splitting by the octahedron (O_h) and the tetrahedral site symmetries for Cu^{2+} (d^9) ion under D_{4h} symmetry

Goodenough and Loeb [10] interpreted the migration of Cu-ions to the A-sites in terms of their square-bond formation although Cu-ions are more stable in the B-sites of the spinel lattice. The ground state of Cu^{2+} ion in the octahedral crystal field is an orbital doublet $2E_g$ ($t_{2g}^6 e_g^3$) and so subject to a Jahn-Teller effect which removes the degeneracy of the ground state. Thus, Cu^{2+} -ions at the octahedral (B-) sites tend to suffer from a tetragonal distortion [11]. According to Kim et al. [11], for an octahedral Cu^{2+} compound (C_4X_6) with a $d_e^6 d_\gamma^3$ configuration, a strong Jahn-Teller distortion ($O_h - D_{4h}$) is expected due to its $2E_g$ ground state. With d_γ electron expressed in terms of d_z^2 and $d_{x^2-y^2}$ there are only two possibilities, $(d_z^2)^2(d_{x^2-y^2})^1$ and $(d_z^2)^1(d_{x^2-y^2})^2$. In case of $(d_z^2)^1(d_{x^2-y^2})^2$ configuration, a distortion to a compressed tetragonal structure ($c/a < 1$) is expected. On the other hand, in case of $(d_z^2)^2(d_{x^2-y^2})^1$, configuration, four ligand ions in the xy-plane

are attracted by the central ions on the z-axis, resulting in a distortion of the octahedraon to an elongated tetragonal structure ($c/a > 1$). However, the elongated distrotion rather than the compressed one used to be observed [12].

A precise knowledge of the distribution of cations among the available crystallographic sites of the spinel lattice is essential to understand the various physcial properties of ferrites. There is good contrast in the atomic scattering factor of Al^{3+} to that of Fe^{3+} and Cu^{2+} , but the scattering factor of Cu^{2+} is close to that of Fe^{3+} [13]. Thus, it is not possible to obtian the distribution of Fe^{3+} and Cu^{2+} between the A- and B-sites using XRD technique. The x-ray scattering factor of Al^{3+} is significantly low copared to those of the other cations. So, the distribution of Al^{3+} between the two types of sites can be obtained with good accuracy from x-ray analysis. We have used values of axial ratio (c/a) to determine the occupancy of Cu^{2+} ions at the B-sites.

In 1951, the lattice parameteres and the cation ordering parameter, λ , for CuFe_2O_4 as a function of temperature was studied by Bertaut et al. [14]. The parameter λ is the fraction of octahedral interstices occupied by JT ions (Cu^{2+}). The correlation between the axial ratio (c/a) and the concentration of Cu^{2+} ions at the B-sites is well established.

Quantitative correlation between Bertaut's observed axial ratio (c/a) and λ produces the relation: $(\lambda - 0.26) = 3[(c-a)/a]$ for $\lambda \geq 0.26$. The factor $(\lambda - 0.26)$ is a measure of the stress induced by square-bond formation, while the strain is given by: $(c-a)/a$ (Table 5.1). This equation express a linear stress-strain relationship (Hooke's law). We have used here c/a ratio to determine the concentration of

Cu^{2+} - ions ($= 2\lambda$) on the B-sites using the simple relation: $\lambda = 3(c/a) - 2.74$. Once the concentration of Cu^{2+} - ions on the B-sites and corresponding concentration of Cu^{2+} - ions on the A-sites, have been fixed, the distribution of Al^{3+} and Fe^{3+} ions have been determined from x-ray diffraction line intensity calculations using the formula suggested by Buerger [15]. The details are given in the Chapter 4.

Illustrative calculations for the fraction of Cu^{2+} ions on the B-sites, Stress-Strain determination

$$x = 0.4, c/a = 1.055 \text{ (Cu}_{0.15}\text{Fe}_{0.67}\text{Al}_{0.18})[\text{Cu}_{0.85}\text{Fe}_{0.93}\text{Al}_{0.22}]$$

$$\text{From the relation: } \lambda - 0.26 = 3[(c-a)/a]$$

$$\begin{aligned} \lambda &= 3[(c/a)-1]+0.26 \\ &= 3(c/a) - 3 + 0.26 \end{aligned}$$

$$\lambda = 3(c/a) - 2.74 = 3(1.055) - 2.74 = 0.425$$

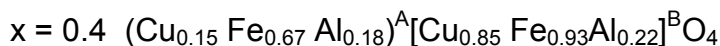
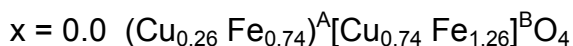
$$\text{Concentration of JT } \text{Cu}^{2+} \text{ - ions on the B-sites} = 2\lambda = 2(0.425) = 0.850$$

$$\text{Stress: } \lambda - 0.26 = 0.425 - 0.26 = 0.165$$

Included by square band formation

$$\text{Strain: } (c/a) - 1 = 1.055 - 1 = 0.055$$

The final cation distributions, thus, determined for different compositions are given by:



Thus, the observed increase in tetragonal distortion (c/a) (Table 5.1) is mainly due to the increasing concentration of in JT Cu^{2+} -ions on the B-sites.

Earlier, it has been reported that the critical number of the B-site Cu^{2+} ions per spinel formula unit for a cooperative Jahn-Teller distortion to tetragonal symmetry ($c/a > 1$) in copper ferros spinel is ~ 0.8 [8]. The B-sites Cu^{2+} - ions per formula unit in the range 0.74 – 0.90 is consistent with the critical number ~ 0.8 .

Table 5.1 Lattice parameters. axial ratio, stress and strain for $\text{CuAl}_x\text{Fe}_{2-x}\text{O}_4$ system.

Al ³⁺ - content (x)	Lattice constants $\pm 0.002 \text{ \AA}$		c/a	λ	Stress	Strain
	a = b	c				
0.0	8.288	8.595	1.037	0.370	0.110	0.037
0.2	8.202	8.588	1.047	0.400	0.140	0.047
0.4	8.135	8.582	1.055	0.425	0.165	0.055
0.6	8.067	8.575	1.063	0.450	0.190	0.063

Structural Parameters

The compositions of the system under investigation $\text{CuAl}_x\text{Fe}_{2-x}\text{O}_4$ possess small deviation from the cubic symmetry, the formula for the various structural parameters determination for fcc structured materials are thus, applicable to this system also with small uncertainty. However, our aim is to study the variation of different structural parameters with Al³⁺-substitution and relative change in the magnitude. The structural parameters are calculated using the formulae presented in Chapter 4, are summarized in Tables 5.2 – 5.5.

Table 5.2. Lattice constants, molecular weight (M), x-ray density (ρ_x), bulk density (ρ), pore fraction (f) and porosity (P) for quenched Cu-Fe-Al-O system.

Al-content (x)	$a^*(\text{\AA})$ $\pm 0.002\text{\AA}$	M(kg) $\times 10^{-3}$	ρ_x $\text{kg/m}^3 \times 10^3$	ρ $\text{kg/m}^3 \times 10^3$	f	P (%)
0.0	8.389	239.23	5.385	4.820	0.105	10.49
0.2	8.329	233.46	5.369	4.691	0.126	12.62
0.4	8.281	227.69	5.328	4.442	0.166	16.63
0.6	8.233	221.92	5.285	4.638	0.122	12.24

$$a^* = (a^2c)^{1/3}$$

Table 5.3 Ionic radius (r), lattice constant (a) and oxygen positional parameter (u) for Cu-Fe-Al-O system.

Al^{3+} - content(x)	r_A (\AA)	r_B (\AA)	a_{th} (\AA)	$u^{\bar{3}m}$ (1/4, 1/4, 1/4)	$u^{\bar{4}3m}$ (3/8, 3/8, 3/8)		
					Eq.(9)	Eq.(10)	Eq.(11)
0.0	0.6671	0.6765	8.3833	0.2621	0.3871	0.3868	0.3872
0.2	0.6521	0.6730	8.3509	0.2615	0.3865	0.3867	0.3867
0.4	0.6380	0.6690	8.3186	0.2611	0.3861	0.3865	0.3863
0.6	0.6227	0.6657	8.2861	0.2605	0.3855	0.3862	0.3858

Table 5.4 Edge length and bond length for Cu-Fe-Al-O system

Al^{3+} - content(x)	d_{AE} (\AA)	d_{BE} (\AA)	d_{BEu} (\AA)	d_{AL} (\AA)	d_{BL} (\AA)
0.0	3.2525	2.6795	2.9729	1.9917	2.0011
0.2	3.2168	2.6727	2.9510	1.9698	1.9907
0.4	3.1872	2.6683	2.9335	1.9517	1.9828
0.6	3.1560	2.6656	2.9160	1.9326	1.9754

Table 5.5 Interionic distances (b, c, d, e, f and p, q, r, s) and bond angles (θ) for Cu-Fe-Al-O system

Al^{3+} - content (x)	0.0	0.2	0.4	0.6
b	2.9659	2.9447	2.9277	2.9108
c	3.4779	3.4530	3.4331	3.4132
d	3.6324	3.6065	3.5857	3.5649
e	5.4487	5.4097	5.3785	5.3473
f	5.1370	5.1003	5.0709	5.0415
p	1.9960	1.9861	1.9785	1.9716
q	1.9917	1.9698	1.9517	1.9326
r	3.8139	3.7720	3.7374	3.7007
s	3.6909	3.6620	3.6386	3.6149
θ_1	121.42	121.59	121.74	121.91
θ_2	137.13	137.76	138.32	138.99
θ_3	95.97	95.69	95.44	95.15
θ_4	126.59	126.53	126.48	126.41
θ_5	69.51	69.92	70.29	70.72

(Distances in Å and angles in degrees)

The variation of various structural parameters with Al^{3+} - substitution (x) is similar to that for slow cooled system, and thus can be explain based on the similar arguments. The observed small difference in the magnitude of parameters is mainly due to change in cation distribution as result of different thermal history of the compositions

5.2 Microstructural Characterization

SEM analysis

Scanning electron microscopy (SEM) was employed to study the grain morphology of the samples. SEM microphotographs of fractured surface of pellets for all the compositions are shown in Figure 5.5. It is seen that grain

morphology (grain size, uniformity, homogeneity) is greatly influenced by Al^{3+} substitution for Fe^{3+} in the system.

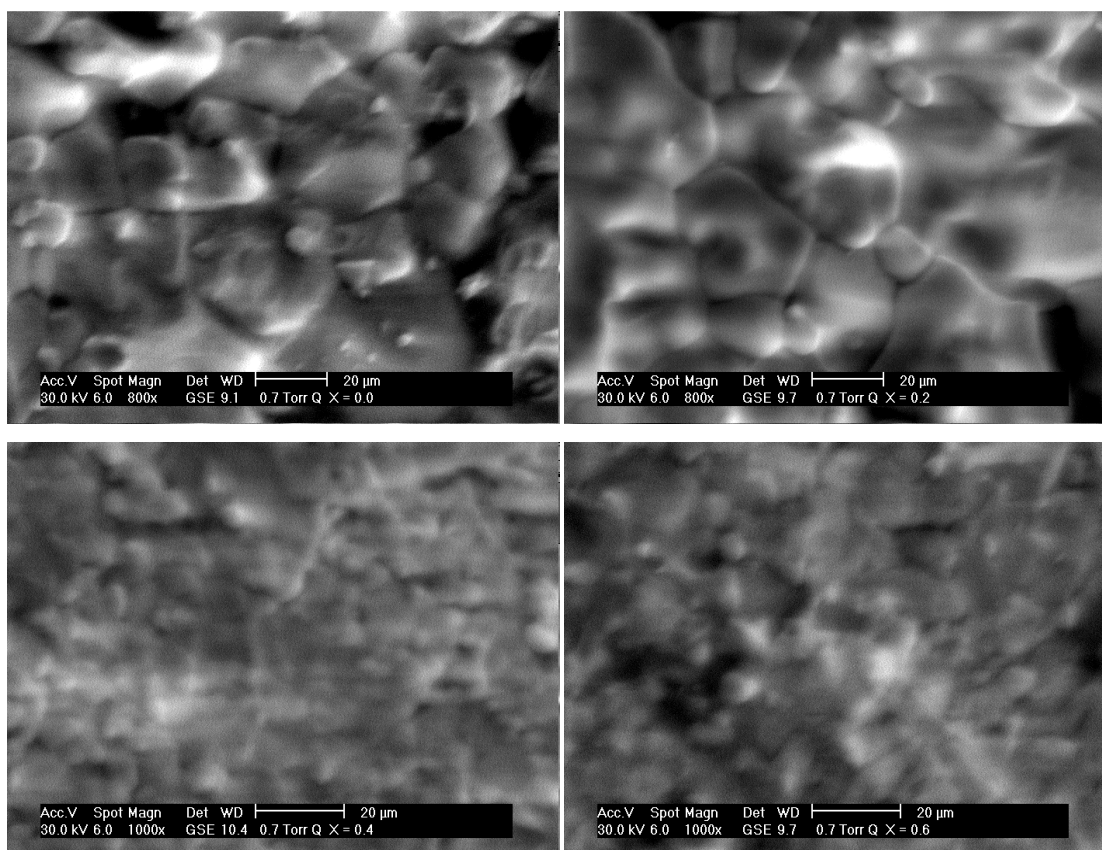


Figure 5.5 The SEM photographs of the fractured surface for the polycrystalline Cu-Al ferrite, $\text{CuAl}_x\text{Fe}_{2-x}\text{O}_4$; $x = 0.0, 0.2, 0.4$ and 0.6 .

We have observed well define grain structure for $x = 0.0$ and 0.2 compositions. With small addition of Al^{3+} - ions ($x = 0.2$), average grain size increases, inter granular voids are found to decrease. The spinel ferrite compositions with $x = 0.4$ and 0.6 show diffused grain structure. Thus, no attempt has been made to determine the grain size, but, certainly average grain size is observed to decrease with increase in Al^{3+} - content(x) for $x > 0.2$. The grain size for $x = 0.0$ composition is found to vary between $20\text{-}25\ \mu\text{m}$ while it is found to vary between $25 - 30\ \mu\text{m}$ for $x = 0.2$ composition. The observed increase in grain

size with Al^{3+} - substitution ($x = 0.2$) is attributed to larger solid solubility of Al^{3+} - ion in the ferrite structure that enhances the grain growth.

The decrease in grain size for $x > 0.2$ compositions can be explained on the similar line of argument as for slow cooled system [16]. The observed difference in grain morphology for slow cooled and quenched systems of copper-ferri-aluminates may be due to different heat treatment employed.

We have observed exaggerated grain growth for $x = 0.0$ and 0.2 compositions. When the grain growth rate is very high, pores may be left behind by rapidly moving grain boundaries, resulting in pores that are trapped inside the grains. The intragranular porosity is practically impossible to eliminate, leading to poor magnetic and mechanical properties. Samples with giant grain and included pores owing to exaggerated grain growth still have good magnetic and mechanical properties than those with normally grown grains provided the distances between pores were the same [17]. We feel that in the present system same mechanism is responsible for excellent magnetic properties of $x = 0.0$ and 0.2 compositions (Table 5.6).

5.3 Magnetic properties of quenched $\text{CuAl}_x\text{Fe}_{2-x}\text{O}_4$ system

(A) M-H loop characteristics and dc magnetization studies

In a unit cell of spinel lattice, eight of the 64 available tetrahedrally oxygen-coordinated A-sites and 16 out of the 32 octahedrally coordinated B-sites are occupied by metal ions or by 1 tetrahedral and 2 octahedral for each formula unit. The type, valence and distribution of these metal ions ultimately control the

physical properties in general and magnetic, electronic properties in particular, of the system.

In the ideal inverse spinel configuration the eight divalent metal ions occupy the B-sites, while the 16 trivalent Fe ions are equally distributed among the A- and B-sites. The magnetic moments of the ions in both A- and B-sublattices are ferromagnetically ordered, while the magnetizations of the these two sublattices are antiparallel with respect to each other.

If CuFe_2O_4 possesses an ideal inverse spinel structure: $(\text{Fe}^{3+}_{1.0})^{\text{A}} [\text{Cu}^{2+}_{1.0}\text{Fe}^{3+}_{1.0}]^{\text{B}}\text{O}^{2-}_4$, its net magnetization can be attributed to the Cu^{2+} ion, amounting to $8\mu_{\text{B}}$ per unit cell or $1\mu_{\text{B}}$ per formula unit. Here, it is assumed that Cu^{2+} ion contribute 1 Bohr magneton.

The replacement of one A-site Fe^{3+} ion by one B-site Cu^{2+} ion: $(\text{Cu}^{2+}_{0.125}\text{Fe}^{3+}_{0.875})^{\text{A}} [\text{Cu}^{2+}_{0.875}\text{Fe}^{3+}_{1.25}]^{\text{B}}\text{O}^{2-}_4$, results in a net-magnetic moment of $16\mu_{\text{B}}$ per unit cell ($\cong 2\mu_{\text{B}}$ / formula unit), assuming each Fe^{3+} ion to contribute $5\mu_{\text{B}}$. Thus, the migration of a single Cu^{2+} ion from the B- to the A-site doubles the magnetic moment. It has been shown that the magnetic moment of CuFe_2O_4 cannot be increased much beyond $2\mu_{\text{B}}$ per formula unit, since the activation energy for the process increases with the presence of on Cu^{2+} at the tetrahedral site, making the transfer of further copper ions increasing unlikely [18].

Recently, enhanced magnetization ($3\mu_{\text{B}}$ at 5K) has been reported for nano particles and thin films of copper ferrite [18]. The role of anisotropy ion, Fe^{2+} , in enhancing and tailoring the magnetization CuFe_2O_4 nanoparticles synthesized from a citrate precursor has been discussed by Thapa et al [18]. The observed

large magnetic moment ($80 \text{ Am}^2/\text{kg}$) for nanosized $\text{Cu}_{0.25}\text{Co}_{0.25}\text{Zn}_{0.25}\text{Fe}_2\text{O}_4$ has been explained in terms of the enhancement in the B-B interaction because of the distortion in the B-sites due to the presence of the Jahn-Teller cation, Cu^{2+} , at this site [19]. It is interesting to note that a high magnetization has also been recently observed in sputter deposited Cu-ferrite grown in a reducing atmosphere [20], sputtering in an oxygen environment followed by subsequent annealing leads to reduced magnetization. On the other hand, 42% increase over the bulk equilibrium value of magnetization has been reported for cation-disordered-enhanced magnetization in pulsed-laser-deposited CuFe_2O_4 films by Harris et al [21]. They have found that Cu^{2+} ion population on the A-sites is systematically increased compared to the bulk value of 0.15 to ~ 0.45 . As a result, the room temperature saturation magnetization is increased as much as 42%. They speculate that lattice strain from both a mismatch in lattice parameter and thermal expansion coefficient between the film and substrate may be responsible for enhancing cation-disorder effect.

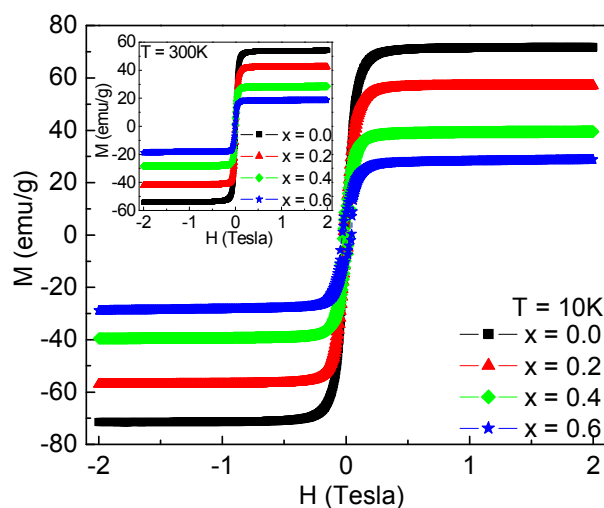


Figure 5.6 Magnetic field dependence of magnetization at 10K; main panel, inset at 300K, for quenched Cu-Fe-Al-O samples.

In Figure 5.6, we show the M-H loops recorded at 10K, while hysteresis loops recorded at 300K are shown in the inset for $x = 0.0, 0.2, 0.4$ and 0.6 compositions. In Table 5.6, the values of saturation magnetization, σ_s (emu/g), and the magneton number, n_B , (saturation magnetization per formula unit in Bohr magneton, μ_B) at 10K and 300K are given. Figure 5.6 displays that there is high field slope to magnetization curve for all the compositions which suggest strong evidence for a canted spin structure, and canting angle varies with applied magnetic field. The observed features may be thought of arising from non-collinear spin arrangement. The high field slope has been established arising due to the high magnetic anisotropy also [22]. Since, all the compositions under study may have very low concentration of magnetic anisotropy ion (Fe^{2+}), this fact does not applicable to the system. The negligible coercivity for different compositions also suggests that these are low anisotropic compounds [23]. From the observed magnetic moment it is clear that the samples show ferrimagnetism behaviour, which decreases with increasing Al^{3+} -content (x) in the system.

The applicability of Neel's two sub-lattice model of ferrimagnetism has been tested for all the samples of the series $\text{CuAl}_x\text{Fe}_{2-x}\text{O}_4$. Accordingly, Neel's magnetic moment, n_B^N , per formula unit in μ_B is expressed as:

$$n_B^N = M_B(x) - M_A(x)$$

where, M_B and M_A are the B- and A-sublattice magnetic moments in μ_B . the n_B^N (μ_B) values for $\text{CuAl}_x\text{Fe}_{2-x}\text{O}_4$ were calculated using cation distribution and ionic magnetic moment of Fe^{3+} , Cu^{2+} and Al^{3+} with their respective values $5 \mu_B$, $1 \mu_B$ and $0 \mu_B$. The experimental values of magnetic moment (n_B) at 10 K are found

lower than the magnetic moment calculated from the Neel's model (n_B^N). This suggests significant canting of the B-site moments or structure to be non-collinear.

The magneton number, n_B , is related to canting angle, (θ_c) by:

$$n_B(x) = M_B(x) \cdot \theta_c - M_A(x)$$

The experimental values of canting angle, θ_c , obtained from the above equation, using measured n_B values (Table 5.6) are listed in Table 5.6.

For a chemically disordered system such as $\text{CuAl}_x\text{Fe}_{2-x}\text{O}_4$ it is quite possible that the canting is not uniform but instead is locally dependent upon the statistical distribution of non-magnetic neighbouring ions. Therefore, the increase in Al^{3+} -substitution leads to the localized non-collinearity of the ferrimagnetic phase. In this region effective moments are created with ferrimagnetic structure by local canting around the magnetic imperfections introduced by aluminium substitution. Therefore, the disagreement between the observed and calculated n_B values can be explained in terms of a random canting of spins (RCS) model proposed by Rosencewaig [24] should be used. According to this model, the B-sites magnetic ions can be considered to be canted with an average canting (θ_c) due to non-magnetic Al^{3+} -substitution which, in the average nearest neighbour approximation is estimated to be:

$$\cos \theta_{\text{RCS}} = \left(\frac{M_A}{M_B} \right) \frac{(J_{AB})}{(J_{BB})}$$

Here, J_{AB} and J_{BB} are exchange integrals. The magnetic coupling, J_{AB}/J_{BB} , remains nearly constant for $x = 0.0 - 0.2$ and thereafter it is getting weakened for

$x > 0.2$ indicates change in the magnetic structure. Furthermore, J_{AB}/J_{BB} is found to be greater than unity for all the compositions and decreases with increase in Al^{3+} -content (x). These suggest $J_{AB} > J_{BB}$ and strength of J_{AB} interaction and relative strength of J_{AB}/J_{BB} interaction decrease with magnetic dilution by non-magnetic Al^{3+} -substitution in the system.

Table 5.6 Magnetic parameters for quenched $\text{CuAl}_x\text{Fe}_{2-x}\text{O}_4$.

Al^{3+} - content (x)	M_B	M_A	n_B^N	σ_s (emu/g) (10K)	$n_B(\text{obs})$ (10K)	$\theta = \cos^{-1} \frac{n_B + M_A}{M_B}$	J_{AB} / J_{BB}
	(μ_B)						
0.0	7.04	3.96	3.08	71.34	3.06	4.32°	1.773
0.2	6.25	3.75	2.50	57.04	2.38	11.25°	1.635
0.4	5.50	3.50	2.00	39.34	1.60	21.99°	1.457
0.6	4.80	3.22	1.58	29.13	1.16	24.15°	1.360

DC magnetization study

Magnetic measurements (field-cooled (FC) and zero-field-cooled (ZFC) magnetization) were performed using the physical property measurement system (PPMS, quantum design). The ZFC magnetization was recorded by first cooling the sample from 325 to 4K in zero magnetic fields, then applying the magnetic field and warming the sample up to 325K in the presence of the magnetic field (10mTesla) and recording the magnetic moment (emu/g) during the warming cycle. Field cooled patterns were obtained by first cooling the sample from 325K down to 4K in the external magnetic field and then warming it up to 325K and recording the magnetic moment.

Data on temperature dependence of magnetization (M-T) recorded in zero-field-cooled (ZFC) and field cooled (FC) modes in and external magnetic

field of 10mTesla for 'virgin' (CuFe_2O_4) and Al^{3+} -substituted ($x = 0.2, 0.4$ and 0.6) samples are shown in Figure 5.7.

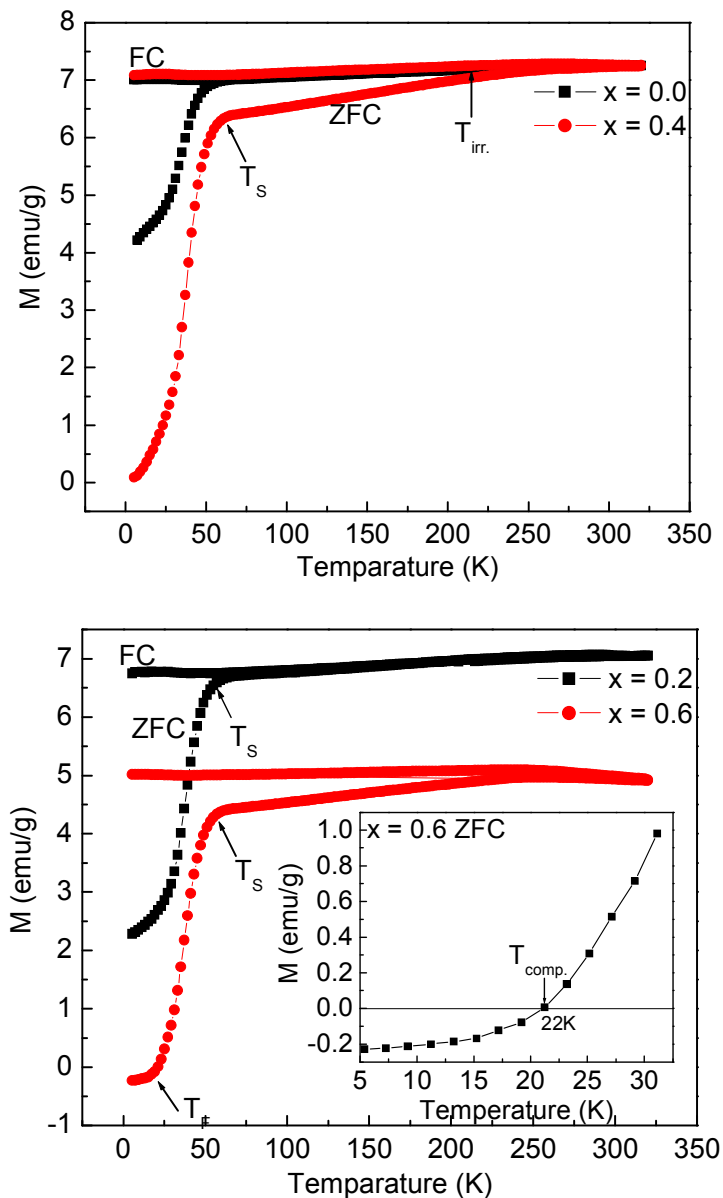


Figure 5.7 Temperature dependence of M_{FC} and M_{ZFC} of Cu-Fe-Al-O system. Inset shows the expanded version of the ZFC mode near the magnetic transition

Table 5.7 Magnetic transition temperature (T) for quenched $\text{CuAl}_x\text{Fe}_{2-x}\text{O}_4$ system.

Al^{3+} - content (x)	T_{irr} (Kelvin)	T_{S} (Kelvin)	$T_{\text{comp.}}$ (Kelvin)
0.0	46	46	-
0.2	55	55	-
0.4	210	60	-
0.6	220	65	22

The following features can be seen from these figures.

(1) All the compositions have shown divergence between FC and ZFC magnetization (i.e. thermo-magnetic irreversibility (T_{MI})).

This is the characteristic feature of all magnetic systems exhibiting magnetic hysteresis behaviour. The FC – ZFC curves bifurcate at about 46K, 55K, 210K and 220K for $x = 0.0, 0.2, 0.4$ and 0.6 compositions respectively. This temperature is referred to as the temperature of irreversibility above with $[(M_{\text{FC}}/M_{\text{ZFC}}) - 1]$ is less than 1%. This suggests that the system is chemically and magnetically homogeneous.

(2) The observed small difference between the FC and ZFC magnetization, flat response of FC magnetization as a function of temperature confirm that all the ferrite compositions studied are low anisotropic materials [25].

(3) We have observed a very broad hump in magnetization curve for $x = 0.4$ and 0.6 compositions in vicinity to temperature of irreversibility (T_{irr}).

This suggests that coercivity for these compositions is much less than the applied magnetic field strength and materials under study are low anisotropy compounds.

(4) For $x = 0.6$ composition ZFC magnetization decreases slowly with decrease in temperature, shows hump centred around 60K, then decreases rapidly, passes through a zero value of magnetization ($M = 0$) at the compensation temperature ($T = 22\text{K}$) (Inset figure). Below this temperature, the magnetization is negative, down to the lowest temperature (4K).

This is due to copper ion moment, with a net effect antiparallel to that of the Fe^{3+} ions with different temperature dependence giving rise to a compensation effect.

(5) We have observed that for all the four compositions, the ZFC curve bifurcate from the FC curve below the temperature, T_{irr} , suddenly falls below T_S and finally saturates at T_F .

Such anomalies at T_S and T_F on the ZFC curves are due to coexistence and interplay between the ferrimagnetic long range ordering and short range ordering in the system [26].

(B) Low field ac susceptibility measurements

Plots of relative low field (0.5 Oe) ac susceptibility, χ_T/χ_{RT} , (RT = room temperature) against temperature (T) for $x = 0.0, 0.2, 0.4$ and 0.6 compositions are shown in Figure 5.8 which exhibit normal ferrimagnetic behavior.

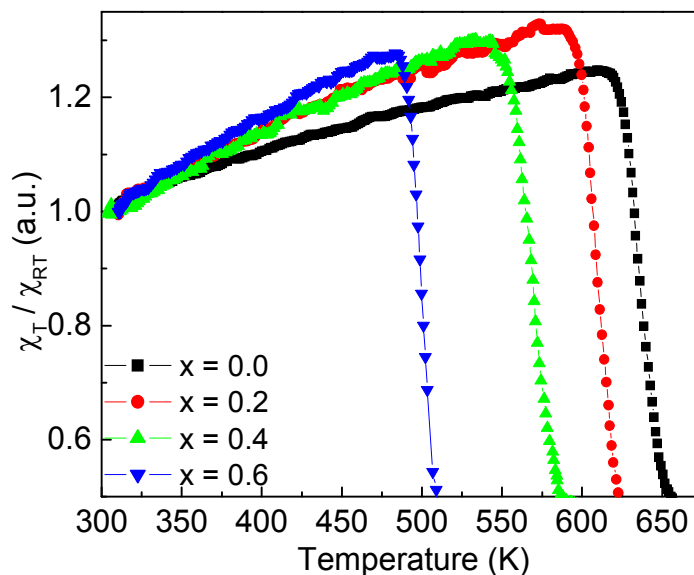


Figure 5.8 Thermal variation of low field ac susceptibility for quenched $\text{CuAl}_x\text{Fe}_{2-x}\text{O}_4$ system for different Al^{3+} -concentration (x).

The Neel temperatures (T_N) determined from ac susceptibility measurements are listed in Table 5.8. It is evident from Table 5.8 that there is a fast decrease in Neel temperature for small addition of aluminum which is due to the decreasing $\text{Fe}^{3+}\text{-O}^{2-}\text{-Fe}^{3+}$ super-exchange linkages resulting from replacement of Fe^{3+} by Al^{3+} in the spinel lattice. In other words the decrease in T_N with increasing Al^{3+} - content (x) suggests reduction in ferrimagnetic ordering and weakening of magnetic coupling.

The Neel temperatures estimated theoretically for the samples with $x = 0.2, 0.4$ and 0.6 using the cation distributions and statistical models based on the modified molecular field theory [27] as described in Chapter 4 (Section 4.4), are in good agreement with the measured values and are given in Table 5.8. The observed difference between experimental and theoretically calculated Neel temperature values is due to the random variation of number of super-exchange

interactions per magnetic ion because of the random distribution of Al^{3+} - ions at the A- and B-sites.

Illustrative calculations for $n(x)$ and $T_N(x)$ determination

$$x = 0.4 \quad (\text{Cu}_{0.15} \text{Fe}_{0.67} \text{Al}_{0.18})^{\text{A}} [\text{Cu}_{0.85} \text{Fe}_{0.93} \text{Al}_{0.22}]^{\text{B}} \text{O}_4$$

$$T_N(x) = \frac{n(x)}{n(x=0)} T_N(x=0.0)$$

$$n(x=0.4) = \frac{24}{1+5(2-0.4)} \left[\frac{(0.85+0.93)}{2} * \frac{(0.15*0.67)}{1} \right]$$

$$= 2.67 [0.89 * 0.82]$$

$$n(x = 0.4) = 1.95$$

$$n(x = 0.0) = 2.18$$

$$T_N(x = 0.4) = (1.95 / 2.18) * 650 \text{ K} = 581 \text{ K}$$

Table 5.8 Neel temperature (T_N) for the quenched $\text{CuAl}_x\text{Fe}_{2-x}\text{O}_4$ system.

Al^{3+} content (x)	n(x)	Neel temperature	
		$T_N(\text{K}) \pm 2\text{K}$	$T_N(\text{Theory})$
0.0	2.18	650	-
0.2	2.06	620	615
0.4	1.95	580	581
0.6	1.83	515	547

All the samples are showing a decrease in normalized susceptibility nearly to zero at Neel temperature indicating that impurity phases are not present in the samples and there is single phase formation. The fact is also evidenced by XRD analysis (section 5.1).

The transition from ferrimagnetic to paramagnetic state is sharp (Figure 5.8), that suggests good quality of structural and microstructural properties as well as presence of magnetic long range order in the samples as evident by large magnetic moment (Table 5.6).

A high temperature asymmetric peak corresponds to ferrimagnetic to paramagnetic transition temperature is result of the two competing agencies, an ordering of spins within the domains and domain wall pinning mechanism [28].

The Neel temperatures for the quenched system are much lower than the slow cooled system of same compositions. Replacement of magnetic Fe^{3+} ($5\mu_B$) with non-magnetic Al^{3+} ($0\mu_B$) and weak magnetic Cu^{2+} ($1\mu_B$) on the B-sites, as evident by cation distributions, decreases $[\text{Fe}^{3+} - \text{O}^{2-} - \text{Fe}^{3+}]$ linkages and therefore transition temperature T_N is decreased. This agrees with previous studies for super-exchange interactions for various oxides [29], which indicated that: Neel temperature or Curie temperature depends primarily upon the number of $[\text{Fe}^{3+} - \text{O}^{2-} - \text{Fe}^{3+}]$ linkages. The Neel temperature, $T_N = 650 \text{ K}$ (Table 5.8) for un-substituted ferrite (CuFe_2O_4) is in excellent agreement to the Neel temperature reported for tetragonal structured (CuFe_2O_4) [29].

5.4 Variation of dc resistivity (ρ_{dc}) as a function of Al^{3+} - content (x) and temperature (T).

The dc resistivity values have been corrected for the pore fraction (f) using the relations [f]: $\rho_{dc} = \rho_p [1+f(1+f^{2/3})^{-1}]^{-1}$. Here, ρ_p is measured values of dc resistivity. It is important to note that this equation seems to hold good for $f < 0.4$. In the present studies f is much less than 0.4, (Table 5.2) one can expect successful application of the above equation.

The compositional dependence of dc resistivity at 403K, is shown in Figure 5.9. It is found that ρ_{dc} (403K) increases with increase in Al^{3+} - content (x) in the system: $\text{CuAl}_x\text{Fe}_{2-x}\text{O}_4$.

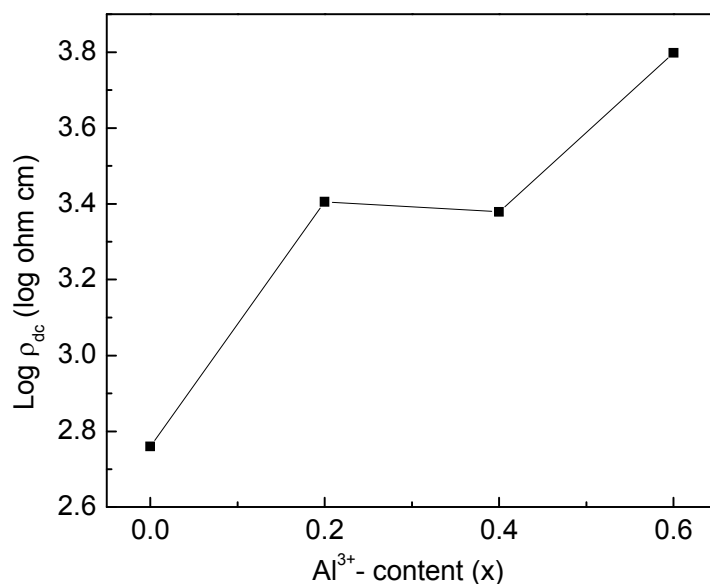


Figure 5.9 Compositional dependence of electrical dc resistivity (ρ_{dc}) at 403K for quenched $\text{CuAl}_x\text{Fe}_{2-x}\text{O}_4$ system.

It is known that non-magnetic cations such as Al^{3+} do not participate in the conduction process. Thus, the substitution of Al^{3+} for magnetic Fe^{3+} ($5\mu_B$) limits the degree of $\text{Fe}^{2+} - \text{Fe}^{3+}$ (or electron exchange) conduction that takes place at the octahedral sites of the spinel lattice.

If the hole exchange between $\text{Cu}^{1+} - \text{Cu}^{2+}$ at the tetrahedral sites of the spinel lattice is responsible for the electrical conduction, then, substitution of Al^{3+} for Fe^{3+} , replace magnetic Cu^{2+} ions ($1\mu_B$) from the A-sites to the B-sites as evident from cation distributions. Thus, observed increase in ρ_{dc} value is rather expected. The high values of resistivity of the order of $\sim 10^3 - 10^4 \Omega\cdot\text{cm}$ near room temperature (300K), suggesting that the ferrite compositions under investigation are good insulators of electricity at 300K.

Phase transition studies on CuFe_2O_4 have been reported extensively in literature [30]. At low temperatures, it exhibits a body centered

tetragonal ($I4_1/amd$) crystal structure with unit cell lattice parameters $a = 8.25 \text{ \AA}$ and $c = 8.65 \text{ \AA}$. Above a phase transition temperature about 663-673K, the crystal structure is face centered cubic ($Fd\bar{3}m$) with $a = 8.40 \text{ \AA}$. The variation in phase transition temperature was either studied as a function of quenching temperature [31] or annealing conditions [32] and was correlated with the variation in cation distributions or oxygen vacancies.

But for CuFe_2O_4 , prepared by ceramic techniques, a lower transition temperature is found. For example, associated anomalies in the temperature dependence of the magnetization [33], the permeability [34], and the specific heat [35] have all been reported near 633K.

Physical properties show variation at phase transformation temperature [30]. Murthy et al [31] have carried out two probe resistivity measurements on CuFe_2O_4 and observed a well defined deviation from the linear decrease in resistivity between 615K and 693K followed by a decrease in resistivity at the phase transition temperature of 693K. For the present samples, we determined the dc resistance at different temperatures. The variations in dc electrical resistivity, ρ_{dc} , with respect to temperature for the pure (CuFe_2O_4 $x = 0.0$) and Al^{3+} -substituted CuFe_2O_4 ($x = 0.2, 0.4$ and 0.6) are compared in Figure 5.10. .

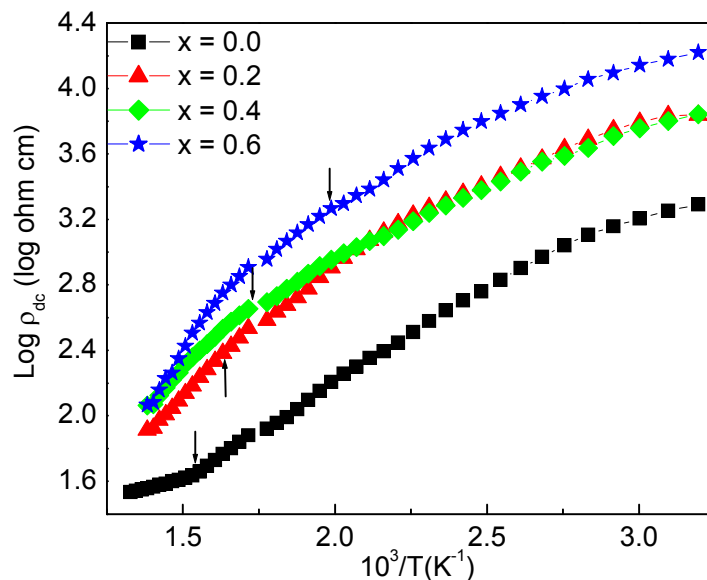


Figure 5.10 Plots showing the variation in electrical resistivity as function of temperature for the pure and Al^{3+} -substitution copper ferrite.

The important features observed from this figure are summarized as: (1) All the compositions show typical semiconducting behaviour, i.e. resistivity decreases with increasing in temperature. (2) The Arrhenius plots for the electrical resistivity for the different ferrite compositions show non-linear variation with temperature. This may be due to the variation in axial ratio (c/a) with temperature [36]. We feel that non-linear variation dc resistivity as a function of temperature is characteristic feature of tetragonal structured copper ferrite based system. (3) We have observed change in the slope in vicinity to temperature that strongly supports the influence of magnetic upon the conduction process [37].

Conclusions

We have investigated the effect of Al^{3+} - substitution on structural, microstructural, magnetic and electrical properties of quenched CuFe_2O_4 system with general chemical formula: $\text{CuAl}_x\text{Fe}_{2-x}\text{O}_4$ ($x = 0.0, 0.2, 0.4$ and 0.6). It has found that

- (1) The ferrite compositions possess tetragonally distorted spinel structure, due to rapid thermal quenching induced large B-site occupancy of Jahn-teller ion (Cu^{2+}) in system.
- (2) The axial ratio (c/a) can be used to determine the concentration of Cu^{2+} ion on the octahedral site of the spinel lattice, stress, strain produced due to square bond formation.
- (3) The magnetic measurements suggest that the ferrite compositions are low anisotropy compounds, the negative magnetization for $x = 0.6$ composition is due to the copper ion moment with a net effect antiparallel to that of the Fe^{3+} - ions with different temperature dependence giving rise to a compensation effect.
- (4) The anomalies at T_S and T_F on the ZFC curves are due to coexistence and interplay between the ferrimagnetic long range ordering and short range ordering in the system.
- (5) The non-linear thermal dependence of dc resistivity is due to the variation in axial ratio (c/a) with temperature.
- (6) Finally it is concluded that the thermal history and heat treatments play an important role in controlling the materials properties.

References

- [1] C. Dong, *J. Appl. Cryst.* 32(1999)838.
- [2] S. S. Ata-Allah and A. Hashhash, *J. Magn. Magn. Mater.* 307 (2006) 191.
- [3] J. Darul, *Z. Kristallogr. Suppl.* 30(2009)335.
- [4] H. M. Rietveld, *J. Appl. Cryst.* 2(1969)65.
- [5] B. H. Toby, *Powder diff.* 21(1) (2006) 67.
- [6] A. B. Naik, S. A. Patil and J. I. Powar, *J. Mater. Sci.* 7(1988)1034.
- [7] I. Nedkov, R. E. Vandenberghe, Ts. Marinova, Ph. Thailhades, T. Merodiiska, and I. Avramova, *Appl. Surf. Sci.* 253(2006)2589.
- [8] X. X. Tang, A. Manthiram and J. B. Goodenough, *J. Solid State Chem.* 79 (1989) 250.
- [9] J. B. Goodenough, in: F. A. Cotton (Ed.) *Magnetism and the chemical bond*. Vol. 1, Inter-Science, Wiley, New York, 1963.
- [10] J. B. Goodenough and A. L. Loeb, *Phys. Rev.* 98(1955)391.
- [11] K. J. Kim, J. H. Lee, and S. H. Lee, *J. Magn. Magn. Mater.* 279(2004)173.
- [12] M. D. Sturge, in: F. Seitz, D. Turnbull, H. Ehrenreich (Eds.) *Solid State Physics*, Vol. 20, Academic Press, New York, 1967.
- [13] B. D. Cullity, *Elements of x-ray diffraction*, 2nd Edn. Addison Wesley Pub. Co. Reading MA 1978.
- [14] E. F. Bertaut, *J. Phys. Radium* 12(1951)252.
- [15] M. J. Buerger, *Crystal Structure Analysis*, Wiley, NY, 1960.
- [16] V. K. Lakhani and K. B. Modi, *Solid State Sci.* 12 (2010) 2134.
- [17] Alex Goldman, *Modern ferrite technology*, 2002, 2nd Ed, Pittsburgh, PA, USA.

- [18] D. Thapa, N. Kulkarni, S. N. Mishra, P. L. Paulose and P. Ayyub, J. Phys.D.: Appl.Phys. 43 (2010) 195004 (5pp).
- [19] H. Bhargava, N. Lakshmi, V. Sebastian, V. R. Reddy, K. Venugoplan, and Ajay Gupta, J. Phys. D: Appl. Phys. 42(2009)245003(8pp).
- [20] M. Desai, S. Prasad, N. Venkataramani, I. Samajdar, A. K. Nigam, and R. Krishan, J. Appl. Phys. 91(4)(2002)2220.
- [21] A. Yang, Z. Chen, Xu. Zuo, D. Arena, J. Kirkland, C. Vittoria, and V. G. Harris, J. Appl. Phys. 86(2005) 252510(1-3).
- [22] R. M. Persoons, E. de Grave, P.M.A. de Bakker, and R. E. Vandenberghe, Phys. Rev. B. 47(1993)5894.
- [23] P. S. Anil Kumar, P. A. Joy, and S. K. Date, Bull. Mater. Sci. 23(2) (2000)97.
- [24] A. Rosencwaig, J. Phys. 48(1970) 2857.
- [25] P. A. Joy, P. S. Anilkumar and S. K. Date, J. Phys. Condens. Matter 10(1998)11049.
- [26] L. R. Maxwell and S. J. Pickart, Phys. Rev. 92(5)(1953)1120.
- [27] G. J. Baldha, R. V. Upadhyay and R. G. Kulkarani, J. Mater. Sci. 23 (1988)3357.
- [28] V. K. Lakhani, B. Zhao, L. Wang, U. N. Trivedi and K. B. Modi, J. Alloys. Compd. 509(2011)4681
- [29] S. S. Ata-Allah and M. Yehia, Physics B 404 (2009) 2382.
- [30] D. Prabhu, A. Narayanasamy, K. Shinoda, B. Jeyadeven, J. M. Greneche and K. Chattopadhyay, J. Appl. Phys. 109(2011)013532.

- [31] K. S. R. C. Murthy, S. Mahantly and J. Ghose Mater. Res. Bull. 22(1987)1665.
- [32] C. Bauber, Ph. Tailhades, C. Bonningue, A. Rousset and Z. Simsa, J. Phys. Chem. Solids 61 (2000)863.
- [33] T. Takei, J. Ist. Elect. Eng. Japan 59(1939)274.
- [34] K. Stierstadt, Z. Phys. 146(1956)169.
- [35] T. Innone and S. Iida, J. Phys. Soc. Japan 13(1958)656.
- [36] Xiao-Xia Tang, A. Manthiram and J. B. Goodenough, J. Solid State Chem. 79(1989)250.
- [37] S. A. Mazen and B. A. Subrah, Thermochim Acta 105 (1986)1.